LONDON'S GLOBAL UNIVERSITY

ON THE OBLIQUE REFLECTION OF A SOLITARY WAVE

by

Qicheng Meng

Principal Supervisor: Prof Guo Xiong Wu

Second Supervisor: Dr Yuriy Semenov

A thesis submitted for the degree of

Doctor of Philosophy

Marine Research Group

Department of Mechanical Engineering

University College London

September 2016

Dedicated to Dr Beiying Zhu

Declaration

I, Qicheng Meng, confirm that the work presented in this thesis is my own. Where information has been derived from other sources, I confirm that this has been indicated in the thesis.

Signature……

Date……...

ABSTRACT

The solitary wave is a gravity water wave that travels with permanent shape and constant phase speed. It has long characteristic wavelength in the longitudinal direction and uniform transverse cross-sections. The present study is concerned with both the surface solitary wave on a homogeneous fluid and the internal solitary wave within a rigid-lid two-layer model. When two identical solitary waves with different propagation directions interact with each other, the collision problem can be converted to an oblique reflection problem replacing the symmetric plane with a rigid slip wall. This work focuses on a specific scenario called the Mach reflection. It is a strongly nonlinear phenomenon. Based on the existing theoretical and experimental research on the surface solitary wave, study has been extended to the internal solitary wave. The analyses are mainly based on the 3D fully nonlinear simulations utilising the CFD software OpenFOAM on UCL's supercomputers. The third-order weakly nonlinear solution of an internal solitary wave has been derived and used to initialise the flow field in corresponding simulations. The code has been verified and validated through test cases on a single solitary wave and 2D collisions. The oblique reflection of a surface solitary wave with moderate amplitude has been simulated. Large-amplitude wave induced by the Mach reflection as observed in the experiment has been analysed. Two cases for internal solitary waves have been simulated where the incident wave amplitudes are small and moderate, respectively. The KP theory is only valid for the small-amplitude case. The wave profile of the moderate-amplitude case shows some distinct features that cannot be well predicted by the existing approximate models. Analyses have also been made on the physical quantities in terms of mass, momentum and energy to understand the transverse variation of the wave field. The research benefits the understanding of rogue waves

induced by long wave interaction in order to protect life and property at coastal areas and in deep sea operations.

ACKNOWLEDGEMENT

I would like to express my sincere gratitude to my principal supervisor Prof. G.X. Wu. He devoted himself to the academic achievement and wellbeing of his students. His guidance is always helpful and profound. I would like to quote his words: “Reality->law in physics->mathematical model (equations)->solution (analytical or numerical)->results (their physics and implications)->applications->new products & technology…->…. There is originality in any part of this chain.” That teaching alone can benefit my whole career. I also own my gratitude to my secondary supervisor Dr Y. Semenov for his full support.

I am truly grateful to the sponsors. Thanks to Lloyd’s Register Foundation (LRF) through the joint centre involving University College London, Shanghai Jiaotong University and Harbin Engineering University. Lloyd’s Register Foundation helps to protect life and property by supporting engineering-related education, public engagement and the application of research. Thanks to the Erasmus Mundus Europe Asia (EMEA) scholarship programme, Faculty of Engineering of University College London, the Henry Lester Trust Ltd. and the CISN hardship fund. I acknowledge the use of the UCL High Performance Computing facilities (Legion@UCL, Grace@UCL and IRIDIS), and associated support services, in the completion of this work. The support from Research Data Services of UCL is also most appreciated.

The study of ocean waves involves a wide range of knowledge. I would like to extend thanks to the scholars who have helped me including Prof Y. Chen, Prof A.K. Liu, Prof C. Yang, Prof D.J. Li, Prof N.K. Liang, Prof C.Z. Wang, Prof H.C. Khoo, Prof J. Grue, Prof R. Grimshaw, Dr Z. Wang, Dr B. Yao, Dr J. Chen, Dr S. Balabani and Ms E. Muk-Pavic. I owe my thanks to Prof G. Sewell for the support of the

software PDE2D. I acknowledge Dr W. Suen who is my tutor. I also learnt a lot from the collaborations with my colleagues, and I am also grateful to them, to name a few, Dr G.D. Xu, Dr B.Z. Zhou, Dr B.Y. Ni, Dr M. Lai, Dr B. Song, Dr C. Zhang, Dr H.C. Huang, Y. Li, A. Charlotte, P. Wang, Dr P. Boselli, Dr S.L. Sun, Dr. Y. Liu, K. Ren. I would like to thank all my friends and the Bahai community for the social support. Special remembrance goes to Yang Chen.

Last, but not least, I would like to acknowledge the family support from my wife Dr Beiying Zhu, my parents, my parents-in-law and all other family members.

TABLE OF CONTENTS

List of Figures

List of Tables

Nomenclature

➢ Abbreviations

1/2/3D	One/Two/Three dimensional
AMR	Adaptive Mesh Refinement
B-O	Benjamin-Ono
CD	Central Differencing
CFD	Computational Fluid Dynamics
CICSAM	Compressive Interface Capturing Scheme for Arbitrary Meshes
DNS	Direct Numerical Simulation
DILU	Diagonal based Incomplete LU
eKdV	Extended Korteweg-de Vries
EKP	Extended Kadomtsev-Petviashvili
FDM	Finite Difference Method
FEM	Finite Element Method
FVM	Finite Volume Method
GAMG	Geometric-Algebraic Multi-Grid
GN	Green-Naghdi
HPC	High Performance Computing
HSV	Hue, Saturation, Value
IEEE	Institute of Electrical and Electronics Engineers
ISW	Internal solitary wave
IWISE	Internal Waves in Straits Experiment
KdV	Korteweg-de Vries
K-H	Kelvin-Helmholtz
KP	Kadomtsev-Petviashvili
LHS	Left Hand Side
LIF	Laser-Induced Fluorescent
MCC	Miyata-Choi-Camassa
mKdV	Modfied Korteweg-de Vries
MUSCL	Modified Upwind Scheme for Conservation Laws
MULES	Multidimensional Universal Limiter for Explicit Solution
NOAA	National Oceanic and Atmospheric Administration
NS	Navier-Stokes
NWT	numerical wave tank
ODE	Ordinary Differential Equation
OpenFOAM	Open Field Operation and Manipulation

PBiCG	Preconditioned bi-Conjugate Gradient
PCHIP	Piecewise Cubic Hermite Interpolating Polynomial
PDE	Partial Differential Equation
PDE2D	A general purpose finite element program, solves 1D, 2D and 3D PDEs
PISO	Pressure Implicit with Splitting of Operator
PLIC	Piecewise-Linear Interface Calculation
RHS	Right Hand Side
SAR	Synthetic Aperture Radar
SCS	South China Sea
SIMPLE	Semi-Implicit Method for Pressure-Linked Equations
SLIC	Simple Line Interface Calculation
SSW	Surface Solitary Wave
TVD	Total Variation Diminishing
VOF	Volume Of Fluid
WISC	Worldwide Internal Soliton Criteria

- **Subscripts**

1	Lower layer
2	Upper layer
c	Characteristic
$eKdV$	eKdV equations
f	The value of the variable in the middle of the face
i	Incident wave
n	Normal direction
r	Reflected wave
KdV	KdV equations
M	Mach stem wave
MCC	MCC equations
S	Surface waves

- **Roman letters**

a	Maximum surface/interface displacement
$\hat{a}$	Physical maximum surface/interface displacement

a_{ij}	Component in the coefficient matrix $\mathbf{A}$ for the analytical solution of the KP equation
$a_{\lim}$	Limiting interface displacement given by the eKdV equation
$a_{\max}$	Limiting interface displacement given by the MCC model
amr_1, amr_2	Scalar field for the AMR
c	The internal wave phase speed
c_0	The phase speed of the infinitesimal linear periodic internal wave
c_S	The surface wave phase speed
c_{S0}	The phase speed of the infinitesimal linear periodic surface wave
$d1$ to $d7$	Dimensions of the 3D computational domain
f	Function
g	Magnitude of gravity
$\mathbf{g}$	Gravitational acceleration (vector)
h	Depth of the lower layer
h_0	Nominal depth for the transformation of the KP and EKP equation
h'	Intrinsic length scale
h_S	The quiescent water depth in the surface wave problem
i	Integer
$\bar{k}$	Wave number of linear periodic waves
k	Interaction parameter in the theory by Miles (1977 a, b)
$\mathbf{n}$	Unit normal vector
p	Pressure
p_{rgh}	Pseudo-dynamic pressure
q^*	Nondimensional continuity quantity in the numerical calculation of the KP and EKP equation by PDE2D
r	H/h
t	Time
Δt	Time step
$\mathbf{u} = (u, v, w), \mathbf{u}' = (u', v', w')$	Velocities in the *O-xyz* coordinate system and *O'-x'y'z'* coordinate system, respectively
$\mathbf{u}_r$	Compression velocity
$\bar{u}$	Layer-mean horizontal velocity
x_0	The initial position
$\mathbf{x}$	The position vector

$(x, y, z), (x', y', z')$ Coordinates

A	The coefficient matrix for the analytical solution of the KP equation
A^*	Wave amplitude in the standard form of the KP equation or the EKP equation
C	Constant/Coefficient
C_{amr1}, C_{amr2}	Coefficients in the AMR algorithm
Co	The maximum Courant number
D	The coefficient of the cubic nonlinear term in the standard form of the EKP equation
E	Total energy
E_K	Kinetic energy
E_P	Potential energy
F	Froude number
F_D	Drag force
F_I	Inertial force
F_h	Hydrodynamic force
H	Total depth in the rigid-lid two-layer model
I	Wave momentum
K^*	Interaction parameter for the standard form of the KP equation
L	The length of the 2D numerical wave tank
L_M	The length of the Mach stem wave
M	Excess mass
Q	The volume flow per unit span
R	The energy per unit span
S	The total force plus momentum flux per unit span
U	The velocity of the uniform flow at infinity
Wr	The Wronskian determinant
(X, Y, Z)	Coordinates in the moving Cartesian coordinate system
$(X^*, Y^*, Z^*), (x^*, y^*, z^*)$	Coordinates
X_S	Function

- **Greek letters**

α	Strain factor in Chapter 3; volume fraction in the CFD notation
β	Small parameter measuring dispersion

γ	Coefficient
δ	ρ_2/ρ_1
ε	Small parameter measuring nonlinearity
η	The surface/interface excursion with respect to the bottom
θ	The surface/interface excursion with respect to the undisturbed water level
$\hat{\theta}$	Physical surface/interface displacement
κ	The modified interaction parameter by Li et al.(2011)
λ	Wavelength
λ_{Sc}	The characteristic wavelength of a surface solitary wave
λ_c	The characteristic wavelength of an internal solitary wave
π	Ratio of the circumference of a circle to its diameter
ρ	Density
σ	Coefficients in the *tau* function
τ	*Tau* function in the Hirota's direct method
ψ	The angle between a line solitary wave and the *y* coordinate
ψ_i	Incident wave angle
ψ_r	Reflected wave angle
ψ_M	Angle of stem-wave development, Mach stem step angle
χ	Amplification
ω	Frequency of linear periodic waves
Δ	Interval
Θ^*	Nondimensional surface/interface displacement in the standard form of the KP equation
Π	Incomplete elliptic integral of the third kind
Φ	Velocity potential
Ψ	Stream function
Ω	Fluid domain

Chapter 1 Introduction

1.1 Background and introduction

1.1.1 Surface solitary waves

The discoveries of new physical phenomena often inspire developments in mathematics. Vice versa, features of new solutions of the governing equations may be observed in the laboratory or in the field. The study on solitary waves is such an example. Breakthroughs on this subject have been continuously made over the last two centuries, and they are closely related to engineering applications.

In 1834, while doing experiments for canal boats, John Scott Russel discovered a phenomenon, which he called wave of translation later in his work (Russell, 1838). He described the phenomenon (Russell, 1844): "I was observing the motion of a boat which was rapidly drawn along a narrow channel by a pair of horses, when the boat suddenly stopped - not so the mass of water in the channel which it had put in motion; it accumulated round the prow of the vessel in a state of violent agitation, then suddenly leaving it behind, rolled forward with great velocity, assuming the form of a large solitary elevation, a rounded, smooth and well-defined heap of water, which continued its course along the channel apparently without change of form or diminution of speed. I followed it on horseback, and overtook it still rolling on at a rate of some eight or nine miles an hour, preserving its original figure some thirty feet long and a foot to a foot and a half in height. Its height gradually diminished, and after a chase of one or two miles I lost it in the windings of the channel. Such, in the month of August 1834, was my first chance interview with that singular and beautiful phenomenon which I have called the Wave of Translation."

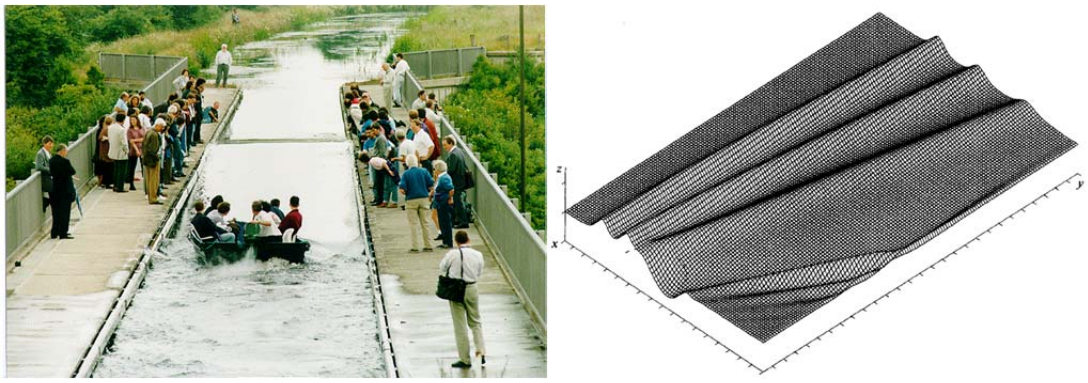

(a) **(b)**

Fig. 1-1 (a): Recreation of a solitary wave on the Scott Russell Aqueduct on the Union Canal near Heriot-Watt University, 12 July 1995. Photograph courtesy of Heriot-Watt University. (*Source: Nature v. 376, 3 Aug 1995, p. 373*) (b): The solitary-wave-like wave pattern in an unbounded fluid generated by a pressure advancing in the *xz*-plane. Photograph courtesy of Pedersen (1988). (*Source: J. Fluid Mech. v. 196, 1988, p. 39-63*)

This wave has a more commonly used name, "solitary wave". Hereman (2011) defined a solitary wave, from the physical perspective, as a localised gravity wave that maintains its coherence, and has a constant shape and propagates with constant speed. The wave has the same cross sections along its transverse direction, and can be generated in a canal by floating bodies as shown in Fig. 1-1(a) or submerged bodies (Xu and Meng, 2016). Interestingly, some solitary-wave-like wave patterns in open water also have quasi-2D features (Fig. 1-1(b)), which indicates the broad applications of the research on ideal 2D solitary waves.

Another name for the surface solitary wave (SSW), "soliton", arose from the study on collisions of two or multiple solitary waves in 2D space. Through numerical integration of the Korteweg-de Vries (KdV) equation, which contains the analytical solution for a single solitary wave, Zabusky and Kruskal (1965) found solitary waves conserved their shapes and speeds after collisions except for a phase shift. This behaviour is similar to particles or photons, and the term, "soliton", was therefore proposed (Zabusky and Kruskal, 1965).

A significant application of the SSW model is to study tsunamis, though the paradigm has been being continuously examined (Madsen et al., 2008). The enormous energy the SSW carries is not scattered via the dispersive effect or dissipated through wave breaking owing to the nonlinear effect. It can travel a long distance across the ocean with a high phase speed and eventually release the energy due to the shoaling effect, which results in flood at coastal areas. The interaction between the SSW and the floating offshore structure has also been paid attention to (Zhou et al., 2016). More details of SSWs can be found in the literature by Miles (1980)， Miles (1981), Schwartz and Fenton (1982), Akylas (1994), Grimshaw (2007).

1.1.2 Internal solitary waves

In addition to surface waves, there are also internal waves underneath the sea surface. As we know, the water in the ocean is stratified in terms of various physical properties (Fig. 1-2). Usually, there is a thin layer called pycnocline or thermocline beneath the surface (roughly the yellow portion in Fig. 1-2), where the density, temperature and conductivity has the largest variation in the vertical direction (Stewart, 2008). Above the pycnocline up to the free surface, the density is lower and the temperature is higher. Beneath the pycnocline down to the bottom, the density is higher and the temperature is lower. The profiles of density, temperature and salinity are relatively uniform within the upper and lower layers. If we replace the pycnocline with an interface between two homogeneous fluids, it yields a two-layer model. Even if the free surface is relatively calm, the internal waves can still induce large displacement of the interface. If an internal wave meets the properties of a solitary

wave, which has a permanent shape with a local peak and propagates with constant speed, it can be called an internal solitary wave (ISW).

Scientists have now found that ISWs are ubiquitous in the ocean. The observations were inspired by the pioneer theoretical deduction within the two-layer model (Keulegan, 1953; Long, 1956). In the 1960s to 1970s, with the development of ocean instrumentation and remote sensing, long nonlinear internal waves began to attract attention of oceanographers (Helfrich and Melville, 2006). Satellites can capture the manifestations of ISWs on the ocean surface (Ray and Mitchum, 1996). On the Synthetic Aperture Radar (SAR) image, each bright (greater surface roughness) and dark (less surface roughness) curvilinear band represents an individual ISW (Fig. 1-3 Layer b). Satellite images can provide precise locations and morphologies of the internal waves, but the accurate measurement of the wave amplitude still needs in-situ measurements including shipboard measurements, glider measurements, moored measurements and *etc.* (Fig. 1-3 Layer c) (Alford et al., 2015). Perry and Schimke (1965), in Andaman Sea, observed the packets of internal waves up to 80m large (in the vertical direction) and 2000m long (in the propagation direction) in 1500m deep water. Osborne and Burch (1980) found that ISWs in Andaman Sea agreed well with the KdV theory. More satellite image evidences can be found in the atlas by Jackson and Apel (2004). Recent in-situ and remote sensing observations have revealed ISWs of very large amplitude. In South China Sea (SCS), where the total depth of the water is approximately 340m and upper-layer depth is approximately 40m, Duda et al. (2004) observed an internal solitary wave of depression with an amplitude of about 150m (Fig. 1-2). Other evidence also shows the frequent activities of strongly nonlinear ISWs in SCS (Liu et al., 1985; Liu et al., 1998; Liu et al., 2004; Yang et al., 2004; Klymak et al., 2006; Cai et al., 2012; Guo

and Chen, 2014; Alford et al., 2015). From Fig. 1-3 Layer b, one can see the transverse length of an ISW can be up to several hundred kilometres. Thus it is appropriate to study the wave in 2D space when the transverse variation is not the concern. With the development of the computational capacity, the 3D numerical modelling has also been put on the agenda (Fig. 1-3 Layer a) (Alford et al., 2015).

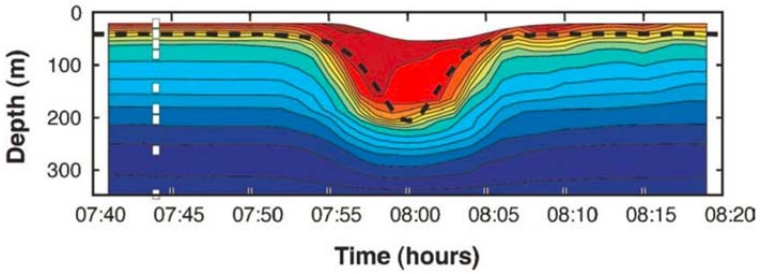

Fig. 1-2 Temperature variation history measured by the thermometers (white squares) in the northeast South China Sea. The contour interval is 1 ℃. The yellow colour indicates the location of the pycnocline. The black dashed line shows the ISW solution of the KdV equation based on the two-layer model. Photograph courtesy of Duda et al. (2004). (*Source: IEEE Journal of Oceanic Engineering v. 29, 2004, p. 1105-1130*)

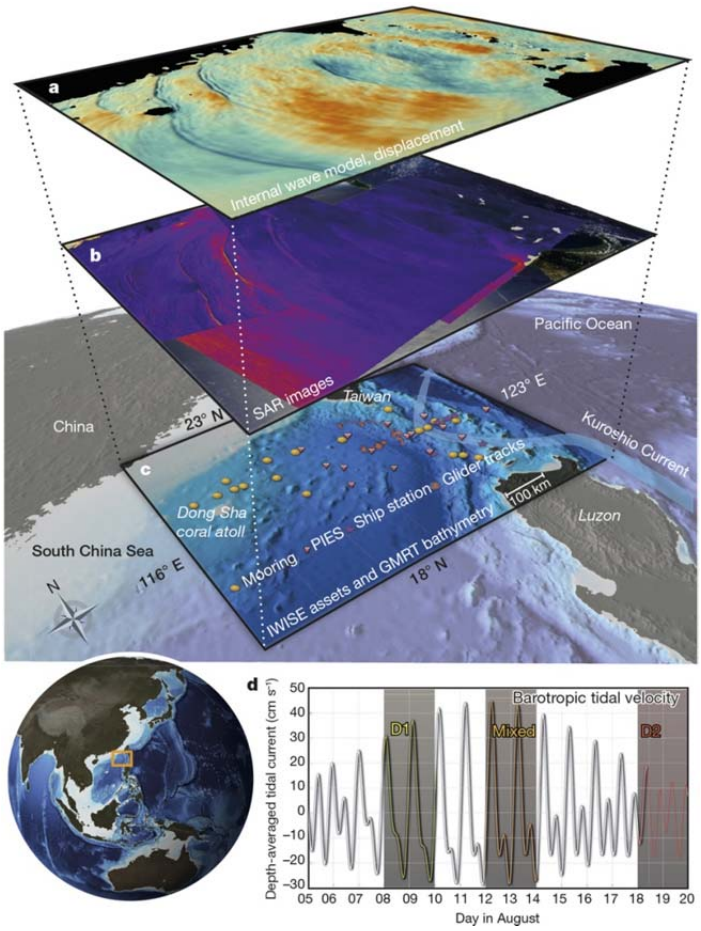

Fig. 1-3 Overview of internal waves in the South China Sea. Layer a: Numerical simulation of the displacement of pycnocline. Orange and blue indicate upward and downward excursions, respectively. Layer b: The Synthetic Aperture Radar (SAR) image from the same area. Red and blue correspond to greater and less surface roughness, respectively. Layer c: Schematic of instrumentation deployment during the Internal Waves in Straits Experiment (IWISE). Bottom right: Time series of depth-averaged tidal current in Luzon Strait. Bottom left: Globe showing location of Luzon Strait and South China Sea. Photograph courtesy of Alford et al. (2015). (*Source: Nature v. 521, 2015, p. 65-69 doi: 10.1038/nature14399*)

The threat to offshore installations in deep water posed by ISWs has been continuously addressed by oceanographers such as, Osborne et al. (1977) and Jackson et al. (2013). Chen (1996) reported a passing internal wave which broke the mooring cable and pulled down the floating hoses in the test operation at Liuhua oilfield in the northern SCS. The Worldwide Internal Soliton Criteria (WISC) project for offshore industry has been initiated (Jeans et al., 2012). There has been research on the hydrodynamic loads on the ocean structure exerted by an ISW, *e.g.*, by Song et al. (2011) and Lee and Yan (2012). Through the length scale analyses between the wave and frequently-used cylindrical structure, the predominant wave force can be roughly evaluated. The amplitude of an ISW can range from a few meters to greater than 100m (Jackson et al., 2013). Suppose an ISW with amplitude of 50m located in a 1000m deep ocean and the pycnocline is approximately 250m beneath the sea surface. The characteristic wavelength is approximately 1000m based on the KdV theory. The wave takes more than 10min to travel four characteristic wavelengths. The diameter of a typical marine riser is around 1m. The diameters of column components of semi-submersible platforms and tension leg platforms are around 10m. The diameter of a cylindrical hull of a Spar platform can be up to 40m. Hence, the radial dimensions of present deep-sea drilling structures can be deemed as short compared with ISWs. The Morison's empirical formula can be used to estimate the forces and torques on cylindrical piles exerted by ISWs (Cai et al., 2003; Cai et al.,

2006； Cai et al., 2008). It is noted that the Morrison formula relies on the knowledge of the flow field undisturbed by the presence of the structure. Provided the prediction given by the Morrison formula was adequate for engineering applications, the deeper understanding of the flow field induced by the wave-wave collision, would still be necessary.

1.1.3 Oblique collisions of solitary waves

In the nature, waves often interact in 3D space, namely, oblique collisions (Figs. 1-4(a) & (b)) (Ablowitz and Baldwin, 2012; Sarbarish and Yuji, 2014). The oblique interaction of SSWs is one of the causes of rogue waves in the ocean (Fig. 1-5) (Kharif and Pelinovsky, 2003; Peterson et al., 2003; Grimshaw et al., 2010). Wiegel (1964) collected the evidence at Hilo, Hawaii, which is vulnerable to tsunamis originated from Alaska or Chile. He reported the extraordinarily high run-up along the cliff, which resulted in the flood into the town. It can be explained by the findings on obliquely interacting solitary waves. As to internal waves, their oblique interactions can be commonly observed in satellite images and aerial photographs (Figs. 1-6(a) & (b)) (Jackson and Apel, 2004; Ramp et al., 2004; Jackson et al., 2013). However, there has been far less research on oblique collisions of ISWs (Helfrich and Melville, 2006). Wang and Pawlowicz (2012) have pointed out that "few (if any) quantitative field measurements" on this subject, especially for large-amplitude ISWs, have been made until recently.

(a)

(b)

Fig. 1-4 (a): Crossing swells. Photograph courtesy of Michel Griffon (2011). (*Source: https://upload.wikimedia.org/wikipedia/commons/3/3e/Ile_de_r%C3%A9.JPG*). (b): A photograph of an X-type interaction between two solitary waves. Photograph courtesy of Ablowitz and Baldwin (2012) (*Source: Phys. Rev. E v. 86, 2012, p. 036305*)

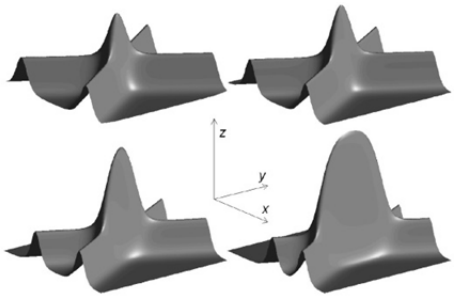

Fig. 1-5 Surface profiles in the interactions of two solitary waves for various angles. Photograph courtesy of Peterson et al. (2003). (*Source: Nonlinear Processes in Geophysics v. 10, 2003, p. 503-510*)

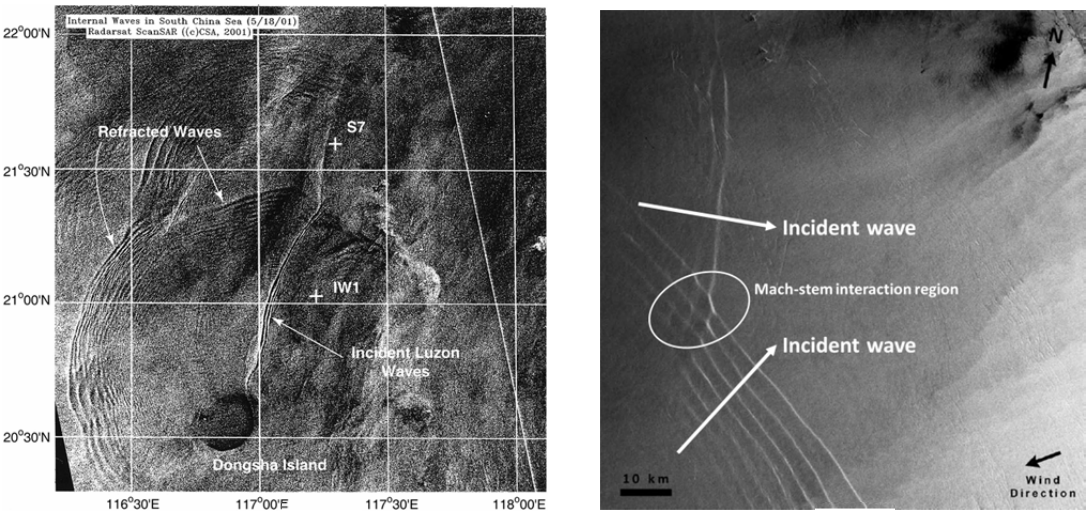

(a) **(b)**

Fig. 1-6 (a): The image of interacting refracted waves around Dongsha Island took by Synthetic Aperture Radar (SAR) on 18th May 2001. Photograph courtesy of Ramp et al. (2004). (*Source: IEEE Journal of Oceanic Engineering v. 29, 2004, p. 1157-1181*) (b): The so-called Mach-stem interaction pattern of two packets of internal solitary waves in the Andaman Sea at 18:20 UTC on 18th November 2006. The original image has been processed with annotations. Photograph courtesy of Jackson et al. (2013). (*Source: Oceanography v. 26(2), 2013, p. 68-79*)

In order to sketch the wave interaction patterns, we can connect the crests or troughs at the transverse cross sections of the wave field to form a crest/trough line in the plan view as shown in Fig. 1-7. The thicker crest/trough line indicates the larger wave amplitude, and the arrow indicates the propagation direction (Fig. 1-7). The

classification in Fig. 1-7 is based on the asymptotic theories for SSW collisions put forward by Miles (1977a, b) with the assumptions of the long longitudinal length scale, small amplitude and mild transverse variation. On-going experimental and numerical efforts are being performed to validate the theories, though it is far away from exhausting all the cases (Melville, 1980; Tanaka, 1993; Li et al., 2011). Taking into account the similar properties of ISWs as those of SSWs especially when the amplitude is small, the classification has been also introduced to the collisions between ISWs, *e.g.*, by Wang and Pawlowicz (2012).

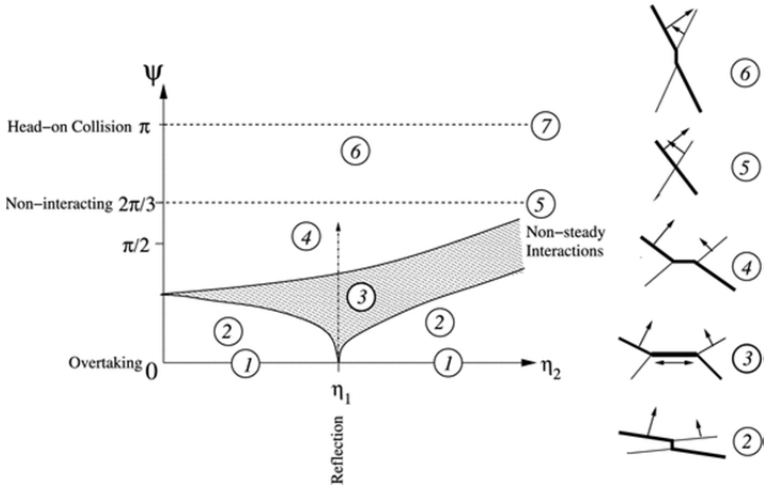

Fig. 1-7* **Categorical diagram for two obliquely crossing solitary waves. η is wave amplitude in this specific figure. The subscripts 1, 2 mark the two interacting waves in far field. Ψ is the interaction angle between the normals of the two waves in this specific figure. At left is shown the regimes for different interactions in a (η_2, Ψ) parameter space. Cases are (1) overtaking, (2) obliquely overtaking, (3) non-steady Mach interaction, (4) regular interaction, (5) non-interacting at $\Psi=2\pi/3$, (6) obliquely colliding, (7) head-on colliding. At right are shown schematic overhead views of the interaction cases by wave crest lines. The wave with larger amplitude is represented by the thicker line. Arrows show the propagation direction and phase speed (the length of the arrow). Photograph courtesy of Wang and Pawlowicz (2012).** ***(Source: J. Geophys. Res., v. 117, 2012, p. C06031)***

The research objective is narrowed down to a simpler scenario. Initially a semi-infinite long solitary wave, taking an SSW as an example, is placed against an

* The nomenclature used in the figure is different from that in the rest of the thesis

infinite long reflection wall at *y'*=0 (Figs. 1-8(a) & (b)). It is propagating towards the reflection wall but with an inclination. The angle between the crest line of the incident wave and the *y'*-axis is the incident wave angle ψ_i, and $0 < \psi_i < 90°$. In the experiment, it can be approximately realised by placing an oblique wave guide in a rectangular wave tank, and the free traveling solitary wave will encounter the wave guide (Fig. 1-9). This scenario, *i.e.*, an incoming wave impinging onto a reflection wall, is equivalent to the interaction between itself and its image about the *x'*-axis, for the frictionless boundary conditions of the wall happen to be the same as the conditions on the symmetric plane. Hence, this initial condition is called the V-shape initial condition conventionally. Intuitively, a reflected wave would elongate while the incident wave is being shortened owing to the reflection wall, and the reflected wave would approach the image of the incident wave about the normal direction to the reflection wall. In other words, the reflected wave angle ψ_r would be equivalent to ψ_i, and the wave profile at a transvers cross section of the reflected wave away from the reflection wall would become as same as that of the incident wave. This pattern can be called the regular reflection. Perroud (1957) found, in the experiment, when $45° < \psi_i < 90°$, a wave pattern that is similar to the regular reflection shown in Fig. 1-8(a) gradually formed with the elongation of the reflected wave. In addition, a hump formed shortly after the impingement and remained steady afterwards. However, when $20° < \psi_i < 45°$, Perroud (1957) found that a quasi-2D stem wave that was perpendicular to the reflection wall formed and its transverse length L_M grew with time. Hence the apex between the crest lines of the incident wave and the reflected wave moved away from the reflection wall. The angle between the trajectory of the apex and the *x'*-axis is called angle of stem-wave development or

Mach stem step angle denoted by ψ_M. The reflected wave also elongated, but $\psi_r > \psi_i$. The amplitude of the well-developed reflected wave a_r is smaller than the incident wave amplitude in the far field a_i. This phenomenon is quite similar to what has been found in aerodynamics, *i.e.*, when a shock wave impinges onto an oblique wall with a small incident angle, a third shock wave perpendicular to the wall forms (von Neumann, 1943). The water wave pattern was then named after the "Mach reflection". Miles (1977b) put forward an asymptotic theory ($t \to \infty$) and predicted that the amplitude of the stem wave a_M can be up to fourfold with respect to a_i asymptotically. The abnormal high amplitude of the stem wave and its elongating nature may cause severe disaster.

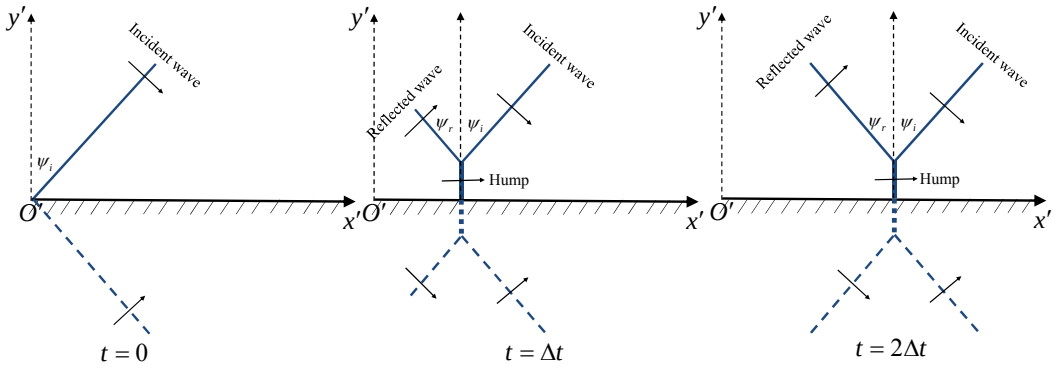

(a) Regular reflection

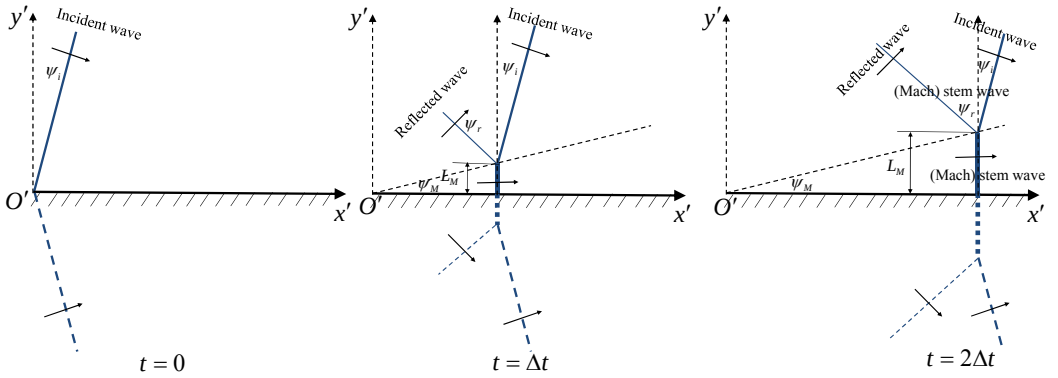

(b) Mach reflection

Fig. 1-8 Schematics of the regular reflection (a) and the Mach reflection (b) in plan views. The solid blue lines represent the crest lines. Their widths represent the wave amplitudes. The thicker is the crest line, the larger is the wave amplitude. *t* is time and Δt is the time interval.

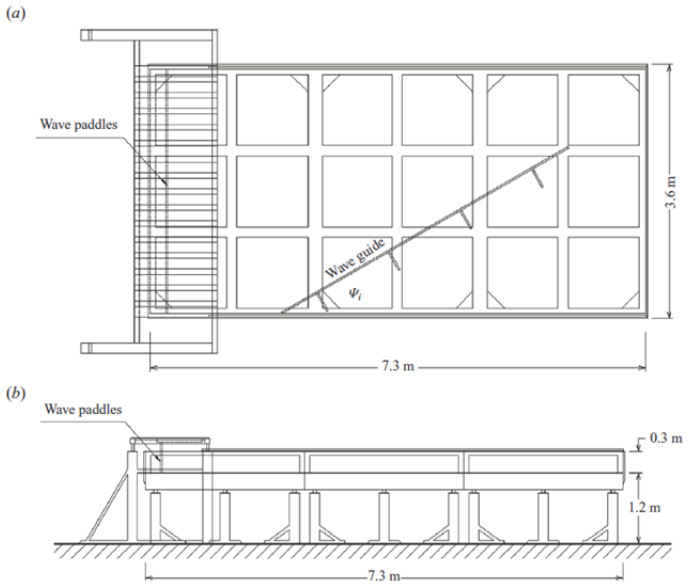

Fig. 1-9 A plan view (a) and an elevation view (b) of the laboratory wave tank for studies on the Mach reflection and the regular reflection of an SSW. Photograph courtesy of Li et al. (2011). (*Source: J. Fluid Mech. v. 672, 2011, p. 326-357*)

1.2 Motivations and the present work

Either a surface wave or an internal wave that propagates with a permanent form of a single and localised peak and a constant phase speed can be called a solitary wave (Sections 1.1.1 and 1.1.2). Based on this broad definition, the mathematical expression for the solitary wave is not unique. Some approximate mathematic models have been derived from the potential theory based on some assumptions. The analytical solution of the approximate model, which satisfies the physical properties of a solitary wave, is called the solitary wave solution. It is noticed that the dynamic boundary conditions on the free surface and interface are not the same. The pressure in the former is constant, while in the latter it is not necessarily constant but just continuous. Thus some equations may be different and their solitary wave solutions are therefore also different, as will be introduced in detail in Chapter 2. Those

solitary wave solutions need to be compared with the experiments or the calculations with the fully nonlinear boundary conditions to assess their validity scopes, *e.g.*, by Camassa et al. (2006). The approximate models containing solitary wave solutions were then used to study the 2D collisions of solitary-like waves. The initial value problem can be solved by numerical methods if analytical solutions have not been found (Zabusky and Kruskal, 1965). By means of the approximate models, the 2D collisions between ISWs have also been studied. Some similar characteristics were found as those in the collisions of SSWs, to name a few, by Mirie and Su (1984), Mirie and Su (1986), Choi and Camassa (1999), Jo and Choi (2002) and Nguyen and Dias (2008). Extensive validation work has confirmed the predominant characteristics discovered via the approximate models for surface waves (Craig et al., 2006). By contrast, relatively less experiments and fully nonlinear simulations have been done for internal waves.

The existing approximate models for 3D collisions of solitary waves are based on the weakly nonlinear assumptions. Those theories hold when the surface or interface displacement at any location is small relative to the undisturbed water depth. When the Mach reflection occurs, the maximum surface or interface displacement can be up to four times of the incident wave amplitude. The present study is concerned with the scenario in which the incident wave amplitude is moderate, but the amplified stem wave amplitude is expected to be large. In other words, the possibility of extremely large rogue waves will be examined by the fully nonlinear simulations, and the similarities and differences between surface wave problems and internal wave problems will be examined. Such comparative study is significant for the criteria establishment of the internal wave loads on the offshore structures. It helps us

to justify whether the models derived from the surface wave problems can be applied to the internal wave problems.

Three case studies on the oblique reflection of a solitary wave in the Mach reflection regime according to the KP theory will be carried out via the fully nonlinear numerical method for inviscid fluid utilising the open source CFD software OpenFOAM. They are for the moderate-amplitude incident SSW, the small-amplitude and the moderate-amplitude incident ISWs, respectively. As preparations, an analytical solution for an ISW will be derived in order to optimise the initial condition of the simulation for ISWs of moderate amplitude; 2D simulations for a single SSW, a single ISW, collisions of SSWs and collisions of ISWs will be carried out and analysed; the EKP equation, which is another mathematical model for the oblique interactions of internal waves, will be numerically solved by the Finite Element Method (FEM) using the software PDE2D; the Adaptive Mesh Refinement (AMR) technique will be implemented to maintain high accuracy over both large spatial and temporal spans in the simulation; verifications and validations of the numerical method will be carried out via comparing 2D and 3D simulated results with the published results. Besides the analyses on the wave profile and velocity field in three simulations, the mass, momentum and energy transfers in 3D space will be analysed through the integrations over transverse slices of the flow field. The underlying physics will be analysed. As introduced, the coastal area, near-shore and offshore structures are always exposed in the complex wave field. The nonlinear wave interaction can result in abnormally large surface/interface displacement and the redistribution of the wave energy in 3D space. Hence, some local areas may be subject to stronger impact than the prediction based on a single incoming wave. The present study may prompt the

re-evaluations of the coastal defences, ocean structure survivability and so on at certain locations.

1.3 Outline of the thesis

Chapter 2: A comprehensive literature review of the research on SSWs, ISWs and the oblique reflection problems will be given.

Chapter 3: A novel derivation of the higher-order weakly nonlinear solutions for a single ISW will be presented. Explicit expressions for the flow field of a KdV-type ISW will be given up to the third order.

Chapter 4: The KP equations for both the surface wave and the internal wave can be transformed to the standard form. The analytical solutions of the standard KP equation for the Mach reflection and regular reflection will be introduced. The EKP equation will also be introduced. The V-shape initial value problems of the KP and EKP equations will be solved numerically by the FEM.

Chapter 5: The physical models and the methodology used in the fully nonlinear simulations will be introduced.

Chapter 6: The appropriate initial conditions for simulations of SSWs and ISWs are to be investigated via 2D numerical experiments. Numerical errors will be evaluated. 2D collisions of SSWs and 2D collisions of ISWs will be simulated and compared with experiments or analytical results.

Chapter 7: The oblique reflection of a moderate-amplitude SSW will be simulated, which is in the Mach reflection regime based on the KP theory. The underlying physics will be analysed, and the applications will be discussed.

Chapter 8: The oblique reflections of a small-amplitude ISW and a moderate-amplitude ISW will be simulated respectively. Both cases are in the Mach reflection regime based on the KP theory. The underlying physics will be analysed, and the applications will be discussed.

Chapter 9: The concluding remarks will be made and future work will be proposed.

1.4 Publications and presentations during the PhD programme

1.4.1 Journal papers

Meng, Q., Wang, C., Chen, Y., Chen, J., 2013. A simplified CFD model for air-lift artificial upwelling. *Ocean Engineering* 72, 267-276.

Wang, C.Z., Meng, Q., Huang, H.C., Khoo, B.C., 2013. Finite element analysis of nonlinear wave resonance by multiple cylinders in vertical motions. *Computers & Fluids* 88, 557-568.

Zhang, C., Li, Y., Meng, Q., 2015. Fully nonlinear analysis of second-order sloshing resonance in a three-dimensional tank. *Computers & Fluids* 116, 88-104.

Meng, Q., Zhang, C., 2016. A third-order KdV solution for internal solitary waves and its application in the numerical wave tank. *Journal of Ocean Engineering and Science* 1(2), 93-108.

Xu, G.D., Meng, Q., 2016. Waves induced by a two-dimensional foil advancing in shallow water. *Engineering Analysis with Boundary Elements* 64, 150-157.

Zhou, B.Z., Wu, G.X., Meng, Q., 2016. Interactions of fully nonlinear solitary wave with a freely floating vertical cylinder. *Engineering Analysis with Boundary Elements* 69, 119-131.

Meng, Q., Zhang, C., Analytical study on a submerged tubular wave energy converter. *Renewable Energy (under review)*

1.4.2 Oral presentations

Meng, Q., 2014. An intuitional introduction of solitary wave theories and their applications. *5th UK Marine Technology Postgraduate Conference, Newcastle, UK*.

Meng, Q., Zhang, C., 2015. Fully nonlinear numerical simulation of large-amplitude obliquely interacting solitary waves. *9th IMACS International Conference on Nonlinear Evolution Equations and Wave Phenomena: Computation and Theory, Athens, GA, USA*.

Zhou, B.Z., Wu, G.X., Meng, Q., 2016. Fully nonlinear solitary wave interaction with a freely floating vertical cylinder. *31th International Workshop on Water Waves and Floating Bodies, Plymouth, MI, USA*.

Xu, G.D., Meng, Q., 2016. Solitons caused by a two-dimensional foil at super-critical and hyper-critical speeds in shallow water. *12th International Conference on Hydrodynamics, Egmond aan Zee, the Netherlands*

1.4.3 Academic awards

The paper “A third-order KdV solution for internal solitary waves and its application in the numerical wave tank” was awarded the FIRST PRIZE of the 2015 Global Student Paper Competition held by the editorial board of the Journal of Ocean Engineering and Science, Elsevier.

Chapter 2 Literature review

2.1 Models for surface solitary waves

We consider a homogeneous, incompressible and inviscid bulk of water which is confined within the domain

$$\Omega_S = \left\{ (x, y, z) \in \mathbb{R}^3 : -h_S \le z \le \theta(x, y, t) \right\}, \tag{2.1}$$

where h_S is a constant standing for the quiescent water depth over a flat bottom, $\theta(x, y, t)$ is the surface excursion with respect to the undisturbed water level (Fig. 2-1) and (x, y, z) and t are spatial and temporal independent variables, respectively. The *z*-coordinate of the earth-fixed Cartesian coordinate system *o-xyz* is pointing vertically upwards from the undisturbed water surface. Another coordinate system $O-XYZ$ that is parallel to the earth-fixed system is also defined. It is located on the undisturbed water level underneath the crest and moving with the phase speed of the wave c_S. Only the gravitational force is taken into account. Surface tension and the Coriolis force are neglected. Viscous effect is ignored. The fluid is, therefore, governed by the Euler equations.

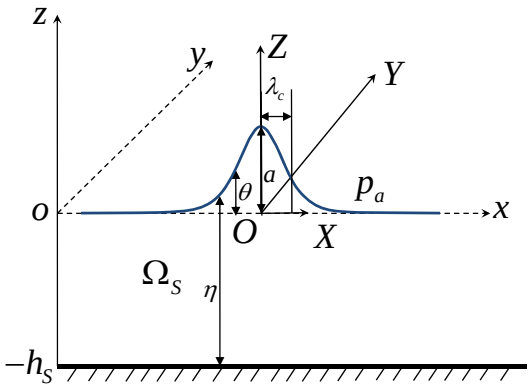

Fig. 2-1 Coordinate systems for the surface solitary wave.

If the flow is assumed to be irrotational, it can be further simplified to the velocity potential flow. The potential Φ, defined as $\nabla\Phi = \mathbf{u}$, where $\mathbf{u} = (u, v, w)$ is the

velocity vector in the fixed coordinate system, can be introduced. It satisfies the Laplace equation

$$\Delta\Phi = 0. \tag{2.2}$$

The boundary condition at the bottom is

$$\frac{\partial\Phi}{\partial z} = 0 \qquad \text{on } z = -h_S. \tag{2.3}$$

The kinematic boundary condition at the free surface is

$$\frac{\partial\theta}{\partial t} + \frac{\partial\Phi}{\partial x}\frac{\partial\theta}{\partial x} + \frac{\partial\Phi}{\partial y}\frac{\partial\theta}{\partial y} = \frac{\partial\Phi}{\partial z} \qquad \text{on } z = \theta. \tag{2.4}$$

The Bernoulli equation is used on the surface and atmospheric pressure is taken as zero. It yields

$$\frac{\partial\Phi}{\partial t} + \frac{1}{2}\left|\nabla\Phi\right|^2 + g\theta = 0 \qquad \text{on } z = \theta. \tag{2.5}$$

where g is the acceleration due to gravity. A wave is a 2D one when there is no change in its transverse direction. A 2D wave will be discussed in this section and its propagation direction is selected as the *x*-axis without loss of generality.

The equations that contain solitary wave solution were first independently put forward by Boussinesq (1871) and Rayleigh (1876). Two parameters are required to be small for implementing the multi-scale perturbation analysis. The first one is

$$\varepsilon = \frac{a}{h_S} \ll 1, \tag{2.6}$$

where a is the wave amplitude with respect to its undisturbed level. It measures the nonlinearity. Since ε is required to be small, the theory is only valid in the so-called weakly nonlinear regime. The second one is

$$\beta = \left(\frac{h_S}{\lambda}\right)^2 \ll 1, \tag{2.7}$$

the wavelength λ is the distance between two successive peaks of a periodic wave. It measures the dispersion effect. Since $\lambda \gg h_S$, it is called long wave model or shallow water model. The wavelength of a solitary wave is infinite, though a majority of the wave energy is localised. In order to depict the influence extent of the wave, λ can be replaced by a characteristic/effective wavelength λ_{Sc}. The characteristic wavelength can be defined as

$$\lambda_{Sc} = \frac{1}{a}\int_0^{\infty} \theta(X)dX. \tag{2.8}$$

If there is a balance of the distortions caused by nonlinear and dispersion effects in time, the solitary wave of permanent form exists. The condition is

$$U_r = \frac{\varepsilon}{\beta} = O(1), \tag{2.9}$$

where U_r is now commonly called as the Ursell number. It was first enunciated by Ursell (1953) and O indicates the order of magnitude. The governing equations can be converted to the Boussinesq equations by omitting the residual terms of $O(\varepsilon^2)$ (Boussinesq, 1871). When wave propagates in one direction, the Boussinesq equation can be simplified to the KdV equation (Korteweg and De Vries, 1895)

$$\frac{\partial \theta}{\partial t} + \left(1 + \frac{3}{2}\frac{\theta}{h_S}\right) c_{S0}\frac{\partial \theta}{\partial x} + \frac{1}{6}h_S^2 c_{S0}\frac{\partial^3 \theta}{\partial x^3} = 0, \tag{2.10}$$

where $c_{S0} = \sqrt{g h_S}$. Its solitary wave solution with amplitude of a can be written as

$$\theta = a\,\mathrm{sech}^2\left[\left(x - c_S t\right)/\lambda_{Sc}\right], \quad \lambda_{Sc} = \frac{2}{\sqrt{3}}\sqrt{\frac{h_S^3}{a}}, \quad c_S = c_{S0}\left(1 + \frac{a}{2h_S}\right). \tag{2.11}$$

Although the KdV equation was derived from the water wave theory, it appeared to be universal in a wide variety of physical contexts. It is a useful tool to discover and study the existence, stabilities and interactions of nonlinear waves in dispersive medium.

Since in the KdV equation, terms of orders higher than $O(\varepsilon,\beta)$ have been neglected, the accuracy of the solution is of $O(\varepsilon^2)$. This solution can be called the first-order approximation to the solitary wave. If the equation preserves higher-order terms with respect to ε and β and the Ursell condition is satisfied, *i.e.*, Eq. (2.9), it can be called the higher-order equation in the KdV family.

Laitone (1960) and Grimshaw (1971) obtained solitary wave solutions in the second-order and third-order KdV equations, respectively. Long (1956) gave a fifth-order expansion for the wave speed by successive approximations. Fenton (1972) obtained the solutions of the surface profile, wave speed up to ninth order of ε. Explicit expressions for the velocity and pressure were given up to the third order.

The third-order solitary wave solution given by Fenton (1972) is given here for the further implementation in the thesis:

$$\begin{aligned}\frac{\theta}{h_S}=&\frac{a}{h_S}\operatorname{sech}^2\alpha\left(x/h_S-c_St\right)-\frac{3}{4}\frac{a^2}{h_S^2}\operatorname{sech}^2\alpha\left(x/h_S-c_St\right)\tanh\alpha\left(x/h_S-c_St\right)\\&+\frac{a^3}{h_S^3}[\frac{5}{8}\operatorname{sech}^2\alpha\left(x/h_S-c_St\right)\tanh^2\alpha\left(x/h_S-c_St\right)\\&-\frac{101}{80}\operatorname{sech}^4\alpha\left(x/h_S-c_St\right)\tanh^4\alpha\left(x/h_S-c_St\right)]+O\left(\varepsilon^4\right),\end{aligned}\tag{2.12}$$

where

$$\alpha=\sqrt{\frac{3}{4}\frac{a}{h_S}}\left(1-\frac{5}{8}\frac{a}{h_S}-\frac{71}{128}\left(\frac{a}{h_S}\right)^2\right)+O(\varepsilon^{\frac{7}{2}}),\tag{2.13}$$

and

$$\frac{c_S}{\sqrt{gh_S}}=1+\frac{1}{2}\frac{a}{h_S}-\frac{3}{20}\left(\frac{a}{h_S}\right)^2+\frac{3}{56}\left(\frac{a}{h_S}\right)^3+O(\varepsilon^4).\tag{2.14}$$

The velocity components are

$$\begin{aligned}\frac{u}{\sqrt{gh_S}} &= \frac{a}{h_S}\operatorname{sech}^2\alpha\left(x/h_S - c_S t\right) - \left(\frac{a}{h_S}\right)^2 [-\frac{1}{4}\operatorname{sech}^2\alpha\left(x/h_S - c_S t\right) + \operatorname{sech}^4\alpha\left(x/h_S - c_S t\right) \\ &+ \left(z+h_S\right)^2\left(\frac{3}{2}\operatorname{sech}^2\alpha\left(x/h_S - c_S t\right) - \frac{9}{4}\operatorname{sech}^4\alpha\left(x/h_S - c_S t\right)\right)] \\ &- \left(\frac{a}{h_S}\right)^3 [\frac{19}{40}\operatorname{sech}^2\alpha\left(x/h_S - c_S t\right) + \frac{1}{5}\operatorname{sech}^4\alpha\left(x/h_S - c_S t\right) - \frac{6}{5}\operatorname{sech}^6\alpha\left(x/h_S - c_S t\right) \\ &+ \left(z+h_S\right)^2\left(-\frac{3}{2}\operatorname{sech}^2\alpha\left(x/h_S - c_S t\right) - \frac{15}{4}\operatorname{sech}^4\alpha\left(x/h_S - c_S t\right) + \frac{15}{2}\operatorname{sech}^6\alpha\left(x/h_S - c_S t\right)\right) \\ &\left(z+h_S\right)^4\left(-\frac{3}{8}\operatorname{sech}^2\alpha\left(x/h_S - c_S t\right) + \frac{45}{16}\operatorname{sech}^4\alpha\left(x/h_S - c_S t\right) - \frac{45}{16}\operatorname{sech}^6\alpha\left(x/h_S - c_S t\right)\right)] \\ &+ O(\varepsilon^4),\end{aligned} \tag{2.15}$$

$$\begin{aligned}\frac{w}{\sqrt{gh_S}} &= \left(\frac{3a}{h_S}\right)^{\frac{1}{2}}\left(z+h_S\right)\tanh\alpha\left(x/h_S - c_S t\right)\{-\frac{a}{h_S}\operatorname{sech}^2\alpha\left(x/h_S - c_S t\right) \\ &+ \left(\frac{a}{h_S}\right)^2 [\frac{3}{8}\operatorname{sech}^2\alpha\left(x/h_S - c_S t\right) + 2\operatorname{sech}^4\alpha\left(x/h_S - c_S t\right) \\ &+ \left(z+h_S\right)^2\left(\frac{1}{2}\operatorname{sech}^2\alpha\left(x/h_S - c_S t\right) - \frac{3}{2}\operatorname{sech}^4\alpha\left(x/h_S - c_S t\right)\right)] \\ &+ \left(\frac{a}{h_S}\right)^3 [\frac{49}{640}\operatorname{sech}^2\alpha\left(x/h_S - c_S t\right) - \frac{17}{20}\operatorname{sech}^4\alpha\left(x/h_S - c_S t\right) - \frac{18}{5}\operatorname{sech}^6\alpha\left(x/h_S - c_S t\right) \\ &+ \left(z+h_S\right)^2(-\frac{13}{16}\operatorname{sech}^2\alpha\left(x/h_S - c_S t\right) - \frac{25}{16}\operatorname{sech}^4\alpha\left(x/h_S - c_S t\right) + \frac{15}{2}\operatorname{sech}^6\alpha\left(x/h_S - c_S t\right)) \\ &+ \left(z+h_S\right)^4\left(-\frac{3}{40}\operatorname{sech}^2\alpha\left(x/h_S - c_S t\right) + \frac{9}{8}\operatorname{sech}^4\alpha\left(x/h_S - c_S t\right) - \frac{27}{16}\operatorname{sech}^6\alpha\left(x/h_S - c_S t\right)\right)]\} \\ &+ O(\varepsilon^{\frac{9}{2}}).\end{aligned} \tag{2.16}$$

The solitary wave profile can be also obtained by solving an exact integral equation numerically, which is significant to evaluate the consistency of the perturbation expansions. Byatt-Smith (1970) compared the numerical results with the first- and second-order approximations and showed that the first-order approximation agreed better with the numerical solution than the second-order approximation. It meant the second-order terms might have led to an overcorrection. The third-order approximation, given by Fenton (1972), has been added into the original figure by Byatt-Smith (1970) in Fig. 2-2. It shows that the third-order approximation agrees with the accurate numerical solution better than the first- and second-order ones.

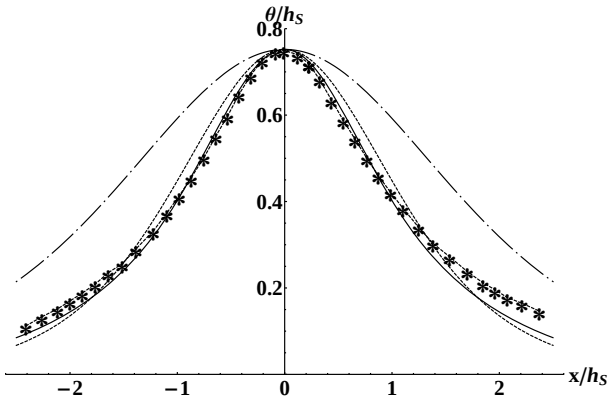

Fig. 2-2 Solitary wave profiles for $a/h_S = 0.752$. The dashed line (- - -) is the first-order solution; the dot dashed (- . -) line is the second-order solution; the solid line (—) is the third-order solution. The asterisk dashed （- * -） line is the numerical result given by Byatt-Smith (1970).

The recognised maximum possible amplitude of an SSW is $0.827h_S$ based on the series expansion and kinematic wave breaking criterion (Longuet-Higgins and Fenton, 1974).

2.2 Rigid-lid two-layer models for internal solitary waves

In a two-layer model for oceanic environment, the difference between densities of the two fluids is very small. Except the external wave mode (Fig. 2-3(a)), in which the surface wave is dominant, there is also the internal wave mode (Fig. 2-3(b)), in which the interface displacement is much larger than the surface displacement (Kakutani and Yamasaki, 1978). The interface movement and the corresponding flow field in the internal wave mode are the core research objectives in the "internal wave problems". As discussed by Evans and Ford (1996), the model with a rigid-lid boundary condition rather than a free surface boundary condition gives "an excellent approximation" for the wave motion in the internal wave mode.

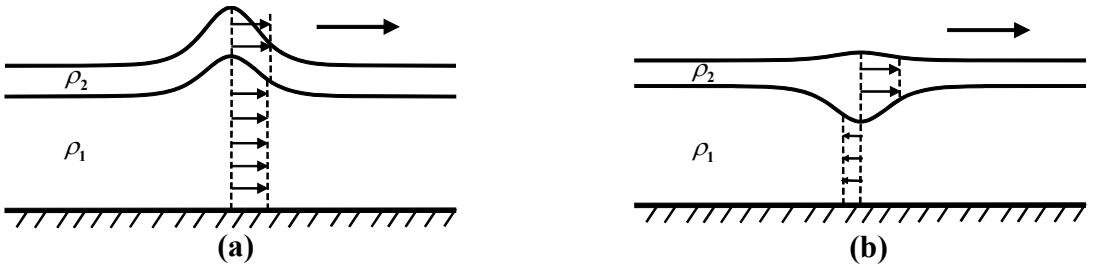

Fig. 2-3 Schematic diagrams in a two-layer system for the external mode (a) and the internal mode (b). In both modes, the surface wave and internal wave propagate with the same phase speed from left to right. The densities of the lower and upper layers are ρ_1 and ρ_2, respectively. $\rho_1 > \rho_2$ and $\rho_1 \simeq \rho_2$. The arrow and its length indicate the direction and magnitude of the instantaneous velocity in the water column.

The fluids in the two layers are assumed to be incompressible and inviscid and confined within

$$\begin{aligned} \Omega_1 &= \left\{ (x, y, z) \in \mathbb{R}^3 : -h \le z \le \theta(x, y, t) \right\}, \\ \Omega_2 &= \left\{ (x, y, z) \in \mathbb{R}^3 : \theta(x, y, t) \le z \le H - h \right\}, \end{aligned} \tag{2.17}$$

where h is the undisturbed depth of the lower layer, H is the total depth, $\theta(x, y, t)$ is the interface excursion with respect to the undisturbed interface (Figs. 2-4(a) & (b)). A fixed Cartesian coordinate system *o-xyz* and a moving Cartesian coordinate system *O-XYZ* are defined as those for the SSW, but the origins are on the undisturbed interface. If $\rho_1 (H - h)^2 < \rho_2 h^2$, the wave is of depression (Fig. 2-4(a)). If $\rho_1 (H - h)^2 > \rho_2 h^2$, the wave is of elevation (Fig. 2-4(b)) (Choi and Camassa 1999). Therefore, the maximum interface displacement *a* can be either positive or negative, and the wave amplitude is |*a*|. The subscripts 1 and 2 in the equation will represent the lower layer and the upper layer, respectively. For the irrotational flow, velocity potentials Φ_1 and Φ_2 can be introduced, and they satisfy

$$\Delta \Phi_i = 0 \qquad i = 1, 2. \tag{2.18}$$

The kinematic boundary conditions at the interface are

$$\frac{\partial\theta}{\partial t}+\frac{\partial\Phi_1}{\partial x}\frac{\partial\theta}{\partial x}+\frac{\partial\Phi_1}{\partial y}\frac{\partial\theta}{\partial y}=\frac{\partial\Phi_1}{\partial z}\quad \text{on } z=\theta(x,y,t), \tag{2.19}$$

$$\frac{\partial\theta}{\partial t}+\frac{\partial\Phi_2}{\partial x}\frac{\partial\theta}{\partial x}+\frac{\partial\Phi_2}{\partial y}\frac{\partial\theta}{\partial y}=\frac{\partial\Phi_2}{\partial z}\quad \text{on } z=\theta(x,y,t). \tag{2.20}$$

The Bernoulli equation can be used on the interface. It yields

$$\rho_1\left(\frac{\partial\Phi_1}{\partial t}+\frac{1}{2}\left|\nabla\Phi_1\right|^2+g\theta\right)=\rho_2\left(\frac{\partial\Phi_2}{\partial t}+\frac{1}{2}\left|\nabla\Phi_2\right|^2+g\theta\right)\quad \text{on } z=\theta(x,y,t). \tag{2.21}$$

The boundary conditions at the upper and lower lids are

$$\frac{\partial\Phi_1}{\partial z}=0\quad \text{on } z=-h;\quad \frac{\partial\Phi_2}{\partial z}=0\quad \text{on } z=H-h. \tag{2.22}$$

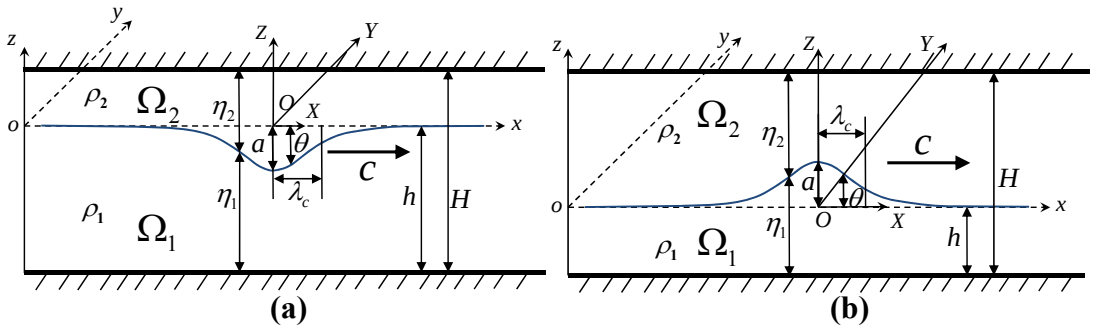

Fig. 2-4 Coordinate systems for the ISW, which is of depression (a) or of elevation (b).

The two small parameters ε and β can still be used to tackle the fully nonlinear interface conditions. Whereas, the depth in the expressions (2.6) & (2.7) is replaced by h', which is an intrinsic vertical scale that may be the depth of either of the two layers rather than the total depth (Helfich and Melville, 2006). That is to say, one of the layers has to be of finite depth, but the total depth can be either finite or infinite. Definitions of the two parameters can be written as

$$\varepsilon=\frac{|a|}{h'},\quad \beta=\left(\frac{h'}{\lambda_c}\right)^2, \tag{2.23}$$

where λ_c is the characteristic wavelength. The definition of the characteristic wavelength put forward by Koop and Butler (1981) can be written as

$$\lambda_c = \frac{1}{a}\int_0^\infty \theta(X)dX. \tag{2.24}$$

Different equations could be derived for long stationary waves with finite amplitude. Dispersion relation illustrates, for linear periodic waves, the frequency ω depends on the wave-number $\bar{k}$. If the depths of the both layers are finite, the phase velocity of periodic internal waves, *i.e.*, $c = \omega/\bar{k}$ could be expressed as (Benjamin, 1966)

$$c = c_0\left[1-\frac{1}{6}\bar{k}^2\left(\frac{\rho_1 h^2(H-h)+\rho_2 h(H-h)^2}{\rho_1(H-h)+\rho_2 h}\right)+O\left(\bar{k}^4 h^2(H-h)^2\right)\right], \tag{2.25}$$

where

$$c_0 = \sqrt{\frac{g(H-h)h(\rho_1-\rho_2)}{\rho_2 h+\rho_1(H-h)}}. \tag{2.26}$$

If the depth of one layer becomes infinite, say the upper layer without loss of generality, the wave speed turns out to be (Benjamin, 1967)

$$c = c_0\left[1-\frac{1}{2}\left|\bar{k}\right|(\rho_2/\rho_1)h+O\left(\bar{k}^4h^2\right)\right]. \tag{2.27}$$

It can be seen that the dispersion relations are different in fluids of finite depth and of great depth. Recall that the balance between the nonlinear and the dispersion effect results in the solitary wave. Different dispersion relations may correspond to different models for ISWs. The weakly nonlinear ISW model in fluids of infinite depth was put forward by Benjamin (1967) and Ono (1975). It was later called Benjamin-Ono (B-O) model. However, in this thesis we are only concerned with the condition that the total depth is small relative to the characteristic wavelength. It is more commonly seen in the ocean (Osborne and Burch, 1980; Helfrich and Melville, 2006).

If $\beta \ll 1$, but ε is not necessary to be small, the governing equations (2.18) to (2.22) can be reduced to two-layer Green-Naghdi (GN) equations by the layer-mean

integration method and preservation of the first-order terms in terms of β (Choi and Camassa, 1999),

$$\frac{\partial \eta_1}{\partial t}+\frac{\partial\left(\eta_1 \overline{u}_1\right)}{\partial x}=0, \quad \eta_1=h+\theta, \tag{2.28}$$

$$\frac{\partial \eta_2}{\partial t}+\frac{\partial\left(\eta_2 \overline{u}_2\right)}{\partial x}=0, \quad \eta_2=H-h-\theta, \tag{2.29}$$

$$\frac{\partial \overline{u}_1}{\partial t}+\overline{u}_1 \frac{\partial \overline{u}_1}{\partial x}+g \frac{\partial \theta}{\partial x}=-\frac{1}{\rho_1} \frac{\partial P}{\partial x}+\frac{1}{3} \eta_1^2 \frac{\partial}{\partial x}\left(\frac{\partial^2 \overline{u}_1}{\partial x \partial t}+\overline{u}_1 \frac{\partial^2 \overline{u}_1}{\partial x^2}-\left(\frac{\partial \overline{u}_1}{\partial x}\right)^2\right)+O(\beta^2), \tag{2.30}$$

$$\frac{\partial \overline{u}_2}{\partial t}+\overline{u}_2 \frac{\partial \overline{u}_2}{\partial x}+g \frac{\partial \theta}{\partial x}=-\frac{1}{\rho_2} \frac{\partial P}{\partial x}+\frac{1}{3} \eta_2^2 \frac{\partial}{\partial x}\left(\frac{\partial^2 \overline{u}_2}{\partial x \partial t}+\overline{u}_2 \frac{\partial^2 \overline{u}_2}{\partial x^2}-\left(\frac{\partial \overline{u}_2}{\partial x}\right)^2\right)+O(\beta^2), \tag{2.31}$$

where P is the pressure at the interface, with

$$\overline{u}_1=\frac{1}{\eta_1} \int_{-h}^{\theta} u_1(x, z, t) dz, \quad \overline{u}_2=\frac{1}{\eta_2} \int_{\theta}^{H-h} u_2(x, z, t) dz. \tag{2.32}$$

The solitary wave solution was found by Miyata (1985); Miyata (1988) and Choi and Camassa (1999), and is conventionally called the MCC model. Supposing that a permanent wave form propagates in the positive *x*-direction with constant speed c_{MCC}, the functions can be transformed to the moving coordinate system with $X=x-c_{MCC} t$. It yields

$$\left(\frac{\partial \theta}{\partial X}\right)^2=\left[\frac{3 g\left(\rho_1-\rho_2\right)}{c_{MCC}\left(\rho_2(H-h)^2-\rho_1 h^2\right)}\right] \frac{\theta^2(\theta-a_{-})(\theta-a_{+})}{(\theta-a_{*})}, \tag{2.33}$$

where a_* is given by

$$a_*=-\frac{h(H-h)\left(\rho_2(H-h)+\rho_1 h\right)}{\rho_2(H-h)^2-\rho_1 h^2}, \tag{2.34}$$

and a_{-} and a_{+} $\left(a_{-}<a_{+}\right)$ are the two roots of the equation

$$\tilde{x}^2+q_1 \tilde{x}+q_2=0. \tag{2.35}$$

In Eq. (2.35), q_1 and q_2 are defined as

$$q_1 = -\frac{c_{MCC}^2}{g} - (H-h) + h, \quad q_2 = (H-h)h\left(\frac{c_{MCC}^2}{c_0^2} - 1\right). \tag{2.36}$$

In addition, c_{MCC} can be obtained by the relation,

$$\frac{c_{MCC}^2}{c_0^2} = \frac{\left((H-h)-a\right)(h+a)}{(H-h)h - \left(c_0^2/g\right)a}. \tag{2.37}$$

Integration of Eq. (2.33) with respect to *X* results in an implicit relation $X = X_s(\theta)$, where X_s is a function in the form of elliptic integrals. For an ISW of depression (Fig. 2-4(a)) when $\rho_1 (H-h)^2 < \rho_2 h^2$

$$\upsilon X = \frac{2}{(a_* - a_-)^{1/2}}\left[\left(\frac{a_* - a_-}{|a_-|}\right)F\left(\phi \,|\, m_1^2\right) - \left(\frac{a_*(a_- - a_+)}{a_+ a_-}\right)\Pi\left(\mu_1; \phi \,|\, m_1^2\right)\right], \tag{2.38}$$

where

$$\sin\phi = \left[\frac{(a_* - a_-)(\theta - a_+)}{(a_* - a_+)(\theta - a_-)}\right]^{1/2}, \quad m_1^2 = \frac{a_* - a_+}{a_* - a_-}, \mu_1 = \frac{a_-}{a_+}m_1^2,$$
$$\upsilon = \left|\frac{3g(\rho_1 - \rho_2)}{c_{MCC}^2\left(\rho_2(H-h)^2 - \rho_1 h^2\right)}\right|^{1/2}. \tag{2.39}$$

In Eq. (2.38), *F* and Π stand for incomplete elliptic integrals of the first kind and the third kind, respectively (Abramowitz and Stegun, 1964).

Horizontal and vertical instantaneous velocities can be obtained from the MCC model by (Camassa et al., 2006)

$$u_i(x,z,t) = \overline{u}_i(x,t) + O(\beta) \quad i = 1,2, \tag{2.40}$$

$$w_i(x,z,t) = (-1)^i\left[\eta_i + (-1)^{i+1} z\right]\frac{\partial \overline{u}_i(x,t)}{\partial x} + O(\beta) \quad i = 1,2, \tag{2.41}$$

in which

$$\overline{u}_i = (-1)^{i+1}\frac{c_{MCC}\theta}{\eta_i} + O(\beta^2) \qquad i = 1,2. \tag{2.42}$$

The MCC model suggests the amplitude of an ISW cannot exceed a threshold (Camassa et al., 2006). The value that limits a is

$$a_{\max} = \frac{-h\rho_2^{1/2} + (H-h)\rho_1^{1/2}}{\rho_1^{1/2} + \rho_2^{1/2}}. \tag{2.43}$$

When $a = a_{\max}$, the phase speed achieves a maximum value, *i.e.*,

$$c_{\max}^2 = \frac{gH(\rho_1 - \rho_2)}{\left(\rho_1^{1/2} + \rho_2^{1/2}\right)^2}. \tag{2.44}$$

If the weakly nonlinear condition, *i.e.*,

$$\varepsilon \ll 1, \tag{2.45}$$

and the Ursell condition $U_r = \varepsilon/\beta = O(1)$ are satisfied, the governing Eqs. (2.18) -(2.22) can be again reduced to the KdV family (Keulegan, 1953; Long, 1956; Benjamin, 1966). Keulegan (1953) and Benjamin (1966) have given the first-order KdV equation by omitting the residuals of $O(\varepsilon^2)$. It can be written as, in dimensional form,

$$\frac{\partial \theta}{\partial t} + c_0 \frac{\partial \theta}{\partial x} + \gamma_1 \theta \frac{\partial \theta}{\partial x} + \gamma_2 \frac{\partial^3 \theta}{\partial x^3} = 0. \tag{2.46}$$

where c_0 has been given by Eq. (2.26), and

$$\gamma_1 = \frac{3c_0}{2h} \frac{1 - h^2\rho_2 / \left((h-H)^2 \rho_1\right)}{1 + h\rho_2 / \left((-h+H)\rho_1\right)}, \tag{2.47}$$

$$\gamma_2 = \frac{c_0}{6} \frac{h(h-H)\left(h\rho_1 + (H-h)\rho_2\right)}{h\rho_1 - H\rho_1 - h\rho_2}. \tag{2.48}$$

The ISW solution of Eq. (2.46) is

$$\theta = a\,\mathrm{sech}^2\left[\left(x - c_{KdV}t\right)/\lambda_{KdV}\right], c_{KdV} = c_0 + \frac{a\gamma_1}{3}, \lambda_{KdV} = \sqrt{\frac{12\gamma_2}{a\gamma_1}}. \tag{2.49}$$

When the higher-order nonlinearity correction is appended to the first-order KdV equation, it yields the Gardner equation (Miura et al., 1968; Lee and Beardsley, 1974; Djordjevic and Redekopp, 1978; Kakutani and Yamasaki, 1978; Ostrovsky and Stepanyants, 1989). It is also named as the extended KdV (eKdV) equation for it does not satisfy the Ursell condition. The eKdV equation is

$$\frac{\partial \theta}{\partial t}+\left(c_0+\gamma_1\theta+\gamma_3\theta^2\right)\frac{\partial \theta}{\partial x}+\gamma_2\frac{\partial^3\theta}{\partial x^3}=0. \tag{2.50}$$

The coefficients γ_1 and γ_2 are the same as those in Eqs. (2.47) & (2.48), and

$$\gamma_3=\frac{3c_0}{h^2\left(H-h\right)^2}\left[\frac{7}{8}\left(\frac{\rho_2h^2-\rho_1\left(H-h\right)^2}{\rho_2h+\rho_1\left(H-h\right)}\right)^2-\frac{\rho_2h^3+\rho_1\left(H-h\right)^3}{\rho_2h+\rho_1\left(H-h\right)}\right]. \tag{2.51}$$

The ISW solution of the eKdV equation is (Kakutani and Yamasaki, 1978; Miles, 1979; Ostrovsky and Stepanyants, 1989)

$$\theta=\frac{a}{G+\left(1-G\right)\cosh^2\left[\left(x-c_{eKdV}t\right)/\lambda_{eKdV}\right]}, \tag{2.52}$$

in which

$$c_{eKdV}=c_0+\frac{a}{3}\left(\gamma_1+\frac{1}{2}\gamma_3a\right),\quad \lambda_{eKdV}=\sqrt{\frac{12\gamma_2}{a\left(\gamma_1+\frac{1}{2}\gamma_3a\right)}},\quad G=\frac{-a\gamma_3}{2\gamma_1+a\gamma_3}. \tag{2.53}$$

If the wave amplitude, $|a|$, is very small, the term $\gamma_3\theta^2\frac{\partial\theta}{\partial x}$ can be omitted and the solution of the eKdV equation degenerates into the solution of the KdV equation. However, when the wave amplitude becomes larger, the ISW solution of the eKdV equation can better capture the broadening of ISWs as what have been observed in the ocean (Helfrich and Melville, 2006). The eKdV equation has a limit on *a*, *i.e.*,

$$a_{\lim}=-\frac{\gamma_1}{\gamma_3}. \tag{2.54}$$

If the wave amplitude approaches $|a_{\lim}|$, the wave is of table-top shape. Although it is deduced from weakly nonlinear theory, its application could be beyond $\varepsilon = 1$ (Ostrovsky and Grue, 2003; Maderich et al., 2009).

If all the second order terms are kept and the Ursell condition is preserved, it yields the second-order KdV equation (Koop and Butler, 1981). Lamb and Yan (1996) carried out numerical calculations based on a fully nonlinear model and compared the results with weakly nonlinear theories. Their comparisons showed that the inclusion of all second-order nonlinear and dispersive terms gave a sufficiently better prediction than that of the eKdV equation. It is noted that if the density of the upper layer is zero, the KdV equation for internal waves should degenerate to that for surface waves. Recalling the comparison in Fig. 2-2, it cannot be concluded that the second-order correction yields better accuracy for all the circumstances.

Through analysing the second-order KdV equation, Long (1956) gave a limiting amplitude beyond which no ISW solution of a single peak and convex shape exists. In the case $\rho_1 \approx \rho_2$, the restriction can be written as

$$|a| \le \frac{4h^2 (H-h)^2 |H-2h|}{H^2 (3h^2 - 3hH + H^2)}. \tag{2.55}$$

Mirie and Su (1984) gave the ISW solution of the third-order KdV equation. Mirie and Pennell (1989) then extended the expansion to the ninth order.

Both the experiments (Koop and Butler, 1981; Ostrovsky and Stepanyants, 2005; Huang et al., 2013) and numerical solutions (Funakoshi and Oikawa, 1986; Pullin and Grimshaw, 1988; Turner and Vanden‐Broeck, 1988; Evans and Ford, 1996;

Grue et al., 1999) can be used to examine the validity of the analytical solutions. Some results will be used for the comparisons in Chapter 3.

2.3 Models for the oblique reflection of a solitary wave

Some results given by Miles' asymptotic theories for surface waves will be introduced briefly (Miles, 1977a, b). The assumptions that $O(\varepsilon)=O(\beta)\ll 1$ are used for the wave profile in the longitudinal direction. The incident wave angle ψ_i introduced in Chapter 1 can be used to weight the transverse disturbance intensity posed by the reflection wall or the 3D effect. Provided $\psi_i^2=O(\varepsilon)$, an interaction parameter

$$k=\frac{\psi_i}{\sqrt{3a_i/h_S}}, \tag{2.56}$$

where a_i is the incident wave amplitude, is introduced to distinguish the Mach reflection regime and the regular reflection regime. When $k<1$, it is the Mach reflection regime (Fig. 1-8(b)). When $k>1$, it is the regular reflection regime (Fig. 1-8(a)). The ratio (amplification) between the maximum run-up at the reflection wall and a_i, denoted by χ_M, is given by

$$\chi_M=\begin{cases}(1+k)^2, & \text{for } k\le 1;\\ \dfrac{4}{1+\sqrt{1-k^{-2}}}, & \text{for } k>1.\end{cases} \tag{2.57}$$

In Eq. (2.57), as k increases from 0 to 1, χ_M increases from 1 to 4 monotonously (Fig. 2-5). The reflected wave amplification $\chi_r\left(\chi_r=a_r/a_i\right)$ is

$$\chi_r=\begin{cases}k^2, & \text{for } k\le 1;\\ 1, & \text{for } k>1.\end{cases} \tag{2.58}$$

The reflected wave angle

$$\psi_r = \begin{cases} \sqrt{3a_i/h_S}, & \text{for } k < 1; \\ \psi_i, & \text{for } k > 1. \end{cases} \tag{2.59}$$

The angle of stem-wave development or the Mach stem step angle

$$\psi_M = \sqrt{\frac{a_i}{3h_S}}(1-k), \quad \text{for } k < 1. \tag{2.60}$$

The Kadomtsev-Petviashvili (KP) equation arose from the analysis of the stability of solitary waves in terms of weakly lateral perturbation (Kadomtsev and Petviashvili, 1970). Chakravarty and Kodama (2009) found certain analytical solutions of the KP equation correspond to the Mach reflection and the regular reflection, respectively. As $t \to \infty$, those analytical solutions can reproduce the relations (2.57)-(2.60) with a slightly different interaction parameter (Li et al., 2011; Kodama and Yeh, 2016). The reason is that the assumption in the KP theory requires that $\tan^2 \psi_i = O(\varepsilon) = O(\beta) \ll 1$. Li et al. (2011) further took into account the higher-order correction for a "small-but-finite" ψ_i and introduced a new interaction parameter:

$$\kappa = \frac{\tan \psi_i}{\sqrt{3a_i/h_S}\cos \psi_i}. \tag{2.61}$$

Solely replacing k in Eqs. (2.57) to (2.60) with κ results in a better agreement with the simulated and experimental results (Li et al., 2011).

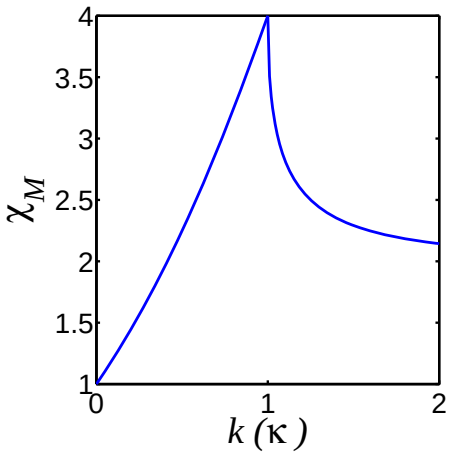

Fig. 2-5 χ_M **versus the interaction parameter** k **or** κ**.**

As introduced, the initial condition of the present oblique reflection problem is of a "V" shape. Two semi-infinite line solitons lie in the upper half plane and lower half plane, respectively (upper panels in Figs. 2-6 (a) & (b)). If we use the KP equation to model this initial value problem directly, the equation has to be solved by the numerical method, such as, the pseudo-spectral method with the window technique (Chakravarty and Kodama, 2009; Kodama et al., 2009; Kodama, 2010, 2012; Kao and Kodama, 2012) and the Finite Difference Method (FDM) (Li et al., 2011). The aforementioned analytical solutions can be obtained by the bilinear transformation but with a different initial condition (Hirota, 2004; Chakravarty and Kodama, 2009; Yeh et al., 2010). The (3142)-type solution corresponds to the Mach reflection. The O-type solution corresponds to the regular reflection. To construct these solutions, the reflected wave, which is a semi-infinite long line soliton, is known *a priori* at the initial time. Hence the initial value problem is of an "X" shape as shown in the leftmost ones in the lower panels of Figs. 2-6(a) & (b). Extensive numerical experiments have been done to compare the solutions of the V-shape and X-shape initial value problems, *e.g.*, Figs. 2-6(a) & (b) (Kodama et al., 2009; Chakravarty and Kodama, 2009; Kodama, 2010; Kao and Kodama, 2012). It was concluded that the solution with the V-shape initial condition converges asymptotically to its

corresponding analytical solution and the error in the vicinity of the interaction point (taking a circular region surrounding the interaction point and subtracting the numerical solution and the analytical solution in that area) drops fast.

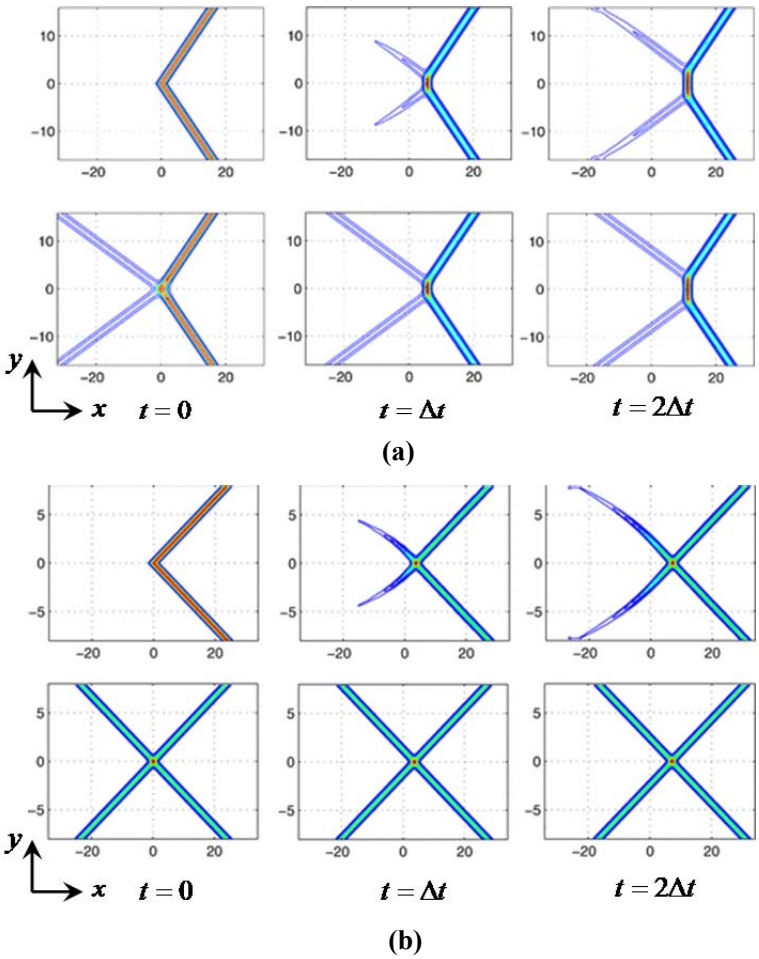

Fig. 2-6 (a): Numerical solution (upper panel) and the (3142)-type solution (lower panel) of the KP equation in the Mach reflection regime. (b): Numerical solution (upper panel) and the O-type solution (lower panel) of the KP equation in the regular reflection regime. The elevation of the free surface is expressed by the isohypse lines and contour plot, where redder colour represents relatively higher displacement and bluer colour represents relatively lower displacement in a Hue, Saturation, Value (HSV) colour space. Photograph courtesy of Chakravarty and Kodama (2009). (*Source: Stud. Appl. Math., v. 123, 2009, p. 83-151*)

Experiments (Melville, 1980) and 3D numerical simulations (Funakoshi, 1980; Barakhnin and Khakimzyanov, 1999) have validated the asymptotic theory when the wave amplitude is small, except for the fourfold amplification (Eq. (2.57)) near the

critical condition when $\kappa \to 1$. Li et al. (2011) found that the KP theory can well predict the development of the wave amplitude at the reflection wall as the time evolves.

The KP equation has been also introduced to model small-amplitude internal waves. Both the KP equations for surface and internal waves can be transformed into a standard form and solved by the Hirota's direct method (Hirota, 2004). According to the KP theory, the interface displacement of the Mach stem wave or the hump appearing in the oblique reflection can be also amplified up to four times with respect to that of the incident wave. It was found that the observed small-amplitude internal wave-wave interaction patterns in satellite images can be qualitatively reproduced by the solutions of the KP equation (Xue et al., 2014). Other modelling works of the 3D internal wave interaction were based on the depth-integrated Boussinesq equations for small-amplitude internal waves (Lynett and Liu, 2002; Cai and Xie, 2010).

Apart from the KP equation, Tsuji and Oikawa (2007) studied the oblique reflections of ISWs via an Extended Kadomtsev-Petviashvili (EKP) equation, which is a weakly three-dimensional generalisation of the eKdV equation. They found that the Mach reflection did not happen when the incident wave amplitude was very close to the limiting amplitude given by the eKdV equation. However, the EKP equation is still based on the weakly nonlinear assumptions.

As mentioned, the present study is concerned with moderate and large amplitude waves. The maximum possible amplitude of a 2D SSW or ISW is used as a reference and the possible fourfold amplification in an oblique reflection is taken into account

to define the scopes of moderate amplitude and large amplitude. If $4|a_i|$ is still far less than the maximum possible amplitude of a 2D solitary wave, the incident wave is of small amplitude; If $4|a_i|$ is comparable to the maximum amplitude of a 2D solitary wave, the incident wave is of moderate amplitude; If $|a_i|$ itself has been close to the maximum possible amplitude of a 2D solitary wave, the incident wave is of large amplitude. For SSWs, we can therefore roughly distinguish small-amplitude, moderate-amplitude and large-amplitude by $\sim 0.1h_S$, $\sim 0.3h_S$ and $\sim 0.7h_S$. For ISW, however, $|a_{\max}|$ given by (2.43) varies with different circumstances of different depth ratio and density ratio of the two layers (Fig. 2-7). In this thesis, we are interested in a specific oceanic environment, *i.e.*, $\rho_2/\rho_1 \approx 0.98$, and $H/h \approx 1.33$. With these parameters, $a_{\max} \approx -0.33h$. Therefore, when $a_i \approx -0.05h$, the incident wave amplitude is deemed as small; when $a_i \approx -0.1h$, the incident wave amplitude is moderate; when $a_i \approx -0.2h$, the incident wave amplitude is large.

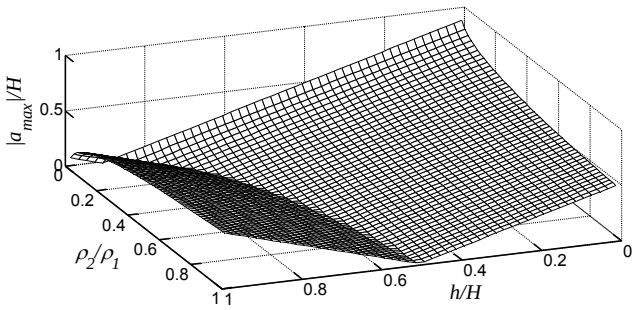

Fig. 2-7 $|a_{\max}|/H$ **versus** h/H **and** ρ_2/ρ_1**.**

As to the oblique collisions of moderate-amplitude or large-amplitude incident ISWs, Wang and Pawlowicz (2012) reported that the observations deviated from the KP theory and the asymptotic theory. For the interactions which are classified as the Mach reflections based on Miles' theory (Miles, 1977b), Wang and Pawlowicz (2012)

summarised four remarkable differences between observations and the theories as follows: 1. The observed ψ_M was greater than zero but much smaller than the theoretical prediction. 2. The observed Mach stem amplitude $|a_M|$ was smaller than the prediction given by Miles' theory. 3. The observed reflected wave amplitude $|a_r|$ was much larger than that given by the theory. But it was quite close to the incident wave amplitude. 4. The observed reflection wave angle ψ_r was much smaller than the theoretical prediction. On the contrary, the ψ_r appeared to be quite close to the incident wave angle ψ_i. To sum up, the appearances shown in the observations tend to be the regular reflections rather than the Mach reflections. Wang and Pawlowicz (2012) cited the conclusion by Tanaka (1993), who studied oblique reflection of an SSW with moderate amplitude, "for larger amplitude waves, the effect of the large amplitude tends to prevent Mach reflection from occurring. If Mach reflection does take place for large amplitude waves, it will differ from small amplitude cases, with the amplitude of the reflected wave close to that of the incident wave." Whereas, the authors also claimed that the data were not credible enough owing to the limited spatial and temporal coverage and lack of in-situ measurements.

2.4 Computational Fluid Dynamics (CFD) methods

Computational Fluid Dynamics (CFD) methods can be used to solve the primitive equations, such as the Euler equations or the Navier-Stokes (NS) equations. It has been widely used in the study of rogue surface waves in 3D space despite the requirement of "huge computational resources" (Dysthe et al., 2008). A lot of 3D simulations of internal waves have been undertaken under increasingly realistic conditions (Simmons et al., 2011; Zhang et al., 2011; Alford et al., 2015). A core technique for simulating waves is to determine the free surface or interface

(Scardovelli and Zaleski, 1999). Generally speaking, there are two ways: surface fitting/tracking methods corresponding to dynamic grids and surface capturing methods corresponding to fixed grids. With dynamic mesh the free surface can be tracked by the Lagrangian particle algorithm (Longuet-Higgins and Cokelet, 1976). The fully nonlinear boundary conditions on the free surface can be satisfied at each time step. However, it is subject to the numerical dissipation due to frequent remeshing and interpolation in order to prevent mesh distortion (Wu and Eatock Taylor, 2003). The Volume Of Fluid (VOF) method, which is a surface capturing method, has been widely used to tackle the fully nonlinear free surface/interface boundary conditions (Hirt and Nichols, 1981). Firstly, both the free surface flow and the interfacial flow are regarded as an immiscible two-phase problem. An unknown indicator scalar defined as the fraction of one phase in an infinitesimal control volume is introduced. The variation of the scalar field is governed by a convective scalar transport equation and the fully nonlinear boundary conditions at the interface are satisfied automatically. The indicator function is supposed to undergo a step change from 0 to 1 representing a sharp interface. However, the convective differencing scheme may result in the excessive diffusion of the transport equation. It is reflected in the smearing of the step-profile interface. Various techniques such as interface reconstructions and higher-order differencing schemes can increase the accuracy dramatically on the premise of the invariant mesh density. One can refer to the theses by Ubbink (1997) and Rusche (2002), respectively, for the comparison of various techniques. One of the advantages of the VOF method, which makes it appropriate for the current problem, is that it has managed to integrate the calculation for the free surface/interface movement into the Euler framework. Hence it is easy to be parallelized in a general form as other governing equations (Hirsch, 1988).

The open source code “Open Field Operation and Manipulation” (OpenFOAM) can be used to implement the VOF method based on Finite Volume Method (FVM) discretization. OpenFOAM is written by the object-oriented language C++ (Weller et al., 1998; OpenFOAM documentation, 2014). The VOF technique has been modularised (Jasak et al., 2007). Various case studies have validated its capacity to simulate the “realistic” waves (Morgan and Zang, 2011; Morgan et al., 2011; Higuera et al., 2013a, b, 2014; Jacobsen et al., 2014). The open source third-party software packages “waves2Foam” offers a user-friendly interface to generate various waves in a 3D numerical wave tank (NWT) (Jacobsen et al., 2012). Furthermore, together with the corresponding libraries, OpenFOAM supports massively parallel computing.

Given the above, techniques have been available for fully nonlinear simulations of 3D wave-wave interactions. In-depth understandings of the oblique reflection of a solitary wave (SSW or ISW) are expected through the analysis of the simulated results.

Chapter 3 Solution of the third-order KdV equation for an internal solitary wave

3.1 Mathematical model

Steady two-dimensional potential flow will be considered in this chapter. The two phases of fluids are immiscible and bounded by two flat rigid-lids as shown in Fig. 3-1. A Cartesian coordinate system moving with the wave peak is defined in Fig. 3-1, in which the *x*-axis lies horizontally on the bottom of fluid and the *z*-axis points upward through the crest or trough of the wave. Consequently, a flow comes from the infinity at uniform constant speed U. The total depth is *H* and the depth of the lower layer is *h*. The displacement of the interface with respect to the bottom is represented by η. For convenience, an ancillary function, $\theta = \eta - h$, is introduced. The maximum displacement of the interface is donated by *a*. The subscripts 1 and 2 label the variables of the lower and upper layers, respectively, such as the density ρ, the horizontal fluid velocity u and the vertical fluid velocity w so on.

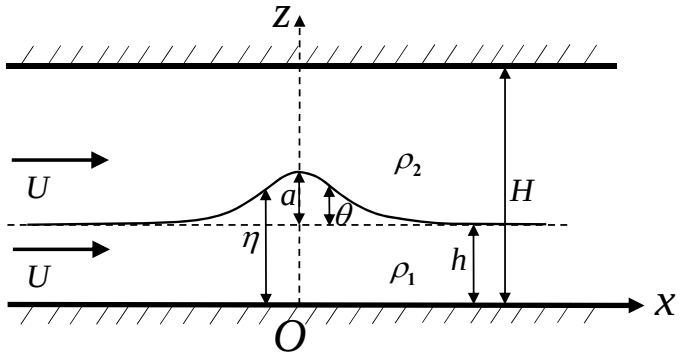

Fig. 3-1 A rigid-lid two-layer model for internal solitary waves.

For a two-dimensional potential flow, stream functions Ψ_1 and Ψ_2 can be introduced. They are defined as

$$\frac{\partial \Psi_i}{\partial z} = u_i, \quad \frac{\partial \Psi_i}{\partial x} = -w_i \qquad i = 1, 2. \quad (3.1)$$

They satisfy the Laplace equation, because the flow is irrotational, *i.e.*,

$$\Delta \Psi_i = 0 \qquad i = 1, 2. \quad (3.2)$$

On a streamline, the stream function will be constant. Thus, the boundary conditions at the lower and upper lids, respectively, are

$$\Psi_1 = 0 \quad \text{on } z = 0; \quad \Psi_2 = UH \quad \text{on } z = H. \tag{3.3}$$

The interface is also a streamline and the kinematic condition on it becomes

$$\Psi_1 = \Psi_2 = Uh \quad \textbf{on } z = \eta(x), \tag{3.4}$$

The dynamic condition based on the Bernoulli equation for the steady flow becomes, on the interface,

$$\begin{aligned} &\rho_1\left(\frac{1}{2}\left(\frac{\partial\Psi_1}{\partial z}\right)^2 + \frac{1}{2}\left(\frac{\partial\Psi_1}{\partial x}\right)^2 - \frac{1}{2}U^2 + g\theta\right) = \\ &\quad \rho_2\left(\frac{1}{2}\left(\frac{\partial\Psi_2}{\partial z}\right)^2 + \frac{1}{2}\left(\frac{\partial\Psi_2}{\partial x}\right)^2 - \frac{1}{2}U^2 + g\theta\right) \quad \text{on } z = \eta(x). \end{aligned} \tag{3.5}$$

Extending the ideas put forward initially by Benjamin and Lighthill (1954), six physical parameters are introduced: the volume flow rate $Q_i\ (i = 1,2)$; the energy per unit span $R_i\ (i = 1,2)$; the force plus momentum flux $S_i\ (i = 1,2)$. They are defined as

$$Q_1 = \int_0^\eta u_1 dz, \tag{3.6}$$

$$Q_2 = \int_\eta^H u_2 dz, \tag{3.7}$$

$$R_1 = p_1 + \rho_1 gz + \frac{1}{2}\rho_1\left(u_1^2 + w_1^2\right), \tag{3.8}$$

$$R_2 = p_2 + \rho_2 g\left(z - H\right) + \frac{1}{2}\rho_2\left(u_2^2 + w_2^2\right), \tag{3.9}$$

$$S_1 = \int_0^\eta \left(p_1 + \rho_1 u_1^2\right) dz, \tag{3.10}$$

$$S_2 = \int_\eta^H \left(p_2 + \rho_2 u_2^2\right) dz, \tag{3.11}$$

$$S = S_1 + S_2, \tag{3.12}$$

where $p_i\ (i=1,2)$ are pressures. According to the mass continuity, $Q_i\ (i=1,2)$ are constants. $R_i\ (i=1,2)$ are constants based on the Bernoulli equation for the steady potential flow. S can be proved to be constant as well (see Appendix A). Substituting the expressions of p_1 and p_2 obtained from Eqs. (3.8) and (3.9) into Eqs. (3.10) and (3.11), respectively, we have

$$S_1 - R_1\eta + \frac{1}{2}\rho_1 g\eta^2 = \frac{1}{2}\int_0^{\eta}\rho_1\left(u_1^2 - w_1^2\right)dz, \tag{3.13}$$

$$S_2 - R_2\left(H-\eta\right) - \frac{1}{2}\rho_2 g\left(\eta - H\right)^2 = \frac{1}{2}\int_{\eta}^{H}\rho_2\left(u_2^2 - w_2^2\right)dz. \tag{3.14}$$

The velocities on the flat bottom and top are tangential to boundaries. With the transformation shown in Appendix B, the stream functions Ψ_1 and Ψ_2 can be expanded into Taylor series from $z=0$ and $z=H$, respectively:

$$\Psi_1 = zu_1(x,0) - \frac{z^3}{3!}u_1''(x,0) + \frac{z^5}{5!}u_1^{(4)}(x,0) - \frac{z^7}{7!}u_1^{(6)}(x,0) + \frac{z^9}{9!}u_1^{(8)}(x,0) - ..., \tag{3.15}$$

$$\begin{aligned}\Psi_2 = {} & (z-H)u_2(x,H) - \frac{(z-H)^3}{3!}u_2''(x,H) + \frac{(z-H)^5}{5!}u_2^{(4)}(x,H) \\ & - \frac{(z-H)^7}{7!}u_2^{(6)}(x,H) + \frac{(z-H)^9}{9!}u_2^{(8)}(x,H) - ... + Q_1 + Q_2,\end{aligned} \tag{3.16}$$

where the primes or the number in brackets in superscripts of *u* denote the order of derivative with respect to x. Eqs. (3.15) and (3.16) give $\Psi_1 = 0$ at $z=0$, $\Psi_2 = Q_1 + Q_2$ at $z=H$, respectively.

Through the stream functions, the horizontal and vertical velocities can be written as

$$\begin{aligned}u_1 = \frac{\partial\Psi_1}{\partial z} = {} & u_1(x,0) - \frac{z^2}{2!}u_1''(x,0) + \frac{z^4}{4!}u_1^{(4)}(x,0) \\ & - \frac{z^6}{6!}u_1^{(6)}(x,0) + \frac{z^8}{8!}u_1^{(8)}(x,0) - ...,\end{aligned} \tag{3.17}$$

$$w_1 = -\frac{\partial \Psi_1}{\partial x} = -z u_1'(x,0) + \frac{z^3}{3!} u_1^{(3)}(x,0) - \frac{z^5}{5!} u_1^{(5)}(x,0) + \frac{z^7}{7!} u_1^{(7)}(x,0) - \frac{z^9}{9!} u_1^{(9)}(x,0) + \ldots, \tag{3.18}$$

$$u_2 = \frac{\partial \Psi_2}{\partial z} = u_2(x,H) - \frac{(z-H)^2}{2!} u_2''(x,H) + \frac{(z-H)^4}{4!} u_2^{(4)}(x,H) - \frac{(z-H)^6}{6!} u_2^{(6)}(x,H) + \frac{(z-H)^8}{8!} u_2^{(8)}(x,H) - \ldots, \tag{3.19}$$

$$w_2 = -\frac{\partial \Psi_2}{\partial x} = -(z-H) u_2'(x,H) + \frac{(z-H)^3}{3!} u_2^{(3)}(x,H) - \frac{(z-H)^5}{5!} u_2^{(5)}(x,H) + \frac{(z-H)^7}{7!} u_2^{(7)}(x,H) - \frac{(z-H)^9}{9!} u_2^{(9)}(x,H) - \ldots. \tag{3.20}$$

We scale all length dimensions by h, time by h/c_0, where $c_0 = \sqrt{\left(g(\rho_1 - \rho_2)(H-h)h\right) / \left(\rho_2 h + \rho_1 (H-h)\right)}$, and densities by ρ_1. The variables

$$r = \frac{H}{h}, \quad \delta = \frac{\rho_2}{\rho_1}, \quad \varepsilon = \frac{a}{h}, \tag{3.21}$$

can be used to simplify the expressions.

We substitute Eqs. (3.13) and (3.14) into Eq. (3.12) and replacing the velocity components with stream functions. It yields

$$S - R_1(1+\theta) + \frac{1}{2}(1+\theta)^2 - \frac{1}{2}\int_0^{1+\theta} \left(-\frac{1}{2}\Psi_{1x}^2 + \frac{1}{2}\Psi_{1z}^2 \right) dz - \frac{1}{2}\delta(1-r+\theta)^2 - R_2(r-1-\theta) - \frac{1}{2}\delta \int_{1+\theta}^{r} \left(-\frac{1}{2}\Psi_{2x}^2 + \frac{1}{2}\Psi_{2z}^2 \right) dz = 0, \tag{3.22}$$

which is equivalent to the dynamic interface boundary condition. In order to obtain the interface displacement θ in Eq. (3.22), we have to find a single equation of θ. By defining

$$\xi = \frac{u_1(x,0)}{U} - 1, \quad \zeta = \frac{u_2(x,r)}{U} - 1, \tag{3.23}$$

we can rewrite the relationships between the interface displacement and the top or bottom horizontal velocities as:

$$\xi = -\theta - \xi\theta + \frac{\xi''}{3!}(1+\theta)^3 - \frac{\xi^{(4)}}{5!}(1+\theta)^5 + \frac{\xi^{(6)}}{7!}(1+\theta)^7 - \frac{\xi^{(8)}}{9!}(1+\theta)^9 + \ldots, \tag{3.24}$$

$$\begin{aligned}\zeta(1-r) = -\theta - \zeta\theta + \frac{\zeta''}{3!}(1-r+\theta)^3 - \frac{\zeta^{(4)}}{5!}(1-r+\theta)^5 + \frac{\zeta^{(6)}}{7!}(1-r+\theta)^7 \\ - \frac{\zeta^{(8)}}{9!}(1-r+\theta)^9 + \ldots.\end{aligned} \tag{3.25}$$

The same assumptions as those used by Long (1956) are adopted here. The n^{th} derivatives of θ, ξ and ζ are assumed to have the same order of $\varepsilon^{1+\frac{n}{2}}$. It is according to the Ursell relationship $U_r = \varepsilon/\beta = O(1)$. We can use the successive approximation method to solve Eqs. (3.24) and (3.25). Recalling that θ is a function of *x*, the magnitude of θ, as *x* varies, is smaller than that of ε. Thus we can use ε to estimate the truncation errors of the approximations. ξ and ζ of lower-order accuracy deduced from Eqs. (3.24) and (3.25) are successively iterated into original equations to obtain solutions of higher-order accuracy. The expressions of ξ and ζ with the truncation errors of $O(\varepsilon^6)$ are

$$\begin{aligned}\xi = &-\theta + \theta^2 - \theta^3 + \theta^4 - \theta^5 - \frac{\theta''}{6} + \frac{\theta'^2}{3} - \frac{7}{360}\theta^{(4)} - \frac{1}{3}\theta\theta'^2 + \frac{11}{180}\theta''^2 + \frac{2}{45}\theta'\theta''' \\ &- \frac{7}{180}\theta\theta^{(4)} - \frac{31}{15120}\theta^{(6)} + \frac{1}{3}\theta^2\theta'^2 + \frac{1}{45}\theta'^2\theta'' + \frac{11}{180}\theta\theta''^2 + \frac{2}{45}\theta\theta'\theta''' + \frac{19}{1260}\theta'''^2 \\ &- \frac{7}{360}\theta^2\theta^{(4)} + \frac{47}{3780}\theta''\theta^{(4)} - \frac{11}{1260}\theta'\theta^{(5)} - \frac{31}{3780}\theta\theta^{(6)} - \frac{127}{604800}\theta^{(8)} + O(\varepsilon^6),\end{aligned} \tag{3.26}$$

$$\begin{aligned}\zeta = &-\frac{\theta}{(1-r)} + \frac{\theta^2}{(1-r)^2} - \frac{\theta^3}{(1-r)^3} + \frac{\theta^4}{(1-r)^4} - \frac{\theta^5}{(1-r)^5} - \frac{\theta''}{6}(1-r) + \frac{\theta'^2}{3} \\ &- \frac{7}{360}\theta^{(4)}(1-r)^3 - \frac{1}{3(1-r)}\theta\theta'^2 + \frac{11}{180}(1-r)^2\theta''^2 + \frac{2}{45}(1-r)^2\theta'\theta''' \\ &- \frac{7}{180}(1-r)^2\theta\theta^{(4)} - \frac{31}{15120}(1-r)^5\theta^{(6)} + \frac{1}{3(1-r)^2}\theta^2\theta'^2 + \frac{(1-r)}{45}\theta'^2\theta'' \\ &+ \frac{11(1-r)}{180}\theta\theta''^2 + \frac{2(1-r)}{45}\theta\theta'\theta''' + \frac{19(1-r)^4}{1260}\theta'''^2 - \frac{7(1-r)}{360}\theta^2\theta^{(4)} \\ &+ \frac{47(1-r)^4}{3780}\theta''\theta^{(4)} - \frac{11(1-r)^4}{1260}\theta'\theta^{(5)} - \frac{31(1-r)^4}{3780}\theta\theta^{(6)} - \frac{127(1-r)^7}{604800}\theta^{(8)} \\ &+ O(\varepsilon^6).\end{aligned} \tag{3.27}$$

To verify the derivation, we substitute Eqs. (3.26) and (3.27) back to Eq. (3.23). The $u_1(x,0)$ and $u_2(x,r)$ are expressed by θ consequentially. Then we substitute $u_1(x,0)$ and $u_2(x,r)$ to the stream functions, namely, Eqs. (3.15) and (3.16). After sorting out the terms and applying the far field conditions, we have, at the interface where $z=1+\theta$,

$$\Psi_1-\Psi_2=O\left(\varepsilon^6\right). \tag{3.28}$$

The streamlines deduced from the two layers coincide at the interface if the terms of $O\left(\varepsilon^6\right)$ and higher are neglected. It, therefore, satisfies the boundary condition at the interface to the correct order.

With the expressions above, Eq. (3.22) is transformed to

$$\begin{aligned}
&S-R_1(\theta+1)+\frac{1}{2}(\theta+1)^2-Q_1^2[\frac{1}{2}-\frac{\theta}{2}+\frac{\theta^2}{2}-\frac{\theta^3}{2}+\frac{\theta^4}{2}-\frac{\theta^5}{2}-\frac{1}{6}\theta'^2+\frac{1}{6}\theta\theta'^2\\
&+\frac{1}{90}\theta''^2-\frac{1}{45}\theta'\theta'''-\frac{1}{6}\theta^2\theta'^2-\frac{1}{45}\theta'^2\theta''+\frac{1}{90}\theta\theta''^2-\frac{1}{45}\theta\theta'\theta'''-\frac{1}{945}\theta'''^2\\
&+\frac{2}{945}\theta''\theta^{(4)}-\frac{2}{945}\theta'\theta^{(5)}]-\frac{1}{2}\delta(\theta+1-r)^2-R_2(r-(\theta+1))\\
&+\delta\left(\frac{Q_2}{r-1}\right)^2[\frac{(1-r)}{2}-\frac{\theta}{2}+\frac{\theta^2}{2(1-r)}-\frac{\theta^3}{2(1-r)^2}+\frac{\theta^4}{2(1-r)^3}-\frac{\theta^5}{2(1-r)^4}\\
&-\frac{1}{6}(1-r)\theta'^2+\frac{1}{6}\theta\theta'^2+\frac{1}{90}(1-r)^3\theta''^2-\frac{1}{45}(1-r)^3\theta'\theta'''-\frac{1}{6(1-r)}\theta^2\theta'^2\\
&-\frac{1}{45}(1-r)^2\theta'^2\theta''+\frac{1}{90}(1-r)^2\theta\theta''^2-\frac{1}{45}(1-r)^2\theta\theta'\theta'''-\frac{1}{945}(1-r)^5\theta'''^2\\
&+\frac{2}{945}(1-r)^5\theta''\theta^{(4)}-\frac{2}{945}(1-r)^5\theta'\theta^{(5)}]=O\left(\varepsilon^6\right).
\end{aligned} \tag{3.29}$$

The constants in Eq. (3.29) are decided by the far field. As there are two superimposed immiscible uniform flows, the values of Q_1, Q_2, R_1, R_2, and S can be given by

$$\begin{cases} Q_1 = U, \quad Q_2 = U(r-1), \\ R_1 = \frac{1}{2}U_1^2 + 1, \quad R_2 = \frac{1}{2}\delta U_2^2 + \delta(1-r), \\ S = U_1^2 + \frac{1}{2} + \delta U_2^2 (r-1) - \frac{1}{2}\delta (r-1)^2 . \end{cases} \tag{3.30}$$

To obtain the solitary wave solution, the velocity of the streams should be supercritical, which means the Froude numbers defined as

$$F^2 = \frac{U^2}{(1-\delta)\dfrac{(r-1)}{(r-1)+\delta}}, \tag{3.31}$$

should be larger than 1 (Benjamin, 1966). We have, from Eq. (3.29),

$$\begin{aligned} & F^2(1-\delta)\frac{(r-1)}{(r-1)+\delta} + \frac{1}{2} + \delta F^2(1-\delta)\frac{(r-1)}{(r-1)+\delta}(r-1) + \frac{1}{2}\delta(r-1)^2 \\ & -\left(\frac{1}{2}F^2(1-\delta)\frac{(r-1)}{(r-1)+\delta} + 1\right)(\theta+1) + \frac{1}{2}(\theta+1)^2 - F^2(1-\delta)\frac{(r-1)}{(r-1)+\delta}[\frac{1}{2} \\ & -\frac{\theta}{2} + \frac{\theta^2}{2} - \frac{\theta^3}{2} + \frac{\theta^4}{2} - \frac{\theta^5}{2} - \frac{1}{6}\theta'^2 + \frac{1}{6}\theta\theta'^2 + \frac{1}{90}\theta''^2 - \frac{1}{45}\theta'\theta''' - \frac{1}{6}\theta^2\theta'^2 \\ & -\frac{1}{45}\theta'^2\theta'' + \frac{1}{90}\theta\theta''^2 - \frac{1}{45}\theta\theta'\theta''' - \frac{1}{945}\theta'''^2 + \frac{2}{945}\theta''\theta^{(4)} - \frac{2}{945}\theta'\theta^{(5)}] \\ & -\frac{1}{2}\delta(\theta+1-r)^2 - \left(\frac{1}{2}\delta F^2(1-\delta)\frac{(r-1)}{(r-1)+\delta} + \delta g(1-r)\right)(r-(\theta+1)) \\ & +\delta F^2(1-\delta)\frac{(r-1)}{(r-1)+\delta}[\frac{(1-r)}{2} - \frac{\theta}{2} + \frac{\theta^2}{2(1-r)} - \frac{\theta^3}{2(1-r)^2} + \frac{\theta^4}{2(1-r)^3} \\ & -\frac{\theta^5}{2(1-r)^4} - \frac{1}{6}(1-r)\theta'^2 + \frac{1}{6}\theta\theta'^2 + \frac{1}{90}(1-r)^3\theta''^2 - \frac{1}{45}(1-r)^3\theta'\theta''' \\ & -\frac{1}{6(1-r)}\theta^2\theta'^2 - \frac{1}{45}(1-r)^2\theta'^2\theta'' + \frac{1}{90}(1-r)^2\theta\theta''^2 - \frac{1}{45}(1-r)^2\theta\theta'\theta''' \\ & -\frac{1}{945}(1-r)^5\theta'''^2 + \frac{2}{945}(1-r)^5\theta''\theta^{(4)} - \frac{2}{945}(1-r)^5\theta'\theta^{(5)}] = O(\varepsilon^6) \end{aligned} \tag{3.32}$$

3.2 The perturbation method

We expand all the variables in terms of ε. We stretch *x* coordinate in the same way as that by Fenton (1972), which was originally introduced by Lighthill (1949), and seek solutions up to the third order

$$\theta(\alpha x) = \varepsilon\theta_1 + \varepsilon^2\theta_2 + \varepsilon^3\theta_3 + O(\varepsilon^4), \tag{3.33}$$

$$F^2 = 1 + \varepsilon F_1 + \varepsilon^2 F_2 + \varepsilon^3 F_3 + O(\varepsilon^4), \tag{3.34}$$

$$\alpha^2 = \frac{\left((1-r)^2 - \delta\right)}{(r-1)^2\left(1+(r-1)\delta\right)}\left(\varepsilon\alpha_1 + \varepsilon^2\alpha_2 + \varepsilon^3\alpha_3\right) + O(\varepsilon^4). \tag{3.35}$$

It should be noted that the subscripts in the perturbation expansions indicate the order and are unrelated to the layers mentioned in Section 3.1. We substitute Eqs. (3.33) -(3.35) into (3.32) and rearrange all the terms in terms of the order of ε. We find that the terms of ε^0, ε^1, ε^2 are eliminated. The coefficient of ε^3 is

$$\frac{(1-\delta)\left((1-r)^2 - \delta\right)}{2(r-1)\left((r-1)+\delta\right)}\left[\theta_1^3 - \frac{(r-1)\left((r-1)+\delta\right)}{\left((1-r)^2 - \delta\right)}F_1\theta_1^2 + \frac{1}{3}\alpha_1\theta_1^{\prime 2}\right]. \tag{3.36}$$

The prime in Expression (3.36) denotes the differentiation with respect to αx. To ensure the terms of $O(\varepsilon^3)$ vanish, we have the equation

$$\theta_1^3 - \frac{(r-1)\left((r-1)+\delta\right)}{\left((1-r)^2 - \delta\right)}F_1\theta_1^2 + \frac{1}{3}\alpha_1\theta_1^{\prime 2} = 0. \tag{3.37}$$

This is the familiar first-order KdV equation. We seek for the normal solitary wave solution, which is of smooth convex-shape without sharp corner. The maximum displacement is on the symmetry axis and the crest is rounded other than cusped. Using the conditions $\theta = \varepsilon$ or $\theta_1 = 1$ and $\theta' = 0$ at the crest, we can determine the Froude number:

$$F_1 = \frac{\left((1-r)^2 - \delta\right)}{(r-1)\left((r-1)+\delta\right)}. \tag{3.38}$$

Suppose the solution has the "sech^2" form, it leads that all the terms in the equation vanish fast as $|x| \to \infty$. It can be called the uniform validity requirement. Substitution of the prescribed form into Eq. (3.37) leads to the determination of α_1, *i.e.*,

$$\alpha_1 = \frac{3}{4}. \tag{3.39}$$

Thus

$$\theta_1 = \mathrm{sech}^2 \sqrt{\frac{3}{4}\varepsilon \frac{\left((1-r)^2 - \delta\right)}{(r-1)^2\left(1+\delta(r-1)\right)}}x. \tag{3.40}$$

The first-order solution above agrees with those given by Long (1956), Benjamin (1966) and Mirie and Su (1984). When $\rho_1 \simeq \rho_2$, and it also agrees with the results given by Keulegan (1953) and Osborne and Burch (1980). If $\rho_2 = 0$, the solution becomes the surface solitary wave solution on one homogeneous fluid. It agrees with the first-order solutions given by Boussinesq (1871), Korteweg and De Vries (1895) and Fenton (1972).

At the order of ε^4, the Eq. (3.32) gives

$$\frac{(1-\delta)\left((1-r)^2-\delta\right)}{3(r-1)\left((r-1)+\delta\right)}\alpha_1\theta_1'\theta_2'+\left[\frac{3(1-\delta)\left((1-r)^2-\delta\right)}{2(r-1)\left((r-1)+\delta\right)}\theta_1^2-(1-\delta)F_1\theta_1\right]\theta_2$$
$$+\frac{(1-\delta)\left((1-r)^2-\delta\right)}{6(r-1)\left((r-1)+\delta\right)}\alpha_2\theta_1'^2-\frac{1}{2}(1-\delta)F_2\theta_1^2+\frac{(1-\delta)\left((1-r)^2-\delta\right)}{6(r-1)\left((r-1)+\delta\right)}F_1\alpha_1\theta_1'^2$$
$$+\frac{1}{90}\alpha_1^2\left(2\theta_1'\theta_1'''-\theta_1''^2\right)\frac{(1-\delta)\left((1-r)^2-\delta\right)^2\left(1-(1-r)^3\delta\right)}{(r-1)^3\left((r-1)+\delta\right)\left(1+(r-1)\delta\right)^2} \tag{3.41}$$
$$+\frac{(1-\delta)\left((1-r)^3-\delta\right)}{2(r-1)^2\left((r-1)+\delta\right)}\theta_1^4+\frac{(1-\delta)\left((1-r)^2-\delta\right)}{2(r-1)\left((r-1)+\delta\right)}F_1\theta_1^3$$
$$-\frac{(1-\delta)^2\left((1-r)^2-\delta\right)}{6(r-1)\left((r-1)+\delta\right)\left(1+(r-1)\delta\right)}\alpha_1\theta_1\theta_1'^2=0.$$

After we substitute the first-order solution into Eq. (3.41), it becomes an inhomogeneous ordinary differential equation for θ_2. Again, we apply the restrictions at the crest, $\theta=\varepsilon$ and $\theta'=0$. In other words, $\theta_1(0)=1$, $\theta_1'(0)=0$, $\theta_2(0)=0$ and $\theta_2'(0)=0$. Substituting these into Eq. (3.41), F_2 can be obtained as

$$\begin{aligned}F_2=&-(1-\delta)(20(r-1)\left((r-1)^2-\delta\right)^2-20(r-1)\left((r-1)+\delta\right)\left((r-1)^3+\delta\right)\\&-\left(\left((r-1)+\delta\right)\left((r-1)^2-\delta\right)^2\left(1+(r-1)^3\delta\right)\right)/\left(1+(r-1)\delta\right)^2)\\&/\left(20(r-1)^3(-1+\delta)\left((r-1)+\delta\right)^2\right).\end{aligned} \tag{3.42}$$

The abbreviation of Eq. (3.41) could be written as

$$\theta_2'+p(x)\theta_2=q(x). \tag{3.43}$$

Here $p(x)$ and $q(x)$ are functions of x. The second-order component can be obtained by the standard procedure for the ordinary differential equation, which leads to

$$\theta_2 = \frac{\int e^{\int p(x')dx'} q(x)\,dx + C_0}{e^{\int p(x')dx'}}, \tag{3.44}$$

where C_0 is an arbitrary constant. When we substitute all the known variables including Eq. (3.42) into Eq. (3.44), it yields

$$\begin{aligned}\theta_2 = {} & C_0 \bullet \operatorname{sech}^2(\alpha x)\tanh(\alpha x) + C_1 \bullet \operatorname{sech}^2(\alpha x)\tanh^2(\alpha x) \\ & + C_2 \bullet x\operatorname{sech}^2(\alpha x)\tanh(\alpha x),\end{aligned} \tag{3.45}$$

where

$$\begin{aligned}C_1 = {} & -3(3(r-1)^4 + (-9+33r-57r^2+81r^3-89r^4+59r^5-21r^6+3r^7)\delta \\ & + (9-30r+48r^2-24r^3-10r^4+14r^5-4r^6)\delta^2 + 3(r-1)^3\delta^3) \\ & / \left(12(r-1)^2\left((r-1)^2-\delta\right)\left(1+(r-1)\delta\right)^2\right),\end{aligned} \tag{3.46}$$

$$\begin{aligned}C_2 = {} & ((15+16\alpha_2)(r-1)^4 + (r-1)(16\alpha_2(3-9r+12r^2-8r^3+2r^4) \\ & + 3(15-40r+63r^2-52r^3+23r^4-6r^5+r^6))\delta \\ & + (16\alpha_2(r-1)^3(-3+3r-3r^2+r^3) + 3(15-50r+88r^2-100r^3 \\ & + 70r^4-26r^5+4r^6))\delta^2 - (-15+16\alpha_2(r-1))\delta^3) \\ & / \left(12(r-1)^2\left((r-1)^2-\delta\right)\left(1+(r-1)\delta\right)^2\right).\end{aligned} \tag{3.47}$$

Since $\theta_2'(0) = 0$, Eq. (3.45) yields $C_0 = 0$. The last term on the right hand side (RHS) of Eq. (3.45), which contains $x \bullet \operatorname{sech}^2(\alpha x)\tanh(\alpha x)$, attenuates much more slowly than the other terms as $|x| \to \infty$. We eliminate this term for the sake of uniform validity. By setting $C_2 = 0$, the unknown α_2 can be obtained explicitly as

$$\begin{aligned}\alpha_2 = {} & -3(5(r-1)^4 + (-15+55r-103r^2+115r^3-75r^4+29r^5-7r^6+r^7)\delta \\ & + (15-50r+88r^2-100r^3+70r^4-26r^5+4r^6)\delta^2 + 5(r-1)^3\delta^3) \\ & / \left(16(r-1)^2\left((r-1)^2-\delta\right)\left(1+(r-1)\delta\right)^2\right).\end{aligned} \tag{3.48}$$

At last the second-order component is given by

$$\theta_2 = C_1 \bullet \operatorname{sech}^2(\alpha x)\tanh^2(\alpha x). \tag{3.49}$$

The second-order solution agrees with those given by Koop and Butler (1981), Gear and Grimshaw (1983) and Mirie and Su (1984). Again if $\rho_2 = 0$, the solution is reduced to the second-order solution for the surface solitary wave given by Laitone (1960) and Fenton (1972).

The same procedure can be used on the coefficients of ε^5. The ordinary differential equation for θ_3 is

$$\begin{aligned}
&C_3\alpha_1\theta_1'\theta_3' + C_4\theta_1^2\theta_3 + C_5F_1\theta_1\theta_3 + C_6\alpha_1\theta_2'^2 + C_7\alpha_2\theta_1'\theta_2' + C_8\alpha_3\theta_1'^2 + C_9F_1\alpha_1\theta_1'\theta_2' \\
&+C_{10}F_1\alpha_2\theta_1'^2 + C_{11}F_2\alpha_1\theta_1'^2 + C_{12}\theta_1\theta_2^2 + C_{13}F_1\theta_2^2 + C_{14}F_2\theta_1\theta_2 + C_{15}F_3\theta_1^2 \\
&+C_{16}\alpha_1^2\theta_1'\theta_2''' + C_{17}\alpha_1^2\theta_2'\theta_1''' + C_{18}\alpha_1^2\theta_1''\theta_2'' + C_{19}\alpha_1^2\theta_1\theta_1'\theta_1''' + C_{20}\alpha_1^2\theta_1\theta_1''^2 + C_{21}\alpha_1^2\theta_1'^2\theta_1'' \\
&+C_{22}F_1\alpha_1^2\theta_1'\theta_1''' + C_{23}F_1\alpha_1^2\theta_1''^2 + C_{24}\alpha_1\alpha_2\theta_1'\theta_1''' + C_{25}\alpha_1\alpha_2\theta_1''^2 + C_{26}\alpha_1^3\theta_1'\theta_1^{(5)} + C_{27}\alpha_1^3\theta_1''\theta_1^{(4)} \\
&+C_{28}\alpha_1^3\theta_1'''^2 + C_{29}\alpha_2\theta_1'^2\theta_1 + C_{30}\alpha_1\theta_1'\theta_2''\theta_1 + C_{31}\alpha_1\theta_1'^2\theta_1^2 + C_{32}\theta_1^5 + C_{33}\alpha_1\theta_1'^2\theta_2 \\
&+C_{34}\theta_1^3\theta_2 + C_{35}\alpha_1\theta_1'^2\theta_1F_1 + C_{36}\theta_1^4F_1 + C_{37}\theta_1^2\theta_2F_1 + C_{38}\theta_1^3F_2 = 0.
\end{aligned} \tag{3.50}$$

The constant coefficients $C_3 - C_{38}$ have been listed in Appendix C. In Eq. (3.50) θ_1, θ_2, F_1 and F_2 are known. In the same way used for the second-order components, we can obtain the third-order components for Froude number, α and wave profile, respectively, as follows

$$\begin{aligned}
F_3 = &[-6(-1+r)^8 + (-1+r)^4(42 - 156r + 22r^2 + 68r^3 - 439r^4 + 680r^5 - 567r^6 \\
&+ 274r^7 - 72r^8 + 8r^9)\delta + (-1+r)^3(126 - 558r + 8r^2 + 1500r^3 - 2667r^4 \\
&+ 3257r^5 - 2709r^6 + 1371r^7 - 431r^8 + 85r^9 - 11r^{10} + r^{11})\delta^2 + (-1+r)^2 \\
&(210 - 1080r + 340r^2 + 4864r^3 - 10590r^4 + 11180r^5 - 8211r^6 + 4964r^7 \\
&- 2342r^8 + 764r^9 - 158r^{10} + 16r^{11})\delta^3 + (-210 + 1440r - 2320r^2 \\
&- 4936r^3 + 25764r^4 - 47716r^5 + 51415r^6 - 36658r^7 + 18873r^8 - 7548r^9 \\
&+ 2319r^{10} - 466r^{11} + 43r^{12})\delta^4 + (126 - 828r + 1358r^2 + 2748r^3 - 15759r^4 \\
&+ 31708r^5 - 36570r^6 + 26256r^7 - 11740r^8 + 3116r^9 - 444r^{10} + 28r^{11})\delta^5 \\
&+ (-42 + 264r - 508r^2 - 332r^3 + 3631r^4 - 8366r^5 + 10668r^6 - 8426r^7 \\
&+ 4119r^8 - 1148r^9 + 140r^{10})\delta^6 + 6(-1+r)^6\delta^7] \\
&/\left(140(-1+r)^5((-1+r)+\delta)^3(1+(-1+r)\delta)^4\right),
\end{aligned} \tag{3.51}$$

$$
\begin{aligned}
\alpha_3 = (&3(30(-1+r)^6 + (-1+r)^2(-150+600r-1234r^2+1392r^3-903r^4+346r^5 \\
&-83r^6+12r^7)\delta + (300-1800r+5502r^2-10800r^3+14451r^4-13496r^5 \\
&+8970r^6-4348r^7+1580r^8-436r^9+88r^{10}-12r^{11}+r^{12})\delta^2 + (-300 \\
&+1800r-5502r^2+11220r^3-16341r^4+17152r^5-12946r^6+7016r^7 \\
&-2720r^8+740r^9-132r^{10}+12r^{11})\delta^3 + (-1+r)^3(-150+450r-784r^2 \\
&+1028r^3-925r^4+501r^5-152r^6+20r^7)\delta^4 - 30(-1+r)^6\delta^5)) \\
&/(80(-1+r)^4((-1+r)^2-\delta)(1+(-1+r)\delta)^4)
\end{aligned}
\tag{3.52}
$$

$$
\begin{aligned}
\theta_3 = (&\operatorname{sech}^4(\alpha x)\bullet\tanh^2(\alpha x)(5\cosh(2\alpha x)(15(-1+r)^8 + 2(-1+r)^4(-45+165r \\
&-297r^2+465r^3-478r^4+297r^5-102r^6+15r^7) + (-1+r)^2(225-1200r \\
&+3216r^2-6108r^3+9329r^4-11540r^5+11322r^6-8640r^7+4997r^8 \\
&-2100r^9+606r^{10}-108r^{11}+9r^{12})\delta^2 - 2(-1+r)^2(150-750r+1962r^2 \\
&-3348r^3+4632r^4-5328r^5+4569r^6-2664r^7+995r^8-218r^9 \\
&+21r^{10})\delta^3 + (225-1500r+4866r^2-9552r^3+12452r^4-11324r^5 \\
&+7542r^6-4000r^7+1884r^8-800r^9+272r^{10}-64r^{11}+8r^{12})\delta^4 \\
&+2(-1+r)^3(45-150r+252r^2-120r^3-137r^4+213r^5-108r^6 \\
&+20r^7)\delta^5 + 15(-1+r)^6\delta^6) - 2(114(-1+r)^8 - (-1+r)^4(684-2508r \\
&+3876r^2-2766r^3-541r^4+3954r^5-4341r^6+2358r^7-648r^8 \\
&+72r^9)\delta + (-1+r)^2(1710-9120r+21888r^2-30156r^3+23132r^4 \\
&-7496r^5+2295r^6-7968r^7+10922r^8-7266r^9+2694r^{10}-540r^{11} \\
&+45r^{12})\delta^2 - (2280-15960r+51072r^2-98952r^3+127272r^4 \\
&-109680r^5+48867r^6+26220r^7-73580r^8+72102r^9-41802r^{10} \\
&+14948r^{11}-3063r^{12}+276r^{13})\delta^3 + (1710-11400r+34428r^2 \\
&-63324r^3+78338r^4-63224r^5+27495r^6-778r^7-3939r^8-530r^9 \\
&+2057r^{10}-928r^{11}+140r^{12})\delta^4 + (-684+4332r-12084r^2 \\
&+20034r^3-21593r^4+16038r^5-9456r^6+5368r^7-2739r^8 \\
&+924r^9-140r^{10})\delta^5 + 114(-1+r)^6\delta^6))) \\
&/(240(-1+r)^4(-(-1+r)^2\rho_1+\rho_2)^2(\rho_1+(-1+r)\rho_2)^4)
\end{aligned}
\tag{3.53}
$$

The horizontal velocities on the bottom and the top can be calculated by Eqs. (3.26) and (3.27) after substituting the wave profile. The speed of the uniform streams at infinity, together with the velocity field in the both layers, is shown in Appendix D. For direct implementation in the code, the velocities have been converted into physical variables in Appendix D.

3.3 Comparison with the published result

Mirie and Su (1984) presented the explicit expressions of the third-order solution of an ISW in a rigid-lid two-layer model with the weakly nonlinear assumptions. The expressions include the wave speed, interface displacement and horizontal bottom and ceiling velocities. Mirie and Pennell (1989) further studied the properties of the ISW based on the ninth-order solution. However, Mirie and Pennell (1989) did not give out the explicit expressions. Therefore, the solution given by Mirie and Su (1984) is chosen for comparison with the third-order solution in the present thesis.

As mentioned before, if the density of the upper layer is set to be zero, the solution of an SSW on a homogeneous fluid emerges from the ISW solution. The SSW solution obtained both from the present thesis and that given by Mirie and Su (1984) have been compared with the existing solutions. It is found that both of the solutions are identical with those of Grimshaw (1971) and Fenton (1972). However, if the density in the upper layer is not zero, θ, F and α obtained in this thesis are different from those given by Mirie and Su (1984).

There is a specific example in the paper by Mirie and Pennell (1989), which gave F^2 for $r=1.5$ and $\delta=0.05$ up to the ninth order. The third-order result taken from Eq. (29) in their paper is

$$F^2 = 1+(8/11)\varepsilon-(784786/1017005)\varepsilon^2-1.206\varepsilon^3. \tag{3.54}$$

With the same parameters, the solution given by this thesis yields

$$F^2 = 1+\frac{8}{11}\varepsilon-\frac{784786}{1017005}\varepsilon^2-\frac{157802664378}{131638076185}\varepsilon^3. \tag{3.55}$$

$\frac{157802664378}{131638076185}\approx 1.20584,$ which is virtually the same as 1.206 in Eq. (3.54). The expression in the paper by Mirie and Su (1984) gives

$$F^2 = 1 + \frac{8}{11}\varepsilon - \frac{784786}{1017005}\varepsilon^2 - \frac{158734610778}{131638076185}\varepsilon^3. \qquad (3.56)$$

$158734610778/131638076185 \approx 1.19876$, which does not agree with the corresponding coefficient in Eq. (3.54).

Furthermore, the solution in the present work and that of Mirie and Su (1984) have been substituted back to the continuity equations and Bernoulli equations. It has been found that, with the solution in the present thesis, the residual of continuity and Bernoulli equations is of the order $O\left(\varepsilon^{7/2}\right)$. Whereas the residual of $O\left(\varepsilon^3\right)$ remains when the solution given by Mirie and Su (1984) is used. Therefore, it can be concluded that the expressions given by Mirie and Su (1984) do not satisfy the governing equations up to the third order but the solution given by the present thesis satisfies the same governing equations up to the third order.

3.4 Validation

As introduced in Chapter 2, the ISW amplitude has been classified into three categories provided that $0.95 < \delta < 1$ and $r \approx 4/3$. There have been some experiments and the fully nonlinear solutions obtained by numerical methods available to validate the analytical solutions for an ISW of small amplitude (Fig. 3-2) or moderate amplitude (Fig. 3-3) or large amplitude (Figs. 3-4 & 3-5). From Figs. 3-2 & 3-3, it can be seen that the ISW solutions of the KdV family equations are capable of depicting the small and moderate-amplitude ISW, and the third-order solution agrees with the experiment or the exact solution the best. The KdV theories are not appropriate to depict the large-amplitude ISW (Fig. 3-4), whereas the eKdV theory and the MCC theory can be used (Fig. 3-5).

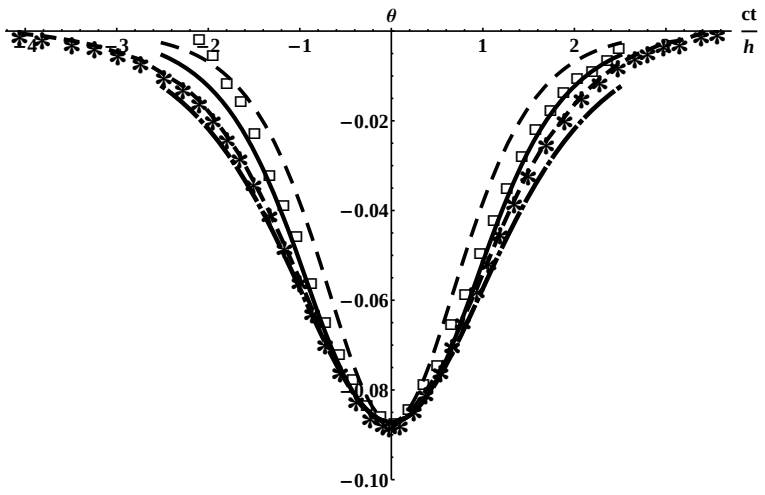

Fig. 3-2 Internal solitary wave profiles for $r = 5.13/4.13$, $\delta = 999/1022$ and $\varepsilon = -0.087$. The dashed line (- - -) is the first-order solution; the dot dashed (- . -) line is the second-order solution; the solid line (—) is the third-order solution in the present thesis. The □ is experimental measurement given by Grue et al. (1999). The asterisk dashed line (-*-) is the exact solution given by Grue et al. (1999).

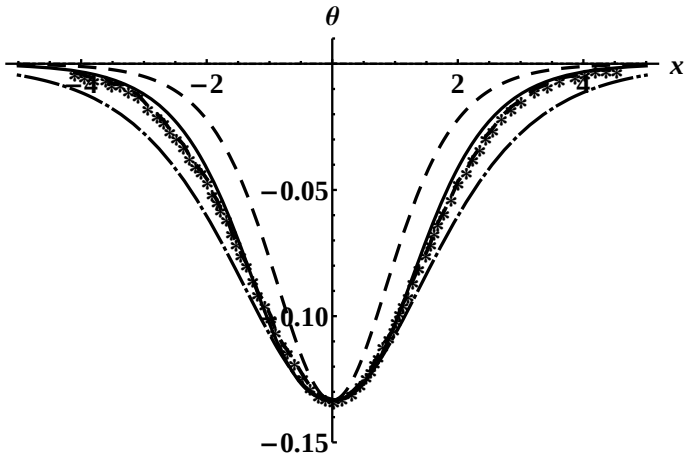

Fig. 3-3 ISW profiles for $r = 4/3$, $\delta = 0.997$ and $\varepsilon = -0.1333$. The dashed line (- - -) is the first-order solution; the dot dashed (- . -) line is the second-order solution; the solid line (—) is the third-order solution in the present thesis. The asterisk dashed line (-*-) is the exact solution given by Evans and Ford (1996).

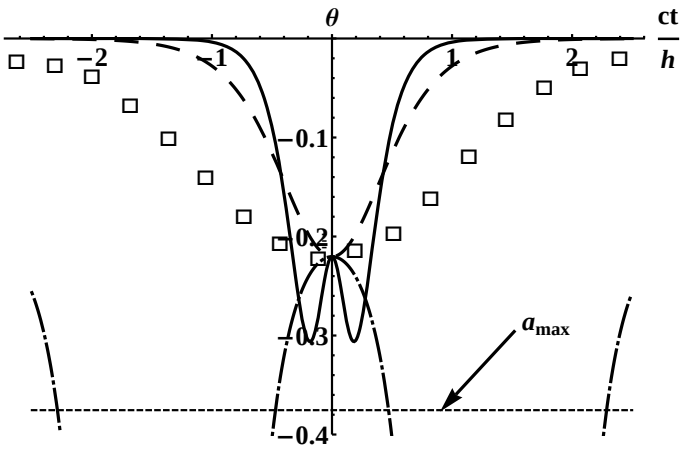

Fig. 3-4 ISW profiles for $r = 5.13/4.13$, $\delta = 999/1022$ and $\varepsilon = -0.22$. The dashed line (- - -) is the first-order solution; the dot dashed (- . -) line is the second-order solution; the solid line (—) is the third-order solution in the present thesis. The □ is experimental measurement given by Grue et al. (1999). a_{max} given by Eq. (2.43) has been marked.

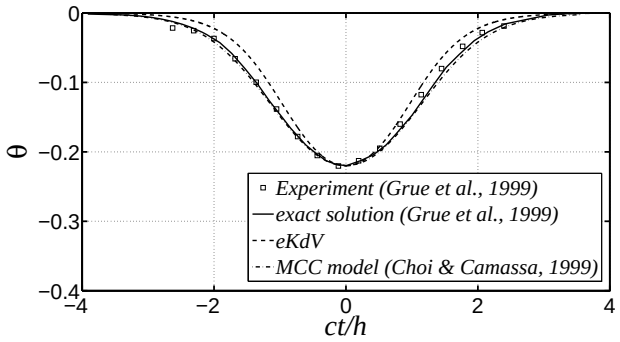

Fig. 3-5 ISW profiles for $r = 5.13/4.13$, $\delta = 999/1022$ and $\varepsilon = -0.22$. Comparison of the experiment, the exact solution, the eKdV model and the MCC model.

3.5 Summary

A novel derivation of the higher-order weakly nonlinear model that contains the ISW solution has been presented. The conserved quantities reveal the mass conservations within each layer, the momentum transfer between two layers and the energy conservation. The successive approximation method has been used to derive equations to any accuracy, with the orders in terms of the nonlinearity. The partial differential equation in terms of the interface displacement has been converted to ordinary differential equations at each order via the perturbation method. The ordinary differential equations can be successively solved with additional restrictions.

This method can be applied to seek for the KdV-type soliton solution up to any order. The third-order solution given by the present thesis corrects an error by Mirie and Su (1984). It agrees better with the experiment and the fully nonlinear solution than the lower-order solutions for ISWs of small amplitude and moderate amplitude.

Chapter 4 Solving the KP and EKP equations

4.1 Introduction

Both the dimensional forms of the KP equations for surface waves and internal waves can be transformed to the standard one. The analytical solutions of the standard form of the KP equation, which correspond to the Mach reflection and the regular reflection, respectively, are to be introduced. The Extended Kadomtsev-Petviashvili (EKP) equation is another approximate model for internal waves (Chen and Liu, 1998; Tsuji and Oikawa, 2007). The V-shape initial value problem of the EKP equation is to be solved numerically to model the oblique reflection of an ISW.

4.2 Coordinate transformations to the standard form of the KP equation

The KP theory is based on the weakly nonlinear, long wave/shallow water, weak three-dimensionality assumptions. In a Cartesian coordinate system with the *z*-axis pointing upward, the surface displacement is denoted by $\theta(x, y, z)$. The primary wave propagation direction is along the *x*-axis, and the dimensional form of the KP equation for surface waves can be written as (Li et al. 2011)

$$\frac{\partial}{\partial x}\left[\frac{\partial \theta}{\partial t}+\left(1+\frac{3}{2}\frac{\theta}{h_S}\right)c_{S0}\frac{\partial \theta}{\partial x}+\frac{1}{6}h_S^2 c_{S0}\frac{\partial^3 \theta}{\partial x^3}\right]+\frac{c_{S0}}{2}\frac{\partial^2 \theta}{\partial y^2}=0, \qquad (4.1)$$

where h_S is the undisturbed water depth. In Chapter 2, we have mentioned the partially higher-order correction ($O(\varepsilon^2)$) implied by the interaction parameter κ taking into account the "small-but-finite" ψ_i (Kodama and Yeh, 2016). Li et al. (2011) have explained why this correction can make the KP theory depict the physical phenomenon better. In reality, the cross section of a solitary wave in the far

field does not change with ψ_i. However, when using the analytical solution of Eq. (4.1) to model the waves, the subtle disparity would happen due to the approximation implied in the theory. Let us first consider the simplest scenario and use Eq. (4.1) to model a single solitary wave. For a single solitary wave that is propagating in an unbounded fluid, an exact solution of Eq. (4.1) exists, *i.e.* (Li et al., 2011),

$$\theta = a\,\mathrm{sech}^2\left[\sqrt{\frac{3}{4}\frac{a}{h_S^3}}\left(x + y\tan\psi - c_{S0}\left(1+\frac{1}{2}\frac{a}{h_S}+\frac{1}{2}\tan^2\psi\right)t\right)\right], \quad (4.2)$$

where ψ is the angle between its crest line and the *y*-coordinate, and *a* is the wave amplitude at a cross section. According to Eq. (4.2), the cross section of the solitary wave varies with ψ. For example, as $\psi \to \pi/2$, $\tan\psi \to \infty$, which means the KP theory is more unrealistic as the ψ increases. With the expansion $\cos\psi = 1 - 1/2\tan^2\psi + O(\varepsilon^2)$ for $\tan^2\psi = O(\varepsilon)$, Eq. (4.2) can be converted to the form

$$\theta = a\,\mathrm{sech}^2\left[\sqrt{\frac{3}{4}\frac{a}{h_S^3\cos^2\psi}}\left(x\cos\psi + y\sin\psi - c_{S0}\left(1+\frac{1}{2}\frac{a}{h_S}\right)t + O(\varepsilon^2)\right)\right], \quad (4.3)$$

which has the same order as Eq. (4.2) and invariant cross sections with respect to ψ. Suppose the physical solitary wave has the "KdV" shape as in Eq. (2.11), $a/\cos^2\psi$ is equivalent to the physical wave amplitude $\hat{a}$. Since $\hat{a} = a/\cos^2\psi = a\left(1+\tan^2\psi\right) = a\left(1+O(\varepsilon)\right)$, the equivalence only causes a higher-order correction. To construct the analytical solutions for the oblique reflection problem, the solitons in the far field are in the form of Eq. (4.2). Supposing $\hat{a}_i$ is the measured incident wave amplitude in the experiment or the fully nonlinear numerical simulation, we can convert it to the KP model by $a_i = \hat{a}_i\cos^2\psi_i = \hat{a}_i\left(1+O(\varepsilon)\right)$. a_i and ψ_i are used as inputs to obtain the analytical

solution $\theta(x,y,t)$. We can then use $\hat{\theta}=\theta/\cos^2\psi_i$ to convert the wave profile to the physical space, and $\hat{\theta}$ approaches the results given by Eqs. (2.57)-(2.60) replacing k with κ asymptotically. For simplicity, the hats on the variables will be eliminated hereinafter. This manipulation is also applicable to the KP and EKP models for internal waves.

For the further comparison, the leading order approximation on the horizontal fluid velocity in the *x*-direction is introduced here. The KP theory implies that $|u|\gg|v|$ and $|u|\gg|w|$. Hence,

$$u=\frac{\theta c_{S0}}{h_S}+O(\varepsilon^2). \tag{4.4}$$

With the following variable transformations:

$$\Theta^*=\frac{3}{2h_S}\theta,\quad X^*=\frac{1}{h_S}\left(x-c_{S0}t\right),\quad Y^*=\frac{1}{h_S}y,\quad T^*=\frac{2c_{S0}}{3h_S}t, \tag{4.5}$$

Eq. (4.1) can be converted to the standard form of the KP equation:

$$\frac{\partial}{\partial X^*}\left(4\frac{\partial\Theta^*}{\partial T^*}+6\Theta^*\frac{\partial\Theta^*}{\partial X^*}+\frac{\partial^3\Theta^*}{\partial X^{*3}}\right)+3\frac{\partial^2\Theta^*}{\partial Y^{*2}}=0. \tag{4.6}$$

If the last term on the LHS of Eq. (4.6) is negative, *i.e.*, $-3\frac{\partial^2\Theta^*}{\partial Y^{*2}}$, it is called the KPI equation conventionally, and can be used to model capillary waves. Correspondingly, Eq. (4.6) is called the KPII equation. The KPII equation is referred to as the KP equation throughout the thesis unless it is specially specified.

The KP equation for internal waves in a two-layer rigid-lid model (Ablowitz and Segur, 1980; Barros and Choi, 2013), *i.e.*,

$$\frac{\partial}{\partial x}\left[\frac{\partial \theta}{\partial t}+c_0\frac{\partial \theta}{\partial x}+\gamma_1\theta\frac{\partial \theta}{\partial x}+\gamma_2\frac{\partial^3\theta}{\partial x^3}\right]+\frac{c_0}{2}\frac{\partial^2\theta}{\partial y^2}=0, \tag{4.7}$$

can be also converted to the standard form (4.6), by the following transformations:

$$\Theta^*=\frac{3}{2h_0}\theta, X^*=\frac{1}{h_0}\left(x-c_0t\right), Y^*=\frac{C_{KP1}}{h_0}y, T^*=\frac{2c_0}{3h_0}C_{KP2}t, \tag{4.8}$$

where

$$h_0=\left(\frac{h^2\left(h-H\right)^2\left(h\left(\rho_1-\rho_2\right)+H\rho_2\right)}{\left(h-H\right)^2\rho_1-h^2\rho_2}\right)^{\frac{1}{3}}, \tag{4.9}$$

$$C_{KP1}=\sqrt{\frac{h\left(h-H\right)\left(h\left(\rho_1-\rho_2\right)+H\rho_2\right)}{\left(-H\rho_1+h\left(\rho_1-\rho_2\right)\right)h_0^2}} \tag{4.10}$$

$$C_{KP2}=h_0\left(\frac{\left(h-H\right)^2\rho_1-h^2\rho_2}{h\left(h-H\right)\left(-H\rho_1+h\left(\rho_1-\rho_2\right)\right)}\right). \tag{4.11}$$

The interaction parameter in a dimensional form for internal waves can be written as

$$\kappa=\frac{\tan\psi_i}{C_{KP1}\sqrt{3a_i/h_0}\cos\psi_i}. \tag{4.12}$$

where a_i is the maximum interface displacement of the incident wave, and can be either positive or negative, ψ_i is the incident wave angle.

4.3 Analytical solutions of the KP equation for the Mach reflection and the regular reflection

By the Hirota direct method (Hirota, 2004), the multi-soliton solution of Eq. (4.6) can be obtained via the *tau* function:

$$\Theta^*\left(X^*,Y^*,T^*\right)=2\frac{\partial^2}{\partial X^{*2}}\left[\ln\tau\left(X^*,Y^*,T^*\right)\right]. \tag{4.13}$$

The *tau* function is defined by the Wronskian determinant:

$$\tau = Wr\left(f_1, f_2, \ldots, f_n\right) = \begin{vmatrix} f_1 & f_2 & \cdots & f_n \\ f_1^{(1)} & f_2^{(1)} & \cdots & f_n^{(1)} \\ \vdots & \vdots & \ddots & \vdots \\ f_1^{(n-1)} & f_2^{(n-1)} & \cdots & f_n^{(n-1)} \end{vmatrix}. \tag{4.14}$$

where $f_i^{(k)} := \partial^k f_i / \partial X^{*k}$ for $i = 1, \ldots, n; 1 \le k \le n-1$. The functions $f_1, f_2, \ldots, f_n$ also have to satisfy the relationships, *i.e.*, $\partial f_i / \partial Y^* = f_i^{(2)}$ and $\partial f_i / \partial T^* = -f_i^{(3)}$. $f_1, f_2, \ldots, f_n$ are then constructed as (Yeh et al., 2010)

$$f_i = \sum_{j=1}^{m} a_{ij} e^{\sigma_j X^* + \sigma_j^2 Y^* - \sigma_j^3 T^*}. \tag{4.15}$$

where the superscripts 2 and 3 indicate square and cube, respectively, and m is an integer. All the coefficients a_{ij} form an $n \times m$ matrix $\mathbf{A}$. The coefficients σ_j are aligned in the order $\sigma_1 < \cdots < \sigma_m$. When $n = 1$ and $m = 2$, the single soliton solution can be obtained. When $n = 2$ and $m = 4$, the multi-soliton solutions for the Mach reflection and the regular reflection can be obtained. The following procedure is to determine the **A**-matrix and σ-parameters for the oblique reflection of a solitary wave.

The incident wave angle ψ_i and the incident wave amplitude a_i for surface waves or internal waves are converted to Ψ_i^* and A_i^*, respectively, through the transformations mentioned above. The interaction parameter for the standard form is

$$K^* = \frac{\tan \Psi_i^*}{\sqrt{2A_i^*}}. \tag{4.16}$$

If $K^* < 1$, it yields the (3142)-type solution, which corresponds to the Mach reflection. If $K^* > 1$, it yields the O-type solution, which corresponds to the regular reflection. In this thesis, the Mach reflection is mainly concerned. The σ-parameters

for the (3142)-type solution can be then obtained as (Chakravarty and Kodama, 2009)

$$\begin{aligned}\sigma_1 &= -\frac{1}{2}\left(\tan\Psi_i^* + \sqrt{2A_i^*}\right), \quad \sigma_2 = \frac{1}{2}\left(\tan\Psi_i^* - \sqrt{2A_i^*}\right), \\ \sigma_3 &= -\frac{1}{2}\left(\tan\Psi_i^* - \sqrt{2A_i^*}\right), \quad \sigma_4 = \frac{1}{2}\left(\tan\Psi_i^* + \sqrt{2A_i^*}\right).\end{aligned} \tag{4.17}$$

The **A**-matrix for the (3142)-type solution is

$$\mathbf{A}_{(3142)} = \begin{bmatrix} 1 & a_{1,2} & 0 & a_{1,4} \\ 0 & 0 & 1 & a_{2,4} \end{bmatrix}, \tag{4.18}$$

where $a_{1,2}, a_{2,4}, a_{1,4}$ can be written as (Chakravarty and Kodama, 2009)

$$a_{1,2} = \frac{\sigma_3 - \sigma_1}{\sigma_3 - \sigma_2}, a_{2,4} = \frac{\sigma_3 - \sigma_1}{\sigma_4 - \sigma_1}, a_{1,4} = -\frac{\sigma_3 - \sigma_1}{\sigma_4 - \sigma_3}. \tag{4.19}$$

The *tau* function is

$$\begin{aligned}\tau = &\left(\sigma_3 - \sigma_1\right) e^{\sigma_1 X^* + \sigma_1^2 Y^* - \sigma_1^3 T^* + \sigma_3 X^* + \sigma_3^2 Y^* - \sigma_3^3 T^*} \\ &+ \left(\sigma_4 - \sigma_1\right) a_{2,4} e^{\sigma_1 X^* + \sigma_1^2 Y^* - \sigma_1^3 T^* + \sigma_4 X^* + \sigma_4^2 Y^* - \sigma_4^3 T^*} \\ &+ \left(\sigma_3 - \sigma_2\right) a_{1,2} e^{\sigma_2 X^* + \sigma_2^2 Y^* - \sigma_2^3 T^* + \sigma_3 X^* + \sigma_3^2 Y^* - \sigma_3^3 T^*} \\ &+ \left(\sigma_4 - \sigma_2\right) a_{1,2} a_{2,4} e^{\sigma_2 X^* + \sigma_2^2 Y^* - \sigma_2^3 T^* + \sigma_4 X^* + \sigma_4^2 Y^* - \sigma_4^3 T^*} \\ &- \left(\sigma_4 - \sigma_3\right) a_{1,4} e^{\sigma_3 X^* + \sigma_3^2 Y^* - \sigma_3^3 T^* + \sigma_4 X^* + \sigma_4^2 Y^* - \sigma_4^3 T^*}.\end{aligned} \tag{4.20}$$

Substituting Eq. (4.20) back to Eq. (4.13), the explicit expression of the multi-soliton solution for the Mach reflection can be obtained. An example has been shown in the lower panel of Fig. 2-6(a). By solving this so-called X-shape initial value problem, four *line*-solitons stretch to the far field. As $\left|Y^*\right| \to \infty$ each branch of these four becomes a one-soliton solution.

The O-type solution (the lower panel of Fig. 2-6(b)) will also be used in the analysis hereinafter. The σ -parameters for the O-type solution are

$$\sigma_1 = -\frac{1}{2}\left(\tan\Psi_i^* + \sqrt{2A_i^*}\right), \quad \sigma_2 = -\frac{1}{2}\left(\tan\Psi_i^* - \sqrt{2A_i^*}\right),$$
$$\sigma_3 = \frac{1}{2}\left(\tan\Psi_i^* - \sqrt{2A_i^*}\right), \quad \sigma_4 = \frac{1}{2}\left(\tan\Psi_i^* + \sqrt{2A_i^*}\right). \tag{4.21}$$

The **A**-matrix for the (3142)-type solution is

$$\mathbf{A}_{\mathrm{O}} = \begin{bmatrix} 1 & a_{1,2} & 0 & 0 \\ 0 & 0 & 1 & a_{2,4} \end{bmatrix}, \tag{4.22}$$

in which

$$a_{1,2} = \frac{\sigma_4 - \sigma_1}{\sigma_4 - \sigma_2}, a_{2,4} = \frac{\sigma_3 - \sigma_2}{\sigma_4 - \sigma_2}. \tag{4.23}$$

The *tau* function is

$$\begin{aligned} \tau = {} & \left(\sigma_3 - \sigma_1\right) e^{\sigma_1 X^* + \sigma_1^2 Y^* - \sigma_1^3 T^* + \sigma_3 X^* + \sigma_3^2 Y^* - \sigma_3^3 T^*} \\ & + \left(\sigma_4 - \sigma_1\right) a_{2,4} e^{\sigma_1 X^* + \sigma_1^2 Y^* - \sigma_1^3 T^* + \sigma_4 X^* + \sigma_4^2 Y^* - \sigma_4^3 T^*} \\ & + \left(\sigma_3 - \sigma_2\right) a_{1,2} e^{\sigma_2 X^* + \sigma_2^2 Y^* - \sigma_2^3 T^* + \sigma_3 X^* + \sigma_3^2 Y^* - \sigma_3^3 T^*} \\ & + \left(\sigma_4 - \sigma_2\right) a_{1,2} a_{2,4} e^{\sigma_2 X^* + \sigma_2^2 Y^* - \sigma_2^3 T^* + \sigma_4 X^* + \sigma_4^2 Y^* - \sigma_4^3 T^*}. \end{aligned} \tag{4.24}$$

4.4 Introduction to the EKP equation

Suppose that the predominant propagation direction of internal waves is in the *x*-direction in a Cartesian coordinate system. The dimensional form of the EKP equation is

$$\frac{\partial}{\partial x}\left(\frac{\partial \theta}{\partial t} + c_0 \frac{\partial \theta}{\partial x} + \gamma_1 \theta \frac{\partial \theta}{\partial x} + \gamma_3 \theta^2 \frac{\partial \theta}{\partial x} + \gamma_2 \frac{\partial^3 \theta}{\partial x^3}\right) + \frac{c_0}{2}\frac{\partial^2 \theta}{\partial y^2} = 0, \tag{4.25}$$

where c_0, γ_1, γ_2 and γ_3 have been given by Eqs. (2.26), (2.47), (2.48) and (2.51), respectively. Comparing with the KP equation, the EKP equation appends a higher-order nonlinear correction, *i.e.*, $\gamma_3 \theta^2 \frac{\partial \theta}{\partial x}$. The higher-order nonlinear correction is only predominant when the wave amplitude is large. Comparing with the eKdV equation, the EKP equation appends a term $\frac{c_0}{2}\frac{\partial^2 \theta}{\partial y^2}$ representing gentle

variation in the *y*-direction. With the transformation shown in Eq. (4.8), the EKP equation can be written in the standard form, *i.e.*,

$$\frac{\partial}{\partial X^*}\left(4\frac{\partial \Theta^*}{\partial T^*}+6\Theta^*\frac{\partial \Theta^*}{\partial X^*}-D\Theta^{*2}\frac{\partial \Theta^*}{\partial X^*}+\frac{\partial^3 \Theta^*}{\partial X^{*3}}\right)+3\frac{\partial^2 \Theta^*}{\partial Y^{*2}}=0. \qquad (4.26)$$

where

$$D=\frac{h_0^4\left[H\rho_1-h(\rho_1-\rho_2)\right]\left[(H-h)^4\rho_1^2+2h(H-h)(h^2-hH+4H^2)\rho_1\rho_2+h^4\rho_2^2\right]}{h^3(H-h)^3\left[h(\rho_1-\rho_2)+H\rho_2\right]\left[H\rho_1+h(-\rho_1+\rho_2)\right]^2}. \qquad (4.27)$$

For a single ISW propagating in the *X**-direction, there is an exact solution with the amplitude A^* (Tsuji and Oikawa, 2007):

$$\Theta^*=\frac{A^*\,\mathrm{sech}^2\lambda_{EKP}}{1-\frac{A^*}{12/D-A^*}\tanh^2\lambda_{EKP}},$$
$$\lambda_{EKP}=C_{EKP1}\left(X^*-X_0^*-C_{EKP2}T^*\right), C_{EKP1}=\frac{1}{2}\sqrt{A^*\left(2-\frac{DA^*}{6}\right)}, C_{EKP2}=C_{EKP1}^2. \qquad (4.28)$$

where X_0^* is a constant. The maximum possible amplitude or the limiting amplitude depends on the environmental parameters. The amplitude A^* has to be smaller than $6/D$ to obtain a convex wave profile. When $g=9.81\,m/s^2$, $\rho_1=1025\,kg/m^3$, $\rho_2=1000\,kg/m^3$, $H=100\,m$ and $h=75\,m$, the limiting amplitude $6/D=0.7599$.

The wave profiles given by the one-soliton solutions of the KP equation and the EKP equation at the same amplitude are compared in Figs. 4-1(a)-(c). When the wave amplitude is small, the wave profiles given by the two theories are almost graphically indistinguishable, as shown in Fig. 4-1(a). When the wave amplitude is moderate, the difference of the two theories becomes obvious as shown in Fig. 4-1(b). When the wave amplitude is close to the limiting amplitude, the two wave profiles become quite different as shown in Fig. 4-1(c). A “table-top” profile has formed based on the

EKP theory, while the profile given by the KP theory still has a narrow peak. Therefore, when the wave amplitude is small, the EKP theory gives the equivalent result to the KP theory. This is also true for the 3D collision scenarios (Tsuji and Oikawa, 2007). According to the experiments and observations of 2D ISWs (see Helfrich and Melville (2006)), the EKP theory should be more appropriate to depict the internal wave, the amplitude of which is close to the limiting amplitude, than the KP theory.

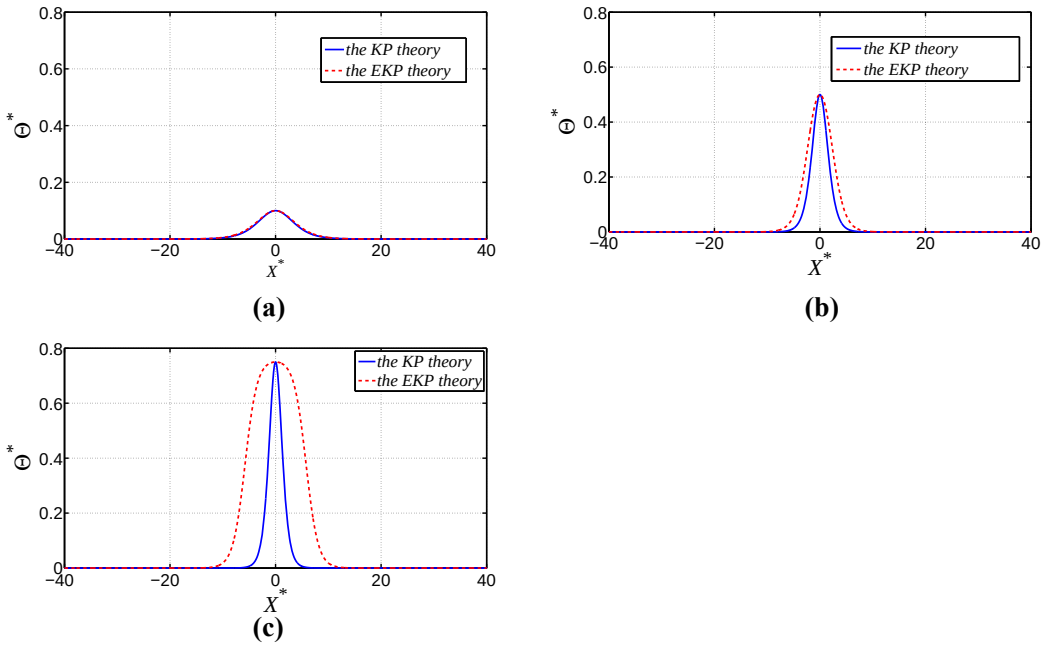

Fig. 4-1 The wave profiles given by the one-soliton solutions of the KP theory and the EKP theory with $A^*=0.1$ (a), $A^*=0.5$ (b) and $A^*=0.75$ (c).

4.5 Solving the KP equation using PDE2D

The software PDE2D uses the Finite Element Method (FEM) to solve partial differential equations, which is developed by Granville Sewell (Fitzgerald and Sewell, 2000; Sewell, 1993, 2005, 2010). Two FEMs have been implemented in PDE2D, which are the collocation finite element method and the Galerkin finite element method. The KPI equation has been successfully solved by the Galerkin method using PDE2D on a moving adaptive grid (Sewell, 2013). However, the KPII

equation has not been solved by any FEM. Firstly, the KPII equation (it will be called the KP equation again hereinafter) will be numerically solved by PDE2D to test the solver using existing results. The same method will be then used to solve the EKP equation with the V-shape initial condition.

From our numerical experience (in collaboration with Granville Sewell), there are severe instability issues when solving Eq. (4.6) directly by the FEM. To avoid that, the KP equation is to be solved in a fixed reference system with the following form, *i.e.*,

$$\frac{\partial}{\partial x^*}\left[4\frac{\partial \theta^*}{\partial t^*}+6\frac{\partial \theta^*}{\partial x^*}+6\theta^*\frac{\partial \theta^*}{\partial x^*}+\frac{\partial^3 \theta^*}{\partial x^{*3}}\right]+3\frac{\partial^2 \theta^*}{\partial y^{*2}}=0. \qquad (4.29)$$

4.5.1 One single solitary wave

The analytical solution of Eq. (4.29) can be used to verify the numerical method. The computational domain is a rectangular region as shown in Fig. 4-2. The length of the domain, which is in the x^*-direction, is 180. The width of the domain, which is in the y^*-direction, is 10.

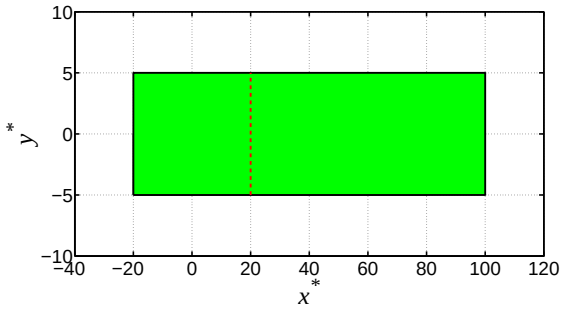

Fig. 4-2 Top view of the computational domain filled by green colour. The crest line (the red dashed line) indicates the initial position of the solitary wave.

The initial condition and boundary conditions are as follows:

$$
\begin{cases}
\theta^* = a^* \operatorname{sech}^2\left[\sqrt{0.5a^*}\left(x^* - x_0^*\right)\right]; \\
\theta^*\left(x^* = -20, y^*\right) = \dfrac{\partial \theta^*}{\partial x^*}\left(x^* = -20, y^*\right) = \dfrac{\partial^2 \theta^*}{\partial x^{*2}}\left(x^* = -20, y^*\right) = 0, \\
\theta^*\left(x^* = 100, y^*\right) = \dfrac{\partial \theta^*}{\partial x^*}\left(x^* = 100, y^*\right) = \dfrac{\partial^2 \theta^*}{\partial x^{*2}}\left(x^* = 100, y^*\right) = 0, \\
\dfrac{\partial \theta^*}{\partial y^*}\left(x^*, y^* = -5\right) = 0, \\
\dfrac{\partial \theta^*}{\partial y^*}\left(x^*, y^* = 5\right) = 0.
\end{cases}
\tag{4.30}
$$

It is found that the collocation finite element method results in noticeable deformation of the wave profile. On the contrary, the Galerkin method gives rational results and will be used hereinafter. The isoparametric triangulation mesh is employed (Fig. 4-3), which is widely used for the FEM, *e.g.*, by Wu and Eatock Taylor (2003). The mesh is uniform in the middle where the main portion of the wave field locates. The sparse mesh is used upstream and downstream to damp the possible upstream reflected wave and the trailing waves. The element size below refers to the fine mesh. The linear basis function is used for the spatial discretisation. The Crank-Nicolson scheme, which is of the second order accuracy, is used to discretise the derivatives in terms of time. The Sparse direct method is used to solve the linear system.

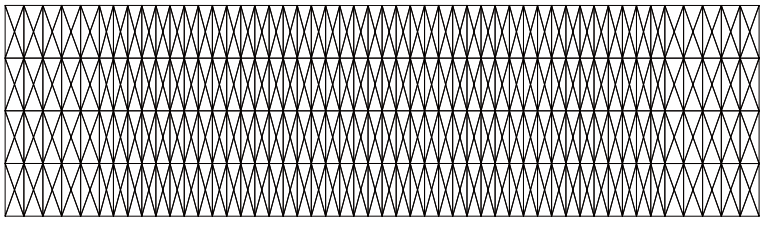

Fig. 4-3 The triangulation mesh.

The convergence study is shown with $x_0^* = 20$ and $a^* = 0.5505$. If the wave is within the computational domain Ω, the mass continuity quantity $q*$, *i.e.*,

$$
q^* = \int_\Omega \theta^*. \tag{4.31}
$$

should be constant. The element size in the x^*-direction and the time interval can be denoted by Δx^* and Δt^*, respectively. Figs. 4-4(a) & (b) show the comparison of the three runs with $\Delta x^* = 0.4$ & $\Delta t^* = 0.1$, $\Delta x^* = 0.2$ & $\Delta t^* = 0.1$ and $\Delta x^* = 0.2$ & $\Delta t^* = 0.05$. The wave profiles are graphically identical. Therefore, $\Delta x^* = 0.4$ & $\Delta t^* = 0.1$ can achieve reasonable convergence. It can be also seen that the calculation is quite accurate as the wave profile maintains its shape and $q*$ is almost constant.

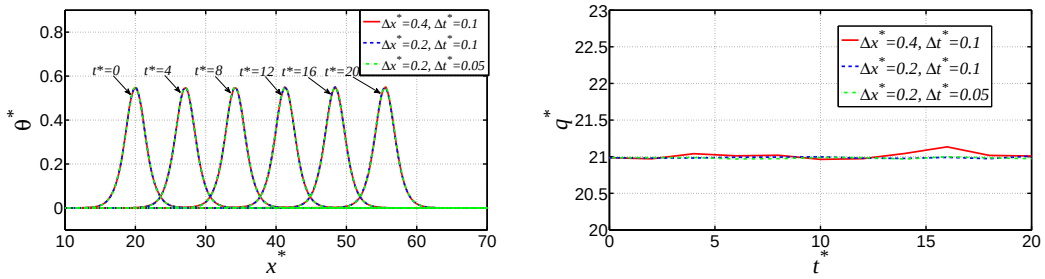

(a) **(b)**

Fig. 4-4 Convergence study for the Galerkin method by a single soliton.

4.5.2 Modelling the oblique reflection problem

As introduced, the V-shape initial value problem is equivalent to the reflection problem, for the boundary condition at the symmetric axis happens to be same as that of a frictionless wall. If the symmetric axis of the V-shape initial condition is at $y^* = 0$, the KP equation yields a symmetric solution. We only need to calculate half of the plane as a reflection problem (Fig. 4-5).

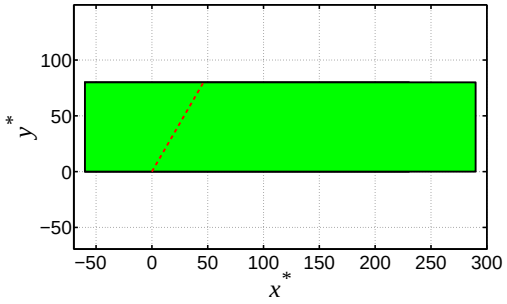

Fig. 4-5 Top view of the computational domain filled by green colour. The crest line (the red dashed line in the plot) indicates the initial position of the incident solitary wave.

The length of the domain is 350, and the width is 80. The angle between the initial crest line and the y*-axis is that $\psi_i^* = \pi/6$. The incident wave amplitude is that $a_i^* = 0.4129$. The initial position $x_0^* = 0$. The initial condition with the boundary conditions is

$$\begin{cases} \theta^* = a_i^* \operatorname{sech}^2\left[\sqrt{0.5a^*}\left(x^* - x_0^* - y^* \tan\psi_i^*\right)\right]; \\ \dfrac{\partial\theta^*}{\partial x^*}\left(x^* = -60, y^*\right) = 0, \\ \theta^*\left(x^* = 290, y^*\right) = \dfrac{\partial\theta^*}{\partial x^*}\left(x^* = 290, y^*\right) = \dfrac{\partial^2\theta^*}{\partial x^{*2}}\left(x^* = 290, y^*\right) = 0, \\ \dfrac{\partial\theta^*}{\partial y^*}\left(x^*, y^* = 0\right) = 0, \\ \dfrac{\partial\theta^*}{\partial y^*}\left(x^*, y^* = 80\right) = a^* \operatorname{sech}^2\left[\sqrt{0.5a^*}\left(x^* - x_0^* - y^* \tan\psi_i^* - \left(1.5 + 0.5a^* + 0.75\tan^2\psi_i^*\right)t^*\right)\right]. \end{cases} \tag{4.32}$$

It is necessary to explain the top boundary condition where $y^* = 80$. Since the computational domain is finite, it cannot simulate a semi-infinite line soliton evolving with time. To remedy this, the wave profile at the top boundary is prescribed by the one-soliton solution at $y^* = 80$ as has been done by Tanaka (1993), Li et al. (2011). It keeps the incident solitary wave in the far field straight. For this case, the element size in the x^*-direction is 0.4, the uniform element size in the y^*-direction is 1.5, and the time interval is 0.1.

The incident wave amplitude and the incident wave angle (in physical space) are actually identical with those of the case in Chapter 7. For the further reference, the results are converted to the *O'-x'y'z'* in Figs. 4-6 & 4-7, where $x' = x^*$, $y' = y^*$, $\theta' = \frac{2}{3}\theta^*$ and $t = \frac{3}{2}t^*$. Li et al. (2011) have solved the V-shape initial value problem of the KP equation by the Finite Difference Method (FDM). Comparing the crest trajectories at *y'*=0 in Fig. 4-6, the results given by the FEM and FDM are consistent. That verifies the present numerical method.

Solving the KP equation by the numerical method is still time and memory consuming. In Fig. 4-7, the corresponding (3142)-type solution for an X-shape initial value problem is compared with the numerical result in terms of the time sequence of the wave profile. Together with Fig. 4-6, it can be seen that the analytical solution gives a reasonably good prediction on the wave profile in the vicinity of the reflection wall. This conclusion is consistent with the previous studies (Chakravarty and Kodama, 2009; Kao and Kodama, 2012). Therefore, the analytical solution of the KP equation will be used to model the oblique reflection problem hereinafter.

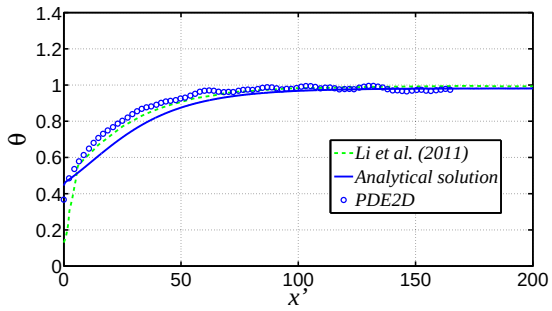

Fig. 4-6 The crest trajectories at *y'*=0 based on the KP theory. The FDM result of the V-shape initial value problem by Li et al. (2011) (- -); the analytical solution of the X-shape initial value problem (—); the FEM result of the V-shape initial value problem using PDE2D (o).

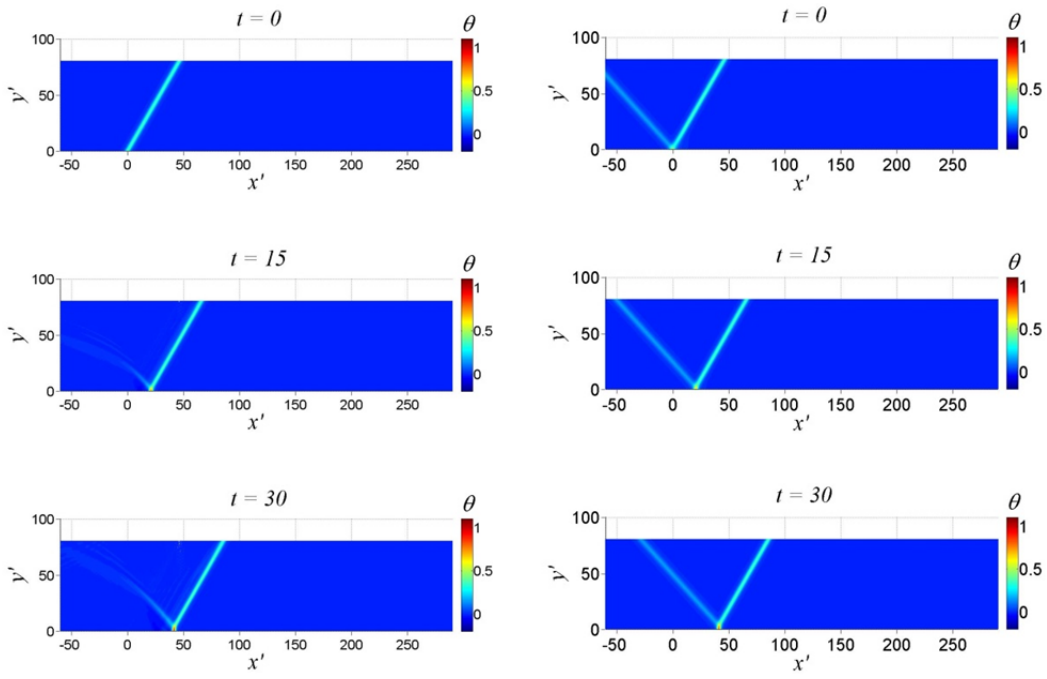

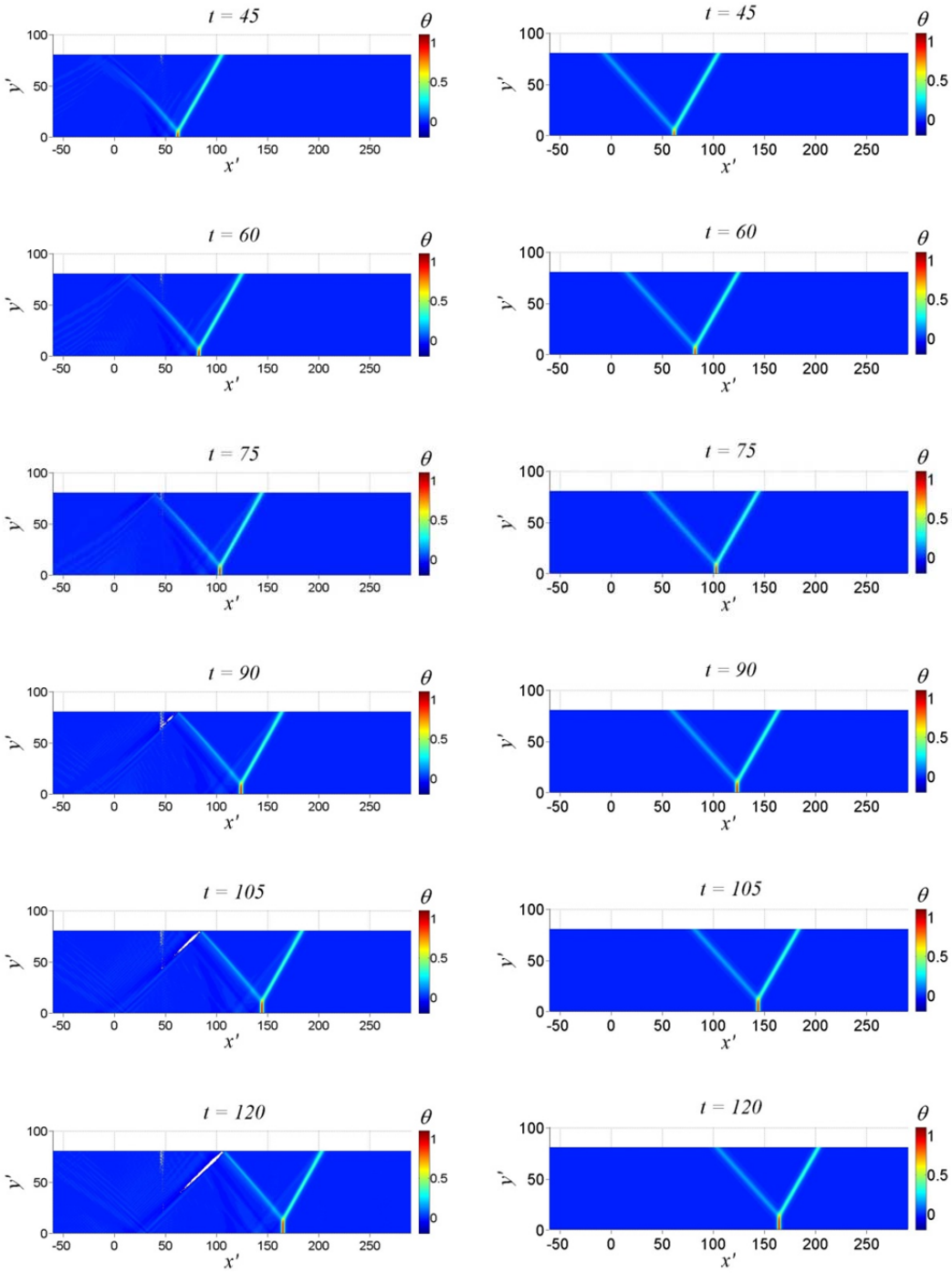

Fig. 4-7 Contour plots on the *x'y'*-plane in terms of the surface displacement at different moments for the V-shape (left column) and the X-shape (right column) initial value problems of the KP equation.

4.6 Solving the EKP equation using PDE2D

The EKP equation will also be solved in a fixed system, *i.e.*,

$$\frac{\partial}{\partial x^*}\left[4\frac{\partial \theta^*}{\partial t^*}+6\frac{\partial \theta^*}{\partial x^*}+6\theta^*\frac{\partial \theta^*}{\partial x^*}-D\theta^{*2}\frac{\partial \theta^*}{\partial x^*}+\frac{\partial^3 \theta^*}{\partial x^{*3}}\right]+3\frac{\partial^2 \theta^*}{\partial y^{*2}}=0. \quad (4.33)$$

where D is given by Eq. (4.27).

4.6.1 One single ISW

Since there is a single ISW solution (Eq. (4.28)) of the EKP equation, it can be used to test the accuracy of the numerical method. The computational domain has the same layout as that in Fig. 4-2. It can be seen from Fig. 4-8 that the numerical result has a permanent waveform travelling at a constant speed. It suggests that the numerical method gives accurate results.

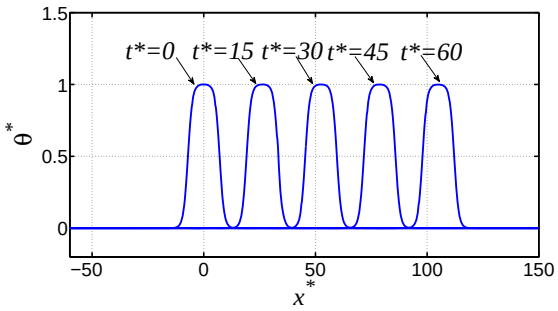

Fig. 4-8 The wave profiles at different moments given by the numerical solution of the EKP equation using PDE2D.

4.6.2 V-shape initial condition

In this section, the V-shape initial value problem of the EKP equation will be solved in the half plane with $y^* \geq 0$. The shape of the computational domain, the boundary conditions and the boundary manipulations are the same as the V-shape case in Section 4.5.2. Nevertheless, the oblique soliton function, *i.e.*,

$$\theta^* = \frac{a_i^* \operatorname{sech}^2 \lambda_{EKP3}}{1-\frac{a_i^*}{12/D-a_i^*}\tanh^2 \lambda_{EKP3}}, \quad (4.34)$$

$$\lambda_{EKP3} = C_{EKP1}\left(x^* - x_0^* - \left|y^*\right|\tan\psi_i^* - C_{EKP2}t^*\right), C_{EKP2} = 1.5 + C_{EKP1}^2 + 0.75\tan\psi_i^{*2}.$$

does not satisfies the EKP equation exactly. Hence the incident wave is only a solitary-like wave.

Two cases will be calculated for verification by the pseudo-spectral results of Tsuji and Oikawa (2007). In both cases, $a_i^* = 1$ and $\tan\psi_i^* = 0.4082$. With the different values of *D*, the limiting amplitudes of a single ISW are not the same. In the first case, a_i^* is much smaller than the limiting amplitude, while in the second case, a_i^* is comparable to the limiting amplitude. The results are shown as follows:

i) The case with $D = 0.5$

The calculated wave profiles at *t**=0 and *t**=80 are mirrored about *x**-axis in Figs. 4-9(a) & (b). They agree with the pseudo-spectrum results by Tsuji and Oikawa (2007) very well. The maximum run-up at the symmetric plane at *t**=80 is 1.63, while the result given by Tsuji and Oikawa (2007) is 1.68. A stem wave grows perpendicularly to the symmetric plane. The transverse length of the stem wave is increasing with the time. The amplitude of the reflected wave is much smaller than that of the incident wave. The reflected wave angle is larger than the incident wave angle. The evidence above shows the pattern can be classified as the Mach reflection. Since $K^* = 0.2886 < 1$, the KP theory also predicts it as a Mach reflection scenario and the asymptotic stem wave amplitude is 1.66.

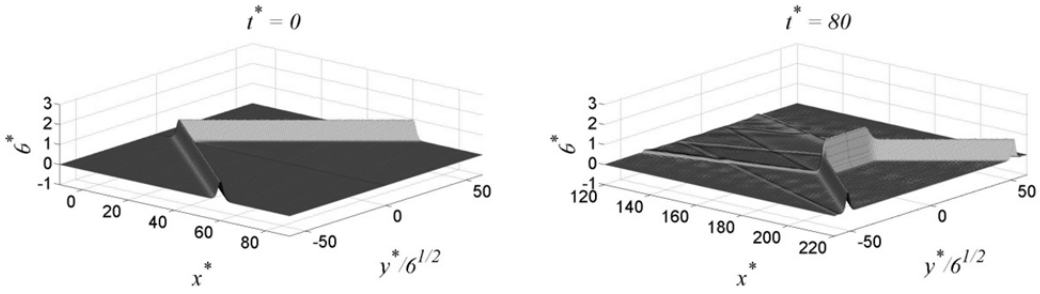

(a) **(b)**

Fig. 4-9 Wave profiles of the case with $a_i^* = 1$, $\tan\psi_i^* = 0.4082$ and $D = 0.5$ at t*=0 (a) and t*=80 (b).

ii) The case with $D = 5$

The calculated wave profiles at t^*=0 and t^*=80 are mirrored about x^*-axis in Figs. 4-10(a) & (b). They agree with the pseudo-spectrum results by Tsuji and Oikawa (2007), too. The maximum run-up at the symmetric plane at t^*=80 is 1.57, while the result given by Tsuji and Oikawa (2007) is 1.54. The incident wave amplitude is very close to the limiting amplitude given by $6/D = 1.2$. It can be seen that no stem wave forms, and the reflected wave is scattered, though the KP theory predicts the appearance of the Mach reflection for K^* is still 0.2886. The EKP theory and the KP theory result in quite different results.

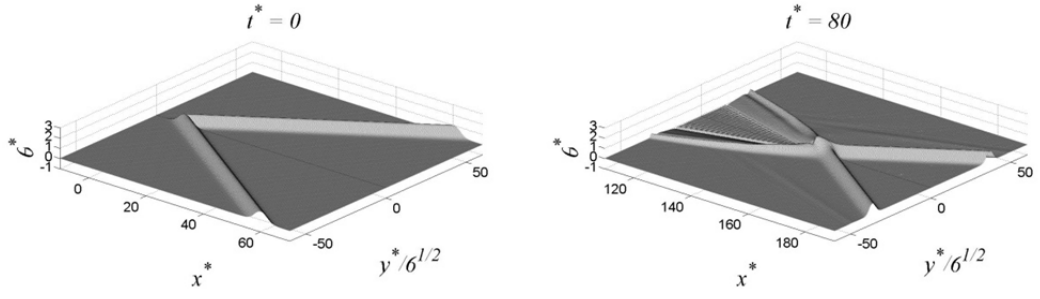

(a) **(b)**

Fig. 4-10 Wave profiles of the case with $a_i^* = 1$, $\tan\psi_i^* = 0.4082$ and $D = 5$ at t*=0 (a) and t*=80 (b).

4.7 Summary

Through verifications, both the V-shape initial value problems of the KP equation and the EKP equation can be solved accurately by the FEM using PDE2D. Besides, another two observations need to be highlighted. One is that, in the framework of the KP theory, the analytical solution with an X-shape initial condition agrees well with the numerical solution with a V-shape initial condition in the vicinity of the reflection wall. It is acceptable to use the (3142)-type solution to model the Mach reflection and the O-type solution to model the regular reflection. The other observation is the deviation between the KP theory and the EKP theory. When the incident wave amplitude is much smaller than the limiting amplitude of an ISW given by the EKP or eKdV model, the two theories give consistent results; When the incident wave amplitude is comparable to the limiting value, the two theories give quite different results. It suggests the necessity of the further research taking into account the fully nonlinear boundary conditions.

Chapter 5 Physical model and methodology for fully nonlinear numerical simulations

5.1 Physical model

The oblique reflection of an SSW will be simulated in a numerical wave tank as shown in Fig. 5-1. The oblique reflection of an ISW will be also simulated in a similar wave tank shown in Fig. 5-2. But the boundary conditions on the top, *i.e.* FJIHG, are different. FJIHG in Fig. 5-1 is connected to the open atmosphere. FJIHG in Fig. 5-2 is a rigid wall. Two right-handed Cartesian coordinate systems *O-xyz* and *O-x'y'z'* are defined. Their origins are respectively located on the undisturbed free surface or interface, and *z* and *z'* axes point upward. The *x*-axis is parallel to the walls BCHG and ABJF. *x'*-axis is parallel to the wall EDIJ.

A solitary wave lies initially in parallel with the side wall AFGB and propagates to the *x*-direction. For convenience, the wall EDIJ is called the reflection wall, and the wall BCHG is called the offshore wall. The set up for numerical simulation of SSWs resembles the laboratory apparatus by Li et al. (2011) (Fig. 1-9). It is noted that the boundary condition at the rightmost boundary in Fig. 5-1 is different from the experiment in which the boundary was open to the external water. Nevertheless, the simulation stops when the incident wave is sufficiently far away from the rightmost boundary, and no noticeable reflection waves coming from the wall CDIH have been observed. The specific set-ups, such as the dimensions $d1$ to $d4$ (Figs. 5-1 & 5-2), will be introduced in the case studies.

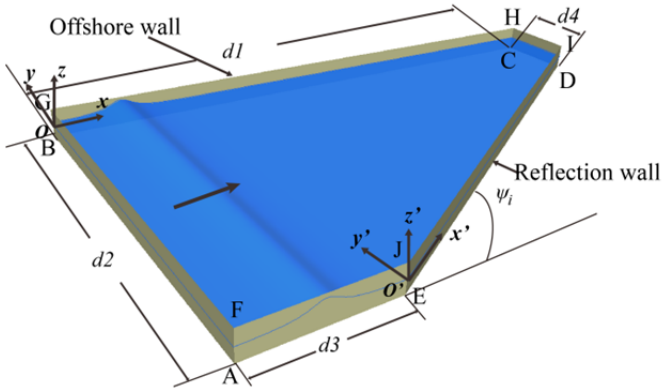

Fig. 5-1 3D view of the physical model for the oblique reflection of an SSW. The wave profile shows the initial state.

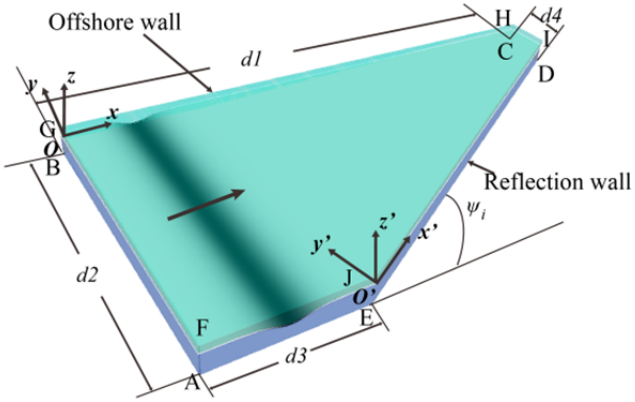

Fig. 5-2 3D view of the physical model for the oblique reflection of an ISW. The wave profile shows the initial state. The vertical dimensions and the wave amplitude have been exaggerated.

5.2 Governing equations

The computation will be performed in the *O-xyz* coordinate system based on the Euler equations:

$$\nabla \cdot \mathbf{u} = 0, \tag{5.1}$$

$$\frac{\partial}{\partial t}(\rho \mathbf{u}) + \nabla \cdot (\rho \mathbf{u}\mathbf{u}) = -\nabla p + \rho \mathbf{g}, \tag{5.2}$$

where $\mathbf{u} = (u, v, w)$ is velocity, ρ is density, p is pressure and $\mathbf{g}$ is the gravitational acceleration.

In order to implement the VOF method for capturing the free surface or interface, a scalar field is introduced. α is designated as the volume fraction in an infinitesimal

element of the dense phase, referring to water in an air-water system for surface waves or heavier water in a two-layer system. In this way, the surface wave problem is incorporated into the multi-phase problem. The transition of α from 0 to 1 indicates the location of the interface. α is driven by the flow, which results in an advection equation:

$$\frac{\partial \alpha}{\partial t} + \nabla \cdot (\mathbf{u}\alpha) = 0. \tag{5.3}$$

The method to compress the smeared interface due to the numerical diffusion in OpenFOAM is different from the geometrical methods, such as Simple Line Interface Calculation (SLIC) method (Noh and Woodward, 1976) and Piecewise-Linear Interface Calculation (PLIC) method (Kothe et al., 1996), or the higher order differencing schemes, such as Compressive Interface Capturing Scheme for Arbitrary Meshes (CICSAM)(Ubbink and Issa, 1999). Inspired by the two-fluid Eulerian model, Eq. (5.3) is replaced by (Rusche, 2002)

$$\frac{\partial \alpha}{\partial t} + \nabla \cdot (\mathbf{u}\alpha) + \nabla \cdot \left[\mathbf{u}_r \alpha (1-\alpha) \right] = 0, \tag{5.4}$$

in which $\mathbf{u}_r$ is designated as the "compression velocity" (Berberović et al., 2009). $\mathbf{u}_r = \mathbf{u}_1 - \mathbf{u}_2$, where the subscripts 1 and 2 represent the heavier fluid and the lighter fluid, respectively, and $\mathbf{u}_i \, (i = 1, 2)$ indicate the velocities on both sides of the interface (Berberović et al., 2009). The "compression term" or $\nabla \cdot \left[\mathbf{u}_r \alpha (1-\alpha) \right]$ is zero when $\alpha = 0$ or 1. Thus, if the interface is of a step-profile, Eq. (5.4) degenerates to Eq. (5.3). The functionality of the "compression term" is to compress the transitional layer where $0 < \alpha < 1$.

In OpenFOAM, a pseudo-dynamic pressure is defined by

$$p_{rgh} = p - \rho \mathbf{g} \cdot \mathbf{x}, \tag{5.5}$$

where $\mathbf{x}$ is the position vector. Eq. (5.2) can be written as

$$\frac{\partial}{\partial t}(\rho \mathbf{u}) + \nabla \cdot (\rho \mathbf{u}\mathbf{u}) = -\nabla p_{rgh} - \mathbf{g} \cdot \mathbf{x} \nabla \rho. \tag{5.6}$$

The density field is determined by the weighted average of both phases, *i.e.*,

$$\rho = \alpha \rho_1 + (1-\alpha)\rho_2. \tag{5.7}$$

Eqs. (5.1), (5.4) and (5.6) compose the governing equations (Rusche, 2002).

5.3 Numerical procedure†

5.3.1 Discretisation

The transport equation for a scalar $\phi = \phi(\mathbf{x}, t)$, where $\mathbf{x}$ is the position vector and t is time, within an inviscid fluid can be written as (Wu and Hu, 2008)

$$\underbrace{\frac{\partial \rho \phi}{\partial t}}_{\text{temporal derivative}} + \underbrace{\nabla \cdot (\rho \mathbf{u} \phi)}_{\text{convection term}} = \underbrace{S_\phi(\phi)}_{\text{source term}} \tag{5.8}$$

where ρ is the density, $\mathbf{u} = (u, v, w)$ is the velocity, $S_\phi(\phi)$ is the volume source/sink of ϕ, and ϕ can be α or u or v or w. To use the Finite Volume Method to discretise the solution domain (Fig. 5-3), Eq. (5.8) can be written in the integral form over the control volume V_P with the centroid point P, *i.e.*,

$$\int_t^{t+\Delta t} \left[\frac{\partial}{\partial t} \int_{V_P} \rho \phi dV + \int_{V_P} \nabla \cdot (\rho \mathbf{u} \phi) dV \right] dt = \int_t^{t+\Delta t} \left[\int_{V_P} S_\phi(\phi) dV \right] dt. \tag{5.9}$$

ϕ at any position can be obtained by the Taylor series around the point P, where $\phi = \phi_P$ (Wu and Hu, 2008). In OpenFOAM, the variation of ϕ in space is assumed

† The nomenclature in this section is independent from the rest of the thesis.

linear (Jasak, 1996). The variation of ϕ in time for our simulations is also assumed to be linear. With the linear variation assumption, it is easy to prove that

$$\int_{V_P} \phi dV = \phi_P V_P. \tag{5.10}$$

Using the Gauss' theorem on a polyhedral control volume/cell, we have

$$\int_{V_P} \nabla \phi dV = \int_{\Gamma} d\mathbf{S} \cdot \phi = \sum_f \mathbf{S}_f \cdot \phi_f, \tag{5.11}$$

where ϕ_f is the value of ϕ at the face centres and $\mathbf{S}_f$ is the product of the face area and the normal vector pointing outward. ϕ_f is only interpolated by the values on the centroids of two neighbouring cells (Fig. 5-3), *i.e.*,

$$\phi_f = f\left(\phi_P, \phi_N\right), \tag{5.12}$$

where *f*() stands for the interpolation scheme. Eq. (5.9) is also discretised in time. Supposing ϕ_P^n and ϕ_N^n are the values at the new time step in the control volume around *P* and in its neighbour, respectively, we have an algebraic equation:

$$a_P \phi_P^n + \sum_N a_N \phi_N^n = R_P, \tag{5.13}$$

where a_P and a_N are coefficients, $\sum_N$ means the summation of the quantities in all the neighbouring cells, and R_P is constant. Reassembling the equations for all the cells, we have a system of algebraic equations:

$$[A][\phi] = [R], \tag{5.14}$$

where $[A]$ is a sparse matrix, $[\phi]$ is the vector for ϕ in each cell, and $[R]$ is the source term vector. After the linear equation system is solved, ϕ at the new time step in each cell can be obtained.

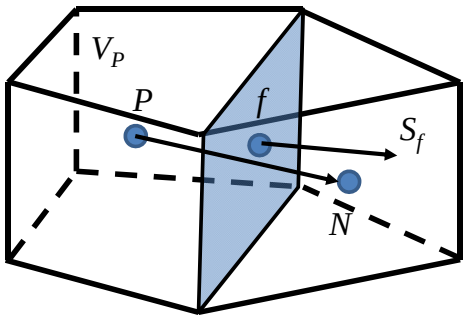

Fig. 5-3 The control volumes for the discretisation

The velocity field obtained from the procedure introduced hereinbefore does not always satisfy the continuity equation Eq. (5.3) (Wu and Hu, 2008). The pressure field and the velocity field can be corrected iteratively to satisfy both the continuity equation and the momentum equation.

5.3.2 Schemes and linear equation solvers

The time marching is achieved by the first-order implicit Euler scheme. The second-order Total Variation Diminishing (TVD) differencing schemes are used for the interpolation of variables in the convection terms in Eqs. (5.4) & (5.6) (Harten, 1983). The Central Differencing (CD) scheme is used for other variables (Jasak, 1996). The boundedness of α, i.e., confining $0 \le \alpha \le 1$, is achieved by the Multidimensional Universal Limiter for Explicit Solution (MULES) algorithm (Rusche, 2002). The scheme for the "compression term" can be found in Berberovic et al.(2009). The coupled pressure-velocity field is tackled by the Pressure Implicit with Splitting of Operator (PISO) algorithm (Issa, 1986). The assembled linear

system of equation for pressure is solved by the Geometric-Algebraic Multi-Grid (GAMG) with Gauss-Siedel smoother solver (Behrens, 2009). The linear system of equations for velocity and the volume fraction is solved by the Preconditioned Bi-Conjugate Gradient (PBiCG) solver with Diagonal based Incomplete LU (DILU) preconditioner (Wesseling, 2009).

5.4 Mesh generation and refinement

5.4.1 Initial mesh

Hexahedral mesh for the discretisation is generated by the application "blockMesh" (Fig. 5-4). The grid lines are uniformly distributed along *x*-axis and *z*-axis. In *y*-direction, the grid lines are uniform away from the reflection wall, but their intervals decrease exponentially in the vicinity of the reflection wall towards – *y*-direction.

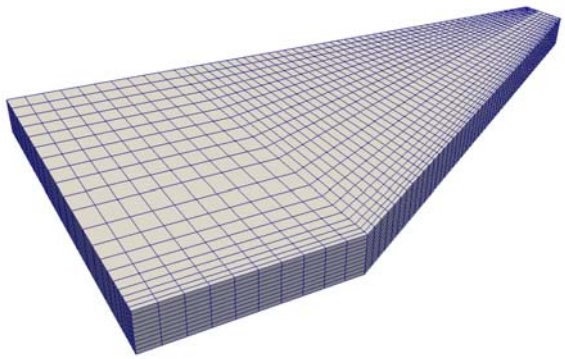

Fig. 5-4 Schematic plot of a typical 3D mesh.

5.4.2 Local refinement

The static mesh can be refined in a certain area where a higher spatial resolution is required via the application "refineMesh". As shown in Fig. 5-5, the mesh within the virtual box defined by the user has been refined. The cells are divided evenly along the selected direction. At the edge between the refined region and the original mesh,

a transitional layer of cells is generated in order to guarantee one face is only shared by two neighbour cells. Hence it becomes unstructured mesh. But it does not affect the FVM discretisation implemented in OpenFOAM. From the numerical experience, it is still not efficient for simulations of travelling solitary waves. Therefore, an adaptive mesh refinement (AMR) technique is to be introduced, which is particularly suitable for the present simulations.

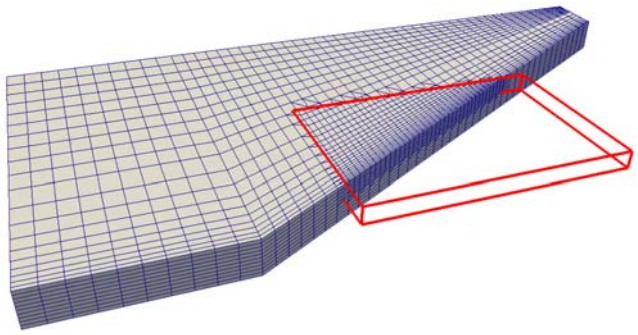

Fig. 5-5 Local refinement on initial mesh within the red box.

5.4.3 Adaptive mesh refinement (AMR) in parallel

The higher local resolution and the affordable computational cost when simulating large-scale unsteady geophysical events can be achieved by using the adaptive mesh refinement (AMR) technique (Popinet, 2003, 2011, 2012; Castro et al., 2009; Oishi et al., 2013; Hill et al., 2014). The AMR technique has been also implemented in OpenFOAM (Hrvoje, 2009). For the present problem, both the interface displacement and the fluid velocity magnitude in a solitary wave field have maximal values at the crest/trough, and they decay fast away from the crest/trough. The wave motion is still localised in an oblique reflection process as observed in the experiment by Li et al. (2011). It means that the wave does not influence the whole computational domain evenly like a periodic wave. The high resolution at the interface and the fluid with noticeable velocity is beneficial for the investigation of

the wave field. Low resolution at other quiescent areas can save a considerable amount of the computational cost.

The refinement algorithm is the octree method. A hexahedron is split into 2X2X2 through the middle of the edges resulting in eight "child" hexahedrons. A scalar field, designated as the "refinement level" of the cell, is attached to the mesh starting from 0. Since OpenFOAM can handle both unstructured mesh structured mesh with no difference, auxiliary cells are generated automatically to guarantee one face is only shared by two neighbour cells. In the reverse process called unrefinement, the child cells are removed and the parent cells are recovered recursively. The refinement level in the child cell increases by 1 after the refinement and reduced by 1 in the parent cell after unrefinement. Users can define the maximum refinement level to limit the refinement procedure. Buffer layers can be specified to make the transition of the refinement level smooth. The "refinement step" defines the time steps between two successive mesh manipulations.

Next step is to determine which cells are to be refined. It can be achieved by assigning another scalar field which changes its value with time. The scalar fields are different for surface wave cases and internal wave cases. 2D solitary wave cases are used as examples below for illustration.

Normally, the refinement of mesh is performed where the velocity gradient is greater, *i.e.*, the flow is varying more rapidly. Looking into the velocity field of an SSW (Fig. 5-6(a)), the greatest gradient of the velocity magnitude does not occur at the crest, but at the two sides of the symmetric axis of the wave profile passing through the crest. However, we are particularly interested in the wave behaviours near the crest,

and it is required that the mesh in the vicinity of the crest should be always fine. The horizontal velocity u is predominant in a solitary wave field. u has the largest at the crest and its magnitude decays fast away from the crest. At the area which is sufficiently far from the crest, both u and the velocity gradient are very small. Therefore, the horizontal velocity magnitude is used as a criterion for the mesh refinement. The cell at the free surface/interface should be also refined. A scalar field is constructed as follows

$$amr_1 = \begin{cases} u\alpha; \\ u_{\text{unit}} \end{cases} \quad \text{if } 0.001 < \alpha < 0.999, \tag{5.15}$$

where u_{unit} is the unit velocity in dimensional form. $C_{amr1}u_{unit}$ is the threshold value, and $C_{amr1} < 1$. When amr_1 is less than the threshold, the cell will be refined. In the code, if just one of the faces is on the interface, the cell will be also refined.

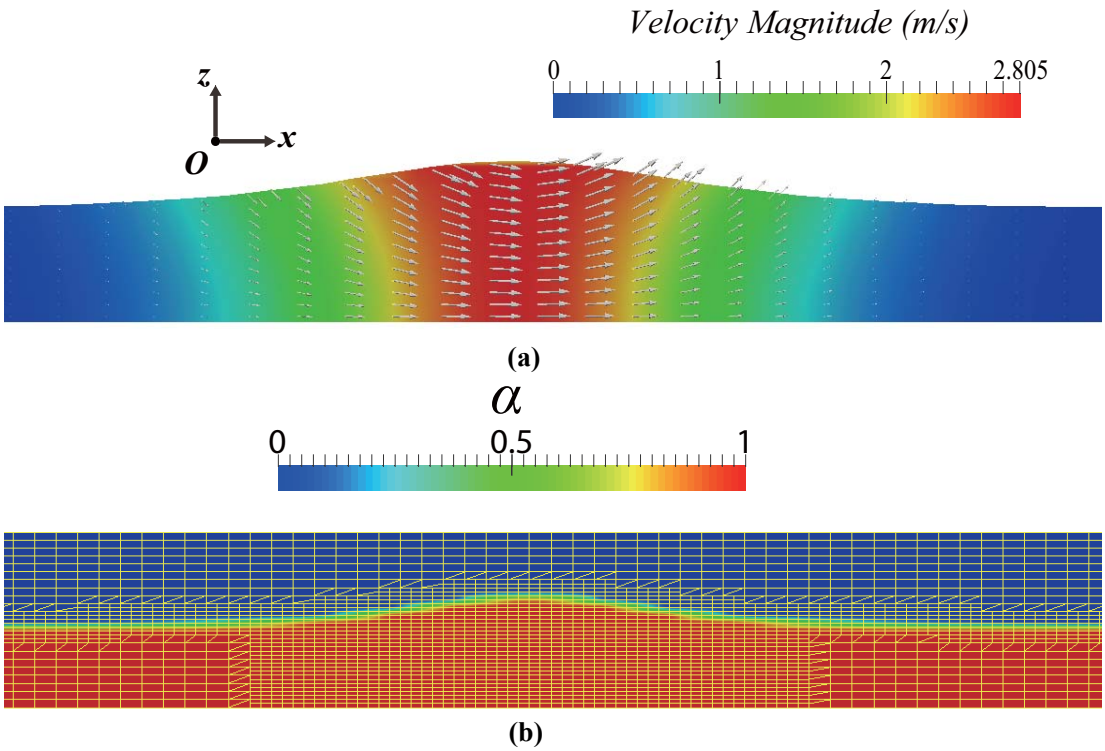

Fig. 5-6 A typical velocity field of an SSW (a) and the corresponding mesh (b).

The refinement algorithm for ISWs has to take into account the flow fields in both layers (Fig. 5-7). The scalar field is constructed by

$$amr_2 = \begin{cases} |u|; \\ u_{\text{unit}} \end{cases} \quad \text{if } 0.001 < \alpha < 0.999. \tag{5.16}$$

The threshold value is $C_{amr2}u_{unit}$, where $C_{amr2} < 1$. When amr_2 is less than the threshold, the cell will be refined. In the code, if just one of the faces is on the interface, the cell will be also refined.

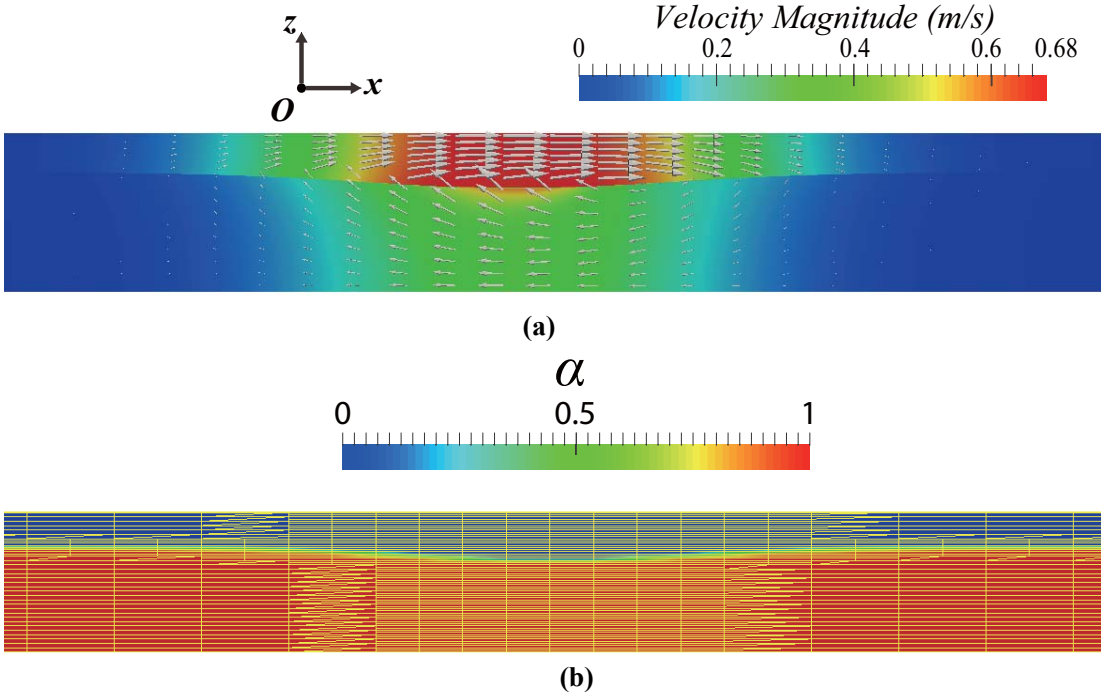

Fig. 5-7 A typical velocity field of an ISW (a) and the corresponding mesh (b).

The mesh changes with time. The results on the old mesh need to be transferred to the new mesh. The value on a cell centre is interpolated from that on the closest cell centre from the original mesh linearly. Special treatment is applied for the "flux" on the cell face. The concept of the flux is to be introduced first. It starts from a problem when solving the nonlinear term in the NS/Euler equation, *i.e.*, $\nabla \cdot (\rho \mathbf{uu})$. If the nonlinear term is solved directly, it will result in a non-linear algebraic equation system and consumes huge computational effort. In OpenFOAM, the nonlinear term

is linearised, *i.e.*, supposing one velocity item is constant in that time step. The constant velocity item is then converted to the flux on the cell face in the FVM discretisation owing to the Gauss' theorem. The cell surface flux field is required to satisfy the continuity constraint or Eq. (5.1) accurately. The flux field interpolated from the original mesh cannot guarantee to satisfy the continuity constraint accurately. Alternatively, the flux is recalculated based on the interpolated velocity field on the cell centres. An auxiliary field p_{corr} is introduced acting as a pressure field. Using the discretised continuity equation and the semi-discretised momentum equation, a similar procedure as the pressure-velocity decoupled algorithm is performed to correct the flux iteratively. The calculation stops until p_{corr} converges (Jasak, 1996).

The implementation of the AMR technique also affects the load distribution in the parallel computing. In the present study, the load (cell quantity) is not redistributed during the computation. It means that each processor has a fixed portion of the domain according to the decomposition of the initial mesh, and manipulates the mesh according to the flow field and the refinement criterion individually. Therefore, the initial mesh should be decomposed to guarantee an approximately balanced load distribution. The decomposition orientation is selected based on the flow field characteristics of this specific oblique reflection problem. The initial mesh is decomposed into slices aligning in the *z*-direction (transverse direction of the wave). Since the processor manipulates the cell individually, the incompatibility may arise at the edge between the decomposed meshes. It has been found that, if there are indented edges between the decomposed meshes, it always causes the calculation to crash. Through numerical experiments, it has been also found that decomposing the

mesh in the vertical direction would not improve the efficiency. A workable decomposition is shown in Fig. 5-8. Every edge between the decomposed regions is vertical.

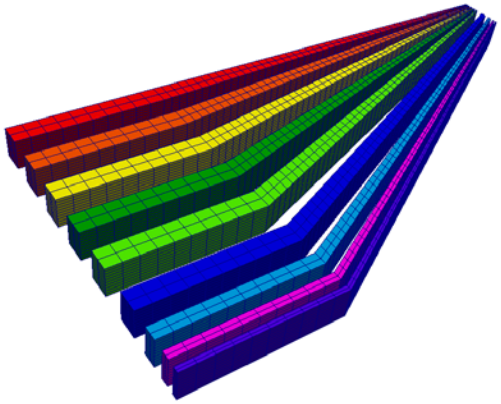

Fig. 5-8 A sketch for the decomposition of the initial mesh.

5.5 Wave generation

The incoming wave is a solitary wave. It can be generated by initialising the flow field by the analytical solution of a solitary wave. Since the pressure is obtained by the iterative algorithm. The initial pressure field only affects the convergence speed within the first time step. Therefore, the pressure is assigned to be zero for convenience. Only the volume fraction field and the velocity field are assigned initially. The programming and the pre-processing operations are based on the third-party application waves2Foam (Jacobsen et al., 2012). Some technical details are introduced as follows.

It is remarked that the analytical solutions are based on the potential theory, while the governing equations in the simulation are the Euler equations. According to Stokes' theorem and Kelvin's circulation theorem, if the initial condition of in an inviscid fluid is irrotational flow, the flow field remains irrotational afterwards. In other words, the solution of the Euler equations is potential flow when the initial condition

is potential flow. The truncated perturbation solution of a solitary wave satisfies the Laplace equation exactly. However, it does not satisfy the irrotational flow criterion by leaving a higher-order residual. That fact does not violate the potential theory within the given order. But if the truncated solution is used as the initial condition for the calculation governed by the Euler equations, it results in a rotational flow, which may affect the global wave profile. It also suggests that the higher-order solitary wave solution with a smaller error in irrotationality may result in a more stable solitary wave in the simulation.

In the code, the *x*-coordinate of a cell centre is first substituted into the wave profile expression to obtain a vertical interface location, and whether the cell is above or below the interface can be confirmed. α and $\mathbf{u}$ can be assigned to that cell accordingly. Most of the models for a solitary wave introduced in Chapter 2 give explicit expressions for the wave profile and velocity with respect to *x*-coordinate. An exception is the MCC model that only gives the implicit expression with respect to *x*-coordinate. In order to implement the MCC model in the code, we can use explicit polynomial functions to fit the profile, and obtain velocity through the fitting functions. Taking into account the leading order approximation of the velocity field, the fitting function and its first derivative should be continuous. The piecewise cubic Hermite fitting function, therefore, is adopted (Kreyszig, 2011). Suppose that there is a set of sequential data points $\left(x_k, z_k\right)$, where $k = 1, \cdots, n$, and $x_k < x_{k+1}$, obtained from the MCC model with the prescribed z_k. Let us consider the fitting function $P(x)$ on the *k*th interval, in which $x_k < x < x_{k+1}$. The function coincided with the data at each point, *i.e.*,

$$P\left(x_k\right) = z_k, P\left(x_{k+1}\right) = z_{k+1}. \tag{5.17}$$

The length of the interval is denoted as l_k, or

$$l_k = x_{k+1} - x_k. \tag{5.18}$$

The tangents of the starting and ending points are

$$d_k = P'(x_k), d_{k+1} = P'(x_{k+1}), \tag{5.19}$$

respectively. With the local distance, $s = x - x_k$, $P(x)$ can be written as

$$P(x) = \frac{3l_k s^2 - 2s^3}{l_k^3} z_{k+1} + \frac{l_k^3 - 3l_k s^2 + 2s^3}{l_k^3} z_k + \frac{s^2(s - l_k)}{l_k^2} d_{k+1} + \frac{s(s - l_k)^2}{l_k^2} d_k. \tag{5.20}$$

If we do not have the first derivative at each point, we need a method to determine the derivative. A "Shape-Preserving Piecewise Cubic" method proposed by Fritsch and Carlson (1980) is chosen. The first order forward difference, δf_k, is defined as

$$\delta f_k = \frac{z_{k+1} - z_k}{l_k}. \tag{5.21}$$

There are several circumstances for the determination of d_k:

(i) If $\delta f_{k-1} \bullet \delta f_k < 0$, or $\delta f_{k-1} \bullet \delta f_k = 0$, then $d_k = 0$.

(ii) If $\delta f_{k-1} \bullet \delta f_k > 0$, then d_k is given by the "weighted harmonic mean" of the neighbour slopes:

$$\frac{wh_1 + wh_1}{d_k} = \frac{wh_1}{\delta f_{k-1}} + \frac{wh_2}{\delta f_k}, \quad wh_1 = 2l_k + l_{k-1}, wh_2 = l_k + 2l_{k-1}. \tag{5.22}$$

(iii) The derivatives at the endpoints (x_1, z_1) and (x_n, z_n) can be obtained by the three-point extrapolation. But for solitary waves, the derivatives at the endpoints can be simply assigned by 0 provided the curvature of the interface is sufficiently large.

If the mesh is coarser, the error brought by assigning the discretised analytical solution is larger. The initial mesh is the coarsest when using the AMR technique. It is better to refine the initial mesh according to the flow field up to the maximum

refinement level, and assign the discretised analytical solution again as the initial condition. It then guarantees that the high accuracy of the initial flow field.

5.6 Wave absorption

The computational domain in the simulation of the wave problem is usually a local area of interest truncated from the open sea, owing to the limited computational capacity. The wave should not be reflected from these truncated boundaries to interfere with the concerned wave motion. Several wave absorption methods can be used individually or together, such as, the Sommerfeld–Orlanski condition and the damping zone method (Wang et al., 2013). The Sommerfeld–Orlanski condition originates from the Sommerfeld radiation condition for linear waves. Orlanski (1976) improved the radiation condition for the application in unsteady nonlinear simulations. The method is efficient, for the radiation condition can be incorporated into the boundary conditions. But its basis is still the linear theory. The damping zone method appends an artificial damping term to the free surface boundary condition within the damping zone (Cointe et al., 1990). By using any of the two methods above, the surface displacement and velocity field are not explicitly known until solving the boundary value problems. Numerical experiments are needed to test the wave absorption effectiveness for tuning the parameters.

The present wave absorption method is an explicit relaxation technique (Mayer et al., 1998; Jacobsen et al., 2012). The relaxation zone is like a numerical sponge layer to reduce the interface displacement and the fluid velocity of the incoming wave gradually. For the problem we simulate, the wave motion is relatively localised in the vicinity of the wave crest/trough. The wave crest/trough is far away from both the upstream and downstream side walls BAFG and CDIH (Figs. 5-1 & 5-2) throughout

the simulation. The disturbances to the water near BAFG and CDIH (Figs. 5-1 & 5-2) are weak. The explicit modification of the flow variables will not lead to instabilities. The layout of relaxation zones is shown in Fig. 5-9 schematically. A predominated direction is selected, which is along the *x*-axis and points outward to the computational domain. A local one-dimensional coordinate χ_R is normalised to $[0,1]$ by the length of the relaxation zone. A relaxation factor is defined as

$$f_R(\chi_R) = 1 - \frac{e^{\chi_R^{3.5}} - 1}{e - 1}, \tag{5.23}$$

which has smooth profile reducing from 1 to 0. The $\mathbf{u}_{\text{computed}}$ and α_{computed} are results calculated with the original boundary conditions. $\mathbf{u}_{\text{target}} = 0$, and α_{target} is calculated according to the undisturbed water level. The corrections, *i.e.*,

$$\mathbf{u} = (1 - f_R)\mathbf{u}_{\text{target}} + f_R\mathbf{u}_{\text{computed}}, \tag{5.24}$$

$$\alpha = (1 - f_R)\alpha_{\text{target}} + f_R\alpha_{\text{computed}}, \tag{5.25}$$

are performed explicitly. The prescribed values at the boundaries can be achieved exactly. $\mathbf{u}$ and α are then used for the calculation at the next time step. The process damps the wave energy with the marching time, and eliminates the reflected wave. It can be also seen that the relaxation zone can be turned on or off at any time step.

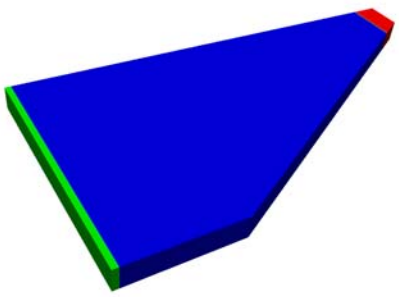

Fig. 5-9 Schematic plot of the relaxation zones, which have been marked by the green and red colours.

5.7 Time step control

The time step in OpenFOAM can be adjusted adaptively. The maximum Courant number is defined as

$$Co = \max\left\{\frac{\left|\mathbf{u}_f \bullet \mathbf{S}_f\right|}{\mathbf{d}\bullet\mathbf{S}_f}\Delta t\right\}, \tag{5.26}$$

where $\mathbf{u}_f$ is the velocity at the face centre, $\mathbf{S}_f$ is the outward-pointing face area vector, Δt is the time step and $\mathbf{d}$ is a vector between two centroids of the cells sharing the calculated surface. Δt is limited by Co (Berberović et al., 2009). Co should not exceed 1 taking into account the stability of the PISO algorithm.

5.8 Solution control

The residual is the error induced by the iterative method for solving the linear equation system. The iteration will stop when the residual is smaller than the prescribed tolerance. The tolerances for different variables are listed in Table 5-1. The tolerances are normalised by L1-norm, and its derivation is shown in Appendix E.

Table 5-1 The absolute tolerances for iterations

variable	tolerance
p_{rgh}	1.0×10^{-8}
$\mathbf{u}$	$(1.0,1.0,1.0)\times10^{-9}$
p_{corr}	1.0×10^{-7}
α	1.0×10^{-7}

Chapter 6 Verification, validation and error analysis based on 2D simulations

6.1 Introduction

As explained previously, the incident wave in the far field from the reflection wall can be regarded as a 2D solitary wave. It propagates with a permanent shape and constant phase speed. These properties should be reproduced by the present numerical method. However, the simulated wave form does change slightly with time. There are mainly two factors affecting the variation of the waveform in the simulation. One is owing to the initial condition. Zhou et al. (2016) have pointed out that the truncated perturbation solution is an approximation to the exact fully nonlinear solution, which leads to the change of the waveform, including the amplitude, with time in the fully nonlinear simulation. The deformation with respect to the initial waveform is more obvious with larger amplitude. Based on that knowledge, the more accurate approximate model may lead to the more stable wave profile in the simulation. The appropriate initial condition for the further 3D simulations of SSWs and ISWs will be investigated. The other factor affecting the waveform is the numerical error. The error sources are various. The spatial discretisation error and the temporal discretisation error can be eliminated by the spatial (grid) convergence examination and the temporal convergence examination, respectively. The iterative error, the interpolation error and even the machine error are usually insignificant. However, they are cumulative and dissipate the wave energy gradually. If the wave travels a long distance, the influence of the cumulative numerical errors becomes noticeable. The global influence is reflected in the slow attenuation of the wave amplitude. Another situation is that the numerical error may

be amplified due to the instability issues and changes the whole wave profile significantly.

The purpose of the error analysis is to guarantee that the numerical error does not cover the physical process we are interested in. 2D collisions between solitary waves are special cases of the 3D wave-wave interaction. There are two scenarios: the head-on collision and the overtaking collision. The interested period of the overtaking collision is long relative to the head-on collision. We will show that even with cumulative numerical errors the simulation can still reveal the major characteristics of the collisions.

6.2 A single surface solitary wave

The 2D computational domain for SSWs is shown in Fig. 6-1. The boundary conditions on the bottom (AD) and left and right sides (AB and CD) are "slip walls". The boundary condition on the top (BC) is to maintain the "total pressure" to be zero, *i.e.*, $p \equiv 0$. The static quadrilateral mesh is employed. Δx and Δz are the cell sizes in the *x*-direction and *z*-direction. The maximum Courant number *Co* is set to be 0.4. Other settings are listed in Table 6-1. In the following analyses for surface waves, all the length variables are scaled by the undisturbed water depth h_S, time is scaled by $h_S / \sqrt{g h_S}$.

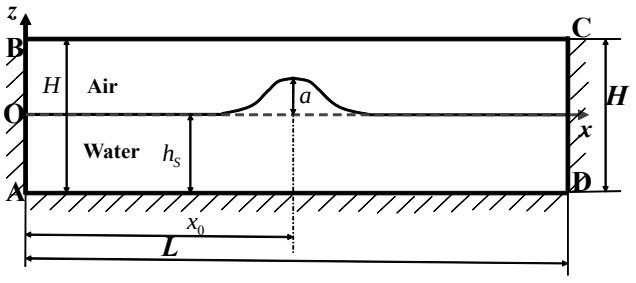

Fig. 6-1 Computational domain for 2D simulations of SSWs.

Table 6-1 The parameters of the single SSW cases (Part 1)

Case	*L*	*H*	Cell size ($\Delta x * \Delta z$)
1	200	2	0.067*0.01
2	60	2	0.067*0.01
3	200	2	0.067*0.01

Table 6-1 The parameters of the single SSW cases (Part 2)

Case	Initial condition	Initial wave amplitude	Initial characteristic wavelength λ_{Sc}	Initial position of the crest x_0	End time
1	1st-order KdV solution	0.4	1.826	30	77.042
2	2nd-order KdV solution	0.4	2.582	30	21.011
3	3rd-order KdV solution	0.4	2.122	30	77.042

Case 1 is chosen for the convergence study. The wave profile is used for comparison. Strictly speaking, the free surface is within the cell of $0 < \alpha < 1$. The contour line where $\alpha = 0.5$ is conventionally used to locate the free surface, though this postprocessing method may bring in error. The wave profiles given by three runs (Table 6-2) are graphically identical as shown in Figs. 6-2(a)-(d). The influences of the cell size and the time step on the deformation of the wave shape can be excluded.

Table 6-2 The cell sizes and *Co* for the convergence study on SSW cases

Run	Cell size ($\Delta x * \Delta z$)	*Co*
1	0.067*0.01	0.4
2	0.033*0.005	0.4
3	0.033*0.005	0.2

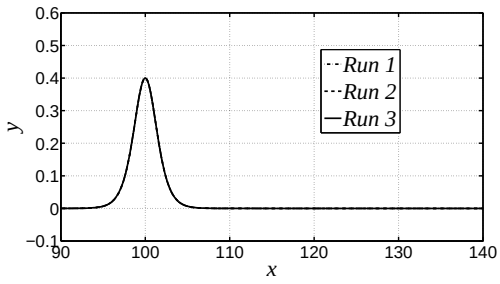

(a)

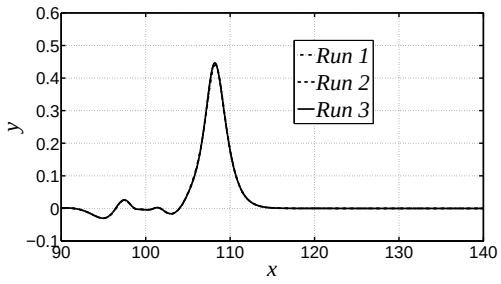

(b)

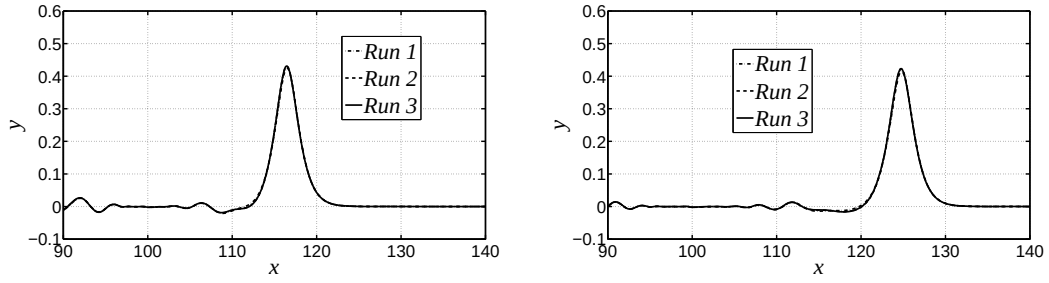

Fig. 6-2 Convergence study of SSW through wave profiles at *t*=0(a), *t*=7.004(b), *t*=14.007(c) and *t*=21.011(d) (Runs are defined in Table 6-2).

The variation of the wave profile is to be further discussed. Although the flow field of Case 1 is initialised by the first-order SSW solution, after the wave travels for a while, the wave profile agrees better with the third-order analytical solution (the second-order solution is the least accurate) (Fig. 6-3(a)). This is because that the wave adjusts itself to satisfy the fully nonlinear boundary conditions and evolves to an exact SSW. Through some physical quantities, that process can be seen more clearly. We can define the kinetic energy of the wave as

$$E_K = \frac{1}{2}\rho \int_\Omega |\mathbf{u}|^2 \, d\Omega, \tag{6.1}$$

where $\int_\Omega$ means integration over the computational domain, and the potential energy as

$$E_P = \frac{1}{2}\rho g \iint \theta^2 dxdy, \tag{6.2}$$

where $\iint$ means integration over the bottom area of the computational domain. The superscript (0) is used to denote the value at the initial time. In Fig. 6-4(b), the fluctuations of the kinetic energy and the potential energy at beginning suggest that the kinetic energy converts to the potential energy. Hence, the wave profile changes. The smooth decline of the wave energy in Fig. 6-4(b) is owing to the cumulative

numerical error. Other physical quantities show more information. The excess mass is defined as the total mass that is above the undisturbed water level, or

$$M = \rho \iint \theta dxdy. \tag{6.3}$$

The total horizontal momentum is defined as

$$I_x = \rho \int_\Omega u d\Omega \tag{6.4}$$

From Fig. 6-3(c), it can be seen that the mass is well conserved by the code. We can use the momentum to test the influences of the air phase and the side walls AB and CD. Fig. 6-3(d) suggests that those influences are quite small, for the momentum is well conserved. From the time histories of the wave amplitudes (Fig. 6-4), it can be seen that there is a fluctuation of the wave amplitude during the incipient period for Cases 1 and 3. Then the amplitude decreases gradually in similar rates afterwards owing to the cumulative numerical errors. Comparing the wave amplitude of Case 1 in Fig. 6-4 and the energy variation in Fig. 6-3(b), the energy transformation only lasts a short period, but the wave profile takes much longer time to stabilise. According to Fig. 6-4, using the more accurate solution can result in a stable SSW much faster, and the amplitude of the stable SSW is closer to the prescribed amplitude. Using the third-order solution as the initial condition can save the computational resources significantly in the following 3D simulation. The third-order SSW solution is also sufficiently accurate for the present study.

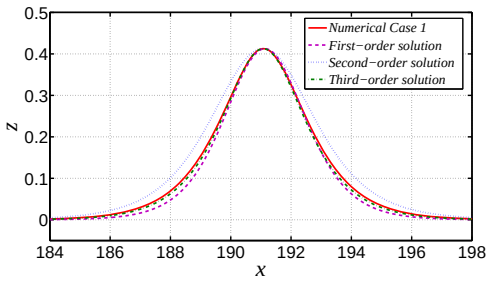

(a)

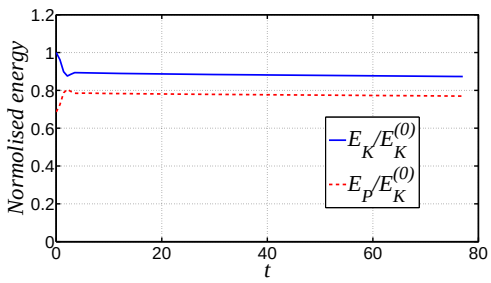

(b)

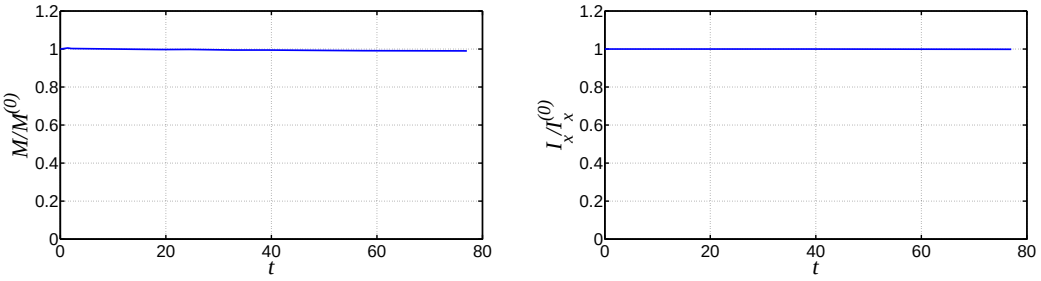

(c) **(d)**

Fig. 6-3 The simulated wave profile in Case 1 for an SSW at *t*=77.042 and the analytical solutions with the same amplitude (a). The kinetic energy and potential energy (b), excess mass (c) and horizontal momentum (d) in Case 1.

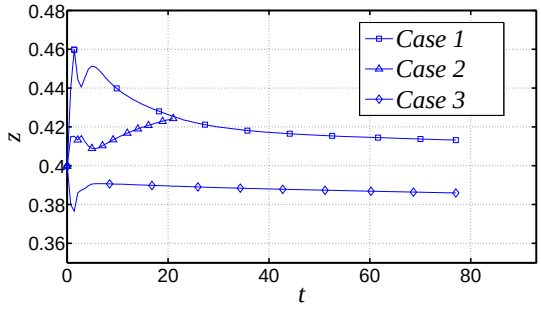

Fig. 6-4 The wave amplitudes in the simulations for an SSW versus time.

6.3 A single internal solitary wave

The 2D computational domain for ISWs is shown in Fig. 6-5. The total length L equals 40 for the cases in Table 6-3. The ratio between the upper layer depth and the lower layer depth, $(H-h)/h$, is 1/3. The ratio of the densities in the upper layer and the lower layer, ρ_2/ρ_1, is 1000/1025. The boundary conditions on the bottom (AD), the top (BC) and left and right sides (AB and CD) are "slip walls". The static quadrilateral mesh is employed unless the AMR is specified. Δx and Δz are the cell sizes in the x-direction and z-direction. In analyses for internal waves hereinafter, all the length variables are scaled by the depth of the undisturbed lower layer h, time is scaled by h/c_0 where c_0 is given by $\sqrt{g(H-h)h(\rho_1-\rho_2)/(\rho_2 h+\rho_1(H-h))}$. Among the 15 cases in Table 6-3, the cell

size for Case 1-5 is 0.067*0.01 ($\Delta x * \Delta z$); the cell size for Case 6-15 is 0.026*0.0035 ($\Delta x * \Delta z$). The maximum Courant number *Co* is set to be 0.4.

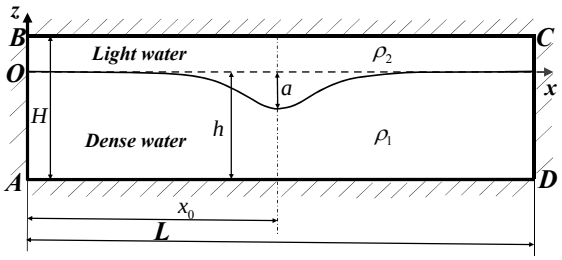

Fig. 6-5 2D computational domain for ISWs.

Table 6-3 The parameters of the ISW cases

Case	Model for the initial condition	Initial maximum interface displacement a	Initial characteristic wavelength	Initial position of the trough	End time
1	1st-order KdV	-0.0267	2.919	13.333	11.402
2	2nd-order KdV	-0.0267	3.122	13.333	11.402
3	3rd-order KdV	-0.0267	3.114	13.333	11.402
4	eKdV	-0.0267	3.012	13.333	11.402
5	MCC	-0.0267	3.153	13.333	11.402
6	1st-order KdV	-0.0667	1.846	13.333	11.402
7	2nd-order KdV	-0.0667	2.228	13.333	11.402
8	3rd-order KdV	-0.0667	2.169	13.333	11.402
9	eKdV	-0.0667	2.061	13.333	11.402
10	MCC	-0.0667	2.237	13.333	11.402
11	1st-order KdV	-0.1333	1.306	13.333	11.402
12	2nd-order KdV	-0.1333	2.131	13.333	11.402
13	3rd-order KdV	-0.1333	1.736	13.333	11.402
14	eKdV	-0.1333	1.687	13.333	11.402
15	MCC	-0.1333	1.925	13.333	11.402

Case 11 is chosen for the convergence study. The contour line where $\alpha = 0.5$ is used to locate the free interface. The wave profiles given by three runs (Table 6-4) are graphically identical as shown in Figs. 6-6(a)-(c). Both the cell size and *Co* used in the case study are appropriate.

Table 6-4 The cell sizes and *Co* for the convergence study on ISWs

Run	Cell size ($\Delta x * \Delta z$)	*Co*
1	0.026*0.0035	0.4
2	0.013*0.0017	0.4
3	0.013*0.0017	0.2

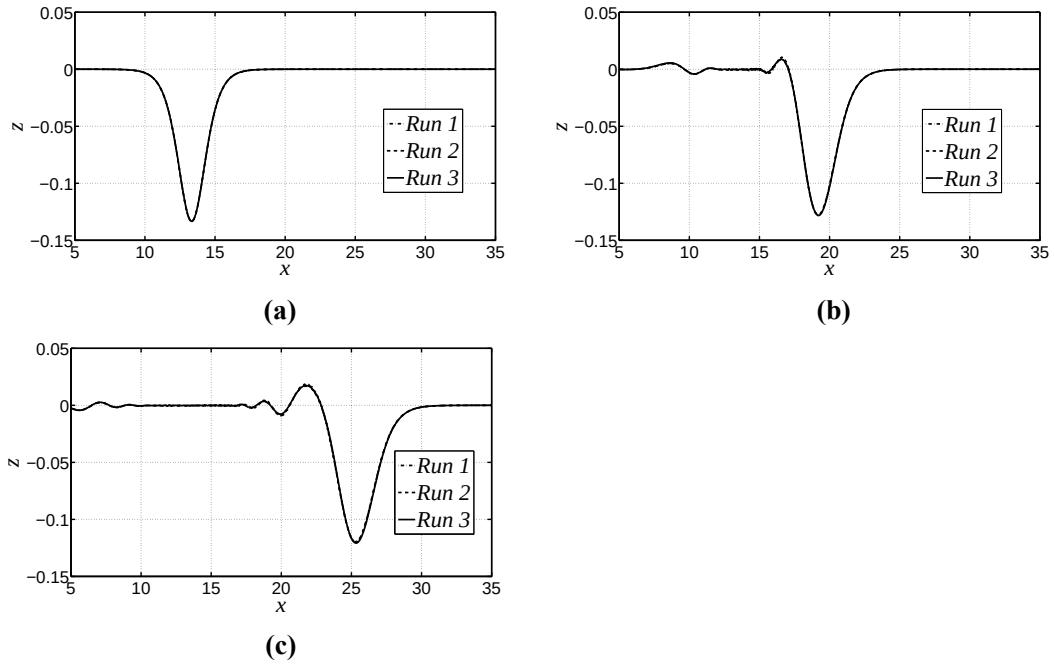

Fig. 6-6 Convergence study through wave profiles at *t*=0(a), *t*=5.701(b) and *t*=11.402 (c) (Runs are defined Table 6-4).

The wave profiles are examined to compare different initial conditions. Cases 1-15 in Table 6-3 are divided into three groups, according to their initial wave amplitudes. The wave profiles are shown in Figs. 6-7(a)-(e) (Group 1), 6-8(a)-(e) (Group 2) and 6-9(a)-(e) (Group 3), respectively. The wave amplitudes in Group 1-3 increase in sequence. The wave amplitude in Group 3 is still smaller than approximately half of

the maximum possible amplitude based on the MCC model, and it can be classified as moderate amplitude in the present context. Hence, the current discussion is confined within the weakly nonlinear regime.

Within each group, the initial conditions are different. When the initial wave amplitude is very small (Figs. 6-7(a)-(e)), the simulated wave profiles at different moments of all cases are closely similar to the initial profiles. The wave travels with a permanent form and at a constant wave speed. It suggests that all the initial conditions are appropriate. However, as the initial amplitude gets larger as those in Groups 2 and 3, the variations of the wave profiles with time become more visible. As the wave propagates, the main portion of the wave remains similar as the initial shape but emits trailing waves. The vertical displacement of the trough has the largest variation with time. The trough leaves a trajectory on the *xz*-plane, which can be used to represent the variation. Overall, the cases initialised by the third-order KdV model undergo the smallest variation. The wave amplitudes at the final time step in the cases of Groups 2 and 3 are compared to their initial amplitudes, and the relative differences are shown in Fig. 6-10. The cases in Fig. 6-10 are labelled by the initial ISW models. The ISW solution of the third-order KdV equation performs the best to keep the wave form stable. It can be explained as follows. In the simulation, both the wave form and the velocity field have to be initialised. The worse performances of the first-order and second-order KdV models are owing to the less accurate approximations both on the wave form and the velocity field. Nevertheless, the wave profiles given by the third-order KdV, the eKdV and the MCC models are nearly indistinguishable for the ISW with a of -0.1333. Hence, the worse performances of the eKdV model and the MCC model are owing to the less accurate approximation on the velocity field. In this thesis, the third-order KdV model will be

used to initialise the flow field of the relevant simulations for ISWs of small and moderate amplitudes.

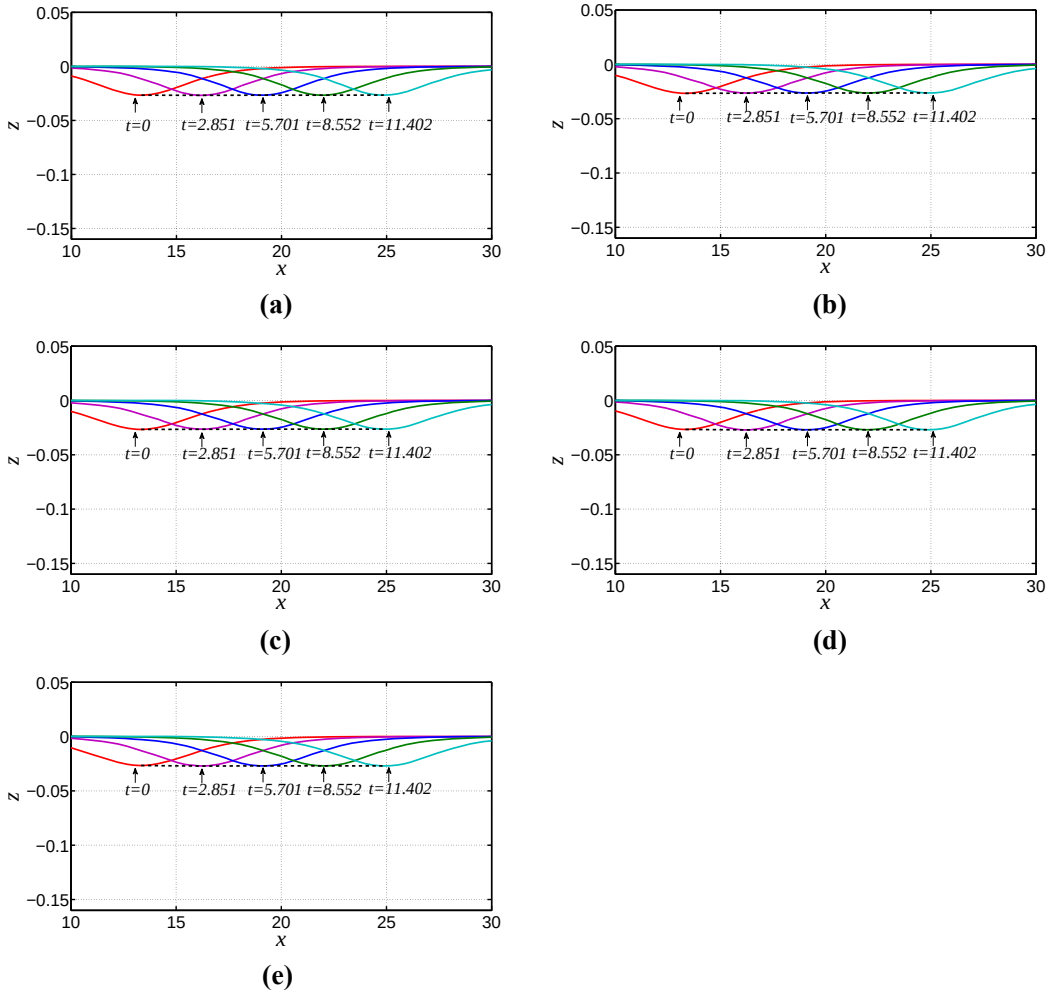

Fig. 6-7 The wave profiles at different moments given by Case 1 (a), Case 2 (b), Case 3 (c), Case 4 (d) and Case 5 (e). The dashed line connects the troughs of the wave profiles.

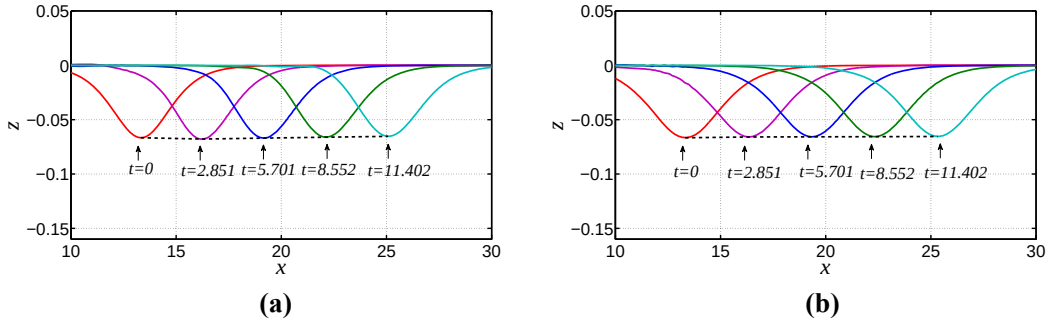

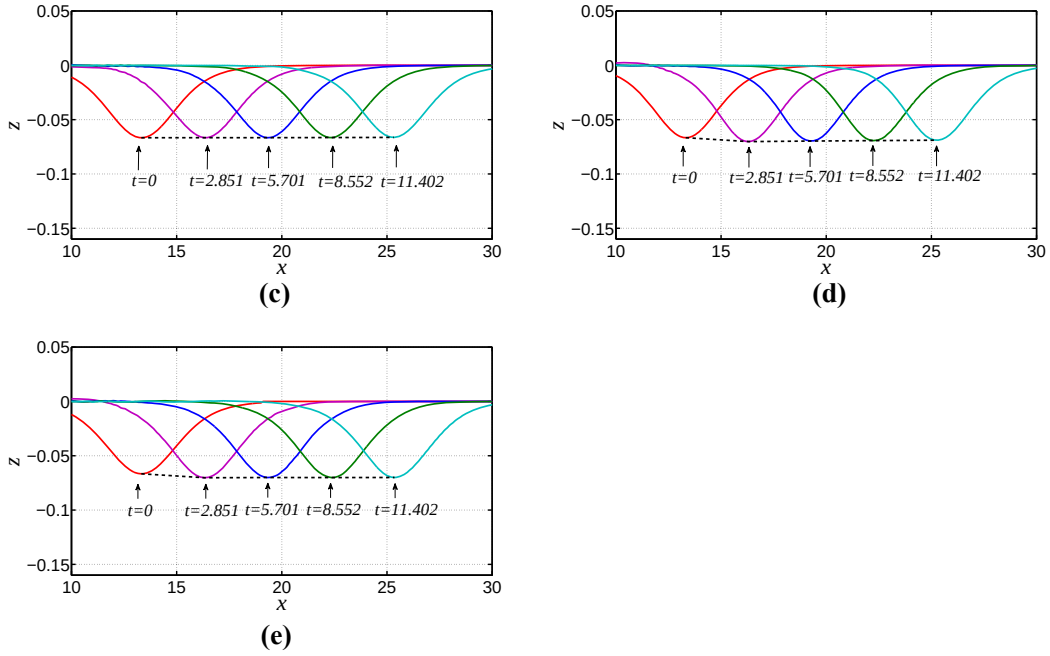

Fig. 6-8 The wave profiles at different moments given by Case 6 (a), Case 7 (b), Case 8 (c), Case 9 (d) and Case 10 (e). The dashed line connects the troughs of the wave profiles.

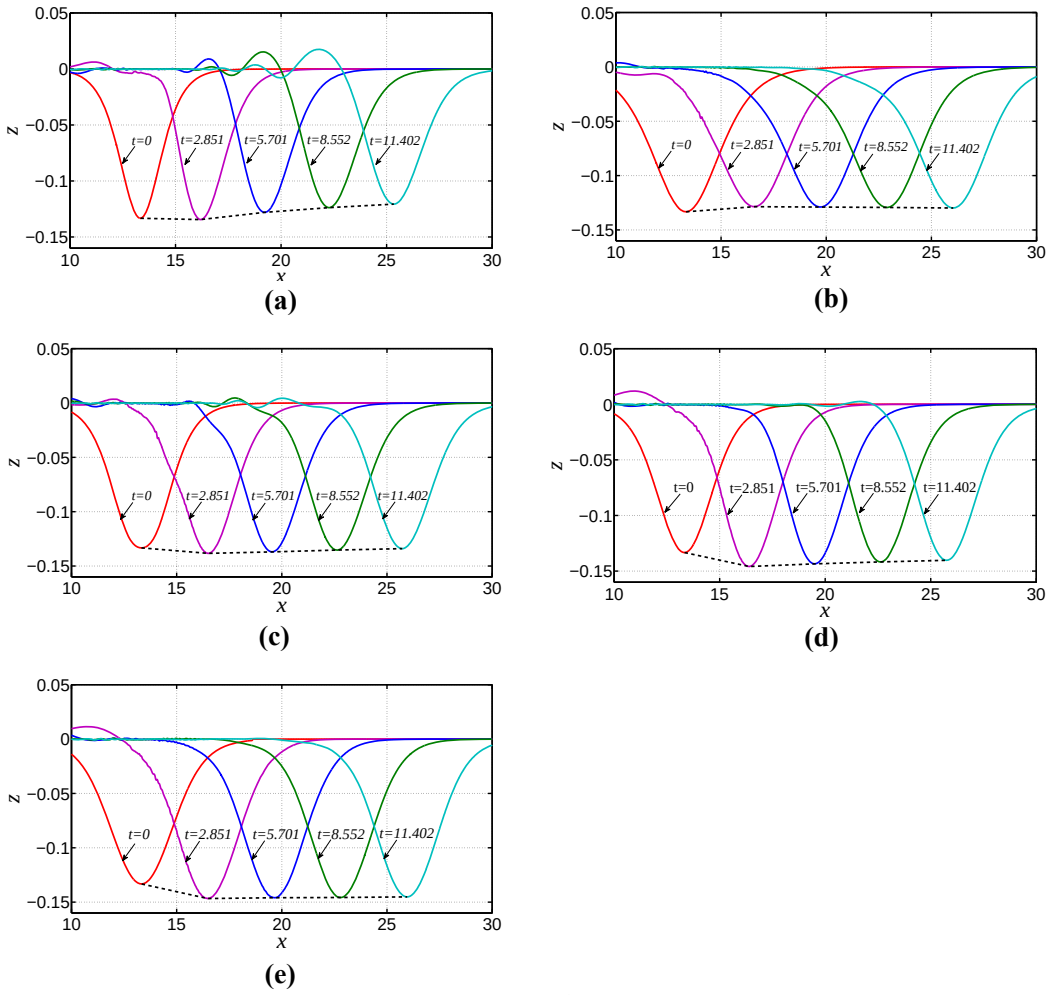

Fig. 6-9 The wave profiles at different moments given by Case 11 (a), Case 12 (b), Case 13 (c), Case 14 (d) and Case 15 (e). The dashed line connects the troughs of the wave profiles.

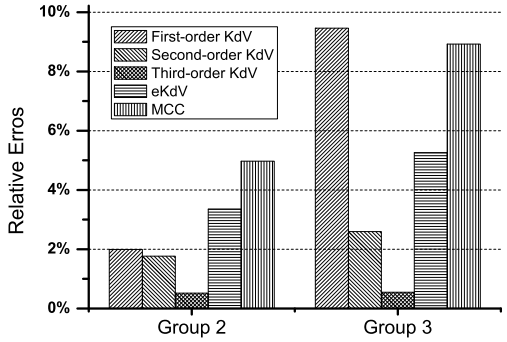

Fig. 6-10 The relative errors of the wave amplitudes at t=11.402 with respect to their initial amplitudes.

An additional simulation is shown in Fig. 6-11 with the same set-ups as Case 13 in Table 6-3 except for a longer length of the numerical wave tank and a longer simulated duration. We can define the excess mass for internal waves, or

$$M = (\rho_2 - \rho_1) \iint \theta dxdy, \tag{6.5}$$

where $\iint$ means integration over the bottom area of the computational domain, the horizontal momentums in the two layers, or

$$I_{xn} = \rho_n \int_{\Omega_n} u_n d\Omega_n, \quad n = 1, 2, \tag{6.6}$$

where $\int_{\Omega_i}$ means integration over the lower layer or upper layer, the kinetic energy of the wave, or

$$E_K = \frac{1}{2} \int_{\Omega_1} \rho_1 |\mathbf{u}_1|^2 d\Omega_1 + \frac{1}{2} \int_{\Omega_2} \rho_2 |\mathbf{u}_2|^2 d\Omega_2, \tag{6.7}$$

the potential energy, or

$$E_P = \frac{1}{2} (\rho_1 - \rho_2) g \iint \theta^2 dxdy. \tag{6.8}$$

The superscript (0) is used to denote the value at the initial time. The wave profile (Fig. 6-11), the excess mass (Fig. 6-12(a)), the horizontal momentum (Fig. 6-12(b))

and energy (Fig. 6-12(c)), do not deviate from the initial state a lot as the time elapses. It suggests the third-order KdV model is very accurate. The slow attenuation of the wave amplitude can be recognised through the trajectory of the through in Fig. 6-11. The attenuation seems to be more noticeable than the SSW cases. The constant excess mass in Fig. 6-12(a) suggests that the volume fraction α has been accurately calculated. The decline of the momentums in Fig. 6-12(b) illustrates the cumulative error of the horizontal velocity is noticeable. The error probably comes from the iterative error to correct the coupled pressure field and the velocity field, for the pressure gradient in the vicinity of the interface is large. That results in the attenuation of the kinetic energy (Fig. 6-12(c)). The reduction of the kinetic energy in turn reduces the potential energy of the wave. Consequently, the wave amplitude decreases gradually.

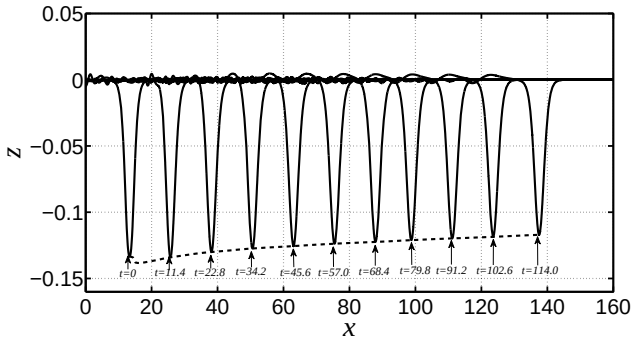

Fig. 6-11 The wave profiles initialised by the third-order KdV model at different moments. The dashed line shows the trajectory of the trough.

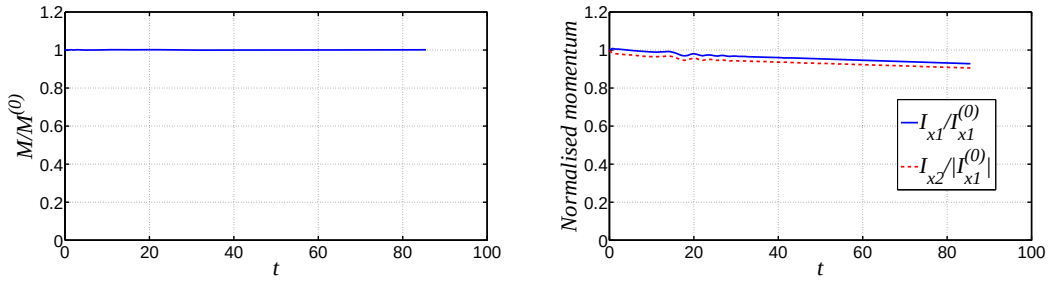

(a) **(b)**

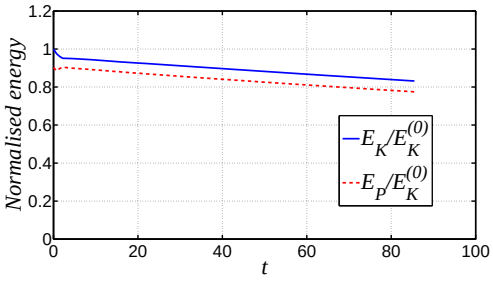

(c)

Fig. 6-12 The excess mass (a), horizontal momentums (b) and kinetic energy and potential energy (c) in the case initialised by the third-order KdV ISW model with *a*=-0.1333.

The instability issue is encountered particularly in the simulation of internal waves of moderate and large amplitude. The appearance, *i.e.*, the saw-toothed (Fig. 6-13(a)) or even roll-up (Fig. 6-20(b)) interface, is likely to be due to the physical Kelvin-Helmholtz (K-H) instability (Grue et al., 1997; Jo and Choi, 2008). The jump of the tangential velocity at interface induces the K-H instability. Grue (1997) argues that the K-H instability can be suppressed by local nonlinearity, viscous effects and/or interfacial tension of the real fluid, and by using the smoothing method within a model that does not take into account the viscous effect and interfacial tension "may provide a reasonable approach to large-scale behaviour of interfacial waves". Grue et al. (1997) used the smoothing method and Jo and Choi (2008) used a low-pass filter every few time steps to remove short disturbances. In the present study, the smoothing method is only employed in the postprocessing procedure without interference with the calculation. The smoothing method called "lowess" in MATLAB™ is adopted, which is an abbreviation of "locally weighted scatter plot smooth". It is based on the local regression using weighted linear least squares and a 1st degree polynomial fitting function. The method can smooth the saw-toothed interface well and maintain the mean interface position that is important to the study of the long-wave behaviours. However, when the interface rolls up, the mean

position of the interface varies a lot with different sampling points, which affects the credibility of the result.

The simulated interface is more likely to be unstable to disturbances with shorter wavelength. The wavelength of the disturbances in the numerical simulation is usually proportional to the cell size due to the discretisation (Štrubelj and Tiselj, 2005). When the internal wave amplitude increases, or the cell size is reduced with the unchanged time step, the simulation becomes more unstable and the saw-toothed interface may roll up. It may result in a difficulty for the spatial convergence study when the roll-up interface occurs in the run with a small cell size that needs to be tested. In the 3D simulation in Chapter 8, the large-amplitude internal wave is observed in the runs with different typical cell sizes. However, the roll-up interface appears in the simulation with the finer mesh than what is shown in the thesis. Alternatively, we will use the property of the solitary wave to test the accuracy as a complementary documentation of convergence as what has been done by Grue et al. (1997). We will simulate a 2D propagating ISW with comparable wave amplitude to that of the large internal wave in the 3D simulation. It is aimed to estimate the possible numerical errors when the wave travels a similar distance as that in the 3D simulation.

6.4 Numerical experiments for the 3D simulation of a moderate-amplitude ISW

High efficiency and high accuracy are required in the further 3D simulation. Employing the AMR technique is for that purpose. By using the AMR, more parameters need to be tuned. It is impractical to carry out many 3D simulations. The 2D numerical experiments can help to select the parameters.

6.4.1 The moderate-amplitude internal wave

In the further 3D simulation, the flow field will be initialised by the ISW solution of the third-order KdV equation with a of -0.1333. The maximum refinement level and the number of the buffer layers are unchanged are both 3. Other parameters will be discussed as below.

Four meshes are employed for the spatial convergence study (Table 6-5). The lower limit of refinement is that $C_{amr2} = 0.2$. The time step is fixed, and $\Delta t = 0.0071$. It is approximately equivalent to set Co = 0.4 with the finest mesh. The refinement step is 4.

Table 6-5 The cell sizes for the spatial convergence study with the AMR technique (after refinement)

Run	Δx	Δz
1	0.104	0.0139
2	0.052	0.0069
3	0.026	0.0035
4	0.013	0.0017

The wave profiles at t=31.353 given by Run 1-4 are plotted in Fig. 6-13(a) together with the analytical solution. The simulated results achieve convergence as the cell size reduces. If the cell size is further reduced, the accuracy would be improved little while the ripples with short wavelength occur (Fig. 6-13(b)). Figs. 6-14(a) & (b) show that the smoothing method can filter the short disturbances while maintaining the long-wave features. Smoothed results of Run 4 will be used for analyses hereinafter.

The accuracy of the numerical result can be estimated via the comparison with the analytical solution shown in Fig. 6-13(a). After propagating for approximate 30

characteristic wavelengths, the wave amplitude has decreased by approximately 5.5%. The wave speed has decreased a little as well. The mean wave speed in the simulation is approximately 1.087, while the wave speed given by the third-order KdV model is 1.105. The trough trajectories given by all the runs are plotted in Fig. 6-15 and compared with the third-order solution. Two conclusions can be obtained. One is that the cell size used by Run 3 is fine enough. The other is that the error of the simulated wave amplitude after the wave propagates for 46 characteristic wavelengths is approximately within 10%, and the error of the simulated wave phase speed is approximately within 2%.

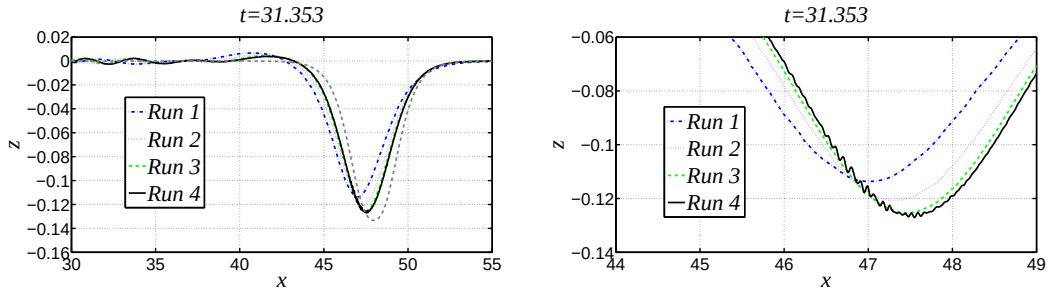

(a) **(b)**

Fig. 6-13 (a): Comparison of the wave profiles given by the numerical simulations with various cell sizes; the ISW solution of the third-order KdV equation is plotted by the grey dashed line. (b): Enlarged detail in the vicinity of the trough.

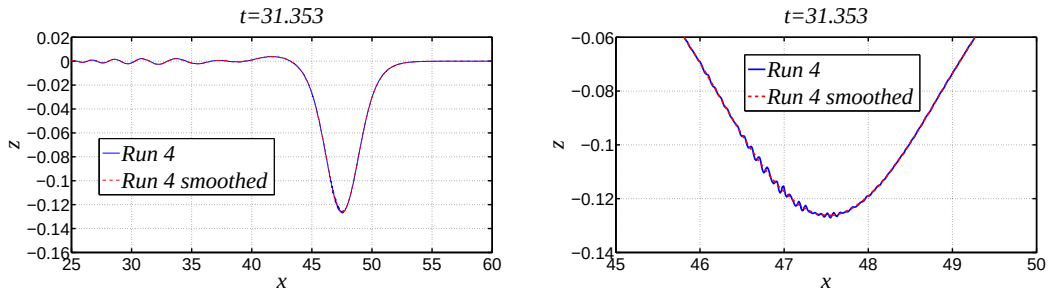

(a) **(b)**

Fig. 6-14 Comparison between the original wave profile and the smoothed result. (a): the whole range; (b): enlarged view in the vicinity of the trough.

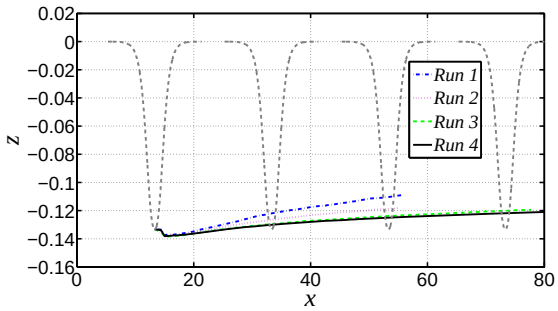

Fig. 6-15 The trajectories of the troughs given by all the runs. The analytical ISW profiles are plotted by grey dashed lines.

In the temporal convergence study, $\Delta x = 0.026$, $\Delta z = 0.0035$ (refined) and $C_{amr2} = 0.2$. The refinement step is 4. The trajectories of the troughs given by the simulations with different *Co* are plotted in Fig. 6-16. They are graphically identical. Hence, *Co*=0.4 can give the convergent result in terms of the time step.

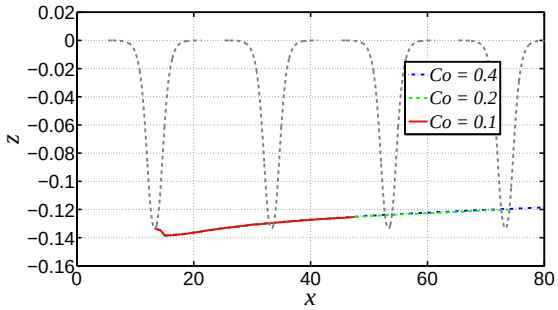

Fig. 6-16 The trajectories of the trough given by the simulations with different maximum Courant numbers. The analytical ISW profiles are plotted by grey dashed lines.

By using the AMR technique, only a portion of the mesh is of high resolution and the fine mesh area depends on the lower limit of refinement C_{amr2}. With different values of C_{amr2} the global wave pattern should not be affected much. The static mesh with uniform high resolution can be deemed as $C_{amr2} = 0$. Run 3 in Table 6-5 is compared with the calculation on the fine static mesh (Fig. 6-11) in Fig. 6-17. It can be seen, from the trajectory of the trough, that the attenuation in the simulation with the dynamic mesh is slightly faster than that with the static mesh. In essence, the major error brought by the AMR technique can be classified as the discretisation

error. Therefore, the smaller C_{amr2} is, the more accurate the result is. The exact solitary wave solution should have invariant wave form. The gradual attenuation of the wave amplitude in the simulation is due to the numerical errors. The difference of the wave amplitude between the simulated result and the initial condition can be used to evaluate the summation of the numerical errors. The difference of the wave amplitude between runs with different meshes can be used to evaluate the discretisation error. From Fig. 6-17, the discretisation error has been at the same order as other numerical errors. Taking into account the computational expense, $C_{amr2} = 0.2$ is appropriate for the following simulations.

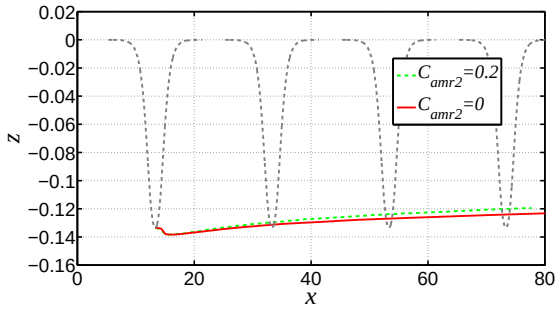

Fig. 6-17 The trajectories of the troughs given by the simulations with different lower limits of refinement. The analytical ISW profiles are plotted by grey dashed lines.

The value of C_{amr2} has a big influence on the calculations on the sparse mesh. In Fig. 6-18, the two simulated wave profile with $\Delta x = 0.104$ (refined) are different due to different C_{amr2}. The result with smaller C_{amr2} is much more accurate than that with larger C_{amr2} comparing with the result on the fine mesh (Fig. 6-18).

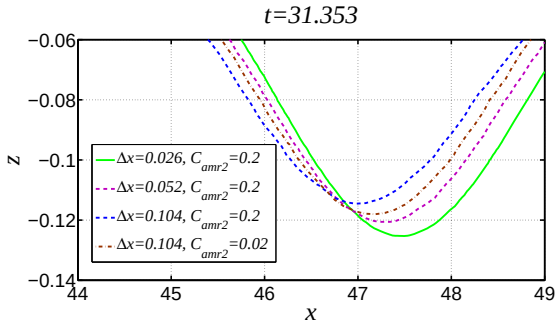

Fig. 6-18 Comparison of the wave profiles given by the numerical simulations with different cell sizes and C_{amr2}.

Increasing the refinement step can significantly improve the efficiency, for the dynamic mesh manipulation and the continuity correction consume a lot of time. The refinement step cannot be too many, either. As a rule of thumb, the refinement step used in the present study is less than 6. Fig. 6-19 shows different refinement steps result in almost the same result.

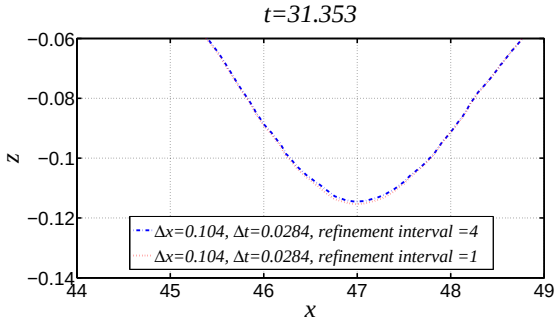

Fig. 6-19 Comparison of the wave profiles given by the numerical simulations with different refinement steps.

6.4.2 The large-amplitude internal wave

The simulation of a large-amplitude ISW is to be used to estimate the computation accuracy in Chapter 8. The flow field is initialised by the ISW solution of the eKdV equation with a = -0.255. The common settings of the two runs shown in Figs. 6-20(a) and (b), respectively, are that Co=0.4 and $C_{amr2} = 0.2$. The roll-up phenomenon, which is typical when the K-H instability occurs, can be seen in Fig. 6-20(b) with the finer mesh. Nevertheless, the simulated result on the sparser mesh fits the solitary wave criteria (constant wave profile and phase speed) reasonably well (Fig. 6-20(a)). More discussion will be given in Chapter 8.

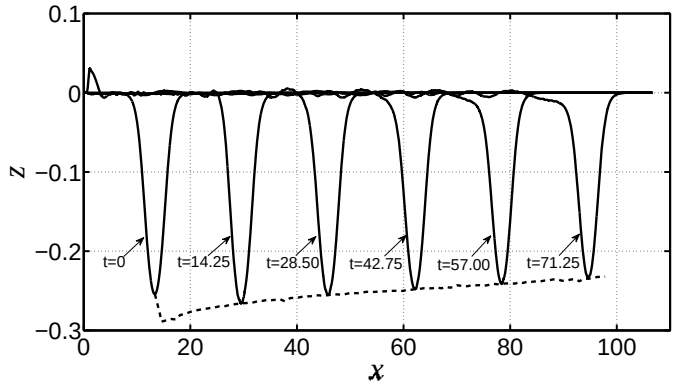

(a)

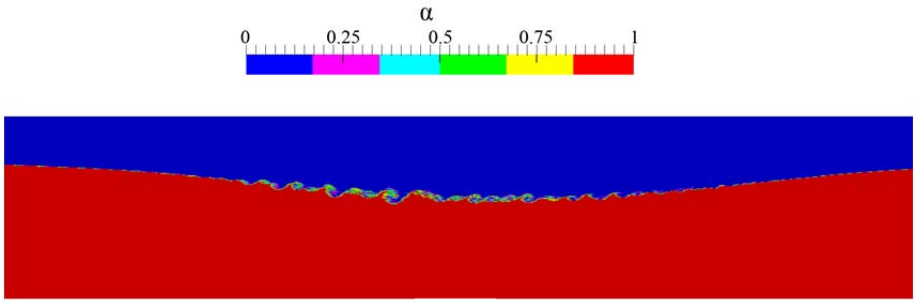

(b)

Fig. 6-20 (a): The simulated wave profiles (smoothed) initialised by an ISW solution of the eKdV equation. The dashed line shows the trajectory of the trough. The refined cell size is 0.026*0.0035 ($\Delta x * \Delta z$). (b): The K-H instability observed in the simulation with the finer mesh. The refined cell size is 0.013*0.0017 ($\Delta x * \Delta z$).

6.5 Collisions of two surface solitary waves

For the head-on collision of SSWs, the computational domain and the boundary conditions are the same as those in Fig. 6-1, which resemble a wave tank of finite length. Figs. 6-21(a)-(h) show the wave profiles at different moments. As the solitary wave decays exponentially away from its peak, when two waves are sufficiently apart, they can be treated as two independent waves. The wave profile and velocity field are initialised by the superposition of two third-order solitary wave solutions in Fig. 6-21(a). Slight discrepancies between the simulated results and the experimental results can be seen during the collision process (Figs. 6-5(b)-(f)). Overall, the simulated results agree well with the experiment. The re-emergence of the two SSWs

as if they passed through without touching each other is reproduced by the simulation (Figs. 6-21(g)-(h)).

Figs. 6-22(a)-(h) show the wave profiles in the overtaking collision. The larger SSW is propagating with a faster speed than that of the smaller SSW. If the larger SSW is behind the smaller SSW initially, they will collide and interact with each other. Gradually, two SSWs will emerge again. The larger SSW will overtake the smaller SSW. Comparing with the head-on collision, the interaction time in the overtaking collision is much longer (Figs. 6-21(h) & 6-22(h)), which needs a longer wave tank as well. To use a computational domain with short length, the boundary conditions on AB and CD are changed to a pair of periodic boundary conditions, which resembles a circulating water channel. A side effect is the interference between the trailing waves and the main peaks. The trailing waves need to be eliminated or suppressed. Some manual manipulations on the flow field have been done in the incipient period. There are still two difficulties when comparing with the experimental measurement. One is about the initial conditions. In the first snapshot of the experiment given by Craig et al. (2006) in Fig. 6-22(a), two waves have already been interacting with each other. Therefore, the simple superposition is not valid for that moment. In our simulation, the distance between the crests of two SSWs is 30 initially. The two waves are sufficiently apart and two third-order solutions are superposed. Many numerical experiments were performed to match the experimental result in Fig. 6-22(a). The amplitudes of the two SSWs at the initial time are then determined to be 0.5624 and 0.146, respectively. The other difficulty is about the phase. In the experiment, the wave profile is captured by wave gauges on a travelling instrumentation carriage. The time intervals between the figures were recorded precisely, but not the carriage position. It means that the accurate relative

phases between peaks rather than their individual absolute phases were presented. For that reason, the simulated results and the experimental measurements are plotted by aligning their respective peak positions. Comparing Figs. 6-22(a) and (h), the attenuation of the larger-amplitude wave in the simulation is noticeable. However, the simulation reproduces the overtaking process with excellent agreement with the experiment. The attenuation in the experiment is due to viscosity and the attenuations in the simulation is due to the cumulative numerical errors. But both the simulation and the experiment show the re-emergence of two solitary-like waves after the overtaking collision.

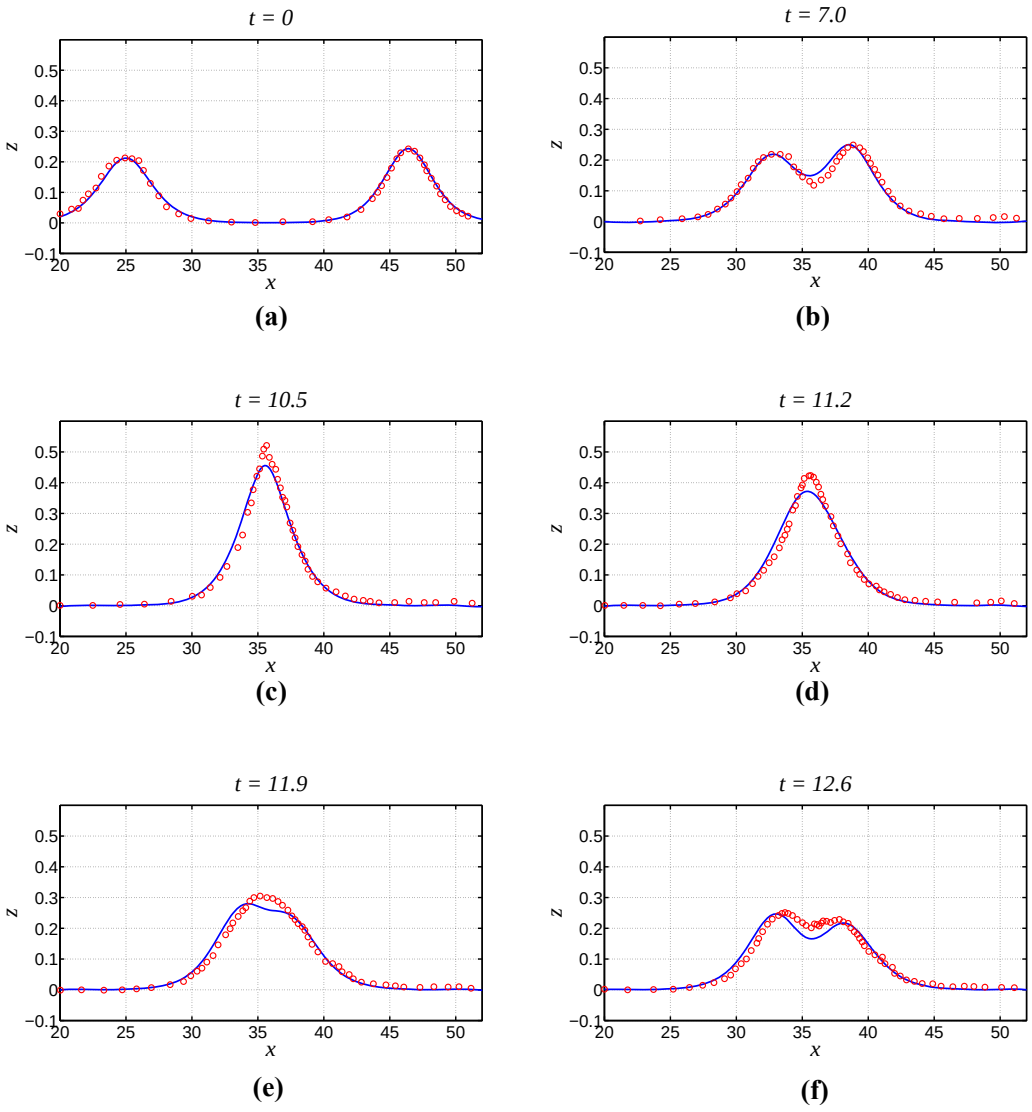

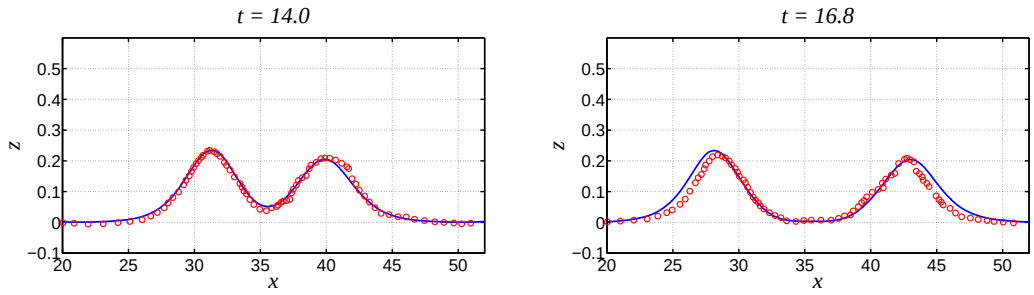

Fig. 6-21 CFD results (blue thick lines) and experimental measurements by Craig et al. (2006) (red circles) of the head-on collision of two SSWs. The amplitudes of the SSWs are 0.243 and 0.213 initially.

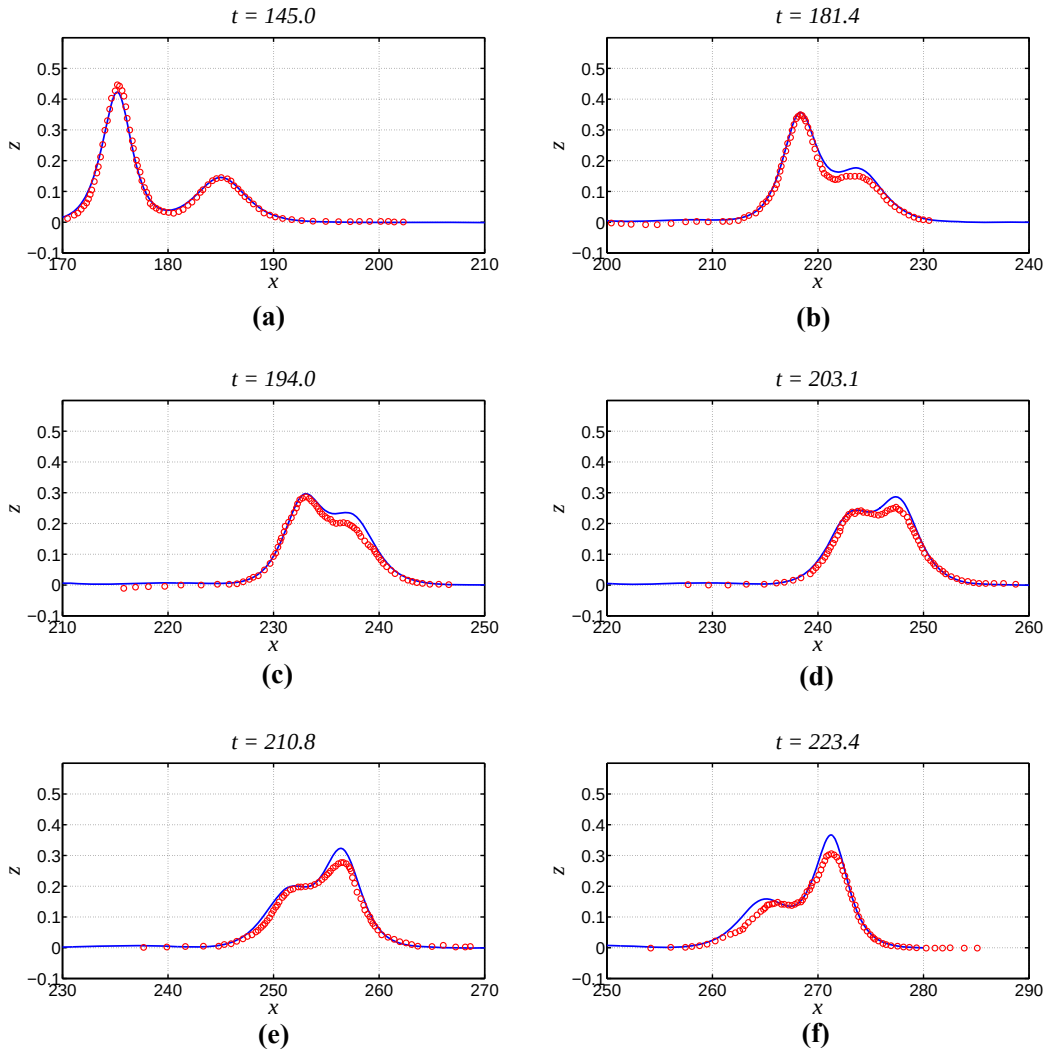

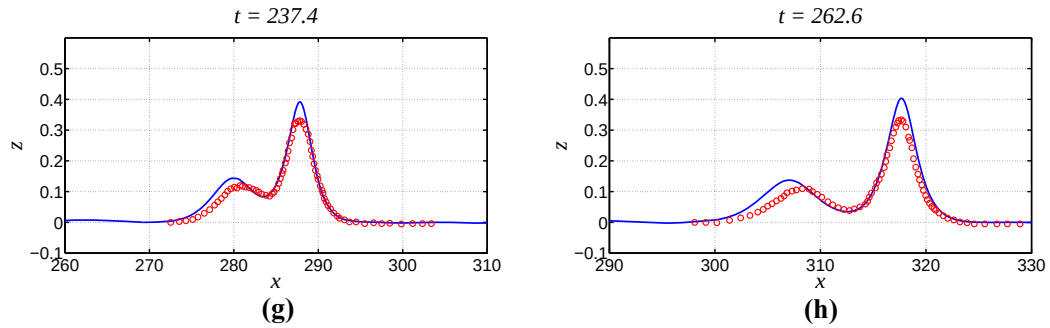

Fig. 6-22 CFD results (blue thick lines) and experimental measurements by Craig et al. (2006) (red circles) of the overtaking collision of two SSWs. The amplitudes of the SSWs are 0.562 and 0.146 initially.

6.6 Collisions of two internal solitary waves

In Figs. 6-23(a)-(h), the head-on collision of two ISWs is simulated in the same numerical wave tank as that in Fig. 6-5 where $\rho_2/\rho_1 = 1000/1025$; $(H-h)/h = 1/3$. The initial amplitudes of the two ISWs are 0.1333 and 0.0667, respectively. The collision process is quite similar to the head-on collision of two SSWs (Figs. 6-21(a)-(h)). Two solitary-like waves with the same amplitudes as those of the incident waves emerge after the collision. The greatest interface excursion during the collision is conventionally called run up, though in reality it is of depression. In Fig. 6-24, the run ups in the collision of two identical ISWs are plotted versus the amplitudes of the incident wave according to the simulated results and the third-order perturbation results by Mirie and Su (1984). The simulated results and the third-order results agree with each other well. Figs. 6-25(a)-(h) show the simulated overtaking collision of two ISWs. Periodic boundary conditions are again used. Some manual manipulations of the flow field have been done in order to suppress the trailing waves. The overtaking collision of internal waves is quite similar to that of SSWs shown in Figs. 6-22(a)-(h), too. During the interaction process, the maximum interface displacement is smaller than that of the initial larger ISW. Gradually, two

solitary-like waves occur. The larger wave is ahead of the smaller one. These features in the 2D collision of ISWs have also been reported by other researchers via different models, to name a few, by, Choi and Camassa (1999), Jo and Choi (2002) and Nguyen and Dias (2008). Comparing Figs. 6-25 (a) & (h), the profiles of the smaller waves in both figures are almost identical. By contrast, the amplitude of the larger wave is noticeably smaller than that of the initial larger ISW. Recalling the previous simulations of a single wave propagating for a long time, it is probably due to the cumulative numerical error. Similar to the overtaking surface wave case, the error does not affect the analysis of the major characteristics of this internal wave collision.

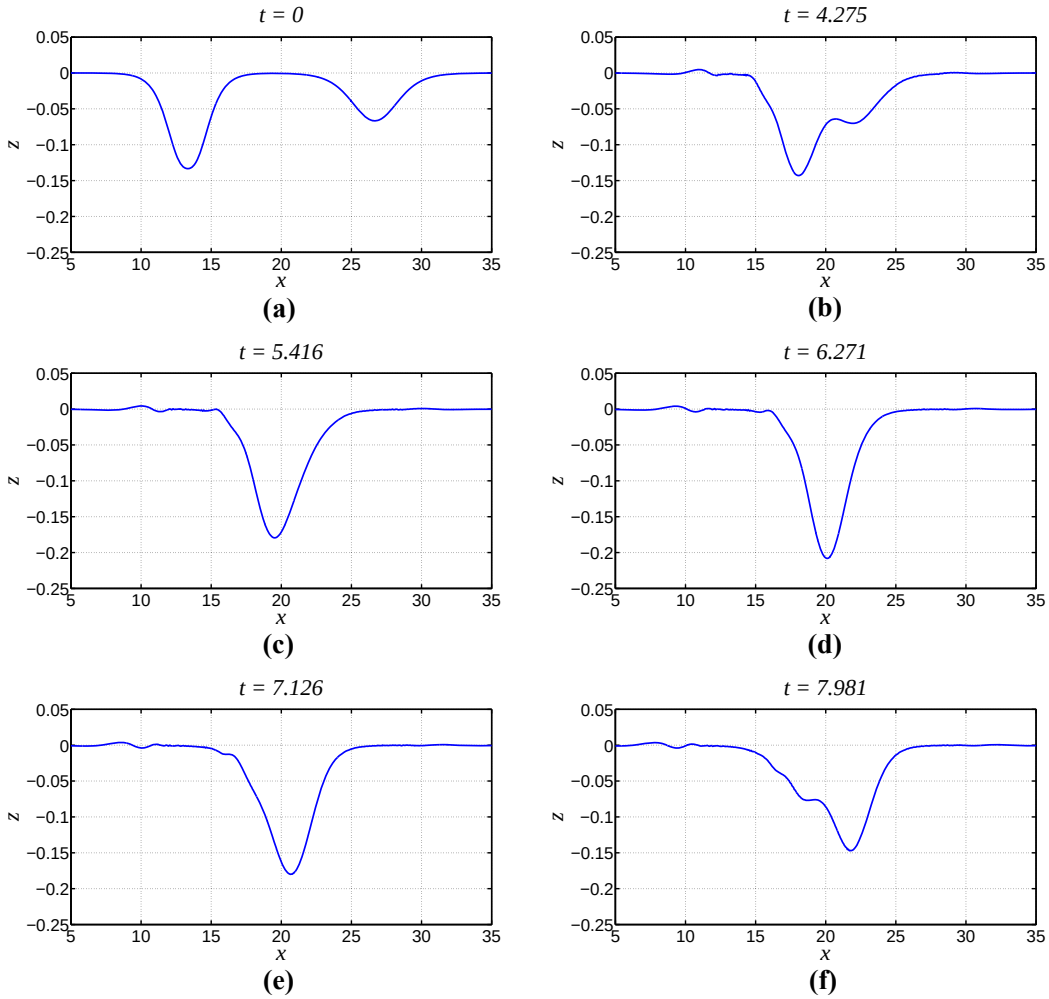

(a) **(b)** **(c)** **(d)** **(e)** **(f)**

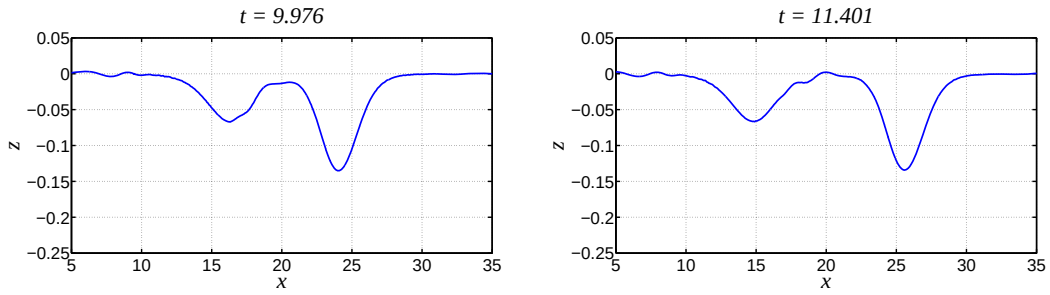

(g) **(h)**

Fig. 6-23 CFD results (blue thick lines) of the head-on collision of two ISWs. The amplitudes of the ISWs are 0.1333 and 0.0667 initially.

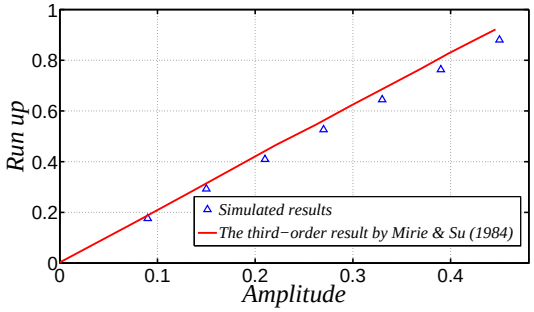

Fig. 6-24 CFD results (blue triangles) and third-order result by Mirie and Su (1984) (red line) for the run up in the head-on collision of two identical ISWs. The abscissa is the amplitude of the incident ISW. $\rho_2/\rho_1 = 0.8$; $(H-h)/h = 2.5$.

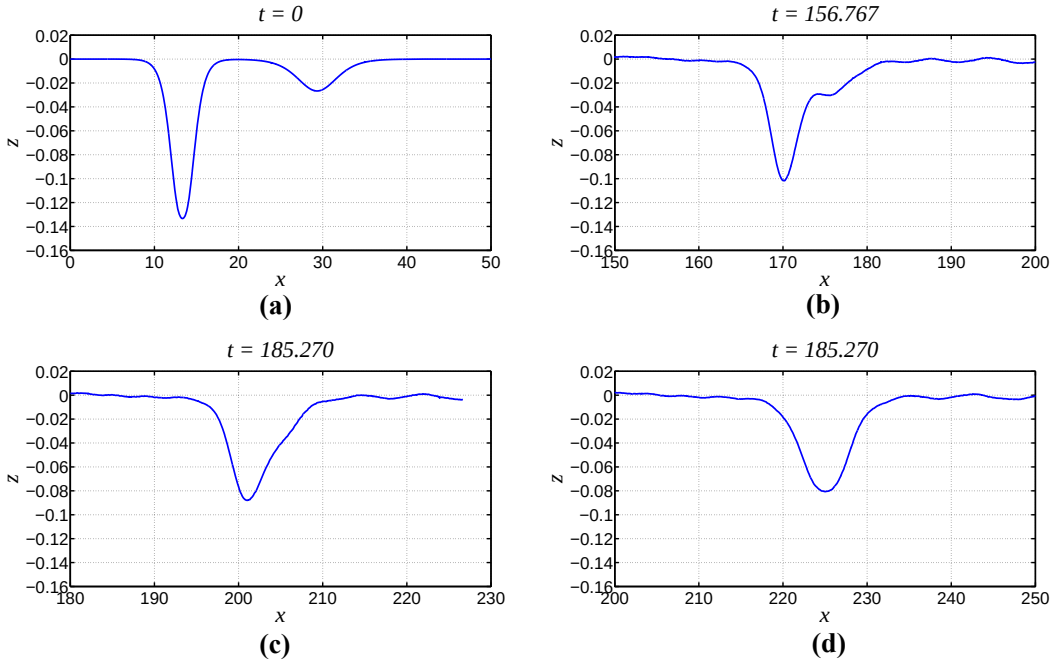

(a) **(b)**

(c) **(d)**

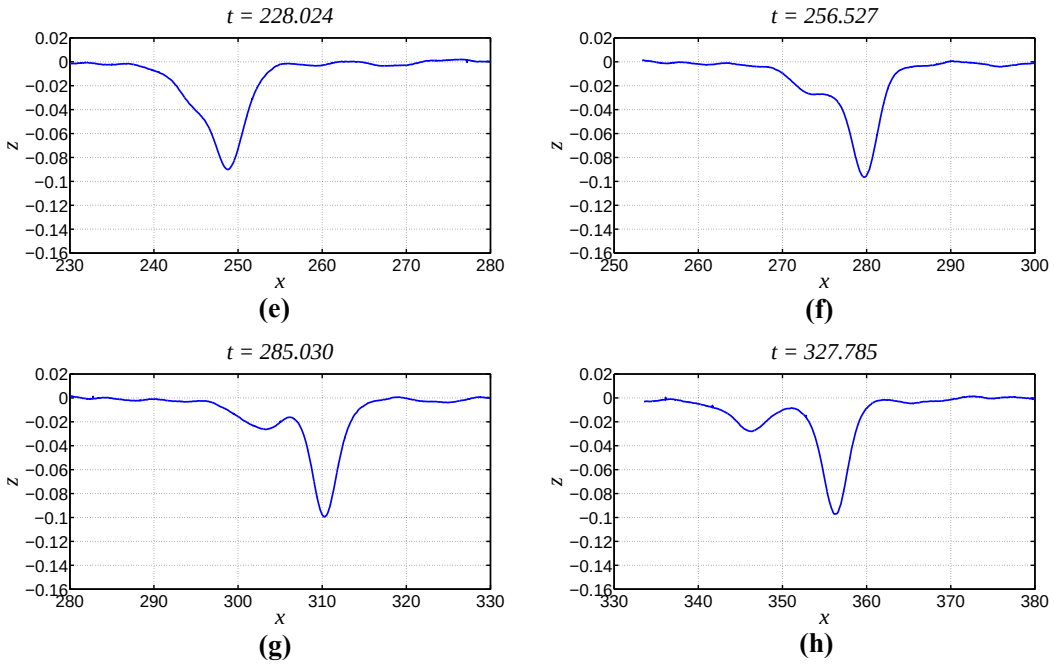

Fig. 6-25 CFD results (blue thick lines) of the overtaking collision of two ISWs. The amplitudes of the ISWs are 0.1333 and 0.0267 initially.

6.7 Summary

Based on the tests on an SSW and an ISW and the comparisons of 2D collision cases, the code is capable of simulating both the surface wave and the internal wave problems.

Extensive numerical experiments have been performed to test the convergence and evaluate the accuracy. The third-order SSW solution is sufficient for the generation of an SSW of moderate amplitude in the fully nonlinear simulation. 5 models were used for the generation of an ISW. Among them, the ISW solution of the third-order KdV equation can result in the most stable ISW in the simulation with up to the moderate amplitude. 2D numerical experiments have been performed to assist the parameter selection in the further 3D simulation. The simulations of solitary wave collisions suggest that if the interested process has a shorter time scale than that of

the gradual attenuation owing to the numerical error, the major long-wave features can still be readily distinguished from the simulation.

It is worth noting the similar collision processes of SSWs and ISWs. This similarity yields a question that whether the 3D collisions of ISWs are still similar to the corresponding scenarios of SSWs especially when the wave amplitude is not small.

Chapter 7 Numerical simulation on the oblique reflection of a moderate-amplitude surface solitary wave

7.1 Introduction

In the experiments, Li et al. (2011) observed a maximum wave height of $0.910h_S$ at the reflection wall when the incident wave amplitude $a_i = 0.367h_S$, and the incident wave angle $\psi_i = \pi/6$. This case will be simulated by the fully nonlinear numerical method. The strong nonlinearity on the free surface is a challenge to the numerical method, but this case is significant to coastal engineering and ocean engineering. The experimental measurements in terms of the wave profile will be used to validate the CFD method with the AMR technique. The numerical simulation can provide information of the velocity field and the wave phase speed, which has not been measured in the experiment. With that information, better understanding of the kinematics and dynamics of the large Mach stem wave can be gained.

The essence of waves is the transformation and propagation of energy. Take a classic tsunami scenario modelled by a 2D SSW as an example. The energy that an SSW carries is relatively localised in the longitudinal direction, and is not scattered via the dispersive effect. Research on the energy of an SSW on a flat bottom has been carried out in the 2D space, to name a few, by Longuet-Higgins (1974), Longuet-Higgins and Fenton (1974), Klettner and Eames (2012). When the wave is climbing up the slope of the continent shelf, the kinetic energy first converts to the potential energy to lift up the centre of gravity of the water hump, and the potential energy can be then converted back to the kinetic energy to accelerate the fluid parcel at the crest before overturning (Grilli et al., 1997; Klettner and Eames, 2015). It is likely to correspond to the dyke overtopping by the tsunami waves. Besides energy,

other physical quantities are also useful for estimations of the overall influence of the wave. The total mass that is above the undisturbed water level (excess mass) is related to the total flood volume. The horizontal momentum is related to the estimation of the major hydrodynamic force on the structure. Hence, analyses on the physical quantities in terms of mass and momentum have also been presented by the aforementioned authors. Extending to 3D wave phenomena, in the presence of the vertical wall that is oblique to the longitudinal direction, the excess mass, momentum and energy will be transferred in the normal direction to the wall. The regular reflection meets our intuitions, as reflected in its name. The reflected wave gradually forms the mirrored image of the incident wave about the normal direction. So the energy can be spread out through the propagation of the reflected wave. However, it is not straightforward to predict the transfers of the energy together with other quantities freed from shortening the incident wave in a Mach reflection (Melville, 1980; Li et al., 2011). They probably partly go into the stem wave and partly go into the reflected wave. Thus, the in-depth understanding has to be achieved from the quantitative analysis. Here we propose an analysing method based on the flow field features. Whether these quantities will be heaped up in the vicinity of the reflection wall and increase the hazardous intensity at local areas will be investigated.

The 3D wave pattern and flow field are induced by the coupled nonlinear effect, the dispersive effect and the 3D effect. The wave amplitude corresponds to the nonlinear effect; the wave slope corresponds to the dispersive effect; the incident wave angle corresponds to the 3D effect. The KP theory of the first-order accuracy models those effects with prescribed scaling relations. By comparison with the KP theory, these effects will be discussed.

In the rest of this chapter, all the length variables will be scaled by the undisturbed water depth h_S and time will be scaled by $h_S/c_{S0} \equiv h_S/\sqrt{gh_S}$, unless otherwise specified.

7.2 Set-ups

The incoming SSW has an amplitude of 0.376 and the characteristic wavelength of 2.186 (Fig. 7-1), which is modelled by the third-order solitary wave solution. The initial position of the crest line is at *x*=8. It guarantees that the wave amplitude at the offshore wall is precisely 0.367 when the wave impinges onto the reflection wall. The dimensions of the computational domain (*H* is the vertical length of the domain) are listed in Table 7-1 to resemble the wave tank by Li et al. (2011). With $a_i = 0.367$ and $\psi_i = \pi/6$ the interaction parameter given by Eq. (2.61) is $\kappa = 0.6354 < 1$. The boundary conditions at the side walls and bottom are "slip-walls" and the top boundary condition is that the "total pressure" equals 0.

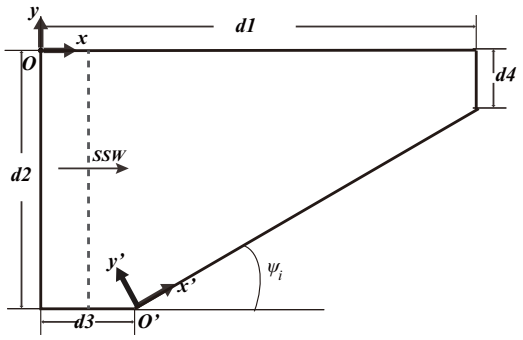

Fig. 7-1 The dimensions of the computational domain in the plan view. The initial wave crest line is drawn by the dashed line with an arrow indicating the propagation direction.

Table 7-1 The dimensions of the numerical wave tank

d1	*d2*	*d3*	*d4*	*H*	ψ_i
74.3333	43.8675	16	10.1887	2.1667	$\pi/6$

7.3 Convergence study

Owing to the limited computational resources, not many runs can be performed. The extensive 2D numerical experiments that have been shown in Chapter 6 can facilitate the initial guess of the cell size and time step. Nevertheless, two questions remain. One is that which appropriate resolution is needed to capture the highest stem wave. The other is that which resolution is appropriate in the transverse direction.

Since the smaller time step is safer considering stability and accuracy, the maximum Courant number *Co* is set to be 0.2 for all the runs. It is smaller than the *Co* used in the 2D simulations in Chapter 6 and is found to be sufficient. Consequently, the spatial resolutions will be focused on. According to the characteristics of the mesh (Fig. 5-4, Chapter 5), the cell to the origin *O'* is selected as a typical one for comparison. The sizes of the typical cell in different runs are listed in Table 7-2. In Run 5, the local refinement on the mesh is performed within a rectangular box with two vertices of (46.31, -10.67, 0) and (61.90, -43.87, 1.17) in the *O-xyz* coordinate system. The typical cell size in Table 7-2 for Run 5 is calculated by virtually applying the equivalent refinement method on the typical cell. In addition, the initial condition of Run 5 is mapped from Run 4 at t=33.885 when the main portion of the wave has already entered the refined area. In Run 6 the AMR technique is implemented, which refines the mesh dynamically near the free surface and the area where the *x*-component of the velocity, *i.e. u*, in a cell is larger than a threshold. u_{unit} in Eq. (5.15) is approximately 1.303. C_{amr1} is set to be 0.025. The maximum refinement level is 3. The refinement step is 1 time step. Viewing in a combination of the wave profile (Fig. 7-2) and the underneath velocity field (Fig. 7-3(a)), the

incident wave, the Mach stem wave and the reflected wave all induce positive u. However, due to the threshold value, only part of the reflected wave flow field is refined (Fig. 7-3(b)). Therefore, the feasibility of this AMR method has to be verified by the result on the fine static mesh.

Table 7-2 The meshes used in the convergence study

Run	Mesh type	Cell sizes of a typical cell $(\Delta x, \Delta y, \Delta z)$	The number of cells at the final time step
1	Static	(0.063, 0.021, 0.011)	28,072,000
2	Static	(0.063, 0.011, 0.011)	56,144,000
3	Static	(0.045, 0.021, 0.005)	71,610,000
4	Static	(0.045, 0.019, 0.0026)	135,625,000
5*	Static	(0.0081, 0.021, 0.005)	28,852,270
6*	Dynamic	(0.016, 0.018, 0.01)	21,698,633

*: Refined typical cell size by virtually using the refinement method on the initial mesh.

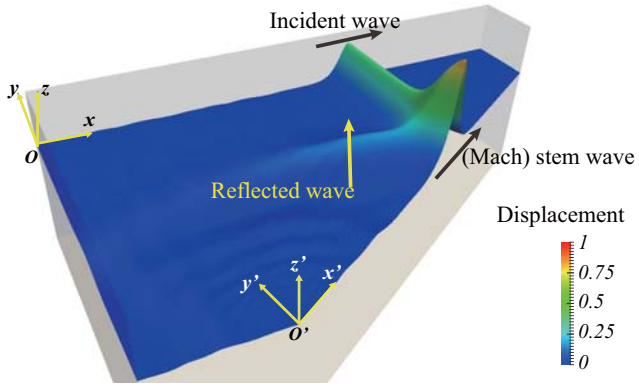

Fig. 7-2 The contour plot of the surface displacement at t=33.885. The vertical coordinate has been magnified by a factor of 16.

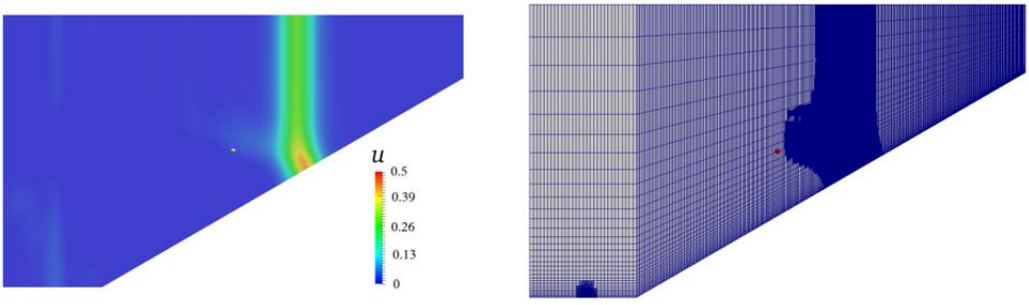

(a) **(b)**

Fig. 7-3 The contour plot of u on the cross section at z=-0.75 (a); The mesh at the cross section at z=-0.75 (b). t=33.885.

The computations have been carried out on the cluster Legion funded by University College London (UCL) for High Performance Computing (HPC). The processor quantities, consumed memories and execution times are listed in Table 7-3. The AMR method can reduce the processor quantity and the memory dramatically. In terms of the CPU time (number of processors X execution time), Run 4 with the finest static mesh consumed 105,216 hours, while Run 6 using dynamic mesh consumed 20,896 hours. Nevertheless, mesh manipulation, interpolation and loop for continuity correction for the AMR consume extra time. Particularly, loop for continuity correction consumes the majority of the extra execution time. An existing issue is that the execution time with the present AMR method cannot be further reduced by increasing processors. It has been found that only the present decomposition method for parallel computing shown in Fig. 5-8 is workable. Issues exist with other decomposition methods, *e.g.*, the calculation is not stable due to the communication problems between processors or the efficiency is not improved. A defect using the present decomposition method limits the maximum processors employed, for the processor number cannot exceed the transverse cell number of the initial mesh.

Table 7-3 Computation resource consumptions

Run	Processor quantity	Memory (GBs)	Execution time (Hours)
1	105	420	66
2	156	624	153
3	196	784	226
4	256	1024	411
5	128	512	90
6	32	128	653

Some parameters are to be introduced for the convergence study. Being similar to the 2D simulations, the maximum difference in terms of the wave profile between different runs occurs at the wave crest. Therefore, the wave crest trajectories on the offshore wall, *i.e.*, the *xz*-plane where y=0, and on the reflection wall, *i.e.* the *x'z'*-plane where y'=0, will be used to check the cell sizes in the *x*-direction and *z*-direction. The transverse length of the stem wave will be used to test the spatial convergence in terms of the cell size in the *y*-direction. The postprocessing method to obtain the transverse length of the stem wave is to be introduced as follows.

As introduced in Chapter 1, a notable feature of the Mach reflection is a growing stem wave which is perpendicular to the reflection wall. Whether this feature can be captured in the simulation should be examined first. The postprocessing for the stem wave is performed in the *O'-x'y'z'* coordinate system. The free surface is cut into discrete sections parallel to the *x'z'*-plane as shown in Fig. 7-4(a). On each section the point with the maximum elevation can be located. Then the locus of the maximum free surface elevations can be drawn passing through all the points. Taking some sampling points out of the locus and using linear fittings, the intersection point between the incident wave and the stem wave can be determined (Fig. 7-4(b)). It has been found that at any moment before wave breaking, the fitting crest line for the stem wave is always almost perpendicular to the reflection wall. Therefore, we can simply draw a perpendicular line from the crest point on the reflection wall where y'=0 to obtain the intersection point with the linear fitting crest line of the incident wave. It does not make much difference with the previous method. Actually, Li et al. (2011) also used the latter simple method. The transverse length of the stem wave can be then determined by the perpendicular distance between the intersection point and the reflection wall.

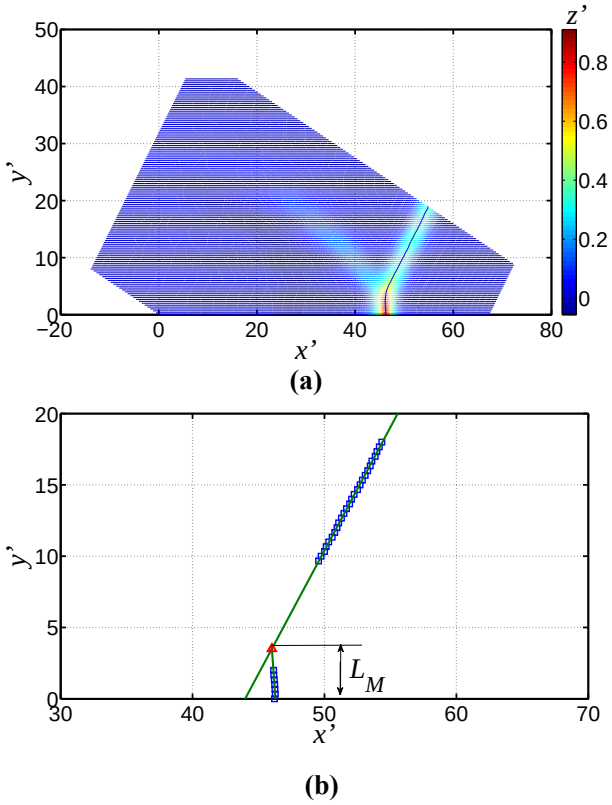

Fig. 7-4 (a): Cutting the fluid domain into sections to find the locus (blue solid line) of the maximum free surface elevations. The contour plot is coloured by the vertical displacement of the free surface. (b): Using linear fittings via the sampling points (□) to find the intersection point (△). Data are extracted from Run 6 and t=39.639.

The comparisons in terms of the wave crest trajectories on the offshore wall and the reflection wall and the transverse length of the stem wave given by all the runs are shown in Figs. 7-5(a)-(c). The wave crest trajectories on the offshore wall (Fig. 7-5(a)) show the spatial resolutions of all runs are sufficient for the simulation of the incident solitary wave. Small fluctuations of the trajectory given by Run 5 can be seen, for the cells in the vicinity of the offshore wall are not refined. In each run, the stem wave amplitude at the reflection wall grows monotonously to a maximum value accompanied with a smooth wave profile. Then the wave breaks at the reflection wall which results in a decrease of the wave amplitude at the reflection wall. In Fig. 7-5(b) good convergence is shown as the amplitude of the stem wave grows up to 0.84. When the wave breaks, the simulated results do not converge anymore. It suggests

that the present methodology is incapable of studying the phenomenon after the wave breaks. Nevertheless, with higher longitudinal resolution as in Run 5 and 6, the wave breaking can be postponed and the maximum wave height reaches 0.910 as observed by Li et al. (2011). Fig. 7-5(c) shows that the cell size in the *y*-direction used by Run 6 is also appropriate, for L_M given by Run 6 coincides with that of Run 2 as well as other runs. According to the comparisons, the cell sizes used in Run 6 are appropriate to model the nonbreaking wave. The AMR technique gives sufficient accuracy. The result of Run 6 will be used in the following analyses for it has the high local resolution and the small amount of cells.

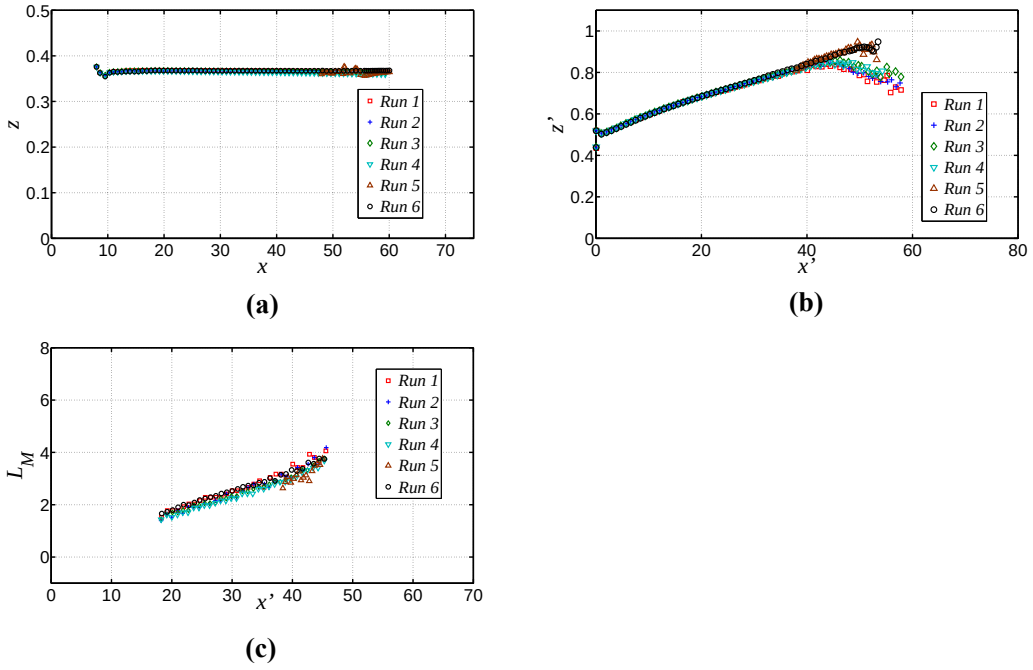

Fig. 7-5 The wave crest trajectory at the offshore wall (a), the wave crest trajectory at the reflection wall (b) and the transverse length of the stem wave versus the *x*'-coordinates of the crest at that moment (c) for spatial convergence study.

7.4 Results and discussions

7.4.1 Wave profiles at the offshore wall

The time series of the wave profile at the offshore wall is plotted in Fig. 7-6(a). The wave maintains an approximately unchanged form and travels at an approximately constant speed. In Fig. 7-6(b), the wave profile is compared with the analytical solution of an SSW. The initial phases of the analytical solutions are the same as that of the incoming SSW. The comparison shows good agreement between the simulated result and the third-order solution in terms of both the wave form and the wave speed. The simulated wave profile is also well predicted by the first-order solution, but the wave speed of the first-order solution is slightly faster than the simulated result reflected in the subtle phase shift. It suggests that the nonlinearity is still weak, and the first-order approximation is sufficiently accurate at the offshore wall. In addition, the influence of the reflection wall on the global wave pattern is negligible.

The amplitudes of the incident wave in both experiment and the fully nonlinear numerical simulation decay slowly, though they are due to different reasons. Li et al. (2011) quantify the attenuation by the exponential fitting of the wave crest trajectory. The averaged e-folding distance in their experiment was 925 (or the exponential decay rate 0.00108) and the dimensions of the tank were 121.67*60 (*d1*d2*). In the present simulation, the e-folding distance is $1.24*10^{5}$ (or the exponential decay rate $8.061*10^{-6}$). No matter it is an experiment or a simulation, the incident wave can be deemed as a solitary wave as long as the e-folding distance of the crest trajectory is much larger than the longitudinal dimension of the experiment apparatus or the computational domain.

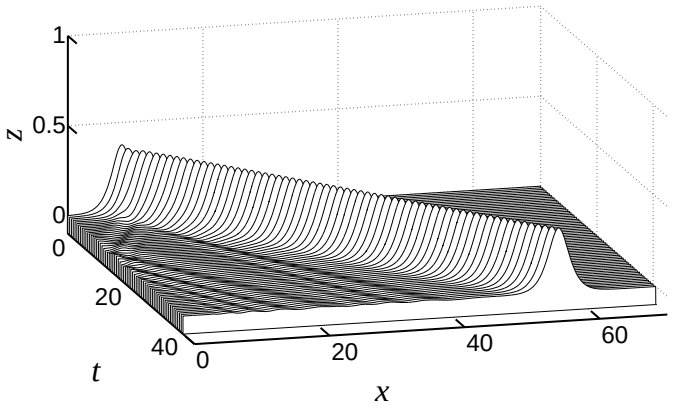

(a)

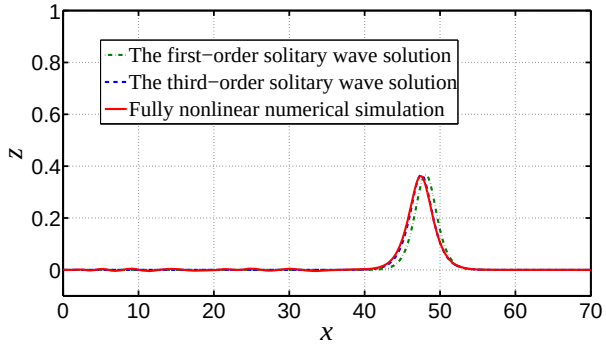

(b)

Fig. 7-6 (a): The wave profiles at the offshore wall at different times. It starts from *t*=0, and the time step between adjacent profiles is 0.6393; (b): Comparison of the simulated wave profile at the offshore wall at t= 33.885 with the first-order and third-order analytical solutions.

7.4.2 Wave profiles at the reflection wall

The wave profiles at different times at the reflection wall are shown in Fig. 7-7(a). After the peak of the incoming wave has impinged on the wall, the wave profile almost maintains its form, but its amplitude increases approximately linearly with the *x*'-coordinate of the crest. A typical wave profile is compared with the analytical solution from the KP theory in Fig. 7-7(b). Due to $\kappa < 1$, the wave interaction process is in the Mach reflection regime, which corresponds to the (3142)-type solution of the KP equation. The initial condition for the (3142)-type solution (Chakravarty and Kodama, 2009) is of an X-shape, and the intersection point of crest lines of the multiple solitons is set to be at *O*'. A problem is that the starting time

used in the analytical solution is not the same as that in the simulation. Instead of using the time, we can use the *x'*-coordinate of wave crest at the reflection wall to tag the wave parameter at that moment like in Figs. 7-5(c) and 7-8 to 7-11. In Fig. 7-7(b), to compare the wave profile, the *x'*-coordinates of wave crest given by the (3142)-type solution and the simulation are identical but the times are different. The first-order and third-order SSW solutions are also drawn with the same amplitude and crest position. Comparing with the symmetric wave profiles given by the analytical solution of the KP equation, it is easy to tell the simulated wave form is asymmetric. On the forward side in the propagation direction, the simulated wave profile and the (3142)-type solution almost coincide with each other. But on the backward side, the simulated wave profile is not as steep as predicted by the (3142)-type solution. In addition, the wave profile at the reflection wall is different from that of a solitary wave. Li et al. (2011) also found the wave profile given by the KdV soliton solution is steeper than the measurement. The trailing wave train led by a flat depression was also observed by Li et al. (2011).

The characteristic wavelength can be used to estimate the dispersive effect of the wave in the longitudinal direction. Shorter characteristic wavelength corresponds to the stronger dispersive effect. Taking into account the asymmetry of the numerical result, the lower limit of integral in Eq. (2.8) can be extended to $-\infty$. It is simply marked as $2\lambda_{Sc}$. The comparison in terms of $2\lambda_{Sc}$ at different moments between the numerical simulation and the KP theory is shown in Fig. 7-8. The simulated stem wave is much wider than the prediction given by the KP theory.

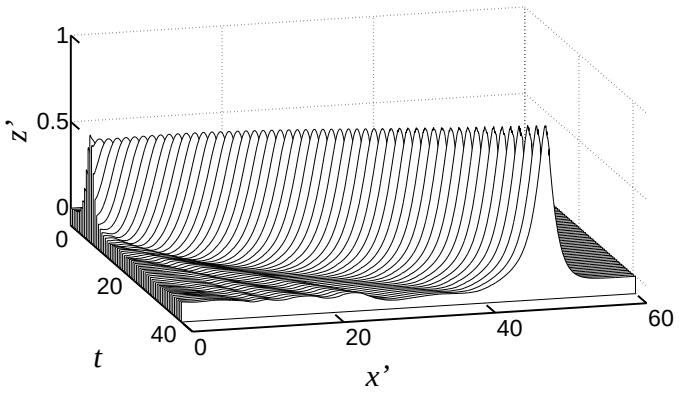

(a)

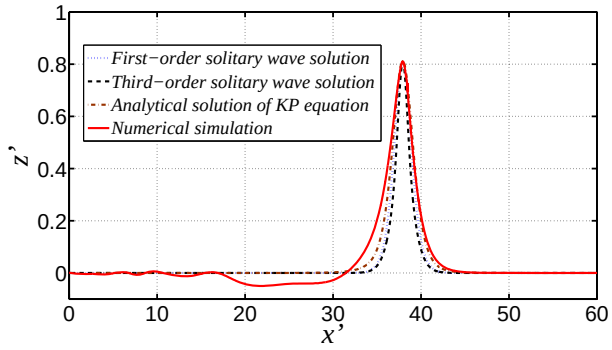

(b)

Fig. 7-7 (a): The wave profiles at the reflection wall at different times. It starts from *t*=0, and the time step between adjacent profiles is 0.6393; (b): The simulated wave profile at the reflection wall at *t*=33.885 and analytical solutions (N.B. time is different).

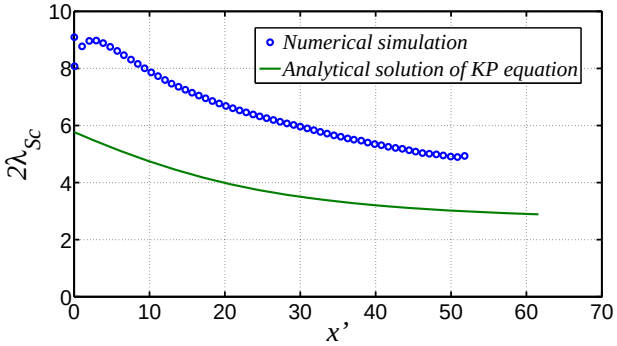

Fig. 7-8 Two-fold characteristic wavelength of the stem wave at the reflection wall versus the *x*'-coordinates of the crest at that moment.

The crest trajectories of the stem wave given by the present simulation, the experimental measurement and solutions of the KP equation are plotted in Fig. 7-9. The simulated result agrees well with the experimental measurement as the wave

propagates. The asymptotic line is based on the theory proposed by Miles (1977) (Eq. 2.57). It can be seen that the asymptotic theory is incapable of depicting the development of the stem wave. Li et al. (2011) solved the V-shape initial value problem of the KP equation numerically. Both of the numerical solution and the analytical solution of the KP equation give quite good predictions to the stem wave amplitude until wave breaks, despite different initial conditions. It suggests that the first-order approximation in terms of the nonlinearity is still predominant. The higher-order approximation may better depict the wave profile as suggested in Fig. 7-8.

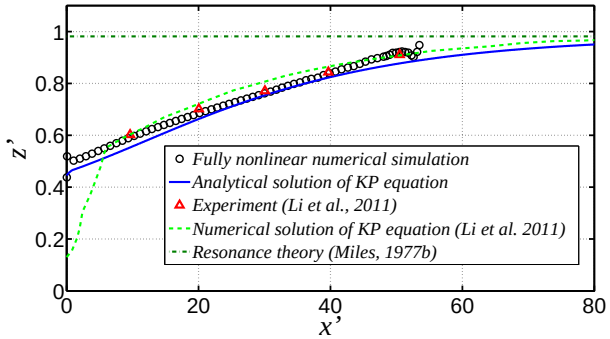

Fig. 7-9 The crest trajectory of the stem wave at the reflection wall.

The largest possible wave induced by the wave interaction is always an interesting problem and of practical significance. Li et al. (2011) also did experiments for $a_i = 0.351$ and $a_i = 0.359$ with the same incident wave angle $\psi_i = \pi/6$. Overall, the wave height at the reflection wall can grow to 0.88 to 0.910, and then the wave breaks. Therefore, the simulated case is representative for the study of the largest possible nonbreaking wave. Tanaka (1993) also simulated a case with $a_i = 0.3$ and $\psi_i = 35°$ via the high-order spectral method. The maximum run-up at the wall exceeded the maximum possible amplitude of an SSW. The truncation error of the calculation can be estimated by the formula $O(\varepsilon^{1.5M})$, where $M = 3$ (or 4) is

the truncation order. The maximum run-up at the wall was given by 0.869 when $M=3$ and 0.905 when $M=4$. However, the error could be up to 62.24% when $M=3$ and 53.14% when $M=4$. Therefore, Tanaka's (1993) result for highest possible stem wave was not very accurate. As to the present simulation, the maximum run-up at the reflection wall can reach 0.910 and the error can be controlled within 10% from the convergence study. The developing process and the breaking mechanism of this large stem wave will be discussed later.

7.4.3 Transverse length of the stem wave

From Fig. 7-2, it can be seen that the stem wave has a 3D shape in this developing stage. Nevertheless, using the proposed method to determine the transverse length of the stem wave is still meaningful to estimate the influence extent of the stem wave in the transverse direction. In Fig. 7-10, the transverse length of the stem wave grows linearly with the *x'*-coordinate of the crest at the reflection wall as it moves along the reflection wall. This growth process starts as soon as the peak of the incoming wave impinges onto the reflection wall. Recalling Fig. 7-9, during this simulated duration, both of the wave amplitude and the transverse length of the stem wave are increasing. Hence, the energy transfer as well as other physical quantities from the incident wave to the stem wave is complex, and will be analysed later.

As shown Fig. 7-10, the simulated result agrees well with the experiment. The analytical solution of the KP equation also gives a good prediction. Nevertheless, the simulated result almost coincides with the prediction given by the KP theory, but deviates from the experimental result slightly. It suggests that the mathematical model could be improved by taking into account other physical factors.

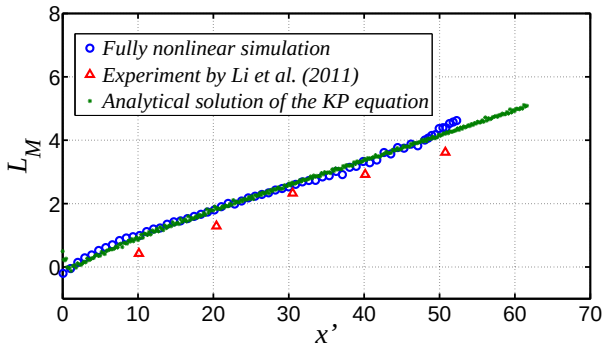

Fig. 7-10 The transverse length of the stem wave versus the *x*'-coordinates of the crest at that moment.

The linear growth of the transverse length of the stem wave is due to the difference between the incident wave speed c_i and the stem wave speed c_M. One advantage of the numerical simulation over the experiment is that the detailed flow field data can be stored in an intensive time sequence. The midpoint rule is used to approximately calculate the stem wave speed at the reflection wall (Fig. 7-11). The stem wave speed is approximately constant, which is independent of its amplitude. The mean value of c_M in Fig. 7-11, is about 1.420. c_i is 1.166. Since $c_M \cos\psi_i \approx 1.230 > c_i$, riding on the stem wave crest, one can see that the intersection point between the incident wave and the stem wave is moving off with a constant speed.

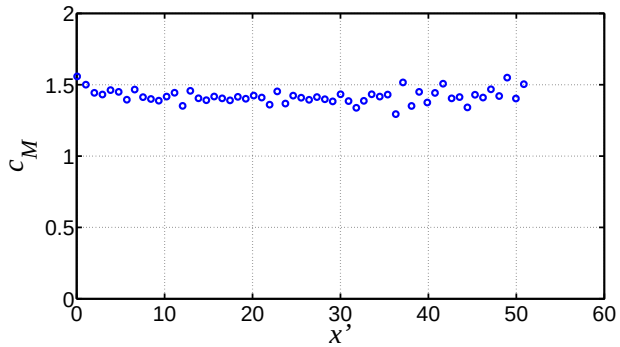

Fig. 7-11 The stem wave speed versus the *x*'-coordinates of the crest at that moment.

7.4.4 The reflected wave

From the 3D view of the wave profile at t=39.639 (Fig. 7-12(a)), except the quasi-2D incident solitary wave and the large stem wave, we can also distinguish a reflected wave with a single peak at its cross section stretching out from the interaction area. Using the same method as that in Fig. 7-4(a), the crest line of the reflected wave can be extracted. The projection of the reflected wave crest line onto the $y'z'$-plane is plotted in Fig. 7-12(b). Li et al. (2011) did not unambiguously state their sampling position for the reflected wave amplitude. Nevertheless, according to their sampling range and the context, the reflected wave amplitude $a_r = 0.164$ given by Li et al. (2011) should be taken at y'=12.5, which fits the simulated result well. The reflected wave angle ψ_r read from the projection of the crest line on the $x'y'$-plane is approximately 0.809, which is smaller than ψ_i. For reference, the reflected wave amplitude and angle given by the KP theory are $a_r = 0.148$ and $\psi_r = 0.738$, respectively.

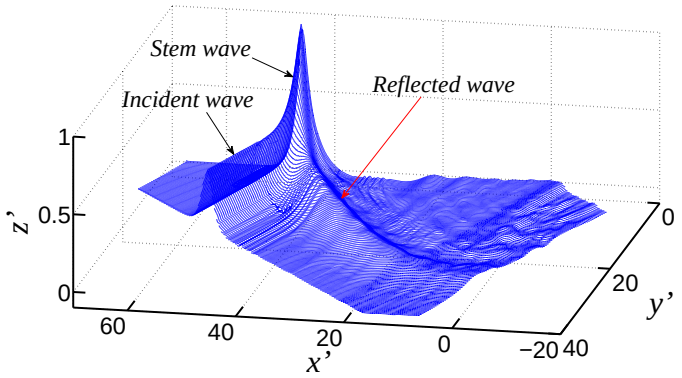

(a)

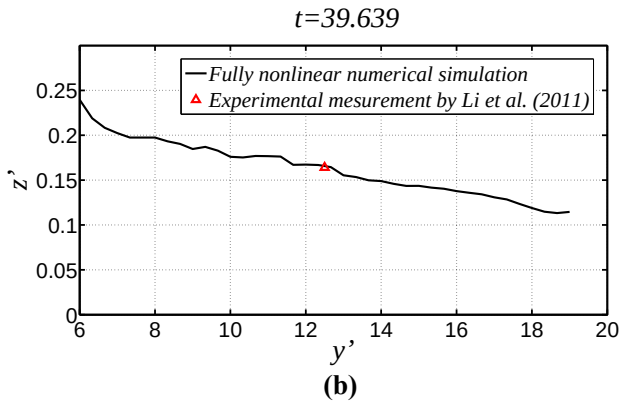

(b)

Fig. 7-12 (a): 3D view of the wave profile at *t*=39.639; (b) The projection of the reflected wave crest line onto the *y'z'*-plane at *t*=39.639 and the experimental measurement.

7.4.5 Velocity fields

The velocity fields at the reflection wall at different moments are shown in Figs. 7-13(a)-(c). When the stem wave amplitude is not large (Fig. 7-13(a)), the velocity field is similar to that of an SSW (Fig. 5-6(a)). The horizontal velocity (u') is predominant and approximately uniform over a water column. u' decreases as the free surface displacement decreases. The vertical velocity (v') is seemingly anti-symmetric about the vertical plane passing through the crest. As the stem wave amplitude grows (Figs. 7-13(b)-(c)), the magnitude of the horizontal velocity increases, as well as the vertical velocity. In addition, an obvious variation of u' in a water column can be seen from Figs. 7-13(b)-(c). Fig. 7-14 is composed of the wave profiles at different moments at the reflection wall and the instantaneous velocity in the water column right beneath the wave crest at that moment. Notice that the phase speed of the stem wave is nearly constant (Fig. 7-11), which is approximately 1.4. But the horizontal fluid velocity is increasing with time. From Fig. 7-16, the maximum horizontal fluid velocity at the crest reaches approximately 1.3 prior to the wave breaking at $x' \approx 50$. Li et al. (2011) observed the overturning wave and the wave amplitude decreased after breaking. Both the experimental observation

and the present simulated result suggest that the horizontal velocity of the fluid particle at the crest will eventually catch up with the stem wave phase speed, and results in the wave breaking. That satisfies the kinematic wave breaking criterion. Let us look into the wave profile at t=39.639 of the approximately largest nonbreaking wave amplitude in Fig. 7-15. From the outskirt to the crest, the free surface first becomes steeper, and then gets gentler. The profile is convex in the vicinity of the crest, and no cusp appears. In Fig. 7-15, we take several points on the wave profile and use the linear fittings to approximate the maximum slopes on both sides. According to the slope angles, the inner angle of the wave profile at the crest is larger than 120°. The 2D symmetric wave profile has a cusp shape with an inner angle of 120° when the particle velocity at the crest catches up with the wave phase speed (Stokes, 1880). The 2D asymmetric nonbreaking wave can contain more energy than that of the maximum possible solitary wave and evolve into a plunging breaker (Longuet-Higgins and Fenton, 1974).

The statistical data are shown in Fig. 7-16, the depth-mean horizontal fluid velocity at the crest of the stem wave is much larger than that induced by the incoming solitary wave. The KP theory predicts that the horizontal fluid velocity u' at the stem wave crest can become approximately 2.67 times of the horizontal velocity at the incoming wave crest. According to the simulated result, the depth-mean horizontal fluid velocity at the stem wave crest reaches only approximately 2 times of that at the incoming wave crest before the stem wave breaks, but the maximum horizontal fluid velocity in the stem wave can be larger than 3 times of that at the incoming wave crest.

The practical concern of the study is the threats to the lives and structures posed by the nonlinear wave motion. The stem wave appearing in the Mach reflection may cause more severe damages than the incoming SSW. The high wave amplitude of the stem wave suggests a large hydrostatic pressure. The large fluid velocity within the stem wave suggests the large pressure at the stagnation point on the upstream face of the structure. As mentioned, the breaking of the stem wave is likely to be a "plunging" type rather than a "spilling" type. The plunging breaker steepens the forward face and then throws the crest into the forward face violently. If the breaking stem wave encounters the structure in its path, it may lead to a large impact force of short duration at a local area (Goda et al., 1966). We may further consider the dimension of the structure. Suppose the structure has very large horizontal dimension, *e.g.*, a dyke or the flood protection embankment, and is placed with an oblique angle relative to the propagation direction of an SSW, like the reflection wall in the simulation. It not only bears large wave loads itself, but also can change the wave field via the nonlinear wave interaction and influence other areas through the large and elongating stem wave. When the dimension of the structure is comparable to the characteristic wavelength, the wave diffraction has to be taken into account. From the fully nonlinear simulation of the interaction between an SSW and a vertical and truncated cylinder, Zhou et al. (2016) have found that the horizontal force, vertical force and moment on the cylinder all increase with the wave amplitude. The stem wave has similar properties to the SSW and could exert a large hydrodynamic force on the cylinder. Zhou et al. (2016) also observed the persistent oscillation of the freely floating cylinder after the SSW has moved away. That is related to the ringing behaviour which threats the oil platform. The same phenomenon is likely to happen when a stem wave passes the floating structure and more research is badly needed. If

the horizontal dimension of a structure is small relative to the characteristic wavelength, *e.g.*, the leg of a jack-up platform, the horizontal hydrodynamic force on the vertical structure can be estimated by the Morison equation (Morison et al., 1950). Two major components of the hydrodynamic force, *i.e.*, the inertial force and the drag force, per a unit length can be obtained. The inertial force is related to the fluid acceleration, which cannot be straightforwardly found in the velocity field figures at given *t*. The magnitude of the drag force is proportional to u'^2, assuming that the drag coefficient C_D is constant. Hence, the drag force on the structure would increase with the stem wave amplitude due to the corresponding fluid velocity (Fig. 7-14) and it would be much larger in the stem wave field than that in the incoming solitary wave field (Fig. 7-16). It should be noted that the Morison equation implies the 2D flow field assumption. The assumption of the Morison equation holds when the stem wave amplitude (a_M) is not very large for u' is approximately constant along the depth (Fig. 7-14). However, the present result shows a large variation of u' with *z'* when a_M is large (Fig. 7-14). The large $|u'_{z'}|$, where the subscript indicates the differentiation with respect to z', indicates a strong shear flow. It may lead to the complex 3D flow field due to the fluid-structure interaction and a quite different C_D from that in a 2D flow (Liu, 1996).

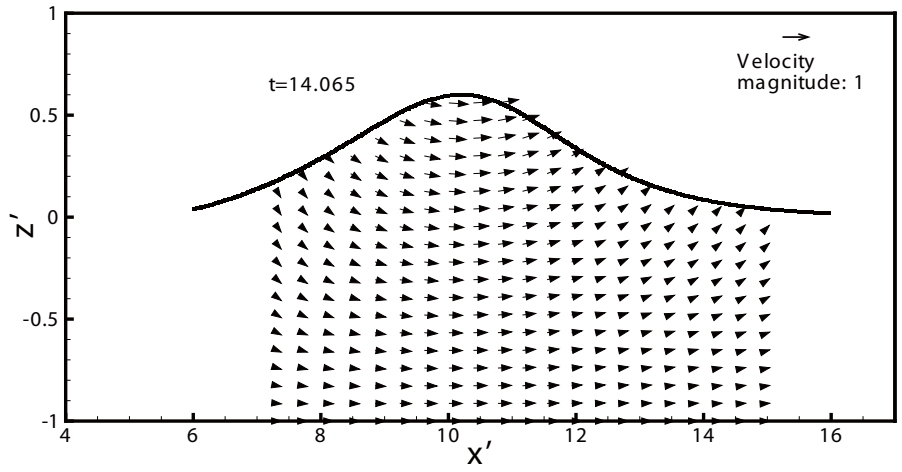

(a)

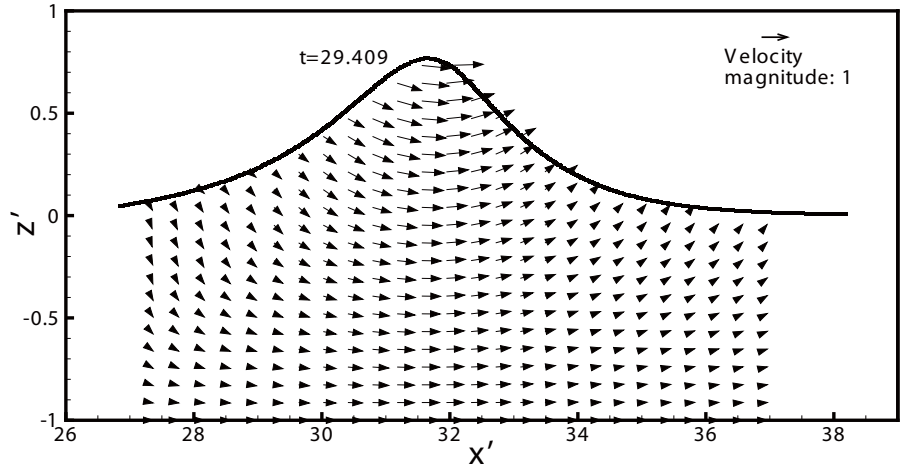

(b)

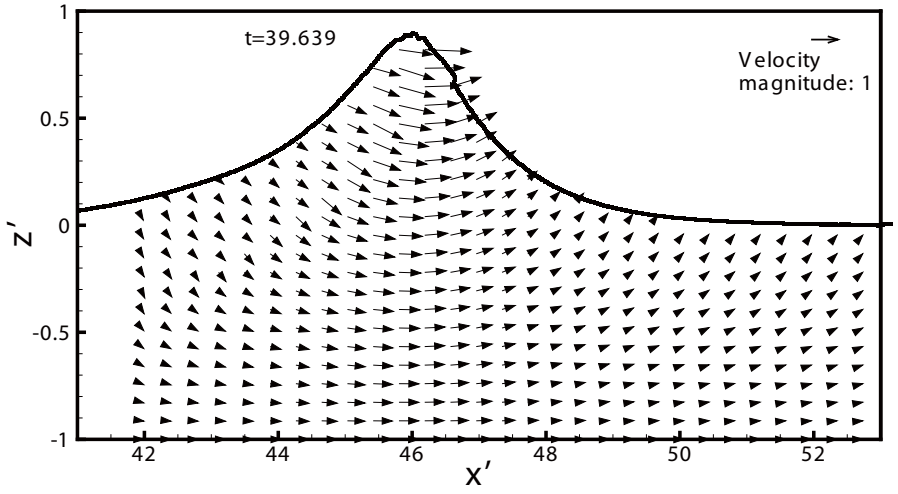

(c)

Fig. 7-13 The velocity fields at the reflection wall at t=14.065 (a), t=29.409 (b) and t=39.639 (c). The arrow which is anchored at the end point indicates the velocity magnitude and the direction.

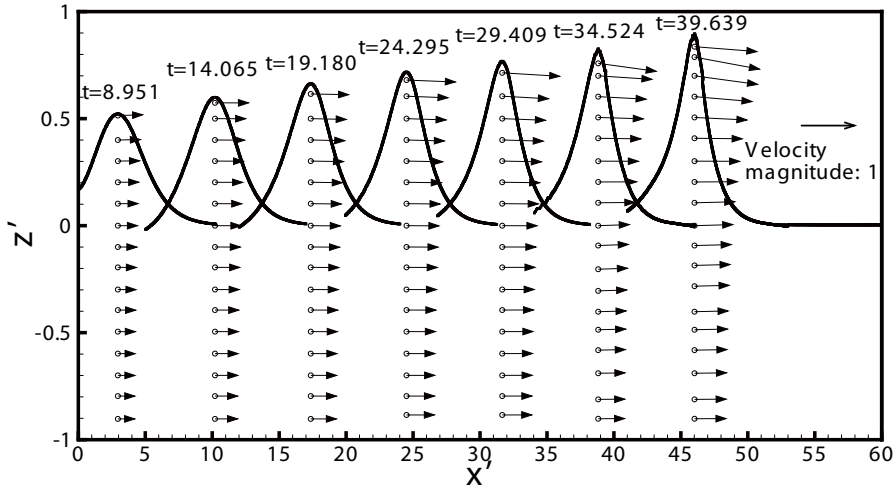

Fig. 7-14 Partial wave profiles at the reflection wall at different moments together with the velocity vectors in the water column beneath the crests.

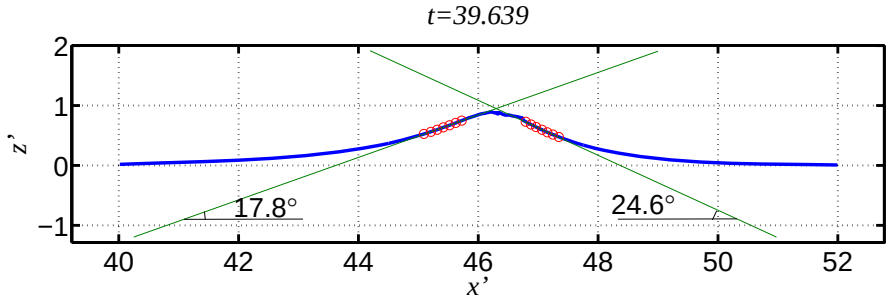

Fig. 7-15 Using linear fittings to approximate the maximum slope angles at both sides of the crest. The sampling points on the stem wave profile at t=39.639 are indicated by the red circles. The green lines are the linearly fitted lines based on the sampling points.

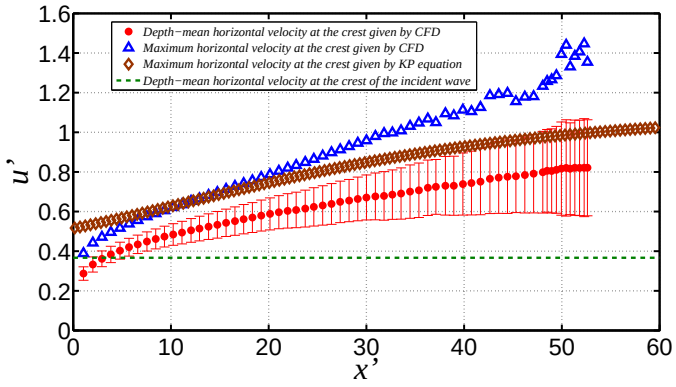

Fig. 7-16 Statistical data of the horizontal velocity in the water column beneath the crests of the stem waves at different moments and the depth-mean horizontal velocity given by the KP theory. The abscissa is the *x*'-coordinates of the stem wave crests at different moments. The error bar

indicates the standard deviation of the horizontal velocity in that water column. The depth-mean horizontal velocity at the crest of the incoming wave is also plotted for reference.

7.4.6 Transverse transfers of the mass, momentum and energy

As introduced, when a single solitary wave is propagating on an unbounded body of water, there is no mass, momentum and energy transfers in its transverse direction. Hence, it can be studied in the 2D space. In the presence of an oblique reflection wall, it seems that the water heaps up in the vicinity of the reflection wall according to the variation of the wave profile. It is obviously due to the blockage of the reflection wall, which poses the 3D effect or three-dimensionality on the wave field. From the interaction parameter, *i.e.*, κ, it can be seen that the nonlinear effect and the 3D effect together rule the interaction pattern. In this section, we will analyse the variation in the transverse direction. Specifically, we are interested in how the physical quantities coming from the incident wave is transmitted outwards from the reflection wall. In order to study the transverse transfers, we can divide the whole domain into separate control volumes. The control volumes are partitioned as follows: First, two basic control volumes are introduced. One is selected as a thin slice of the fluid from bottom to the free surface adjacent to the offshore wall, which is denoted by Ω (Fig. 7-17), and the other is selected as a thin slice of the fluid from bottom to the free surface adjacent to the reflection wall, which is denoted by Ω' (Fig. 7-17). Ω' can be translated in the *y'*-direction with an offset value (Fig. 7-18). The quantities in those different control volumes that are parallel to the *x'z'*-plane are marked by the offset value denoted by y'_{offset}, which is zero for Ω'. The thickness of the slices is 0.1, taking into account the spatial discretisation in the simulation. The variable without a prime is used to denote a quantity about Ω, which is in the *O-xyz* coordinate system, and the variable with a prime is used to denote a quantity in Ω'

or in a control volume that is parallel to the *x'z'*-plane, which is in the *O-x'y'z'* coordinate system. The physical quantities will be defined in dimensional forms to express their physical meanings. But their units will be eliminated by the normalisation in the analysis. We can define the excess mass in the domain which has exceeded that in the calm water, or

$$M = \rho \iint \theta dxdy, \quad M' = \rho \iint \theta dx'dy', \tag{7.1}$$

where $\iint$ means integration over the bottom area of the control volumes. For the total momentum in the *x*-direction or *x'*-direction

$$I_x = \rho \int_\Omega u d\Omega, \quad I'_{x'} = \rho \int_{\Omega'} u' d\Omega', \tag{7.2}$$

where *u* is a velocity component of $\mathbf{u} = (u, v, w)$ and *u'* is a velocity component of $\mathbf{u}' = (u', v', w')$, and $\int_\Omega$ or $\int_{\Omega'}$ means integration over the control volume. For the total momentum in the *z*-direction or *z'*-direction

$$I_z = \rho \int_\Omega w d\Omega, \quad I'_{z'} = \rho \int_{\Omega'} w' d\Omega'. \tag{7.3}$$

For the kinetic energy

$$E_K = \frac{1}{2} \rho \int_\Omega |\mathbf{u}|^2 \, d\Omega, \quad E'_K = \frac{1}{2} \rho \int_{\Omega'} |\mathbf{u}'|^2 \, d\Omega'. \tag{7.4}$$

For the potential energy

$$E_P = \frac{1}{2} \rho g \iint \theta^2 dxdy, \quad E'_P = \frac{1}{2} \rho g \iint \theta^2 dx'dy'. \tag{7.5}$$

For the total energy

$$E = E_K + E_P, \quad E' = E'_K + E'_P. \tag{7.6}$$

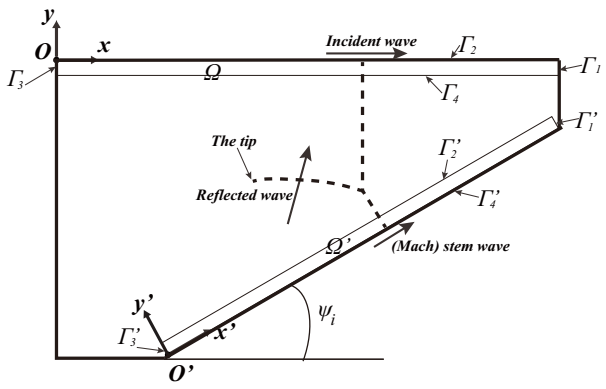

Fig. 7-17 Plan view of the partition of the two basic control volumes. The wave crest lines are sketched by the dashed lines. The control volumes are outlined by the thin lines.

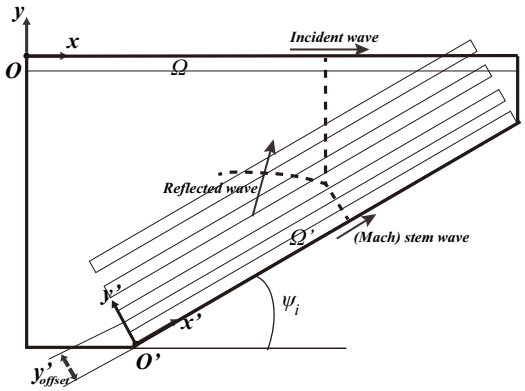

Fig. 7-18 Sketch for obtaining the control volumes parallel to the reflection wall by translating Ω' along *y'*-axis with an offset value y'_{offset}.

The mass, momentum and energy in the control volumes can exchange with its surroundings via the control surfaces (Fig. 7-17). Taking the control volume Ω' as an example, the integral form of the mass and momentum conservation equations (in dimensional form) over the control volume in the Eulerian frame can be written as

$$\frac{\partial}{\partial t}\int_{\Omega'} d\Omega' + \oint_{\Gamma'} (\mathbf{u}' \cdot \mathbf{n})\, d\Gamma' = 0, \tag{7.7}$$

$$\rho \frac{\partial}{\partial t}\int_{\Omega'} \mathbf{u}' d\Omega' + \rho \oint_{\Gamma'} \mathbf{u}' (\mathbf{u}' \cdot \mathbf{n})\, d\Gamma' = \rho \int_{\Omega'} \mathbf{f} d\Omega' + \oint_{\Gamma'} \mathbf{p} \cdot \mathbf{n} d\Gamma'. \tag{7.8}$$

where $\rho\mathbf{f}$ is the body force that is only composed of gravity, $\mathbf{p}\cdot\mathbf{n}$ is the normal pressure on the control face, Γ' is the boundary of Ω' and $\mathbf{n}$ is its normal vector pointing outward. Let us consider the momentum in the *x'*-direction through Eq.

(7.8). The normal pressure components at the control faces Γ_2' and Γ_4' have no contributions to $I_{x'}'$. The water at Γ_1' is approximately undisturbed and the pressure is hydrostatic. The flux through Γ_3' may vary with time. The time history of surface displacement at *O'* is shown in Fig. 7-19. After $t \approx 15$, when the wave has totally impinged onto the reflection wall, the free surface is approximately calm at Γ_3' and the pressure is approximately hydrostatic. After the incipient impingement, the momentum flux through Γ_2', which indicates the transverse transfer within the wave field, would be predominant. It results in the change of the momentum in the control volume. The same argument applies to the mass and energy.

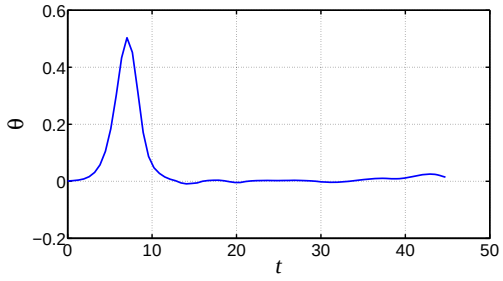

Fig. 7-19: The wave elevation versus time at *O'*.

The offshore wall does not have transverse influence on the 2D incoming solitary wave. Figs. 7-20(a)-(e) show the time histories of the physical quantities in Ω. The initial physical quantities in Ω will be used as references for normalisation. The superscript (0) is used to denote the integral value at the initial time. M is normalised by $M^{(0)}$. I_x and I_z are normalised by $I_x^{(0)}$. E_K and E_P are normalised by $E_k^{(0)}$. Firstly, we can use some known properties of an SSW to check the credibility of the simulation. The symmetric profile of an SSW gives anti-symmetric vertical velocity field about the vertical plane passing the crest (Longuet-Higgins and Fenton, 1974). It yields $I_z = 0$. It is the case in Fig. 7-20(c).

The potential energy of a solitary wave should be approximately equal to its kinetic energy (Longuet-Higgins, 1974). Figs. 7-20(d) & (e) show that the simulated results satisfy that relation. The physical quantities in Figs. 7-20(a)-(e) stay almost unchanged for a long period, for the offshore wall does not have significant influence on the 3D wave interaction pattern during that period. As the reflected wave elongates, its tip as marked in Fig. 7-17 will eventually encounter the offshore wall. It is reflected in the uptrends of the lines in Figs. 7-20(a)-(e) near the end.

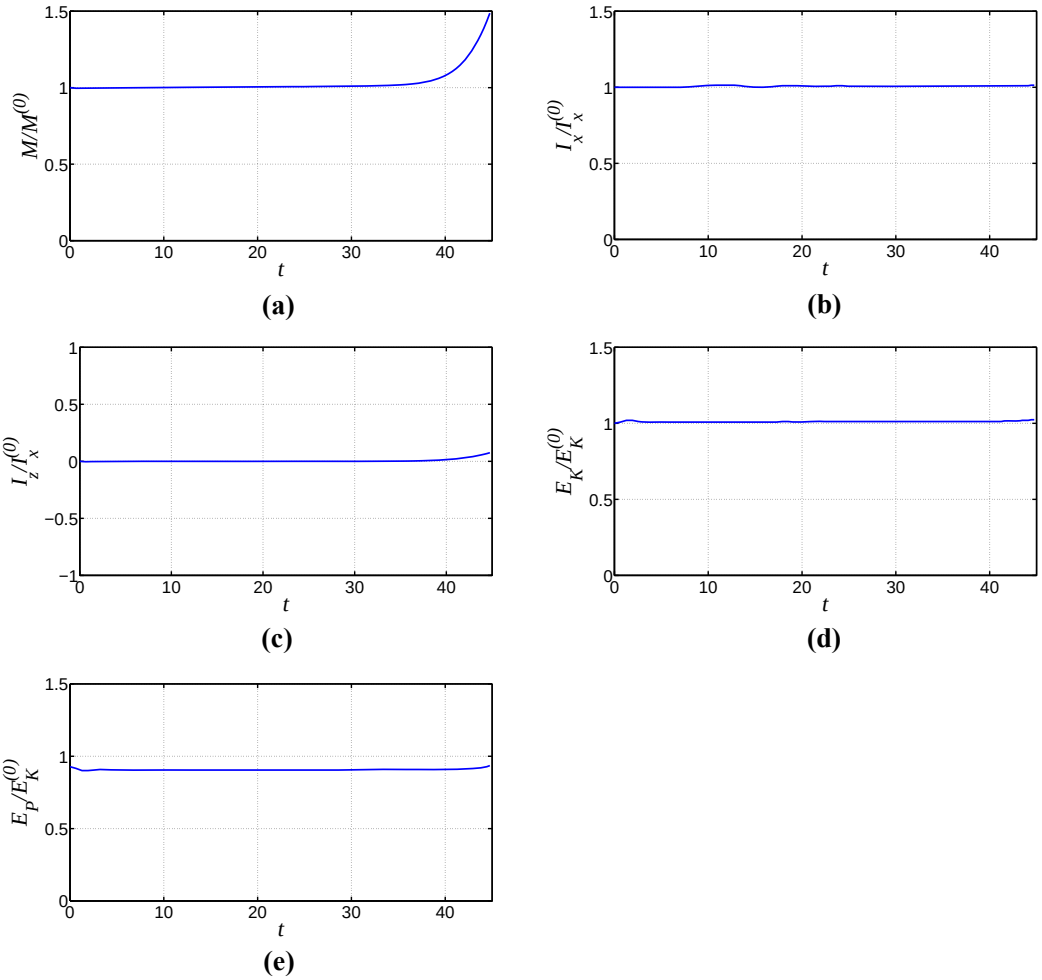

Fig. 7-20 (a): M in Ω, which is normalised by its initial value, versus time. (b): I_x in Ω, which is normalised by its initial value, versus time. (c): I_z in Ω, which is normalised by $I_x^{(0)}$, versus time. (d): E_K in Ω, which is normalised by its initial value, versus time. (e): E_P in Ω, which is normalised by $E_K^{(0)}$, versus time.

The hypothesis on the transverse transfers of the physical quantities will be presented based on the KP theory. Then it will be compared with the simulated result. As mentioned, the (3142)-type solution of the KP equation corresponds to the Mach reflection scenario (Fig. 7-21(a)), while the O-type solution corresponds to the regular reflection scenario (Fig. 7-21(b)). The fully developed reflected waves are known *a priori* to obtain the analytical solutions. When watching the wave in a moving system with $u' = c_i \sec\psi_i$, where c_i is the phase speed of the incident wave, the wave profile given by the (3142)-type solution changes with time, while the wave profile given by the O-type solution is steady. To investigate the transverse transfers, the wave profiles are cut into cross sections, which are parallel to the *x'z'*-plane. The momentum at a section can be estimated via the wave profile. The KP theory is based on the following assumptions: (1) the characteristic wavelength in the longitudinal direction (*x'*-axis) is long relative to the water depth; (2) the wave amplitude is small relative to the water depth; (3) the scale of variation in the transverse direction (*y'*-axis) is long relative to the characteristic wavelength in the longitudinal direction. It then implies $|v'|$ and $|w'|$ are much smaller than $|u'|$. The leading order approximation of the momentum (in dimensional form) in the *x'*-direction at a section can be written as $\rho c_{S0}\int_{-\infty}^{+\infty}\theta dx'$, where $c_{S0} = \sqrt{gh_S}$. For comparison with the simulated result, it is multiplied by the thickness $0.1h_S$ and used to approximate the momentum in a slice that is parallel to the *x'z'*-plane. Therefore,

$$I'_{x'} \approx 0.1h_S\rho c_{S0}\cdot\int_{-\infty}^{+\infty}\theta dx'. \tag{7.9}$$

The excess mass M' and the potential energy E'_P can be obtained similarly by

$$M' \approx 0.1h_S\rho\cdot\int_{-\infty}^{+\infty}\theta dx', \tag{7.10}$$

$$E_P' \approx 0.1 h_S \cdot \frac{1}{2} \rho \cdot \int_{-\infty}^{+\infty} \theta^2 dx', \tag{7.11}$$

, respectively. They will also be normalised by the corresponding initial quantities in Ω.

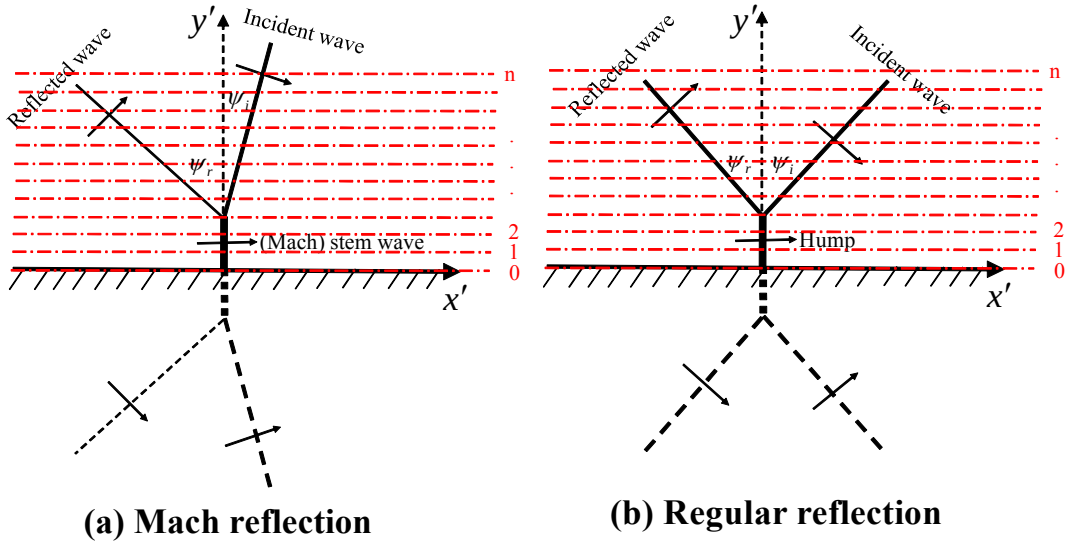

(a) Mach reflection **(b) Regular reflection**

Fig. 7-21 Sketches of the cross sections for the (3142)-type solution (a) and the O-type solution (b) of the KP equation.

a_i and ψ_i can determine a specific (3142)-type solution, which are 0.367 and $\pi/6$, respectively. Figs. 7-22(a)-(c) show variations of M', $I_{x'}'$ and E_P' with space and time. From $t = 0$ to $t \approx 50$, it is roughly equivalent to the simulated duration after the peak of the incoming solitary wave encountered the corner.

According to Miles' theory, it is possible that the wave amplitude at the reflection wall in a regular reflection is equal to the asymptotic stem wave amplitude in the above case (Fig. 2-5). If a_i remains the same, ψ_i in the regular reflection regime should be 0.7321 to meet that requirement. Since the wave field given by the O-type solution is steady in the moving system, M', $I_{x'}'$ and E_P' are plotted only versus y'_{offset} in Figs. 7-22(d)-(f).

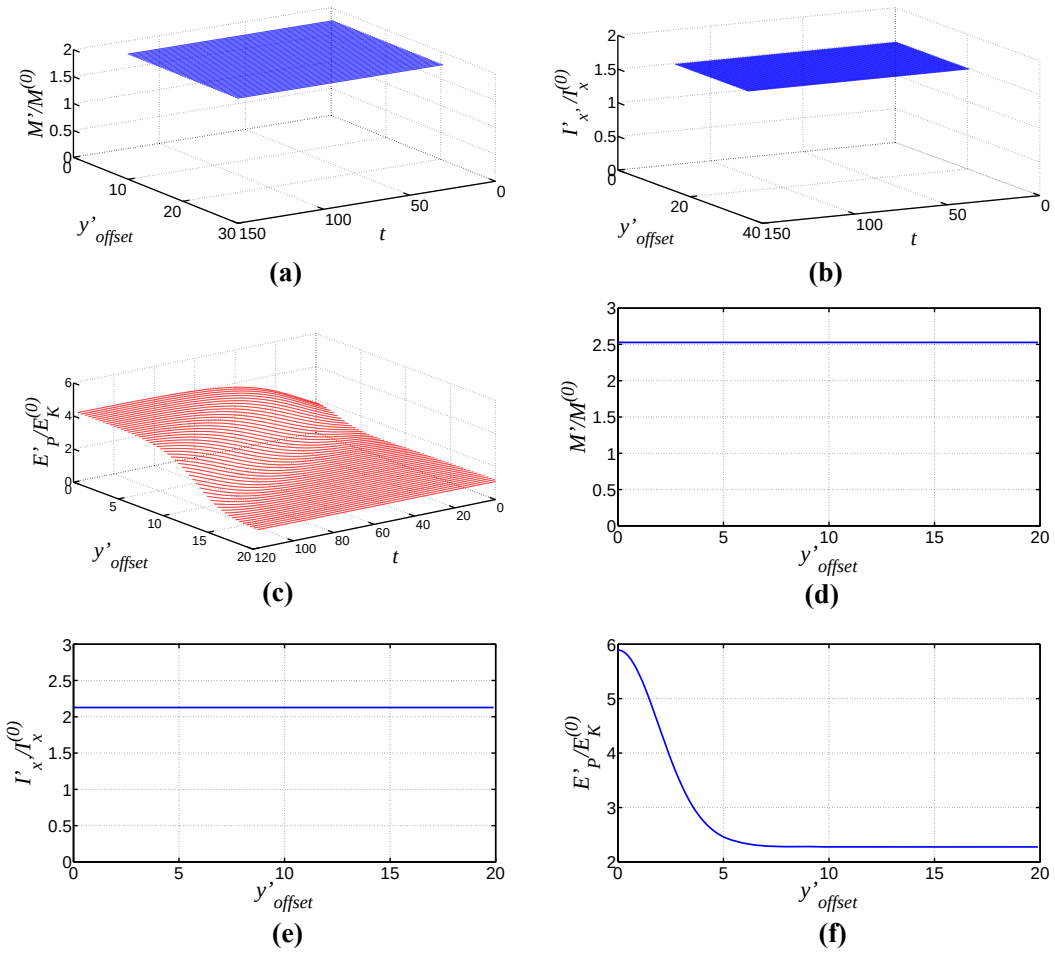

Fig. 7-22 M' **(a),** $I'_{x'}$ **(b) and** E'_P **(c) at parallel slices given by the (3142)-type solution of the KP equation versus** y'_{offset} **and time.** M' **(d),** $I'_{x'}$ **(e) and** E'_P **(f) at parallel slices given by the O-type solution of the KP equation versus** y'_{offset}**.**

The meanings of the figures are to be explained more explicitly. If only a semi-infinite incoming solitary wave was situated in the flow field obliquely, $M'/M^{(0)}$, $I'_{x'}/I_x^{(0)}$ and $E'_P/E_K^{(0)}$ would be a little larger than 1 owing to the different orientations of the control volumes. In a regular reflection, due to the symmetry of the incident wave and the reflected wave about the plane perpendicular to the reflection wall, $M'/M^{(0)}$, $I'_{x'}/I_x^{(0)}$ and $E'_P/E_K^{(0)}$ are approximately 2 in the far field where $y'_{offset} \to \infty$ as anticipated (Figs. 7-22(d)-(f)). In the vicinity of the reflection wall, the unit transverse length of the hump contains more potential energy

than the summation of the incident wave and the reflected wave in the far field (Fig. 7-22(f)). Since the transverse length of the hump is constant, the energy together with other quantities freed from shortening the propagating incident wave all goes into the reflected wave. An analogy can be made for this process. Suppose each control volume that is parallel to the reflection wall is like a reservoir. In a regular reflection, the reservoirs do not accumulate the excess mass flow, momentum flow and the energy flow. Keeping this analogy in mind, it is easier to understand the Mach reflection. Fig. 7-22(a) & (b) show that the stocks of the excess mass and the tangential momentum to the reflection wall in the reservoirs remain unchanged with y'_{offset} and time. So we can say the excess mass and momentum are not accumulated in any of the control volumes. $M'/M^{(0)}$, $I'_{x'}/I_x^{(0)}$ are smaller than 2 in each control volume. It suggests that the transverse transfers of the excess mass and tangential momentum via the reflected wave are faster in the Mach reflection than those in the intuitive/imaginary regular reflection. Interestingly, as shown Fig. 7-22(c), each reservoir blocks the potential energy and slows down the spreading of energy towards the far field. The cumulative E'_P can be up to approximately 4 times of $E_K^{(0)}$. Linking to the wave profile, the stem wave possesses the same excess mass and tangential momentum per unit transverse length as the summation of those of the incident wave and the reflected wave in the far field. But the stem wave has larger energy per unit transverse length than that in the far field. That is the reason why the reflected wave has a smaller amplitude than the incident wave and the stem wave. The stem wave is absorbing energy to elongate itself. The energetic stem wave is more harmful than solely the incoming solitary wave from a practical sense.

With that knowledge, we can then move on to the analysis of the simulated result. Note that the boundary and initial conditions used in the fully nonlinear simulation are not the same as those in the KP theory mentioned hereinbefore. The reflected wave does not exist initially. The flow field is initialised by the third-order solitary wave solution. However, we can speculate the process in the simulation according to the theory. When the solitary wave encounters the oblique vertical wall, the excess mass, tangential momentum to the wall and energy are reflected. But they may spread outward in the different speeds. At the incipient period of a regular reflection, the energy would heap up and quickly form a steady hump. Then all the physical quantities would spread out at the same speed to form a reflected wave with the same cross section as the incident wave. In a Mach reflection, the excess mass and tangential momentum would not be accumulated in the vicinity of the reflection wall, and they would be transferred in the transverse direction at a faster speed than that in an imaginary regular reflection. On the contrary, the energy would be accumulated in the vicinity of the reflection wall and would be spread out very slowly. This process would facilitate the elongation of the stem wave. Although the stem wave would have larger amplitude and more energy, its excess mass and tangential momentum to the reflection wall would remain the same in the transverse direction. That hypothesis is based on the weak three-dimensionality assumed by the theory. Whether some physical quantities, such as, the excess mass and tangential momentum will be constant in the transverse direction as anticipated actually provides an easy way to evaluate the 3D effect rather than judging from the complex surface pattern.

Figs. 7-23(a)-(e) show the time histories of the physical quantities in Ω' adjacent to the reflection wall and they are normalised by the corresponding initial values in Ω.

The variation of M' in Fig. 7-23(a) can be divided into two stages. Before $t \approx 10$, it can be deemed as the impingement period during which the incoming wave encounters the corner around *O'*. After $t \approx 10$, the stem wave has been formed in the vicinity of the reflection wall and M' does not increase but decreases slightly. The (3142)-type solution predicts that $M'/M^{(0)}$ would be a constant that is approximately 1.75. It is very close to the simulated result. As to the momentum, the (3142)-type solution predicts that $I'_{x'}/I_x^{(0)}$ would be a constant that is approximately 1.5. However, in Fig. 7-23(b), $I'_{x'}$ is still slowly growing after $t \approx 10$. The simulated $I'_{x'}/I_x^{(0)}$ becomes larger than 1.5 after $t \approx 15$. It suggests that although the first-order approximation is still predominant, the higher-order effect is already noticeable. Recalling the wave profile at the reflection wall shown in Fig. 7-7(b), although the simulated wave amplitude is well predicted by the KP theory, the simulated wave profile is much wider than the result given by the KP theory. It is because the simulated stem wave contains more momentum. The simulated potential energy E'_P increases monotonously and becomes larger than $4E_K^{(0)}$ (Fig. 7-23(d)). Because of the unchanged excess mass in Ω, the wave profile at the reflection wall has to be thinner and thinner comparing with itself as the time elapses. The growth rate of the kinetic energy E'_K is almost constant (Fig. 7-23(d)). There is a cross point between the curves of the kinetic energy and the potential energy. At the beginning, the kinetic energy is smaller than the potential energy, and then the kinetic energy exceeds the potential energy. Overall, both the potential energy and the kinetic energy increase with time until the wave breaks. In Fig. 7-23(c), $I'_{z'}$ deviates from 0 gradually after the impingement period. It is probably because that

the excessively injected energy makes it impossible for the wave profile to remain symmetric (Longuet-Higgins and Fenton, 1974).

The findings above can be used to evaluate the potential risk brought by the stem wave. We can simplify the dyke as a vertical wall like the rightmost boundary of the simulated wave tank in Fig. 7-1. The mean hydrodynamic force on the dyke per unit transverse length can be estimated via the horizontal momentum of the wave divided by the interaction time. The interaction time can be estimated by the phase speed supposing the mirror-like reflection without phase shift. Therefore, the mean force on the dyke brought by the stem wave should be larger than 1.5 times of that induced by solely the incoming solitary wave due to the larger momentum and faster phase speed of the stem wave. When an SSW climbs a slope, more complex processes would happen including the transformation and dissipation of the energy. Li and Raichlen (2002) found that when the wave reaches the maximum run-up position on the slope, most kinetic energy was transformed to the potential energy. The stem wave may result in very high run-up on the slope taking into account its enormous potential and kinetic energies.

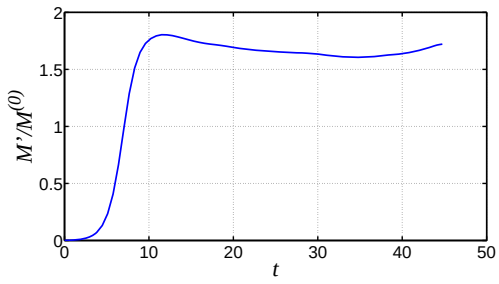

(a)

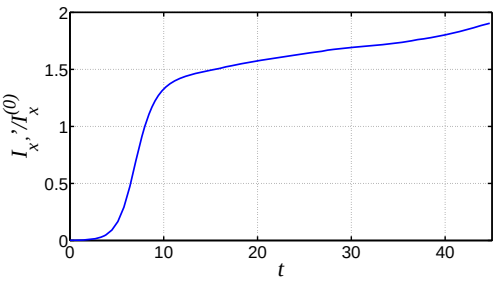

(b)

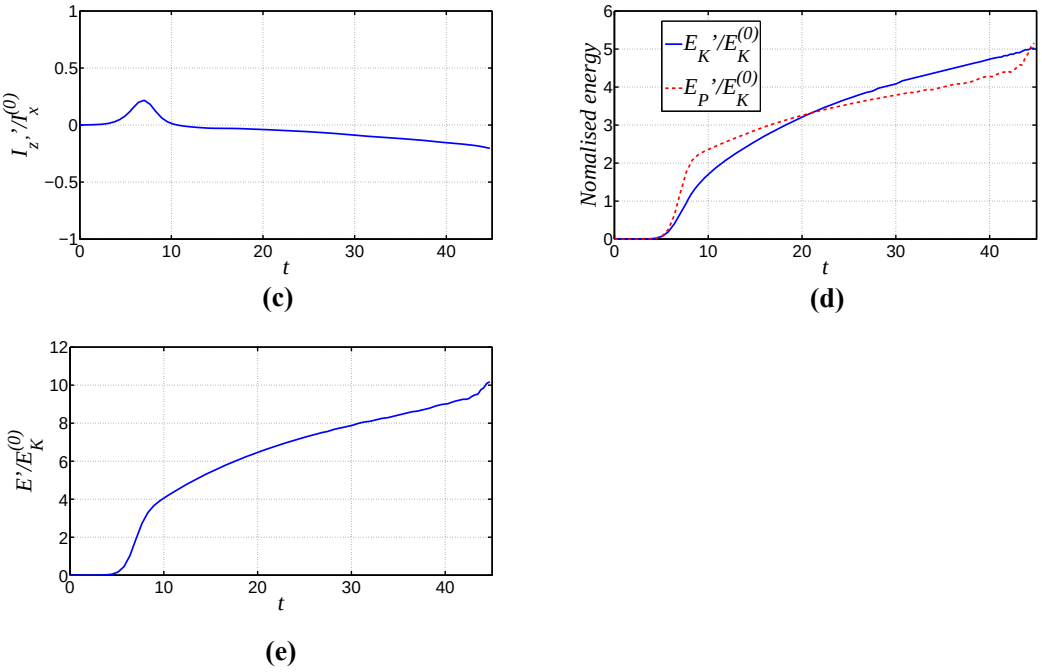

Fig. 7-23 (a): M' in Ω', which is normalised by $M^{(0)}$ in Ω, versus time. (b): $I_{x'}'$ in Ω', which is normalised by $I_x^{(0)}$ in Ω, versus time. (c): $I_{z'}'$ in Ω', which is normalised by $I_x^{(0)}$ in Ω, versus time. (d): E_K' and E_P' in Ω', which are normalised by $E_K^{(0)}$ in Ω, versus time. (e): E' in Ω', which is normalised by $E_K^{(0)}$ in Ω, versus time.

The largest stem wave is comparable to the highest possible solitary wave. The stem wave has a tendency to become a 2D wave referring to Fig. 7-22(c). We may further compare the stem wave and the solitary wave in terms of excess mass, momentum and energy. Suppose a solitary wave in Ω, the excess mass M, momentum in the *x*-direction I_x, kinetic energy E_K, potential energy E_P and total energy E can be obtained according to the data given by Longuet-Higgins and Fenton (1974) for the whole range of amplitude (Figs. 7-24(a)-(c)). M, I_x, E_K, E_P and E reach their maximum values before the amplitude reaches its maximum value. By contrast, the momentum, kinetic energy, potential energy and total energy of the stem wave all increase monotonously with its amplitude until it breaks (Figs. 7-23(b), (d) and (e)). The M' and $I_{x'}'$ of the stem wave with the maximum amplitude are only

approximately 20% and 30% larger than those of the highest possible solitary wave, respectively. However, the maximum energy of the stem wave can become almost twice of the maximum possible energy of a solitary wave. The vertical velocity within the stem wave, therefore, must be much larger than that in a solitary wave. Supposing the flooding scenario when the stem wave has turned into the horizontal flow in the plain coastal area, the potential energy would be totally transformed to the kinetic energy, and the vertical velocity would become negligible. The potential damages induced by the stem wave due to the large horizontal velocity would be much more severe than that induced by the highest solitary wave.

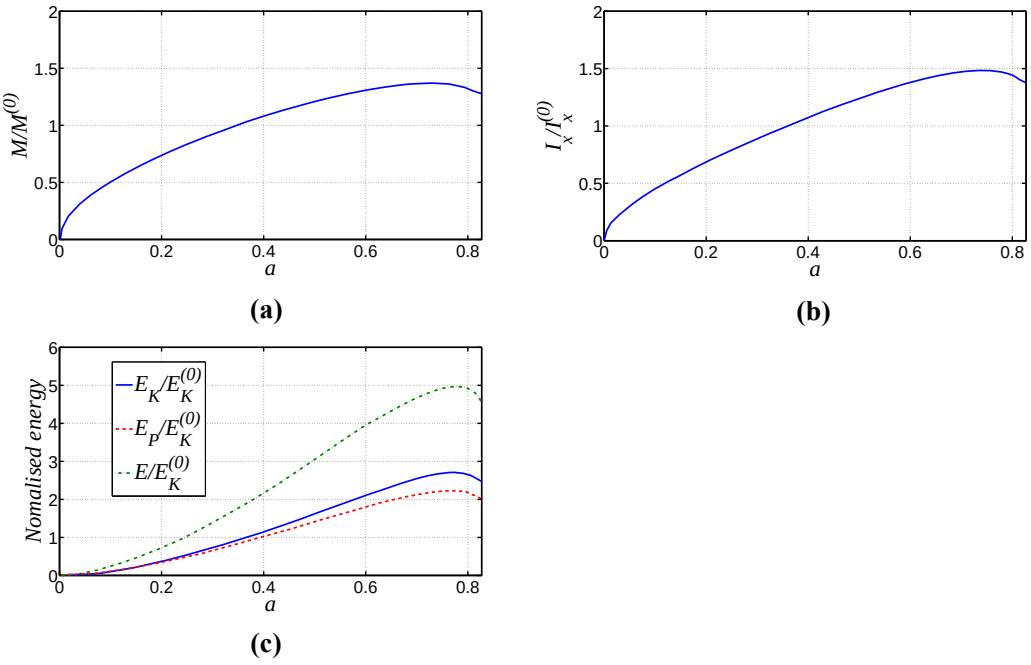

Fig. 7-24 (a): The total excess mass of a solitary wave *M*, which is normalised by $M^{(0)}$ in the simulation, versus the nondimensional wave amplitude. (b): Total horizontal momentum of a solitary wave I_x, which is normalised by $I_x^{(0)}$ in the simulation, versus the nondimensional wave amplitude. (c): The kinetic energy E_K, potential energy E_P and total energy E of a solitary wave, which is normalised by $E_K^{(0)}$ in the simulation, versus the nondimensional wave amplitude.

The transverse transfers of the physical quantities can be further investigated from Figs. 7-25(a)-(e), which show the quantities in the control volumes that are parallel to

the reflection wall. A common feature among Figs. 7-25(a), (b), (d) and (e) is that the curves for different y'_{offset} intersect at approximately one point. There are regular intervals between the curves before the intersection point. The abscissas of the intersection points for the excess mass, momentum and energy are all close to $t \approx 7.5$ and their vertical coordinates are close to 1. It can be inferred that before $t \approx 7.5$, the physical quantities in the control volumes solely depend on the uniform incoming solitary wave. After $t \approx 7.5$, due to the interaction in the vicinity of the reflection wall, the physical quantities are gradually affected by the elongations of both the stem wave and the reflected wave. Looking into Fig. 7-25(a), the tip of the reflected wave containing excess mass passes each control volume in sequence with a constant normal velocity. After the tip has passed, M' in each slice is almost of the same value, which is very close to the analytical solution in Fig. 7-22(a). Fig. 7-25(b) reveals that the transverse momentum transfer is different from the prediction of the KP theory. $I'_{x'}$ in each control volume increases with almost the same constant growth rate after the tip of the reflected wave has passed that slice. It means that the transverse transfers of the excess mass and the tangential momentum are not synchronised. The momentum transfer is delayed comparing to the excess mass transfer. Recalling the analogy of reservoirs, each reservoir/control volume accumulates the tangential momentum at the same rate. Therefore, the reflected wave elongates fast but its amplitude grows slowly. The accumulation of momentum suggests more kinetic energy would be concentrated in the vicinity of the reflection wall, and the kinetic energy may be partly transformed to the potential energy (Fig. 7-25(d)). Comparing Figs. 7-25 (d) and (e), the kinetic energy in each control volume increases with the potential energy. Fig. 7-25(c) shows that if the control volume is not adjacent to the reflection wall $I'_{z'} \approx 0$, though the velocity field can be complex.

Overall, the 3D effect in this case is still weak. The first-order approximation is adequate for the excess mass and energy transfers, but the higher-order three-dimensionality affects the transfer of the momentum noticeably.

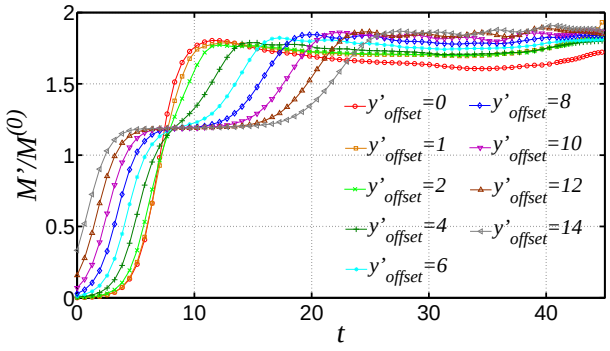

(a)

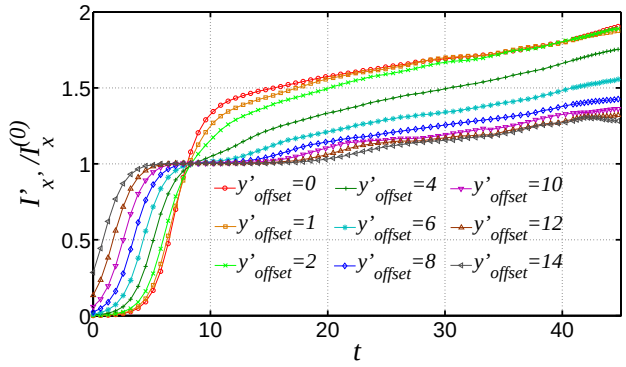

(b)

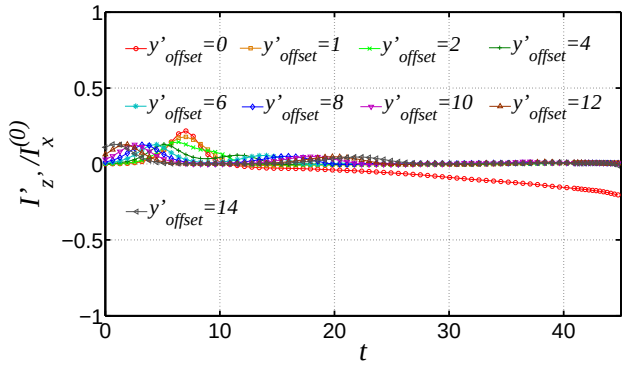

(c)

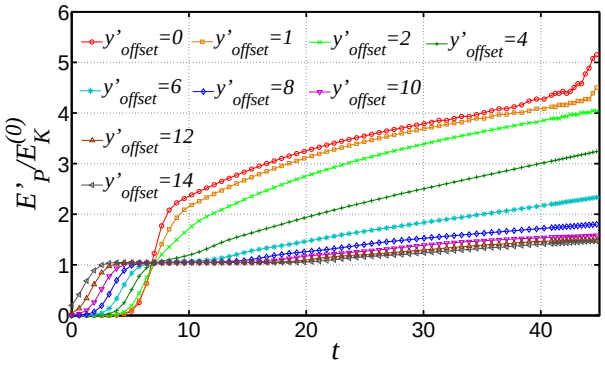

(d)

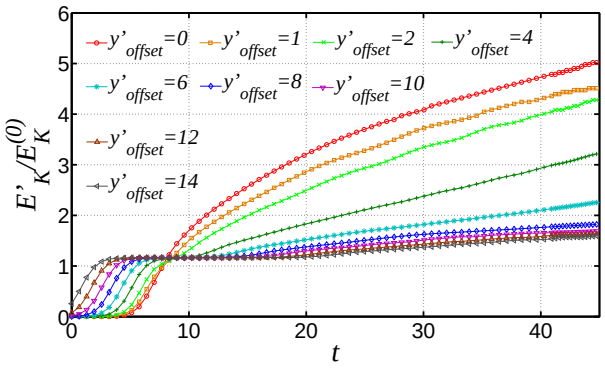

(e)

Fig. 7-25 M' **(a),** $I'_{x'}$ **(b),** $I'_{z'}$ **(c),** E'_P **(d) and** E'_K **(e) in the control volumes with offsets in the *y*'-direction versus time.**

7.5 Summary

The large-amplitude Mach stem wave induced by oblique reflection of a moderate-amplitude incident SSW has been reproduced by the fully nonlinear simulation. The simulated wave profile agrees well with the experimental measurements. Based on the detailed flow field information provided by the simulation, kinematics and dynamics of the Mach stem wave have been analysed. It is found that the breaking of the stem wave is due to the horizontal particle velocity increases to a value that exceeds the constant stem wave phase speed. The nonbreaking stem wave profile becomes asymmetric gradually to accommodate the energy per unit transverse length that is more than 4 times of that of the incoming solitary wave and 2 times of the maximum possible energy of a solitary wave. That

process results in the plunging breaker. It suggests the possible impulsive wave impact on the structure by the breaking stem wave. The situations when the stem wave encounters the structures with different dimensions have been discussed based on the velocity field and the existing research on SSW-structure interactions. Overall, the stem wave would pose a larger risk to the offshore and near shore structures than the incoming SSW. Furthermore, the strong shear flow has been found in the stem wave, and it would induce 3D ambient flow around the structure. The Morison equation would be inaccurate for calculation of the loads on the structure of small dimension exerted by the stem wave of very large amplitude.

The physical quantities in terms of excess mass, horizontal momentum and energy have been analysed in the transverse direction. It is found that the complex phenomena occurring in the oblique reflection problem are due to different transverse transfer speeds of those physical quantities. In the Mach reflection, the excess mass is not concentrated in the vicinity of the reflection wall. The excess mass of the stem wave per unit transverse length is approximately 1.75 times of that of the incoming solitary wave, which equals the summation of the excess mass within the incident wave and the reflected wave in the far field. The concentration of energy in the vicinity of the reflection wall is the main driving force for the elongation of the stem wave in the transverse direction. The tangential momentum to the reflection wall is also slowly accumulated in the vicinity of the reflection wall. That process is not accurately predicted by the KP theory. Furthermore, those physical quantities also correspond to different aspects in the evaluation of the hazardous damages. For example, the excess mass corresponds to the volume of the flood water, the momentum corresponds to the force on the structure, and the energy corresponds to the velocity of the flood flow. Some coastal configurations, *e.g.*, vertical dyke, slope,

and the flooding at the plain area due to overtopping, have been discussed. The stem wave poses a larger risk to the lives and structures at the coastal area than the incoming wave.

Through the comparison with the KP theory, it can be seen that the first-order approximation, with the orders in terms of the nonlinearity, can still well predict some important features of the nonbreaking wave, *e.g.*, the stem wave amplitude and the transverse length of the stem wave. Higher-order nonlinear terms may improve the approximation on the outskirts of the wave profile at the reflection wall. Although there are no more simulated cases available with different ψ_i to examine the 3D effect, the significance of the 3D effect has been analysed by comparing the transverse transfers of physical quantities with the KP theory that is based on the weak three-dimensionality assumption. Overall, the 3D effect in the simulation case is still weak. However, the higher-order approximation may improve the accuracy, which is reflected in the transverse transfer of the momentum.

Chapter 8 Numerical simulation on the oblique reflection of an internal solitary wave

8.1 Introduction

The oblique interactions of internal waves often happen at the oil-producing regions and key navigation routes, *e.g.*, in South China Sea (SCS) (Guo and Chen, 2014; Alford et al., 2015). Taking a typical oceanic environment in northern SCS for example (Fig. 8-1(a)), the bathymetry varies from 1km to 3km; the depth of the pycnocline is ~100m; the distance from the generation area Luzon Strait to South China continent where the life of internal waves comes to an end (wave breaking) is approximately 800km; the amplitude of internal waves can exceed 150m; the characteristic wavelength of an ISW is ~1km; the trough line length of a refracted ISW on the lee side of Dongsha Atoll is ~200km (Fig. 8-1(b)). There is adequate space for the development of the wave-wave interactions.

The observations by Wang and Pawlowicz (2012) have revealed some regular interaction features of two obliquely interacting ISWs with nearly identical large amplitudes despite $\kappa < 1$. Whereas, the error of the estimation based on the observation data could be up to 50%. Nakayama et al. (2012) studied the oblique reflection of an ISW numerically. They expanded the velocity potential into a series with prescribed vertically distributed functions. Their conclusion is that the Mach reflection occurs when the interaction parameter is less than 1 as predicted by the KP theory. However, the incident wave amplitude employed by Nakayama et al. (2012) is still small in the present context. Zhang et al. (2011) undertook the 3D numerical simulation using the FVM to solve the N-S equations and compared the predictions with the in-situ measurement by Ramp et al. (2010) (Fig. 8-1(a)). The smallest horizontal cell size they used was 75m where the water depth was 1000m, and the

mean and the largest cell sizes were 1358m and 4740m, respectively. In their numerical simulation, internal waves were generated at Luzon Strait driven by the tidal model to simulate the real nature. When the internal wave propagated to the measuring point B1 (Fig. 8-1(a)), the numerical simulation underestimated the wave amplitude up to 53%. Nevertheless, the arriving times of ISWs to the measuring points B1 and S7 (Fig. 8-1(a)) were accurately predicted by the numerical simulation. Converting the present study to similar dimensions of the SCS with a total depth of 1000m, the typical cell size we used can be as small as 20m in the wave propagation direction. The fully nonlinear numerical simulations with high resolution are expected to enhance understanding of the strongly nonlinear wave-wave interaction.

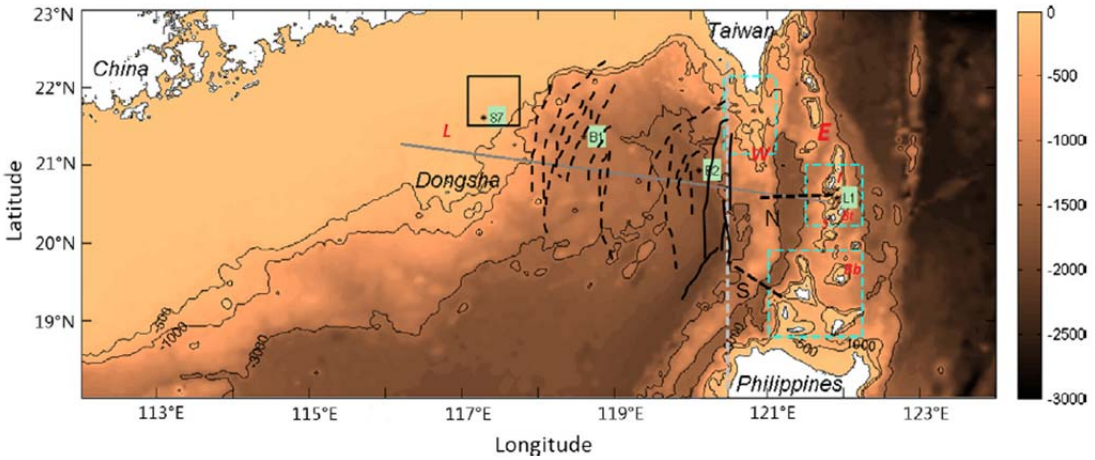

(a)

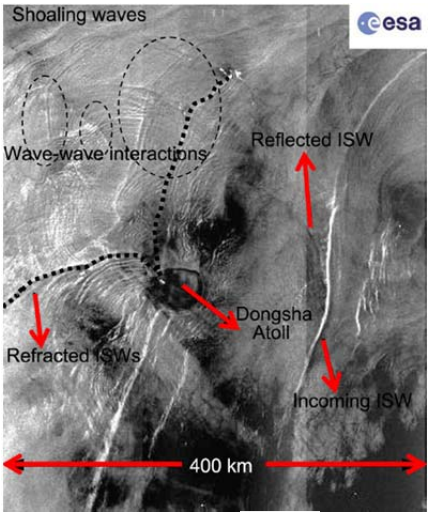

(b)

Fig. 8-1 (a): Bathymetry of the northern SCS. Four asterisks marked by S7, B1, B2 and L1 are the mooring locations of the WISE/VANS experiment (Ramp et al., 2010). The black dashed lines represent the spatial distributions of the ISWs. (b): A satellite image showing the complex wave-wave interaction around the Dongsha Atoll. The black dashed lines indicate the trough lines of refracted waves. Graph courtesy of Guo and Chen (2014) (*Source: Prog. Oceanogr. v. 121, 2014, p. 7-23*)

Understanding the 3D transfers of the physical quantities, *e.g.*, excess mass, momentum and energy, in the oblique reflection of an ISW is important to the applications. It has been found that substantial energy of ISWs goes into significant oceanographic processes, *e.g.*, the vertical mixing, which is significant for the redistribution of nutrients, exchange of heat, etc. (Helfrich, 1992). The present research is also of importance for the subsequent research on the vehicles and offshore structures in complex wave field.

The mechanisms for the distinct 3D patterns are of interest. We will still use the concepts, *i.e.*, the nonlinear effect, the 3D effect and the dispersive effect to analyse the results. Two cases will be simulated by the fully nonlinear method. One has a small-amplitude incident ISW. The other has a moderate-amplitude incident ISW.

In the rest of this chapter, all the length variables will be scaled by the depth of the undisturbed lower layer h, time will be scaled by h/c_0 where c_0 is given by $\sqrt{g(H-h)h(\rho_1-\rho_2)/(\rho_2 h+\rho_1(H-h))}$, unless otherwise specified.

8.2 Set-ups and computation processes

A rigid-lid two-layer physical model is shown in Fig. 8-2. The ratio between the lower and upper layer depths is 3/1. The ratio between their densities is 1025/1000. The incoming ISW is modelled by the ISW solution of the third-order KdV equation,

and the analytical solution is used to initialise the flow field. The maximum interface displacement of the incoming wave is denoted by a_i (also is the maximum interface displacement of the incident wave that is far away from the reflection wall). The incident wave angle is denoted by ψ_i.

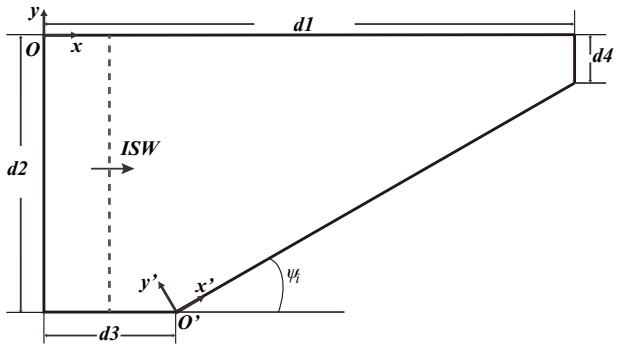

Fig. 8-2 The dimensions of the computational domain in the plan view. The initial wave trough line is drawn by the dashed line with an arrow indicating the propagation direction.

8.2.1 Small incident wave

The dimensions of the computational domain are listed in Table 8-1 (*H* is the total depth). $a_i = -0.0267$ and $\psi_i = \pi/12$ for this case. The initial characteristic wavelength of the ISW is 3.114. The initial position of the trough line is at *x*=13.333. The interaction parameter given by Eq. (4.12) is $\kappa = 0.6968 < 1$. It is in the Mach reflection regime according to the KP theory. The boundary conditions at the side walls, top and bottom are "slip-walls". The simulation stops at *t*=228.0242 when the incident wave is still sufficiently far away from the rightmost boundary. Relaxation zones are implemented and their longitudinal lengths can be found in Table 8-2.

Table 8-1 The dimensions of the computational domain (small incident wave case)

d1	*d2*	*d3*	*d4*	*H*	ψ_i
333.33	135.50	26.67	53.33	4/3	$\pi/12$

Table 8-2 The longitudinal scopes of the relaxation zones (small incident wave case)

Zone 1	Zone 2
x=[0, 1.333]	x=[330.67, 333.33]

The maximum Courant number *Co* is as 0.2. The AMR technique is employed. It refines the hexahedral mesh dynamically near the interface and the area where the absolute value of the fluid velocity in the *x*-direction, *i.e.* $|u|$, is larger than a threshold. u_{unit} in Eq. (5.16) is 0.47. C_{amr2} is 0.06. The maximum refinement level is 3. The refinement step is 4 time steps. The cell adjacent to *O'* is selected as a typical one. The refined cell size of the typical cell measured in the *O-xyz* coordinate system is (0.067, 0.47, 0.01). The number of cells at the final time step is 20,515,905. The computation has taken 336 hours by 36 processors of the cluster Grace funded by University College London (UCL) for High Performance Computing (HPC). A screenshot of the wave profile at *t*=228.0242 is shown in Fig. 8-3.

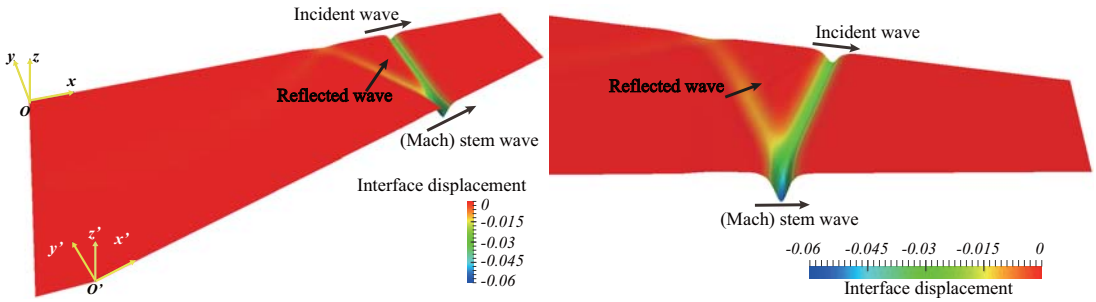

(a) **(b)**

Fig. 8-3 The contour plot of the interface displacement at *t*=228.0242 (small incident wave case). (a): the whole domain; (b): the enlarged detail. The vertical coordinate has been magnified by a factor of 200.

8.2.2 Moderate incident wave

$a_i = -0.1333$ and $\psi_i = \pi/6$ for this case. The initial characteristic wavelength is 1.736. The initial position of the trough line is at *x*=13.333. The interaction parameter

given by Eq. (4.12) is $\kappa = 0.7489 < 1$. It is in the Mach reflection regime according to the KP theory.

The computational domains for several runs (Table 8-3) were determined taking into account both the phenomenon of interest and the limited computational capability. The dimension of the computational domain was initially anticipated according to the prediction of the KP theory. The (3142)-type solution was used to predict the 3D wave pattern. The amplitude of the wave of depression at the reflection wall could gradually grow to a large value as it propagates. $d1$ should be long enough to capture such large wave profile. The width of the computational domain should be much larger than the transverse length of the predicted stem wave by the end of the simulation. From the simulated result on the sparse mesh, it has been found that the wave profile at the reflection wall stabilised in a shorter time than the preceding prediction, and a hump adjacent to the reflection wall appeared without elongation in its transverse direction. So the length and the width of the computational domain could be reduced. A screenshot of the simulated interface with the finest mesh at t=74.1079 is shown in Fig. 8-4. It is noted that the large depression adjacent to the reflection wall is named as a "hump" as that in the regular reflection (Fig. 1-8(a)).

The boundary conditions at the side walls, top and bottom are "slip-walls". The simulation stops when the incident wave is still sufficiently far away from the rightmost boundary. The longitudinal lengths of relaxation zones (if applicable) can be found in Table 8-4.

Table 8-3 The dimensions of the numerical wave tank (moderate incident wave case)

Run	*d1*	*d2*	*d3*	*d4*	*H*	ψ_i
1	426.67	297.61	26.67	66.67	4/3	$\pi/6$
2	226.67	148.80	26.67	33.33	4/3	$\pi/6$
3	106.67	55.52	26.67	9.333	4/3	$\pi/6$

Table 8-4 The longitudinal scopes of the relaxation zones (moderate incident wave case)

Run	Zone 1	Zone 2
1	None	None
2	x=[0, 1.333]	x=[220, 226.67]
3	x=[0, 1.333]	x=[100, 106.67]

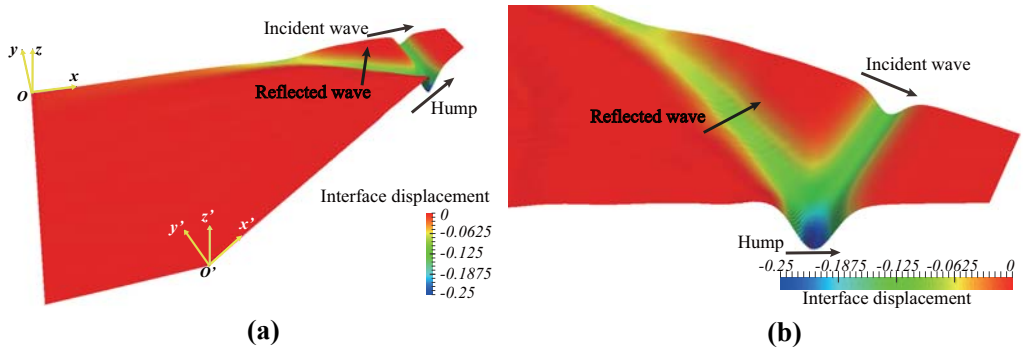

Fig. 8-4 The contour plot of the interface displacement at *t*=74.1079 (moderate incident wave case). (a): the whole domain; (b): the enlarged detail. The vertical coordinate has been magnified by a factor of 25.

The AMR technique is employed for all the runs. Table 8-5 shows the cell sizes of the refined typical cell and the numbers of the cells. The AMR parameters are listed in Table 8-6. *Co* in both Run 1 and Run 2 is 0.4. *Co* in Run 3 is 0.2. Some parameters have been slightly tuned during the computation processes considering the stability.

Table 8-5 The meshes for the convergence study of the moderate incident wave case

Run	Cell size of a typical cell $(\Delta x, \Delta y, \Delta z)$	The number of cells at the final time step
1	(0.098, 0.19, 0.014)	18,626,633
2	(0.056, 0.093, 0.0069)	30,227,308
3	(0.026, 0.10, 0.0035)	35,699,960

Table 8-6 The AMR parameters (moderate incident wave case)

Run	The maximum refinement level	C_{amr2}	The refinement step
1	3	0.07	1
2	3	0.12	4
3	3	0.2	5

Runs 1 and 3 have been computed on the cluster Legion funded by University College London (UCL) for High Performance Computing (HPC). Run 2 has been computed on the cluster IRIDIS jointly owned by UCL, the University of Southampton, and the University of Oxford, which has ended service for UCL users on 31, July, 2015. The processor quantities, consumed memories and execution times are listed in Table 8-7. It took approximately 5 months for Run 3 including waiting time.

Table 8-7 Computation resource consumptions (moderate incident wave case)

Run	Processor quantity	Memory (GBs)	Execution time (Hours)
1	64	256	648
2	64	128	1,428
3	40	160	1,752

8.3 Convergence and accuracy evaluation

8.3.1 Small incident wave

Only one simulation is performed for the small incident wave case, and the convergence study cannot be done. Alternatively, we will evaluate its accuracy via the wave profiles at the offshore wall where *y=0*. The time series of the wave profile is plotted in Fig. 8-5(a). It can be seen that over a long propagation distance (about 77 times of the characteristic wavelength), both the waveform and the wave speed do

not change much. Near the end of the simulation, the reflected wave from the reflection wall impinges onto the offshore wall. Nevertheless, there is no noticeable influence on the incident wave profile. The wave profile at t=228.0242 is compared with the analytical solution of an ISW with the same initial amplitude and the initial position in Fig. 8-5(b). The incident wave amplitude has decreased by approximately 7% by the end of the simulation. The mean wave speed c_i is only slower than the third-order solution by approximately 0.3%.

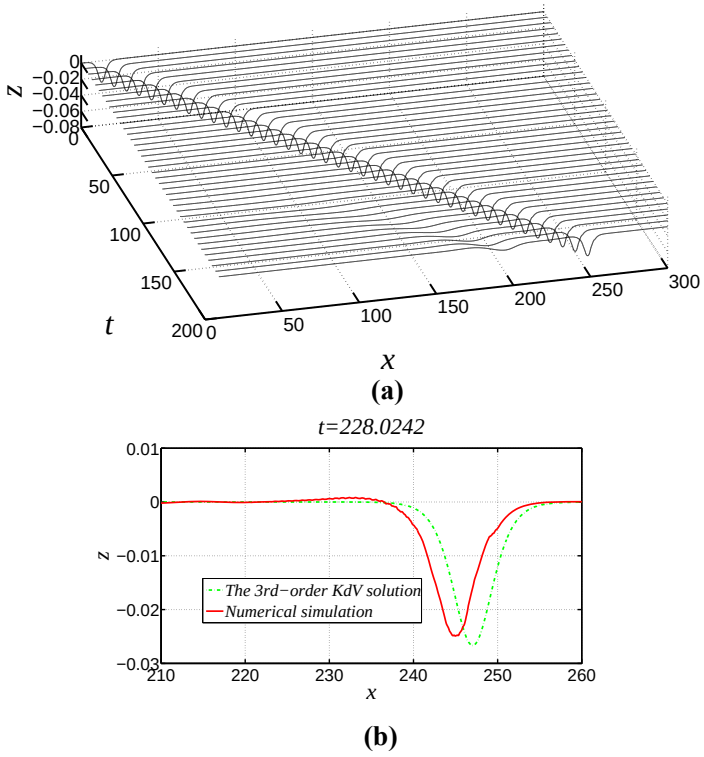

Fig. 8-5 (a): The wave profiles at the offshore wall at different times. It starts from t=0, and the time step between adjacent profiles is 5.7006. (b): Comparison between the simulated offshore wave profile and third-order KdV solution with the same initial amplitude and initial position at *t*=228.0242.

The trajectory of the incident wave trough in Fig. 8-6 shows the slow attenuation of the simulated incident wave due to the cumulative numerical error. The e-folding distance measuring the decay of the wave amplitude is 2273 (or the exponential

decay rate 0.00044), which is much larger than $d1$. The accuracy of the incident wave is sufficient to study the oblique reflection problem of an SSW.

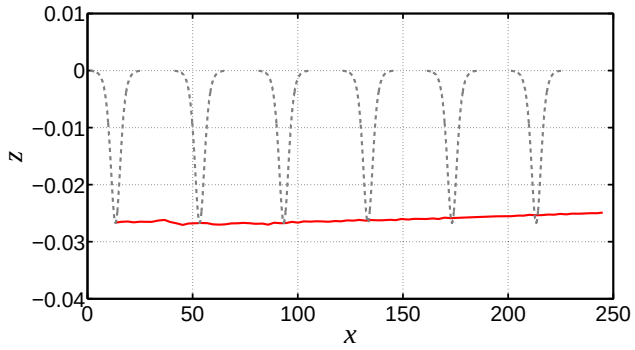

Fig. 8-6 The trajectory of the trough given by the simulation (red solid line). The analytical ISW profiles are plotted by grey dashed lines.

8.3.2 Moderate incident wave

The time series of the wave profile on the offshore wall where y=0 with the finest mesh is shown in Fig. 8-7. Over a long propagation distance of approximately 45 characteristic wavelengths, the main portion of the wave, which is of depression, does not change much in shape and travels at a constant speed. The reflected wave from the reflection wall has no noticeable influence on the incident wave in terms of the wave shape and the wave speed. Figs. 8-8(a) & (b) show that the sparser the mesh is, the faster the wave attenuates. Consequently, the wave speed reduces with the wave amplitude. It is consistent with the convergence study on a 2D ISW in Chapter 6. The greatest difference between the simulated wave profiles is at the trough location. The wave trough trajectories are plotted in Fig. 8-9 together with the 2D result on a finer mesh (Run 4 in Fig. 6-15). From Fig. 8-9, it is concluded that convergence for the incident wave can be achieved by using the mesh in Run 3. The e-folding distance measuring the decay of the incident wave amplitude in Run 3 is 560 (or the exponential decay rate 0.001785), which is much larger than $d1$. Fig. 8-10 shows a 10% decrease of the wave amplitude at t=62.7067 in Run 3 with

respected to the initial wave profile. However, the mean wave speed in the simulation is only 1.4% slower than the ISW solution of the third-order KdV equation.

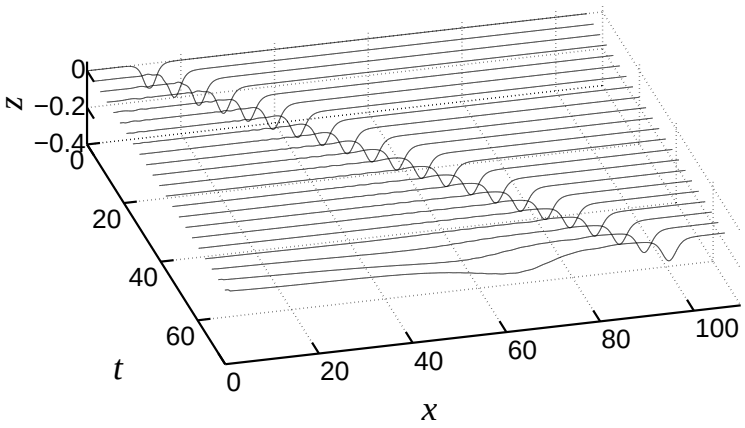

Fig. 8-7 The wave profiles at the offshore wall at different times (Run 3). It starts from t=0, and the time step between adjacent profiles is 3.5629.

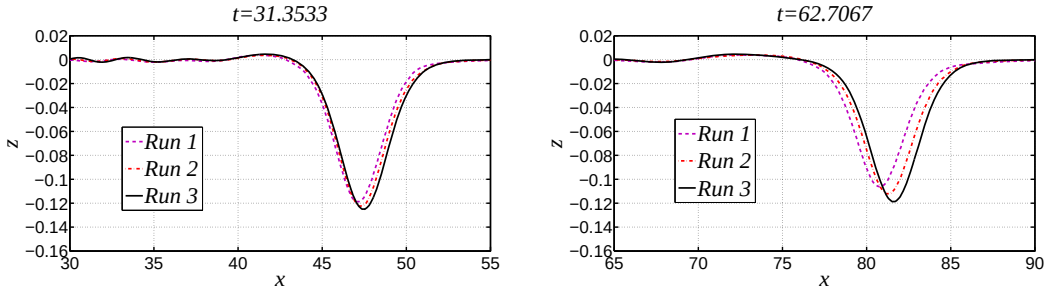

(a) **(b)**

Fig. 8-8 Comparisons of the offshore wave profiles for the convergence study at *t*=31.3533 (a) and at *t*=62.7067 (b).

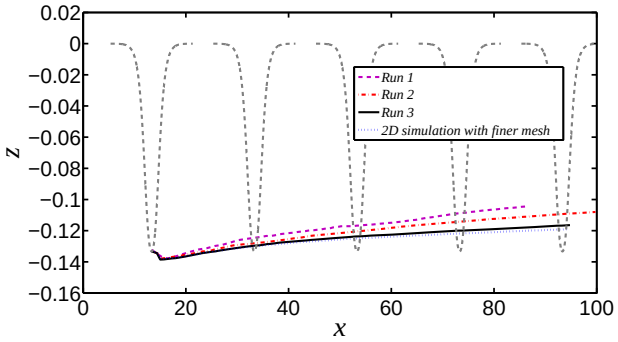

Fig. 8-9 The wave trough trajectories. The analytical ISW profiles are plotted by grey dashed lines.

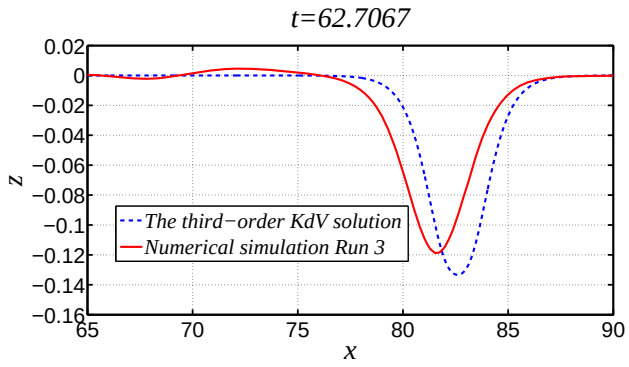

Fig. 8-10 Comparison between the wave profile at the offshore wall in Run 3 and the ISW solution of the third-order KdV equation with same initial amplitude and initial position at *t*=62.7067.

The wave profile on the reflection wall is to be examined. It will be analysed in the *O'-x'y'z'* coordinate system. A large depression with trailing waves has been observed at the reflection wall (Fig. 8-11(a)). In Run 3, slight oscillations of short wavelength are found in the vicinity of the trough (Fig. 8-11(b)). The smoothing method, *i.e.*, "lowess" embedded in MATLAB™ is used to extract the long-wave features (Figs. 8-11(a) & (b)). The comparisons of the wave profiles at the reflection wall (Fig. 8-12 (a) & (b)) show there is a converging trend. The greatest difference between the simulated results is at the trough. There is not yet enough evidence to conclude the convergence according to the trough trajectories shown in Fig. 8-12(c). Alternatively, we provide further accuracy estimation. In Fig. 6-20(a), a 2D propagating ISW is simulated with the same spatial resolution as that in Run 3. The wave amplitude of the 2D ISW is 0.255, which is comparable to the wave amplitude at the reflection wall. The variation of the simulated ISW is used to estimate the accuracy when simulating the internal wave of that amplitude. The evolution of the wave profile is consistent with the previous 2D study. After a short period of fluctuation owing to the inconsistency between the approximate model and the fully nonlinear boundary conditions, the wave amplitude slowly attenuates. The amplitude decays by approximately 11% over a distance of 60. The e-folding distance based on

the trough trajectory is approximately 530 (or the exponential decay rate 0.001891). It is virtually equivalent to the e-folding distance of the incident wave of moderate amplitude. The simulated wave speed is very accurate reflected in the wave profiles at fixed time intervals in Fig. 6-20(a). Therefore, the error in terms of the wave profile can be controlled within ~10%.

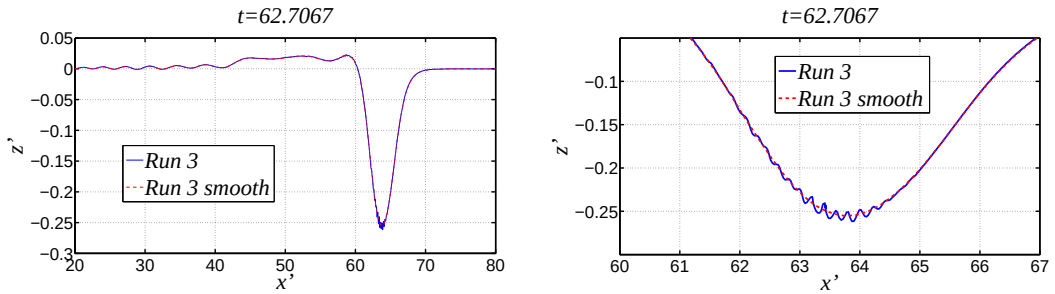

(a) **(b)**

Fig. 8-11 The wave profile at the reflection wall in Run 3 and the smoothed result. (a): the whole range; (b): enlarged view in the vicinity of the trough.

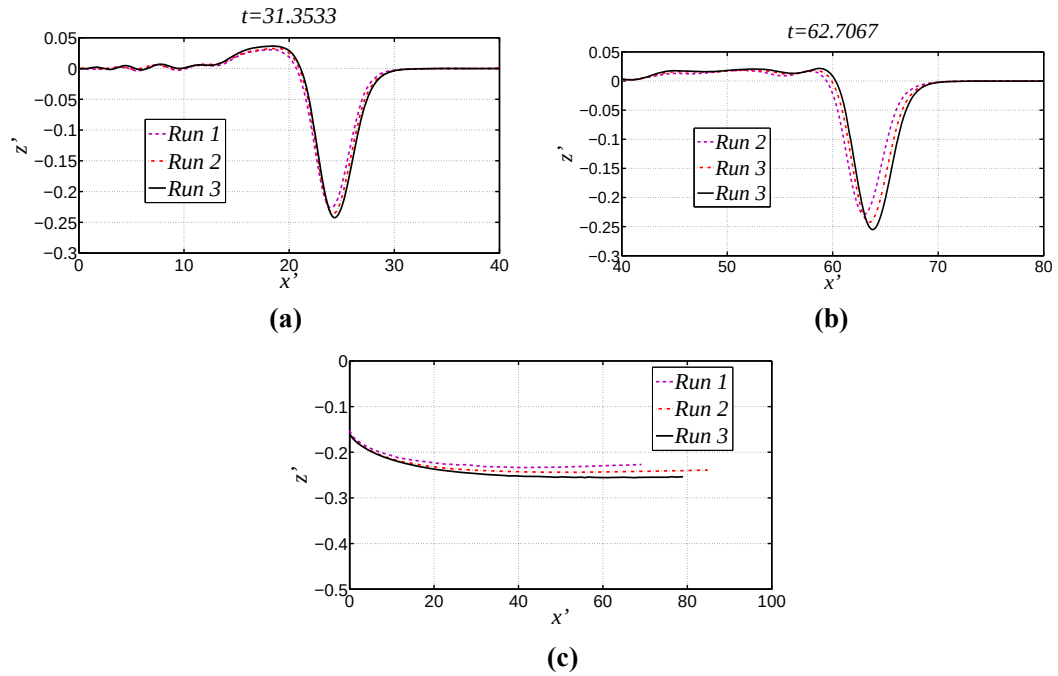

(a) **(b)**

(c)

Fig. 8-12 Comparison of the wave profiles at the reflection wall for the convergence study at t=31.3533 (a) and t=62.7067(b) and the trough trajectories (c).

As mentioned, a "hump" that is perpendicular to the reflection wall appears, and the apex between the trough lines of the incident wave and the reflected wave appears to

have a positive *y'*-coordinate. To name it a hump is because that there is not adequate evidence to conclude that it is a Mach stem wave. The transverse length of the hump (Fig. 8-13(b)) will still be calculated by the same method as used for the stem wave in the small incident wave case (Fig. 8-13(a)). The trough line of the incident wave can be obtained by the linear fitting of sampling points in the far field. Then we can draw a straight line that is perpendicular to the reflection wall from the trough at the reflection wall. The intersection point with the trough line of the incident wave can be obtained. The distance between the reflection wall and the intersection point is taken as the transverse length of the stem wave or the hump, denoted by L_M. L_M can be used to check the cell size in the *z*-direction. Fig. 8-14 shows the cell size in the *y*-direction in Run 3 is appropriate, for Run 1 and Run 3 with different Δy give almost identical results.

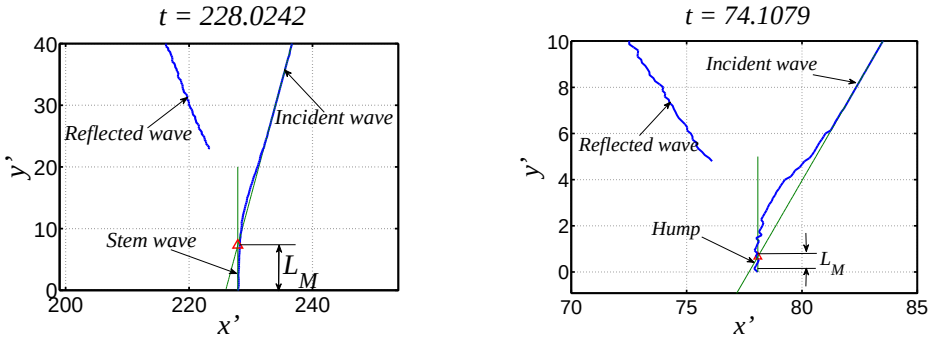

(a) **(b)**

Fig. 8-13 The method to calculate the transverse length of the stem wave in the small incident wave case (a) and the transverse length of the hump in the moderate incident wave case (b). The trough lines of the incident wave, the stem wave/hump and the reflected wave are plotted by the thick blue lines. The green lines are the linear fitting of the incident trough line and the perpendicular line to the reflection wall, respectively, and their intersection point is marked by △.

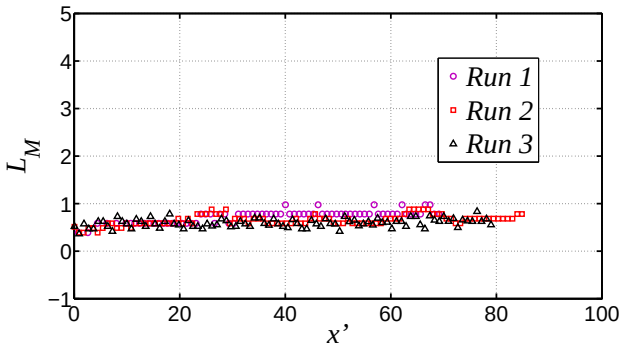

Fig. 8-14 The transverse lengths of the hump for convergence study of the moderate incident wave case.

8.4 Results and discussions

8.4.1 Wave profiles at the offshore wall

(i) Small incident wave

Comparing the simulated wave profile at the offshore wall with the ISW solutions of the first-order and the third-order KdV equations in Fig. 8-15, they match very well. It means that the higher-order corrections are little. It suggests the first-order approximation for the nonlinearity is sufficiently accurate in the far field from the reflection wall.

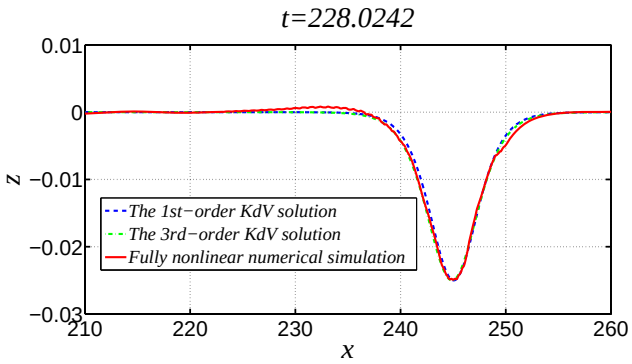

Fig. 8-15 Comparison between the wave profile at the offshore wall (small incident wave case) with the analytical ISW solutions of the same amplitude and phase.

(ii) Moderate incident wave

The wave profile at the offshore wall is compared with the ISW solutions of the first-order and third-order KdV equations in Fig. 8-16. The third-order solution fits

the simulated result very well, while the first-order solution has some discrepancies from the simulated result. It suggests that the weakly nonlinear assumption is still valid, but the higher-order nonlinear effect is noticeable in the far field from the reflection wall.

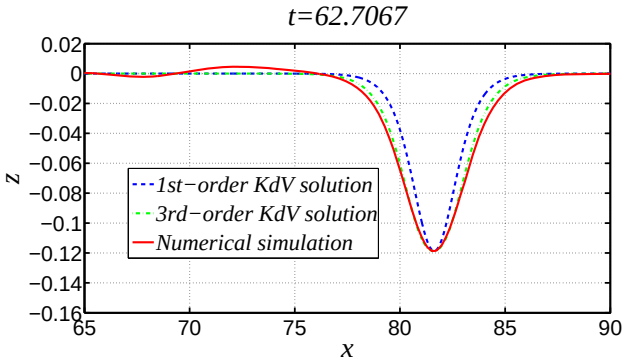

Fig. 8-16 Comparison between the wave profile at the offshore wall (moderate incident wave case) with the analytical ISW solutions of the same amplitude and phase.

8.4.2 The 3D wave profile

(i) Small incident wave

The contour plots of the simulated interface can be used to observe the development of the interaction in 3D space (Fig. 8-17). The interval between two adjacent plots is constant. The elongations of the Mach stem wave that is of larger interface displacement than the incident wave and the reflected wave can be seen. The 3D wave profiles at different moments given by the (3142)-type solution of the KP equation with the X-shape initial condition are shown in Fig. 8-18. The interval between two adjacent plots is constant. Again the initial time is different from that in the simulation. The initial time of the analytical solution is approximately equivalent to t=13.0664 in the simulation when the peak of the incoming solitary wave encounters the corner. The simulated wave pattern near the reflection wall qualitatively agrees with the analytical solution.

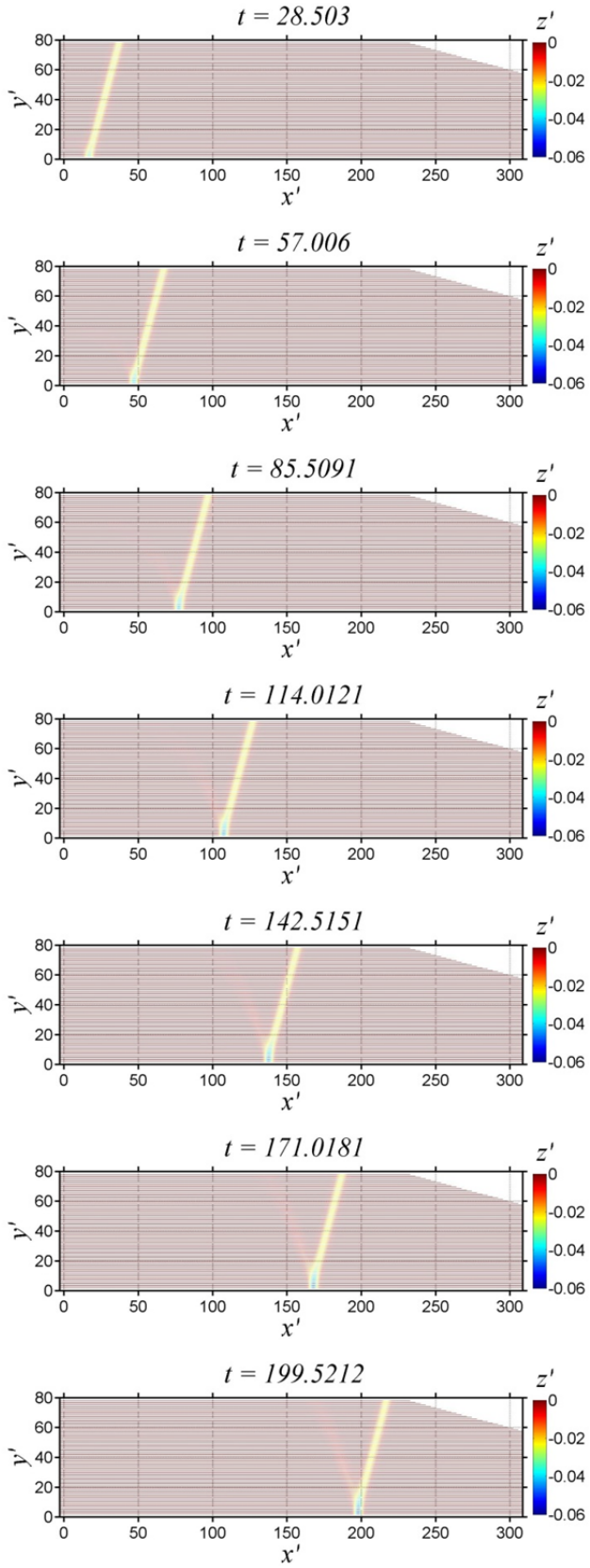
t = 28.503
t = 57.006
t = 85.5091
t = 114.0121
t = 142.5151
t = 171.0181
t = 199.5212
z'
0
-0.02
-0.04
-0.06
y'
0
20
40
60
80
x'
0
50
100
150
200
250
300

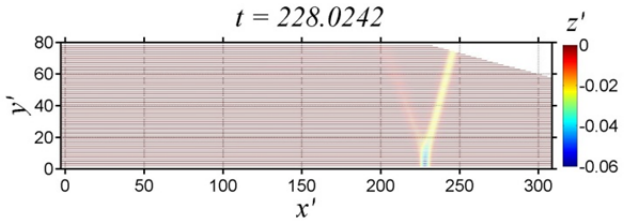

Fig. 8-17 Plan views of the simulated wave profiles at different moments (small incident wave case). The contour plot is coloured by the vertical displacement of the interface.

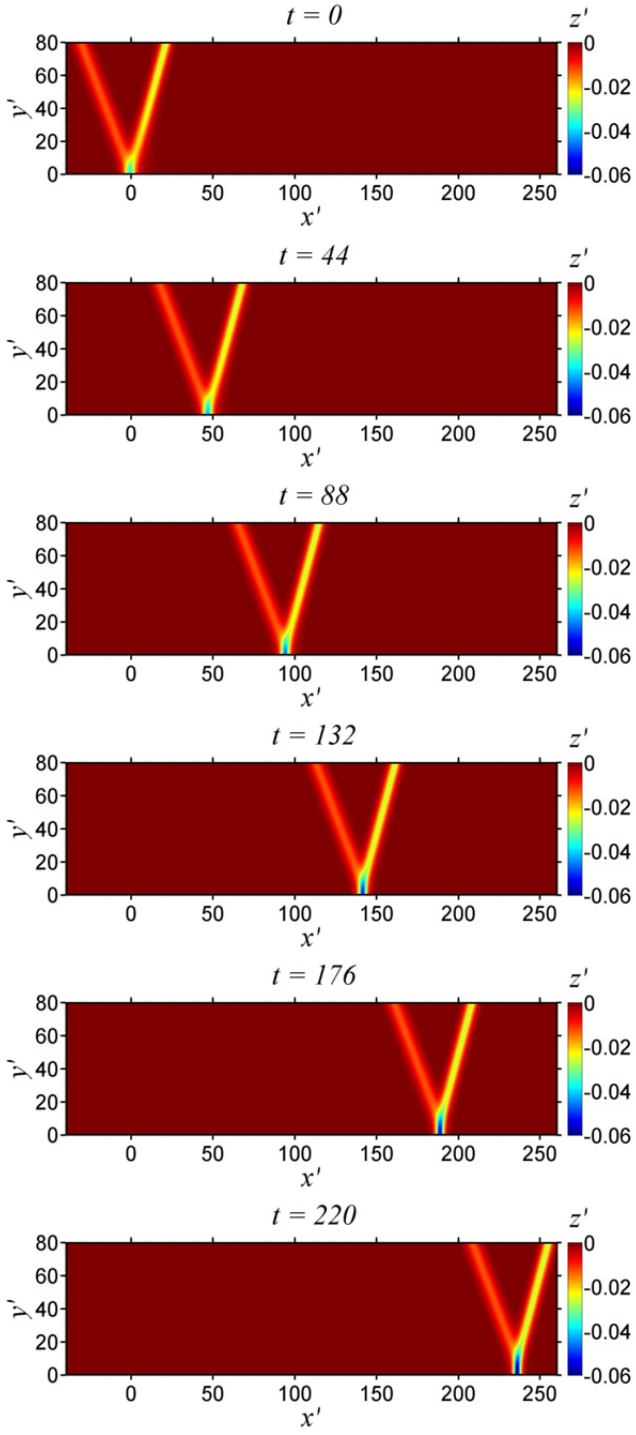

Fig. 8-18 Plan views of the wave profiles given by the (3142)-type solution of the KP equation with a_i=-0.02667 and $\psi_i = \pi/12$ at different moments. The contour plot is coloured by the vertical displacement of the interface.

(ii) Moderate incident wave

The contour plots of the simulated interface at fixed time intervals are shown in Fig. 8-19. The time when the peak of the incoming solitary wave encounters the corner is approximately t=12.2433, which is approximately equivalent to the initial time in the following approximate models. The straight incident wave moves over a constant distance between the adjacent pictures. In the vicinity of the reflection wall, a depression with large vertical displacement, which we call it a hump, quickly forms after the incident wave impinges onto the reflection wall. The 3D shape of the hump is almost unchanged until the end of the simulation. So it is unlikely to be a Mach stem wave. The tip of the reflect wave moves away from the reflection wall. The reflected wave tends to be uniform in its transverse direction. The reflected wave angle is very close to the incident wave angle. It is different from what has been observed for the small-amplitude incident wave case in Fig. 8-17.

The 3D wave profiles at different moments given by the (3142)-type solution of the KP equation with the X-shape initial condition where $a_i = -0.1333$ and $\psi_i = \pi/6$ are shown in Fig. 8-20. A stem wave elongates in the normal direction to the reflection wall and its amplitude increases. The reflected wave is of smaller amplitude than that of the incident wave. The reflected wave angle is larger than the incident wave angle. It is a classic Mach reflection phenomenon.

The EKP equation is numerically solved by the software PDE2D using the Galerkin method with the V-shape initial condition where $a_i = -0.1333$ and $\psi_i = \pi/6$. The 3D wave profiles at different moments are shown in Fig. 8-21. A hump that is

perpendicular to the reflection wall occurs, but the transverse length of the hump stays unchanged. The reflected wave angle is very close to the incident wave angle, and the reflected wave amplitude is very close to the incident wave amplitude. Overall, it is likely to be a regular reflection.

To sum up, the KP theory differs from the simulated result qualitatively. On the contrary, the EKP theory captures some important features of the oblique reflection of a moderate-amplitude incident ISW.

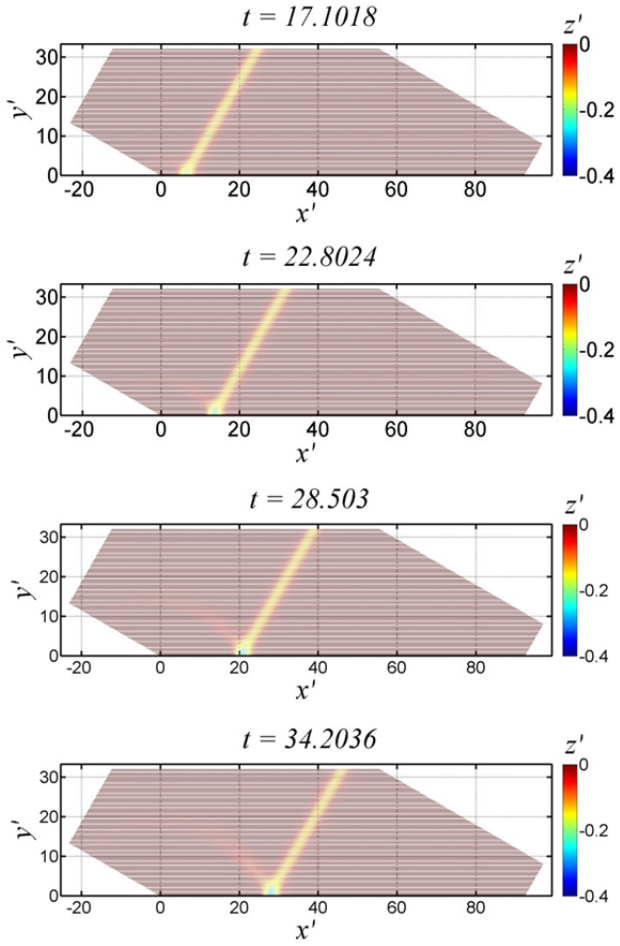

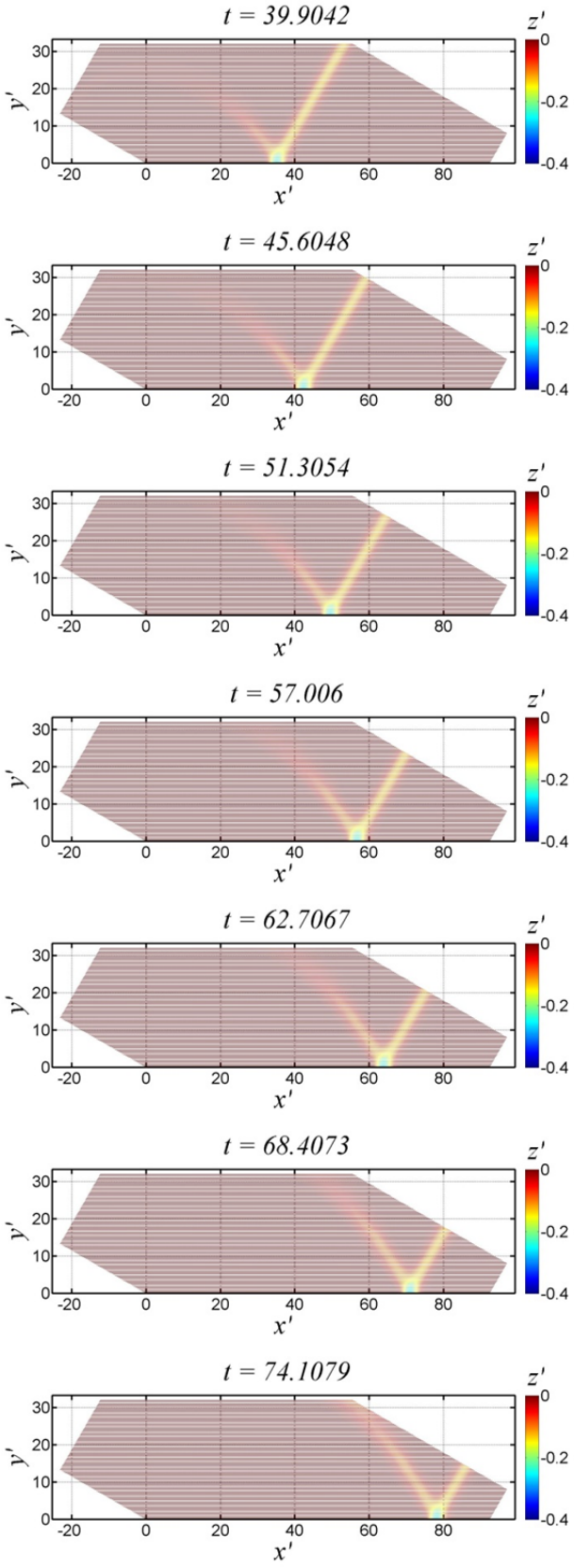

Fig. 8-19 Plan views of the simulated wave profiles at different moments (moderate incident wave case). The contour plots are coloured by the vertical displacements of the interface.

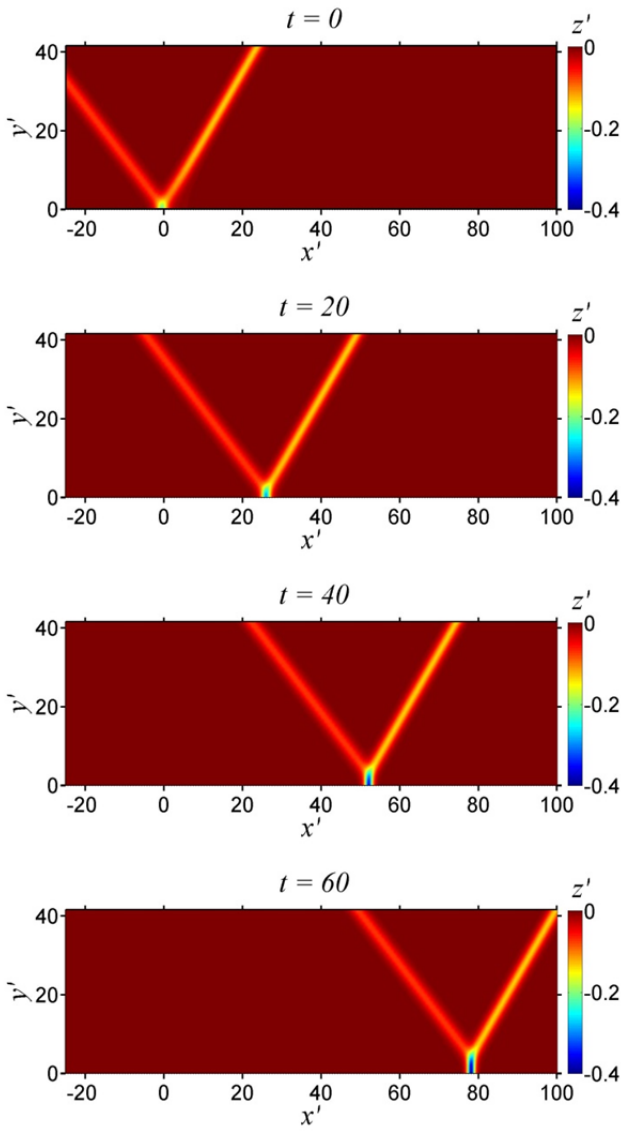

Fig. 8-20 Plan views of the wave profiles given by the (3142)-type solution of the KP equation with a_i=-0.1333 and $\psi_i = \pi/6$ at different moments. The contour plots are coloured by the vertical displacements of the interface.

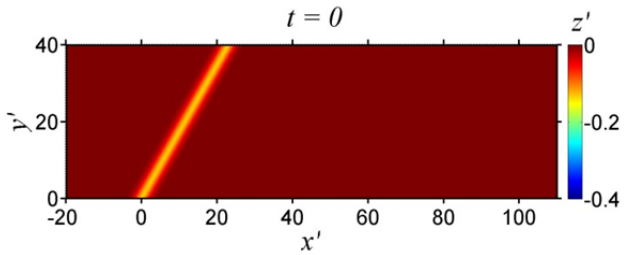

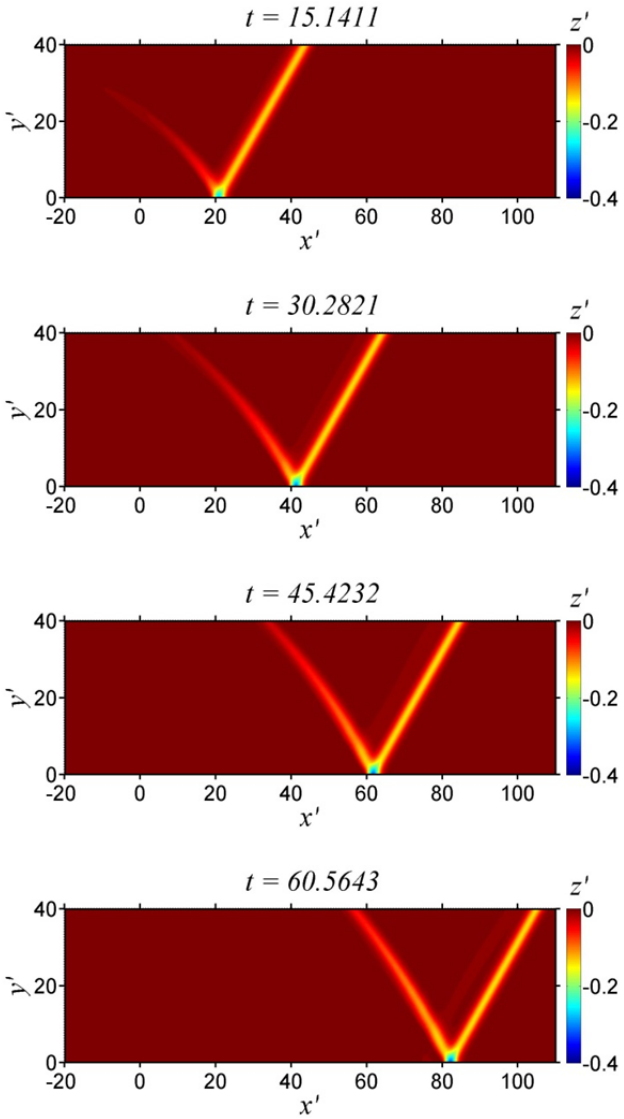

Fig. 8-21 Plan views of the wave profiles given by the numerical solution of the EKP equation with a_i=-0.1333 and $\psi_i = \pi/6$ at different moments. The contour plots are coloured by the vertical displacements of the interface.

8.4.3 Wave profiles at the reflection wall

(i) Small incident wave

The time series of the wave profile at the reflection wall is shown in Fig. 8-22(a). The wave amplitude increases with time while the steepness also increases. The (3142)-type solution of the KP equation with the same incident wave amplitude as the simulation agrees well with the simulated result when t is not large as shown in Fig. 8-22(b). The numerical error has been taken into account. Another (3142)-type

solution is calculated with $a_i = -0.024$, the magnitude of which is 10% less than the initial incident wave amplitude in the simulation. It yields $\kappa = 0.7344 < 1$ together with $\psi_i = \pi/12$, and it is still in the Mach reflection regime. From Fig. 8-22(c), the analytical solution with smaller incident wave amplitude seems to agree with the simulated result better. From the trough trajectories in Fig. 8-22(d), the deviation between the simulated result and the solution of the KP equation with $a_i = -0.02667$ becomes larger as the stem wave amplitude increases. It may be because that the nonlinear effect slows down amplitude increasing rate.

The characteristic wavelength is used to estimate the dispersive effect of the wave in the longitudinal direction. Taking into account the asymmetry of the numerical result, the lower limit of the integral in Eq. (2.24) can be extended to $-\infty$. It is simply marked as $2\lambda_c$. Fig. 8-22(e) shows that the two-fold characteristic wavelength at the reflection wall from the simulation is shorter than the predictions given by the KP theory.

Using the midpoint rule on the saved simulated results, the approximation to the wave speed c_M at the reflection wall can be obtained (Fig. 8-23) and it is almost constant and independent of the wave amplitude. In addition, $c_M \cos\psi_i \approx 1.0226 > c_i = 1.0204$. A linearly growing stem wave is expected to appear owing to the difference between the speeds on the both sides of the inequation.

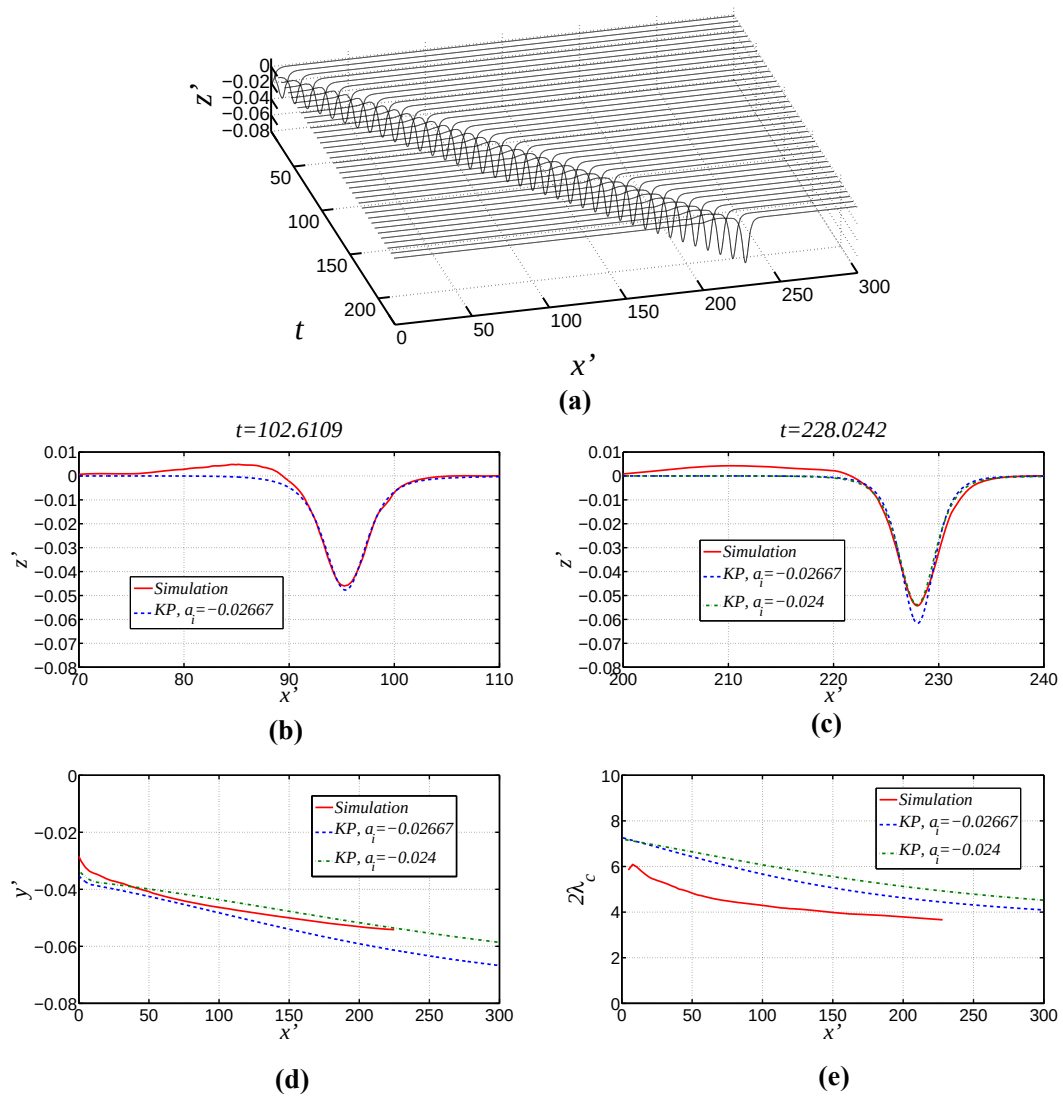

Fig. 8-22 The small incident wave case: (a): The wave profiles at the reflection wall at different times. It starts from t=14.2515, and the time step between adjacent profiles is 5.7006. (b): The simulated wave profile at the reflection wall at *t*=102.6109 and the comparison with the KP theory. (c): The simulated wave profile at the reflection wall at *t*=228.0242 and the comparison with the KP theory. (d): The trough trajectories of the wave at the reflection wall versus the *x*'-coordinates of the wave troughs. (e): Two-fold characteristic wavelengths of the wave at the reflection wall at different times versus the *x*'-coordinates of the troughs.

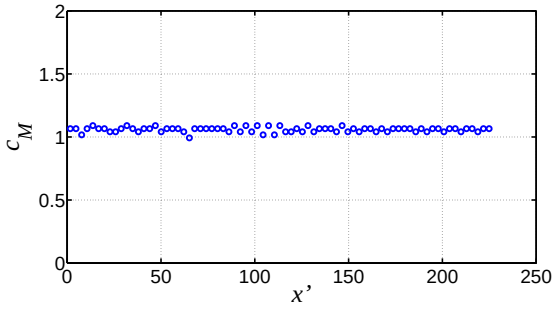

Fig. 8-23 The wave speed at the reflection wall versus the *x'*-coordinates of the wave trough (small incident wave case).

(ii) Moderate incident wave

The time series of the wave profiles at the reflection wall is plotted in Fig. 8-24. The change of the wave shape is gentle and the wave travels at an approximately constant speed. A tailing elevation zone is noticeable and stretching.

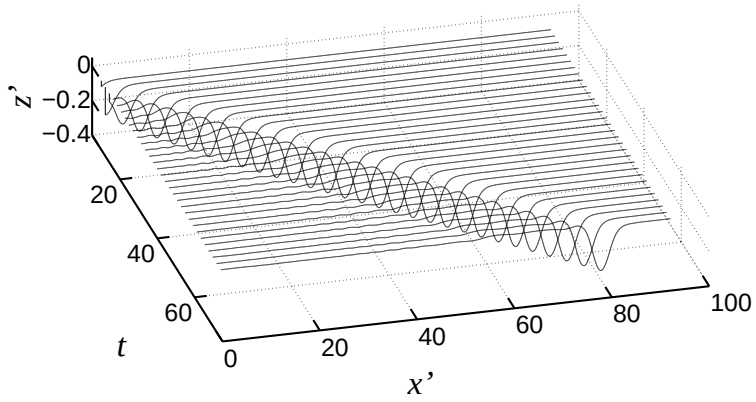

Fig. 8-24 The wave profiles (smoothed) at the reflection wall at different times (moderate incident wave case). It starts from t= 10.6886, and the time step between adjacent profiles is 2.1377.

The developed wave profile at t=62.7067 is compared with the KP and EKP theories in Fig. 8-25. Taking into account the numerical error, the solutions of the KP and EKP equations with a 10% smaller incident wave amplitude are also calculated. When $a_i = -0.12$, $\kappa = 0.7894 < 1$ and it is still in the Mach reflection regime according to the KP theory. From Fig. 8-25, the simulated wave profile does not match the solutions of the approximate models. Besides the difference on the wave amplitude, the simulated wave profile is broader than both the KP and EKP results and the interface steepness from the simulation is gentler.

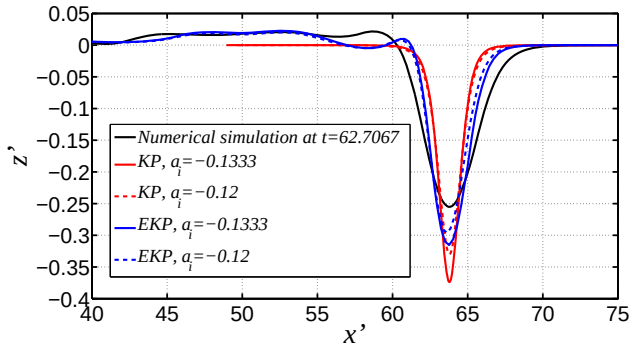

Fig. 8-25 Comparison of the simulated wave profile at the reflection wall at t=62.7067 and the solutions of the KP and EKP equations (moderate incident wave case).

Fig. 8-26 shows the two-fold characteristic wavelength at the reflection wall from the simulation is larger than both the KP and EKP theories. The simulation suggests weaker dispersive effect than that predicted by the KP or EKP theory.

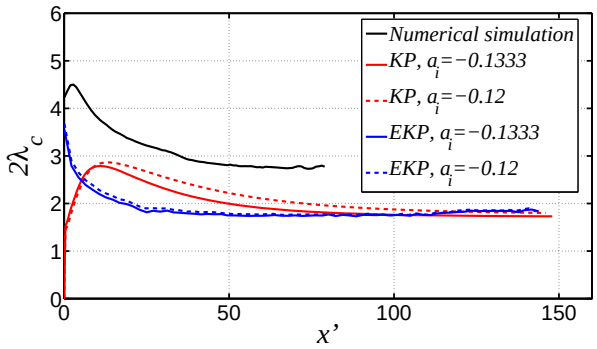

Fig. 8-26 Two-fold characteristic wavelengths of the wave profiles at the reflection wall at different moments versus the *x*'-coordinates of the troughs (moderate incident wave case).

The comparison in terms of the trough trajectory is shown in Fig. 8-27. The maximum amplitude of a single ISW predicted by Eq. (2.55) based on the second-order KdV equation is 0.2143; the maximum possible amplitude of a single ISW given by Eq. (2.54) based on the eKdV equation is 0.2808; the maximum possible amplitude of a single ISW given by Eq. (2.43) based on the MCC equations is 0.3292. It is found that the wave amplitude at the reflection wall is still smaller than that of the maximum possible ISW predicted by the eKdV and MCC models. On the contrary, the KP and the EKP theories predict much larger wave amplitude

than the simulated result. The simulated wave retains large amplitude after the developing stage without breaking.

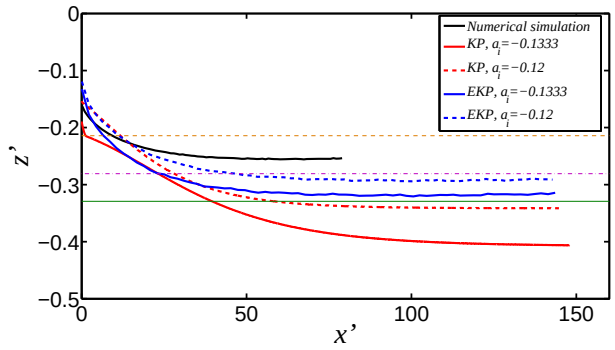

Fig. 8-27 The trough trajectories at the reflection wall (moderate incident wave case). The thin dashed line (orange) designates the limiting interface displacement of an ISW based on the second-order KdV equation given by Long(1956); the thin dot dash line (purple) designates the limiting interface displacement of an ISW based on the eKdV equation; the thin solid line (green) designates the limiting interface displacement of an ISW based on the MCC model.

In Fig. 8-28, the wave profile at the reflection wall is compared with the models for an ISW. The ISW solutions of the second-order and third-order KdV equations are not plotted, for they cannot provide the prescribed convex shape with that large amplitude. The KdV model is quite different from the simulated wave profile. The eKdV model and the MCC model fit the simulated wave profile well. Let us further compare the wave speed. Using the midpoint rule on the saved simulation results, the approximation to the wave speed at the reflection wall c_M can be obtained (Fig. 9-29). It seems that c_M is constant, which is approximately 1.259. The ISW speeds of the same amplitude given by the eKdV theory and the MCC theory are 1.138 and 1.144, respectively. Therefore, the wave at the reflection wall is different from a 2D steadily progressing ISW.

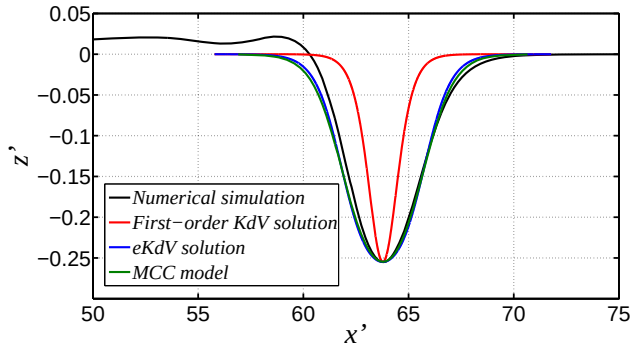

Fig. 8-28 Comparison of the simulated wave profile at the reflection wall at t=62.7067 (moderate incident wave case) and the analytical solutions of a single ISW.

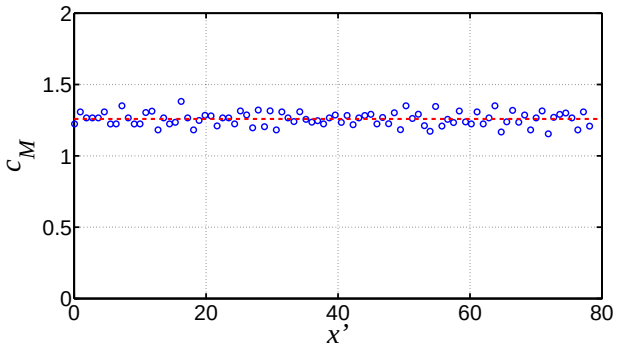

Fig. 8-29 The wave speeds at the reflection wall versus the *x'*-coordinates of the wave troughs at different moments (moderate incident wave case).

The phenomenon observed in the oblique reflection of a moderate-amplitude ISW is quite different, in terms of the wave profile at the reflection wall, from that in the oblique reflection of a moderate-amplitude SSW. To have some in-depth understanding of the mechanisms behind the different phenomena, we can look into the governing equations and the boundary conditions introduced in Chapter 2. In the framework of the potential theory, the difference between the surface wave model and the two-layer model is between the dynamic boundary conditions on the surface and the interface. More specifically, the core problems are in the nonlinear term in Eq. (2.5), *i.e.*, $\frac{1}{2}\left|\nabla\Phi\right|^2$ and the one in Eq. (2.21), *i.e.*, $\frac{1}{2}\left(\rho_1\left|\nabla\Phi_1\right|^2-\rho_2\left|\nabla\Phi_2\right|^2\right)$. The 2D SSWs and ISWs are taken as examples to understand the similarities and differences between the surface wave problem and the internal wave problem. It is

obviously that if $\rho_2 \ll \rho_1$ and $H \gg h$, the two-layer model (Figs. 2-4(a) & (b)) can be reduced to the surface wave model (Fig. 2-1). We will discuss how the conditions that $\rho_2 \approx \rho_1$ and $H/h \sim 1$ affect the behaviours of the ISWs. The KdV theory actually defines the relation between the vertical scale (ε) and the horizontal scale (β) by the Ursell condition. It implies that the characteristic wavelength becomes shorter as the wave amplitude is higher and the density does not affect this monotonicity. It is true for both SSW and ISW of small amplitude (Byatt-Smith, 1970; Evans and Ford, 1996). Byatt-Smith (1970) has shown the scaling relation implied by the KdV theory is still valid for the SSW of large amplitude via the fully nonlinear solutions. The kinematic breaking condition limits the maximum possible amplitude of an SSW (Longuet-Higgins and Fenton, 1974). By contrast, the density ratio between the two layers, *i.e.*, becomes significant when the amplitude of an ISW is large reflected in the wave profile (Evans and Ford, 1996). It suggests that the oceanic condition or $\rho_2 \approx \rho_1$ used in the 3D simulation is not important to the scaling relations in the small incident wave case, but important to those in the moderate incident wave case or the wave of large amplitude occurring at the reflection wall. We also have to take into account the depth ratio in the two-layer model or $(H-h)/h$. The 2D solitary wave is still to be used as an example. We can inspect an ISW of elevation (Fig. 2-4(b)) in a moving reference with the wave phase speed. Suppose $\rho_2 \ll \rho_1$ in the two-layer model, but $H \approx h$. As the wave amplitude gets larger, the flow velocity in the upper layer increases due to the continuity constraint in Eq. (3.7). It means that the importance of $\frac{1}{2}\rho_2 \left|\nabla \Phi_2\right|^2$ increases, and it may result in the larger difference from the SSW with $\rho_2 = 0$. In a two-layer model with the conditions of $\rho_2 \approx \rho_1$ and $H/h \sim 1$, there is another condition to limit the maximum possible amplitude of an ISW, which is the conjugate flow state. It is a

state that the ISW has a flat crest/trough and infinite width, and the parallel flows at the mid-section of the wave in the two layers have the opposite horizontal velocities (Benjamin, 1966; Amick and Turner, 1986; Makarenko et al., 2009). The maximum possible amplitude of an ISW (Eq. (2.43)) is the distance between the interface locations at the hydrostatic equilibrium state and the conjugate flow state (can be also seen in Turner and Vanden‐Broeck (1988)). We are concerned with the slowly varying wave profile and assume that the wave profile of an ISW can be gradually changed by injecting energy slowly. The fully nonlinear results show that as the ISW trough/crest is approaching the conjugate flow state, the ISW can broad its width to absorb enormous energy with little increment of its amplitude (Evans and Ford, 1996). The approximate models for a 2D ISW are obtained by expanding terms with the prescribed scaling relations. The KdV theory expands $\left|\nabla\Phi_i\right|^2, i=1,2$ into Taylor series from the quiescent state or the hydrostatic equilibrium, and those terms are all zero at that state. The nonlinear effect measured by ε is proportional to the wave amplitude with the weakly nonlinear assumptions. As mentioned, the small-amplitude ISW can be well modelled by the KdV theory. Nevertheless, it is possible that $\frac{1}{2}\left(\rho_1\left|\nabla\Phi_1\right|^2-\rho_2\left|\nabla\Phi_2\right|^2\right)$ equals zero as a whole in the case that $\left|\nabla\Phi_i\right|^2, i=1,2$ are nontrivial as at the conjugate flow state. It is noted that the hydrostatic equilibrium state is stable, which allows the oscillation of the surface/interface with finite amplitude; the conjugate flow state is unstable, for vortex sheets are aligned adjacent to the interface, the disturbance may grow and cause instability issues (Batchelor, 2000). The largest possible ISW may not be observed in the experiment due to instability, but the potential theory can indeed describe very large ISW precisely (Grue et al., 1999). The interface location at the

conjugate flow state is approximately $\frac{1}{2}H$ from either the top or the bottom rigid lid in case that $\rho_1 \approx \rho_2$ (This condition will also be used in the following discussions). The eKdV equation arose from the consideration of the nearly equal depths of the two undisturbed layers (Michallet and Barthelemy, 1998). In case of nearly equal depths, γ_1 in Eq. (2.50) becomes a small quantity of the order $O(\varepsilon)$. It results in that the quadratic and cubic nonlinear corrections, *i.e.*, $\gamma_1\theta\frac{\partial\theta}{\partial x}$ and $\gamma_3\theta^2\frac{\partial\theta}{\partial x}$ have the same order. The eKdV theory is still based on the weakly nonlinear assumption, *i.e.*, expanding variables from the hydrostatic equilibrium state. However, it happens to well depict some important features of the large-amplitude ISW phenomenally, *e.g.*, the flat plateau-shaped crest/trough, because of the amended scaling relation (Helfrich and Melville, 2006) (Fig. 8-30(b)). Here comes to the contradictory understanding of the nonlinear effect. If we stick to the understanding that the permanent shape of a solitary wave is owing to the balance between the nonlinear effect and the dispersive effect, we will have the following conclusions. Firstly, we still take the shorter characteristic wavelength (λ_c) as the indication of the stronger dispersive effect. The nonlinear effect on an ISW should change accordingly with the dispersive effect as the amplitude varies. In Fig. 8-31, λ_c is plotted versus the wave amplitude. The KdV theory implies that as the amplitude increases, both effects become stronger. The MCC theory does not have a prescribed restriction on ε, and the theory has been validated especially for large-amplitude ISWs (Camassa et al., 2006). From Fig. 8-31, the MCC theory predicts that there is a minimum value of λ_c between the ISWs of small amplitude and the maximum possible amplitude. It implies that the nonlinear effect has a maximum value before the wave amplitude gets to its maximum value. It can be

explained by the aforementioned two equilibrium states, *i.e.*, the hydrostatic equilibrium state and the conjugate flow state. When the interface is nearer to the equilibrium position, the effect of the nonlinear terms on the wave behaviour is less important or the interface is flatter (Fig. 8-30(a)). The characteristic wavelength also has the smallest value before the wave amplitude gets to its maximum value from the eKdV theory (Fig. 8-31). It is because that in Eq. (2.50), γ_1 and γ_3 have the same sign, and the quadratic and cubic nonlinear corrections have the opposite signs. Hence the nonlinear effect is artificially reduced due to the inclusion of the cubic nonlinear correction. That is the reason why the eKdV theory is still valid for large-amplitude ISW. Now that the 2D problem is already complex, the fully nonlinear simulation is needed to study the scaling relations in the 3D internal wave problems without any prescribed scaling relation.

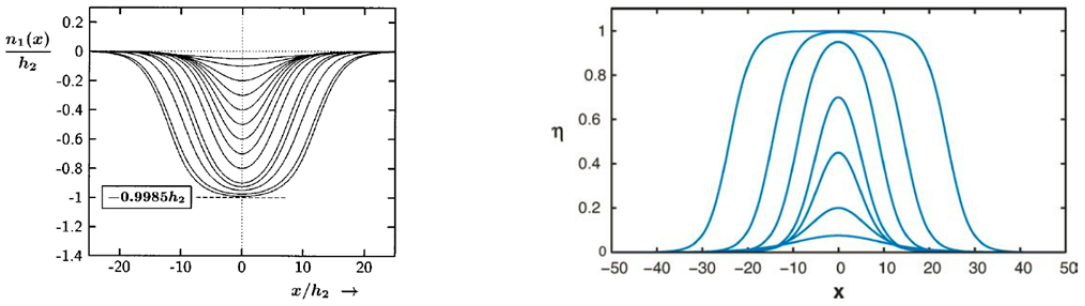

(a) **(b)**

Fig. 8-30 (a): The ISW profiles with different amplitudes given by the fully nonlinear model (Evans and Ford, 1996). The thick dash line indicates the location of the interface at the conjugate flow state. (b): The ISW profiles with different amplitudes given by the eKdV theory (Helfrich and Melville, 2006).

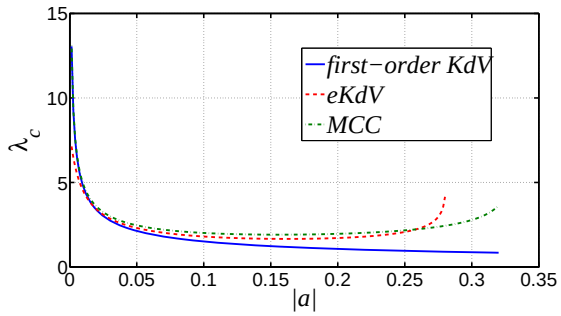

Fig. 8-31 The characteristic wavelength of an ISW versus its amplitude. The ratio between the lower and upper layer depths is 3/1. The ratio between their densities is 1025/1000.

In the 3D simulation, due to the blockage effect of the reflection wall, the energy from the incoming wave can be piled up in the vicinity of the reflection wall. The variation of the energy drives the wave profile at the reflection wall to change. When ψ_i is not large, the energy is slowly accumulated in the vicinity of the reflection wall and the wave profile can change gradually. From Figs. 8-46(f), 8-48(c) and 8-52(c), both the KP theory and the EKP theory predict the potential energy adjacent to the reflection wall per unit transverse length is approaching the same value as the simulated result. However, the wave profile does not agree with the KP theory and the EKP theory. The present simulated result shows that although a huge amount of energy is piled up in the vicinity of the reflection wall, the wave can still have a steady symmetric form about the vertical plane passing its trough and accommodate the energy. The relation between the vertical scale and the horizontal scale is the same as that of a 2D ISW that is governed by the 2D balance between the nonlinear effect and the dispersive effect. According to the properties of the 2D ISW, the density ratio and depth of the two layers must have significant influence on that scaling relation. This internal wave behaviour is first observed, and is not well predicted by the existing approximate models.

The wave amplitude at the reflection wall in the moderate incident wave case is smaller than the maximum possible amplitude of an ISW. It is conjectured that if more energy is injected, the wavelength would increase greatly, but the amplitude would increase little. This phenomenon probably only happens when the interface is near the 2D conjugate flow state (comparing the small incident wave case and the moderate incident wave case). Based on that hypothesis, if there is a gentle upward slope on the seafloor in the propagation direction, the depth of the lower layer will decrease gradually, and the maximum possible amplitude of a 3D ISW will decrease as well. We may expect that the wave amplitude in the vicinity of the reflection wall could be smaller than that on a flat bottom with the same incident conditions.

8.4.4 Transverse length of the stem wave or the hump

(i) Small incident wave

The transverse length of the stem wave is calculated using the method shown in Fig. 8-13(a). The linear growth of the transverse length of the stem wave with the *x'*-coordinate of the trough can be seen from Fig. 8-32. But the growth slopes given by the KP theory are steeper than the simulated result.

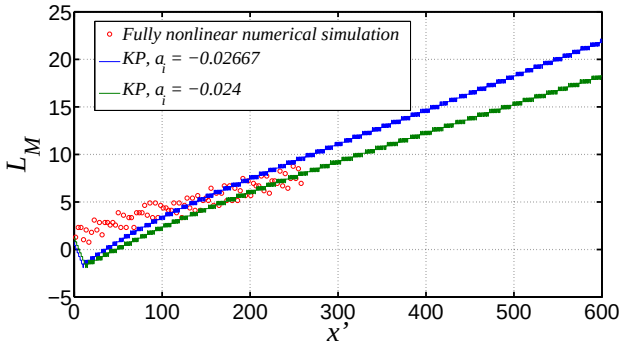

Fig. 8-32 The transverse lengths of the stem wave at different moments versus the *x'*-coordinates of the troughs (small incident wave case).

(ii) Moderate incident wave

The transverse length of the hump (Fig. 8-33) is calculated as that in Fig. 8-13(b). The transverse lengths of the stem wave or hump calculated from the KP and EKP theories are also plotted in Fig. 8-33. The leap among the data points of the EKP theory is because of the error when extracting the trough position from the discrete data. The KP theory is qualitatively different from the simulated result. On the contrary, the EKP theory agrees with the simulated result relatively well. As mentioned, the inclusion of the cubic nonlinear term changes the scaling relation between the interface displacement and the transverse variation implied by the KP equation. The transverse length of the simulated hump is short relative to the characteristic wavelength in the longitudinal direction (Fig. 8-26). It suggests the three-dimensionality in this case is stronger than that predicted by the KP theory.

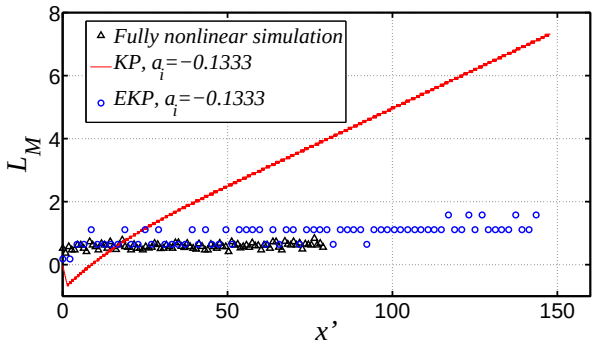

Fig. 8-33 Transverse lengths of the stem wave or hump versus *x'*-coordinates of the troughs at the reflection wall at different moments (moderate incident wave case).

8.4.5 The reflected wave

(i) Small incident wave

The trough line of the reflected wave at the last time step in the simulation has been extracted. From its projection on the *x'y'*-plane (Fig. 8-34(a)), the reflected wave angle ψ_r can be obtained. $\psi_r = 0.356 < \psi_i$. The reflected wave amplitude (measured in a considerable distance away from the reflection wall) $|a_r|$ is smaller

than $|a_i|$ (Fig. 8-34(b)). The transverse cross section of the simulated wave profile (Fig. 8-34(c)) is quite similar to that of the KP theory (Fig. 8-34(d)). For reference, the (3142)-type solution gives $\psi_r = 0.367$ and $a_r = -0.0129$ with a_i=-0.02667 and $\psi_i = \pi/12$.

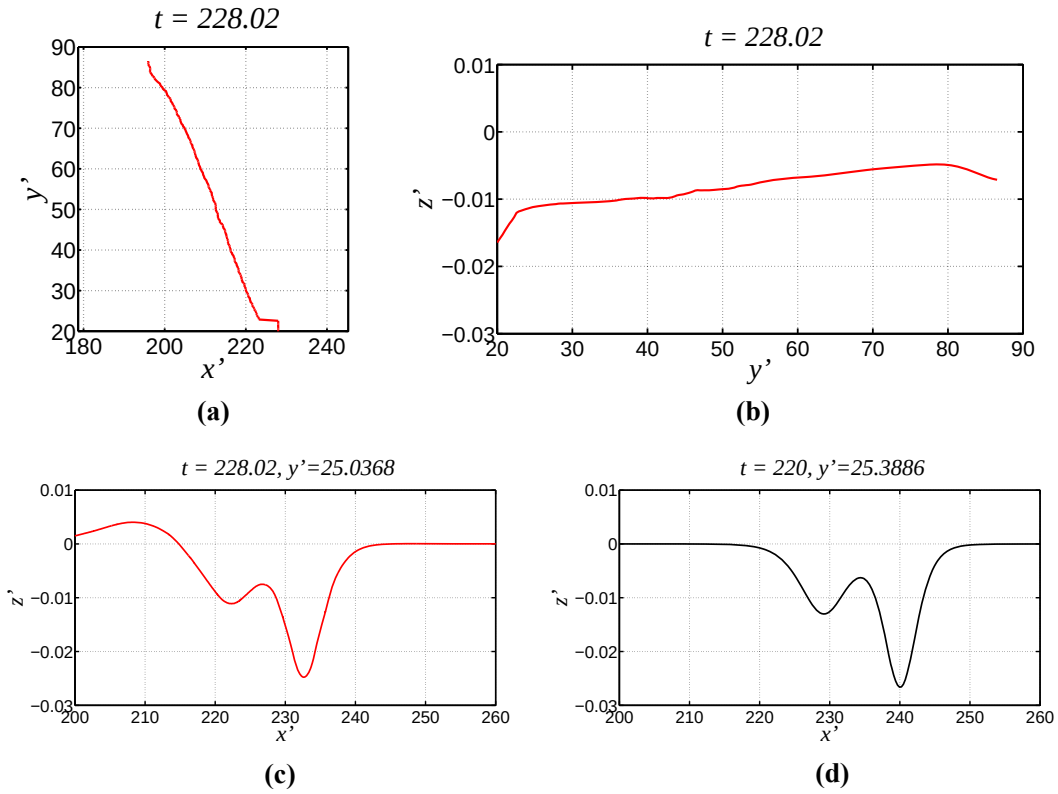

Fig. 8-34 The small incident wave case: (a): The projection of the simulated reflected wave trough line onto the *x'y'*-plane at *t*=228.0242. (b): The projection of the simulated reflected wave trough line onto the *y'z'*-plane at *t*=228.0242. (c): Transverse section at *y'*=25.0368 of the simulated interface at *t*=228.0242. (d) Transverse section at *y'*=25.3886 of the interface at *t*=220 given by the (3142)-type solution of the KP equation with a_i=-0.02667 and $\psi_i = \pi/12$.

(ii) Moderate incident wave

It is found that $\psi_r \approx 0.582$ through the projection of the trough line of the simulated reflected wave at *t*=74.1079 on the *x'y'*-plane. ψ_r is very close to ψ_i. The projection of the trough line onto the *y'z'*-plane is shown in Fig. 8-35. The reflected wave amplitude $|a_r|$ is smaller than the incident wave amplitude $|a_i|$. A cross section of the wave profile is plotted in Fig. 8-36. The reflected waveform on the left

is quite similar to the incident wave on the right, though the amplitude difference is obvious. The reflected wave is tailed by an elevation zone and oscillating trailing waves.

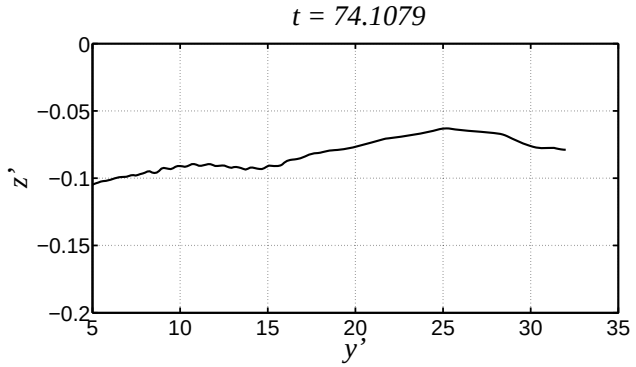

Fig. 8-35 Projection of the trough line of the simulated reflected wave onto the *y'z'*-plane (moderate incident wave case).

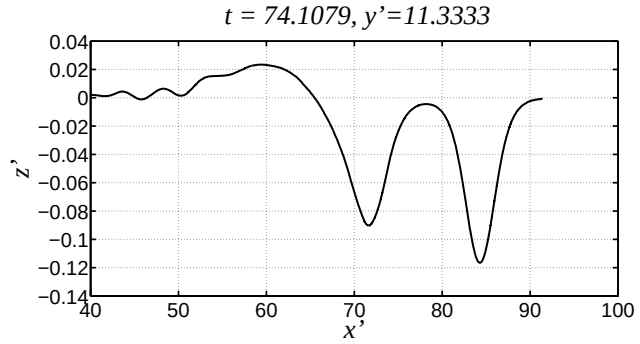

Fig. 8-36 A cross section of the simulated wave profile that is parallel to the reflection wall at *y'*=11.3333 and *t*=74.1079 (moderate incident wave case).

The KP theory gives $a_r = -0.0746$ and $\psi_r = 0.657$. A cross section of the wave profile given by the KP theory is shown in Fig. 8-37, the reflected wave profile on the left is of a solitary wave shape and with small amplitude.

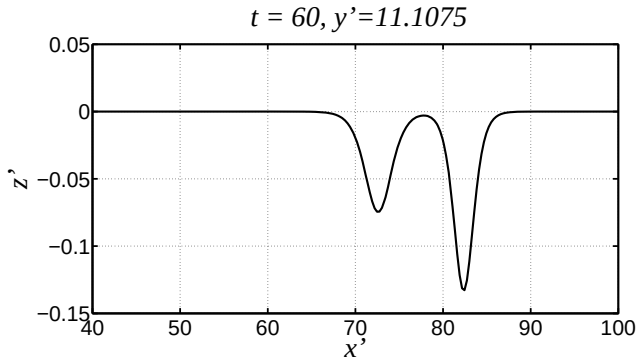

Fig. 8-37 A cross section of the wave profile that is parallel to the reflection wall at y'=11.1075 and t=60 given by the analytical solution of the KP equation (moderate incident wave case).

The EKP theory predicts that $\psi_r = 0.527$. The trough line of the reflected wave given by the EKP theory is projected onto the *y'z'*-plane (Fig. 8-38). The amplitude of the reflected wave that is not far from the reflection wall is already close to the incident wave amplitude. A cross section of the wave profile is shown in Fig. 8-39. The reflected wave profile on the left is very similar to the incident wave profile on the right.

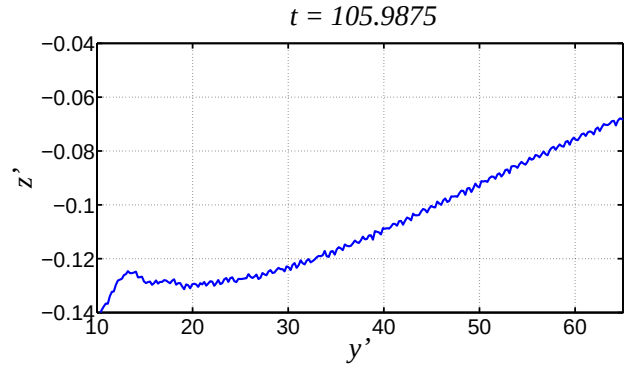

Fig. 8-38 Projection of the trough line of the reflected wave, given by the numerical solution of the EKP equation, onto the *y'z'*-plane (moderate incident wave case).

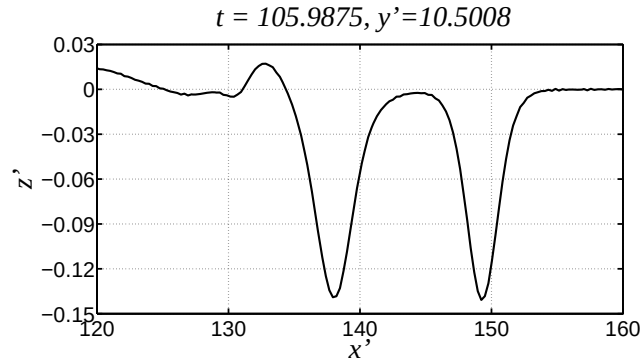

Fig. 8-39 Wave profile slice at *y'*=10.5008 and *t*=105.9875 projected onto the *x'z'*-plane given by the numerical solution of the EKP equation (moderate incident wave case).

8.4.6 The velocity field (moderate incident wave case)

The velocity vector field at the reflection wall at *t*=62.7067 from the simulation is plotted in Fig. 8-40(a). The arrow which anchors at the end point indicates the velocity magnitude and the direction. Note that the velocity has been scaled by c_0. In

the vicinity of the trough, the horizontal gradient of the horizontal fluid velocity in each layer is small and results in the long characteristic wavelength of the wave profile (Fig. 8-26). The vertical gradient of the horizontal fluid velocity in a water column within a layer is small (Fig. 8-40(a)). The horizontal fluid velocity in the water column at the trough at the reflection wall is plotted in Fig. 8-40(b). The first-order approximation implies that the horizontal velocity in each layer is uniform. From Fig. 8-40(b), we can see the higher-order correction to the velocity field is small. But the higher correction can influence the wave profile a lot despite its small magnitude. As a comparison, we draw the horizontal velocity at the trough of the incoming ISW in Fig. 8-40(c), which is the ISW solution of the third-order KdV equation. From Fig. 8-40(c), it can be seen that the higher-order correction on the velocity field is also very small. But as discussed in Chapter 6, the higher-order correction influences the wave profile a lot. The higher-order component of the velocity should also have an important effect on the 3D wave profile. The hump induces stronger shear flow across the interface than the incoming ISW (Figs. 8-40(b) & (c)). The maximum and minimum horizontal fluid velocities in the water column at the trough during the development of the wave at the reflection wall are compared with the KP and EKP theories in Fig. 8-41. The horizontal fluid velocity in the lower layer agrees with theories well, but the theories overestimate the horizontal fluid velocity in the upper layer.

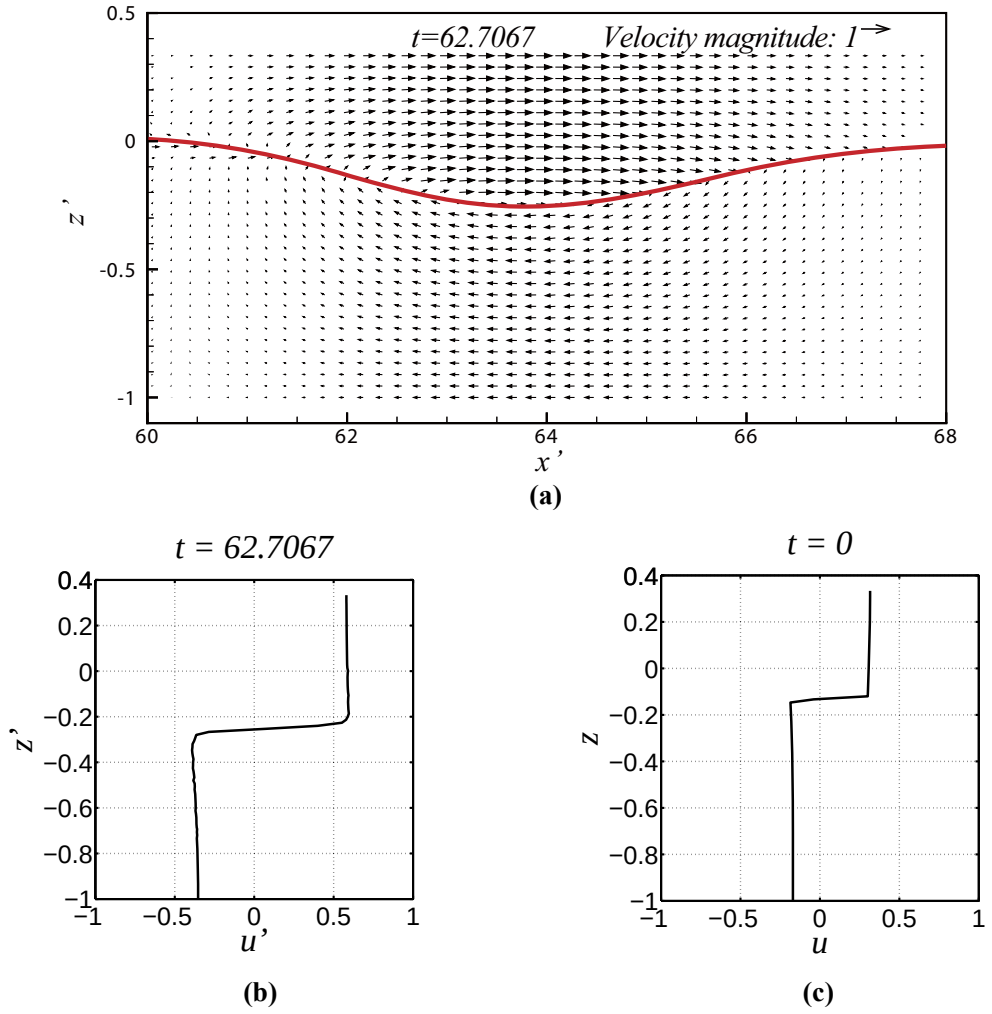

Fig. 8-40 The moderate incident wave case: (a): The simulated velocity vector field at the reflection wall at t=62.7067. The interface profile is plotted by the thick line. (b): The simulated horizontal fluid velocity in the water column at the trough. (c): The horizontal fluid velocity in the water column at the trough of the incoming ISW.

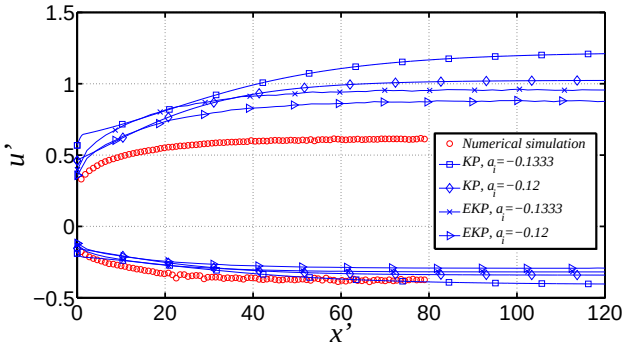

Fig. 8-41 The maximum horizontal fluid velocities (markers above *u'*=0) and minimum horizontal fluid velocities (markers below *u'*=0) in the water column at the trough of the wave at the reflection wall versus the *x'*-coordinates of the troughs (moderate incident wave case).

For the safety of the offshore industry, it is important to evaluate the wave loads on the riser when internal waves pass it. The riser can be simplified as a tubular structure with a small external diameter that is denoted by *d*. In case that $d/\lambda_c \ll 0.15$, the loads on the riser can be estimated solely by the incoming wave field (Morison et al., 1950). In this context, *d* is also supposed to be very small relative to the transverse scale of the wave field. The Morison equation is appropriate to estimate the horizontal hydrodynamic force on the riser exerted by internal waves (Cai et al., 2003). The horizontal force per unit length imposed on the riser can be written as (in dimensional form)

$$F_h = F_I + F_D = \rho_i g C_M \frac{\pi d^2}{4}\frac{\partial u_i}{\partial t} + \frac{1}{2}\rho_i g d C_D u_i |u_i|, i = 1,2 \qquad (8.1)$$

where F_I is the inertial force, F_D is the drag force, C_M is the inertial coefficient, C_D is the drag coefficient. Song et al. (2011) have shown that the magnitude of F_I is much smaller than the magnitude of F_D on a Spar platform exerted by internal waves, for $\max\left\{\left|\frac{\partial u_i}{\partial t}\right|\right\} \ll \max\left\{u_i^2\right\}, i = 1,2$. Suppose the coefficients remain unchanged, F_I is proportional to d^2, and F_D is proportional to d. As d decreases, $|F_I|$ decreases faster than $|F_D|$. The riser has much smaller transverse dimension than the Spar platform, F_I is negligible or $F_h \approx F_D$. C_D can be quite different in case of various complex viscous flows. At present, C_D is assumed to be a constant for simplicity. F_h is nondimensionalised by $\frac{1}{2}\rho_1 g d C_D c_0^2$. $|F_D|$ is proportional to $u_i^2, i = 1,2$ and F_D will have a maximum magnitude when the wave trough passes the riser. We will consider two flow fields. One is shown in Fig. 8-40(b). The other is shown in Fig. 8-40(c). When knowing the wave loads, the riser is further simplified as a beam. Two support conditions are taken into account. One

case is a cantilever beam with a free upper end and a fixed bottom end (Fig. 8-42(a)). The other is a cantilever beam with a fixed upper end and a free bottom end (Fig. 8-43(a)). The shear force and bending moment diagrams for the riser are shown in Figs. 8-42(b)-(e) & 8-43(b)-(e). From Figs. 8-42(b)&(d) and 8-43(b)&(d), the local maximum magnitude of the shear force happens at the intersection between the interface and the riser for all the scenarios. It is because that the approximately uniform flows in the two layers have the opposite directions. Fig. 8-43(b) shows the shear force magnitude at the end of the riser (upper end in the figure) can also be very large. Comparing Figs. 8-42(b) & (d), the internal wave with larger amplitude results in the stronger shear flows and larger shear force. The same conclusion can be drawn from Figs. 8-43(b) & (d). However, the maximum magnitudes of the shear force with different support conditions can be different, *e.g.*, Figs 8-42(b) & 8-43(b). Figs. 8-42(c)&(e) and 8-43(c)&(e) show that the maximum magnitude of the bending moment may occur at different positions other than the intersection between the interface and the riser. It suggests that it is more difficult to predict the vulnerable spot at risk of failure in bending than that at risk of failure in shear. When the bottom end of the riser is fixed, the maximum bending moments occur at the bottom (Figs. 8-42(c)&(e)). It suggests that the structural element near the sea floor is more vulnerable to the failure in bending than the upper part. If the riser was broken in deep water, it would be very difficult to repair it and would probably lead to the severe oil spill. When the upper end of the riser is fixed, the bending moment of the maximum magnitude is likely to happen near the upper end (but does not necessarily happen at the upper end) as shown in Figs. 8-43(c)&(e). In offshore engineering practice, there is usually a connector between the short rigid riser attached to the platform and the long flexible riser in the deep water. Large bending momentum may

induce large tensile stress within the structure and snap the connector in the upper ocean.

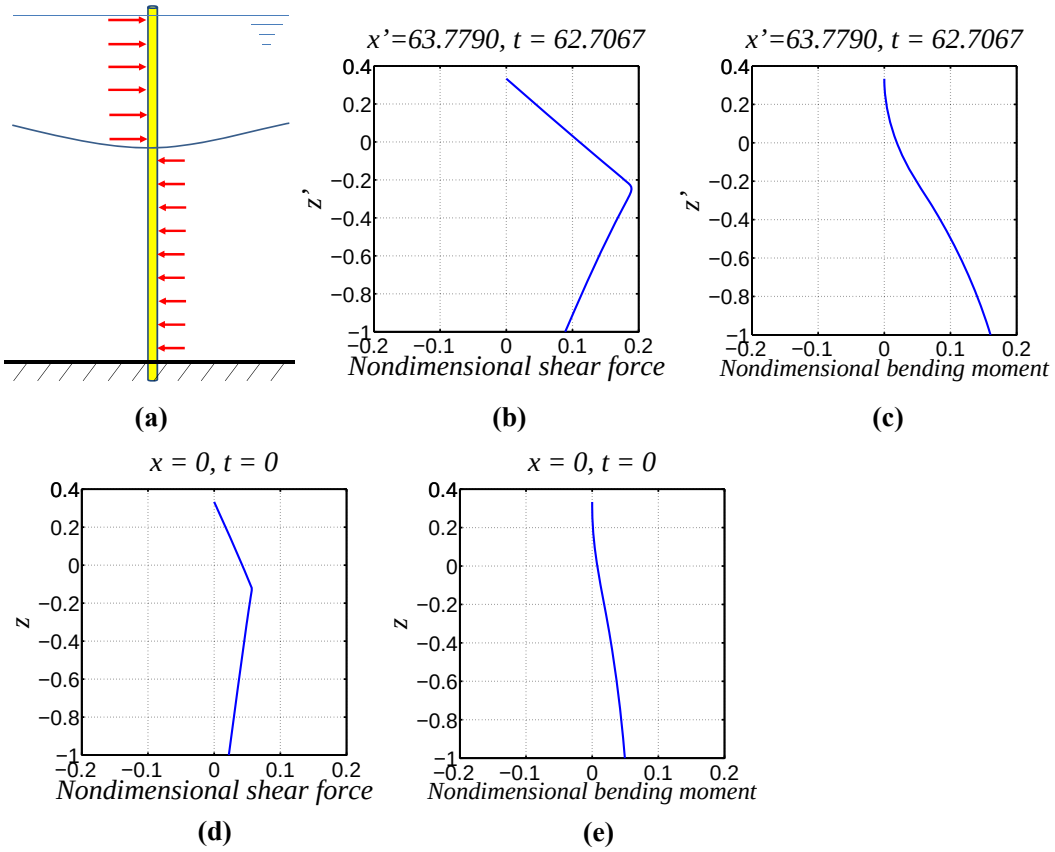

Fig. 8-42 (a): A schematic diagram of the internal wave load on a riser with a free upper end and a fixed bottom end. The shear force diagram (b) and bending moment diagram (c) of the riser exposed in the flow field shown in Fig. 8-40(b). The shear force diagram (d) and bending moment diagram (e) of the riser exposed in the flow field shown in Fig. 8-40(c).

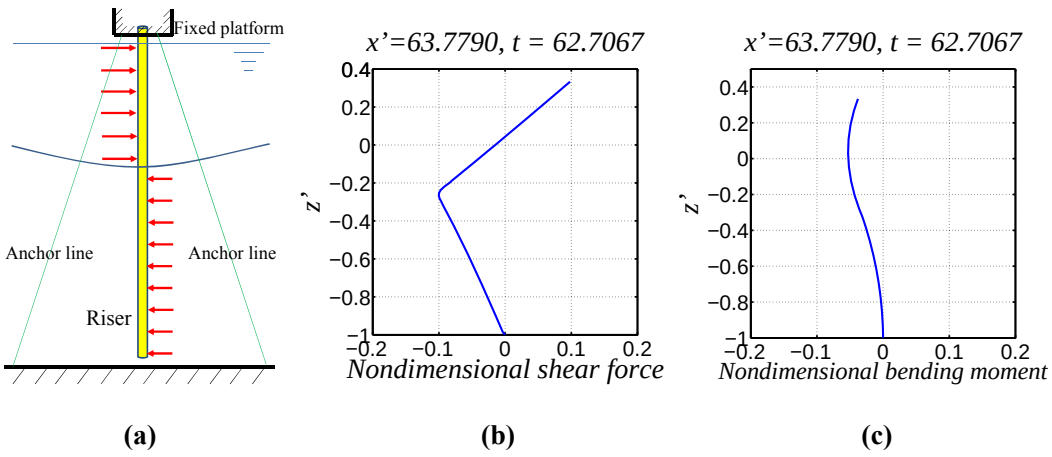

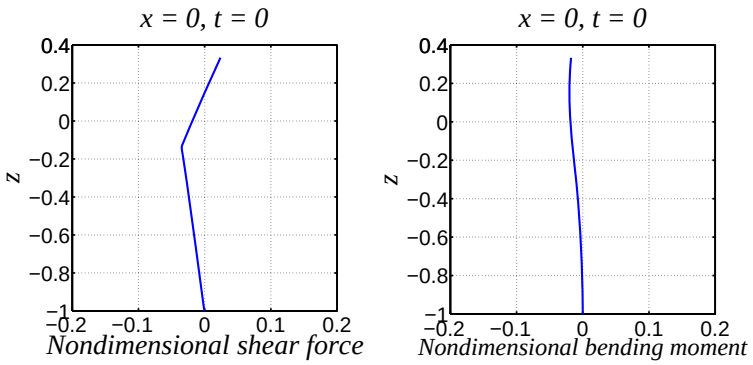

(d) **(e)**

Fig. 8-43 (a): A schematic diagram of the internal wave load on a riser with a fixed upper end and a free bottom end. The shear force diagram (b) and bending moment diagram (c) of the riser exposed in the flow field shown in Fig. 8-40(b). The shear force diagram (d) and bending moment diagram (e) of the riser exposed in the flow field shown in Fig. 8-40(c).

The velocity field in the vicinity of the reflection wall is complicated as shown in Figs. 8-44 (b) & (c). We are concerned about how the wave is reflected by the wall, how the physical quantities, *e.g.*, mass, momentum and energy, are transferred in the transverse direction and how the 3D effect influences the transfer processes and the wave pattern. In the next section, we will use the control volumes to analyse the velocity field as well as other quantities.

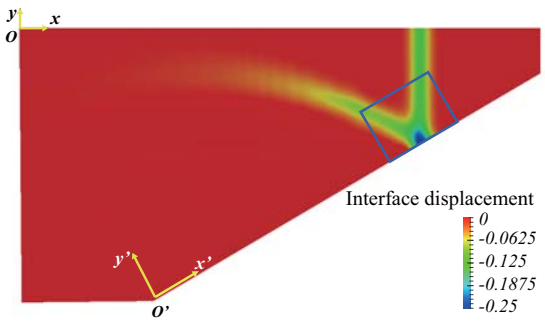

(a)

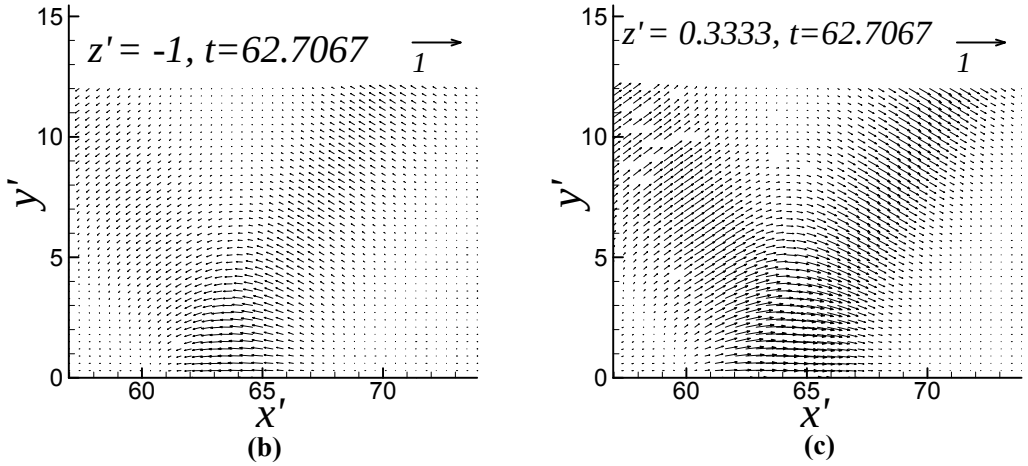

Fig. 8-44 The moderate incident wave case: (a): Plan view of the sampling area, which is within the blue rectangular box. The wave profile at t=62.7067 is shown by the contour plot. (b): The velocity vector field at the bottom. (c): The velocity vector field at the ceiling.

8.4.7 Transverse transfers of the mass, momentum and energy

The oblique reflection wall poses the 3D effect on the flow field and results in the disturbance in the transverse direction. Complex 3D flows can happen in the two layers, as long as the pressure is continuous across the interface. The approximate models assume the long transverse variation scale or the weak three-dimensionality, and the three-dimensionality has a prescribed ratio to the weak nonlinearity. Larger $|a_i|$ corresponds to the stronger nonlinear effect, and the larger ψ_i corresponds to the stronger 3D effect in the KP theory. Either the weaker 3D effect or the stronger nonlinear effect results in the smaller value of the interaction parameter (Eqs. (2.56) & (2.61)) and the wave pattern is more prone to a Mach reflection (Fig. 2-5). The simulated transverse length of the stem wave in small incident wave case qualitatively agrees with the KP theory (Fig. 8-32), which supports the validity of its assumptions. The KP theory also implies that the density and depth ratios of the two layers still have insignificant influence on the transverse variation scale when the interface displacement is small. The EKP theory assumes that the nonlinearity is of

the order $O\left(\varepsilon^2\right)$ and is weaker than that predicted by the KP theory. The weak three-dimensionality assumption remains in the EKP theory. Hence the EKP theory yields the regular reflection pattern rather than the Mach reflection pattern because of the weaker nonlinearity. The EKP theory only reveals the significant influence of the density and depth ratios of the two layers on the wave motion in the longitudinal direction when the interface displacement is large. However, the nonlinear wave interaction may result in multi-scale transverse disturbance or different transverse variation scales at different locations. The 3D effect may be influenced by the vertical interface displacement, the curvature of the wave profile and the density and depth ratios of the two layers. The fully nonlinear results will show that the local 3D effect in the vicinity of the reflection wall in the internal wave cases is actually stronger than predictions given by the theories with the weak three-dimensionality assumption (KP and EKP). The enhanced local 3D effect should be a significant factor to influence the global wave pattern due to the long interaction time. We will discuss the 3D effect via analyses on the transverse transfers of the physical quantities.

Two basic control volumes, which are denoted by Ω and Ω', respectively, have the same horizontal layouts as Fig. 7-17. The difference is that they are bounded by the top and bottom rigid lids in the vertical direction. In order to investigate the momentum in each layer, the control volume can be further divided into two subdomains separated by the free interface. The subscripts 1 and 2 mark the lower layer and the upper layer, respectively. To analyse the transverse excess mass, momentum and energy transfers, Ω' can be translated in the *y*'-direction with an offset value (Fig. 7-18). The quantities in those different control volumes are marked

by the offset value that is denoted by y'_{offset}. Taking into account the different cell sizes in the simulation, the thickness of slices for the small incident wave case is 1, while the thickness of slices for the moderate incident wave case is 0.4. The variable without a prime is used to denote a quantity about Ω, and the variable with a prime is used to denote a quantity in Ω' or in a control volume that is parallel to Ω' (Fig. 7-18). The physical quantities will be defined in dimensional forms to express their physical meanings. But their units will be eliminated by the normalisation in the analysis. We can define the excess mass of the wave in the control volume as

$$M = (\rho_2 - \rho_1)\iint \theta dxdy, \quad \text{or} \quad M' = (\rho_2 - \rho_1)\iint \theta dx'dy', \tag{8.2}$$

where $\iint$ means integration over the bottom area of the control volume. For the total momentum in the *x*-direction or *x'*-direction in the lower or upper layer

$$I_{xi} = \rho_i \int_{\Omega_i} u_i d\Omega_i, \quad \text{or} \quad I'_{x'i} = \rho_i \int_{\Omega'_i} u'_i d\Omega'_i; \quad i = 1,2, \tag{8.3}$$

where u_i is a velocity component of $\mathbf{u}_i = (u_i, v_i, w_i)$; $i = 1,2$, u'_i is a velocity component of $\mathbf{u}'_i = (u'_i, v'_i, w'_i)$; $i = 1,2$. For the kinetic energy

$$E_K = \frac{1}{2}\int_{\Omega_1} \rho_1 |\mathbf{u}_1|^2 d\Omega_1 + \frac{1}{2}\int_{\Omega_2} \rho_2 |\mathbf{u}_2|^2 d\Omega_2, \quad \text{or}$$

$$E'_K = \frac{1}{2}\int_{\Omega'_1} \rho_1 |\mathbf{u}'_1|^2 d\Omega'_1 + \frac{1}{2}\int_{\Omega'_2} \rho_2 |\mathbf{u}'_2|^2 d\Omega'_2. \tag{8.4}$$

For the potential energy

$$E_P = \frac{1}{2}(\rho_1 - \rho_2) g \iint \theta^2 dxdy, \quad \text{or} \quad E'_P = \frac{1}{2}(\rho_1 - \rho_2) g \iint \theta^2 dx'dy'. \tag{8.5}$$

For the total energy

$$E = E_K + E_P, \quad \text{or} \quad E' = E'_K + E'_P. \tag{8.6}$$

The time histories of the physical quantities calculated in Ω for the small-amplitude case and the moderate-amplitude case have been plotted in Figs. 8-45(a)-(i). The

superscript (0) is used to denote the integral value at the initial time. The excess mass (Figs. 8-45(a) & (d)), horizontal momentum (Figs. 8-45(b) & (f)) and energy (Figs 8-45(c), (h) and (i)) first decline slightly due to the numerical error and then vary abruptly due to the wave reflected from the reflection wall. The vertical velocity field without the disturbance from the reflected wave is anti-symmetric about the vertical plane passing through the trough in each layer (Figs. 8-45(b) & (f)). 2D simulated results for an ISW with the same amplitude as the moderate-amplitude incident wave are particularly compared with the 3D results in Figs. 8-45(e) & (g). The comparisons show the offshore wall has influence on the global wave pattern from an early stage. But the influence is gentle at the beginning, and becomes obvious near the end of the simulation.

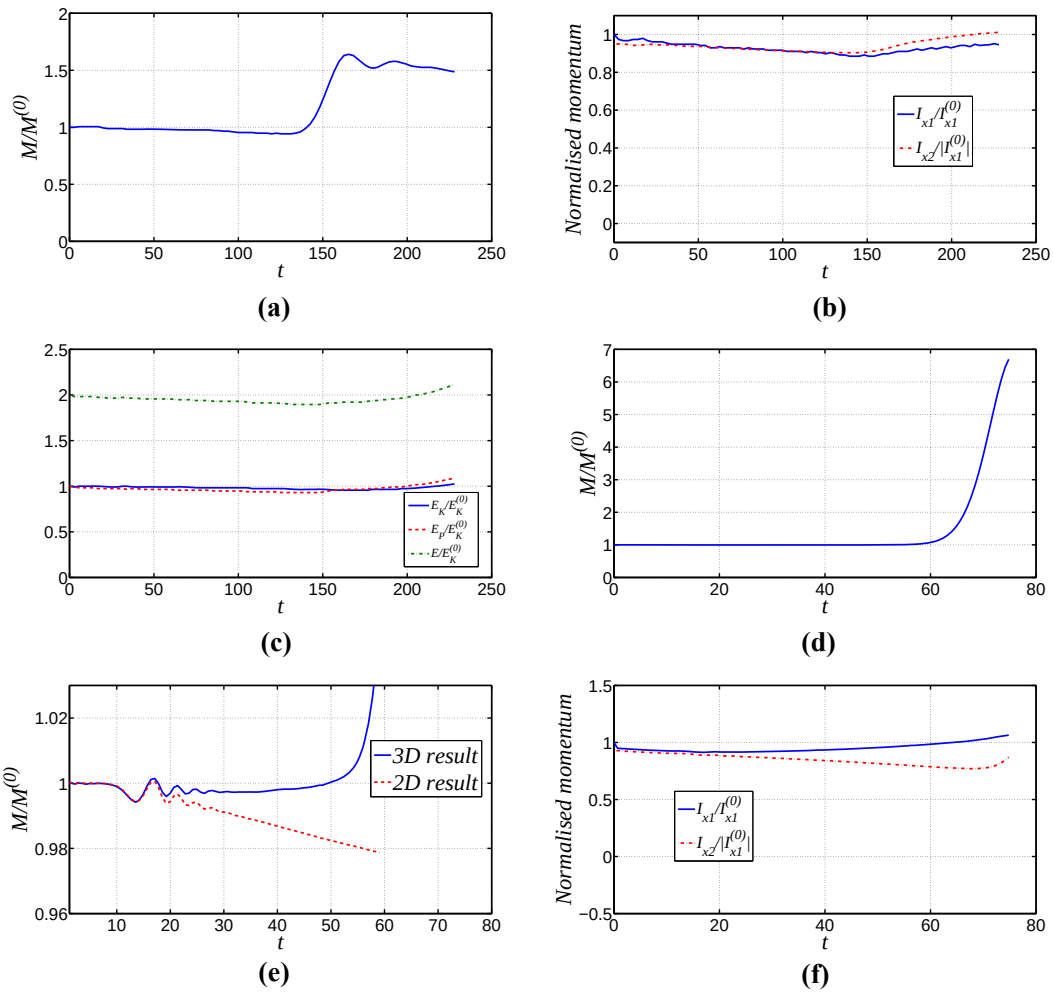

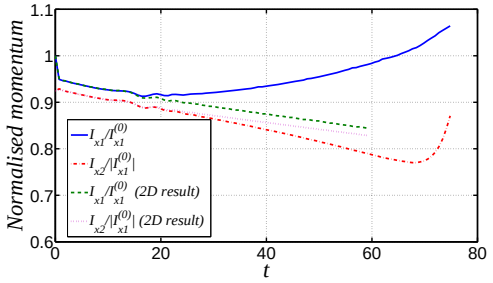

(g)

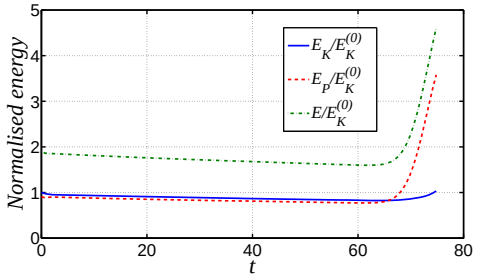

(h)

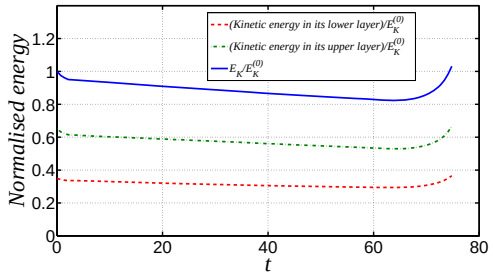

(i)

Fig. 8-45 The small incident wave case: M in Ω, which is normalised by $M^{(0)}$, versus time (a); I_{x1} and I_{z1} in the lower layer of Ω, I_{x2} and I_{z2} in the upper layer of Ω, which are normalised by $I_{x1}^{(0)}$ or $\left|I_{x1}^{(0)}\right|$, versus time (b); E_K, E_P and E in Ω, which are normalised by $E_K^{(0)}$, versus time (c). The moderate incident wave case: M in Ω, which is normalised by $M^{(0)}$, versus time (d) and comparison with 2D result for a single ISW (e); I_{x1} and I_{z1} in the lower layer of Ω, I_{x2} and I_{z2} in the upper layer of Ω, which are normalised by $I_{x1}^{(0)}$ or $\left|I_{x1}^{(0)}\right|$, versus time (f) and comparison with 2D result for a single ISW (g); E_K, E_P and E in Ω, which are normalised by $E_K^{(0)}$, versus time (h) and comparison with the kinetic energy in each layer (i).

The KP theory for internal waves implies an additional relation between the tangential fluid velocities to the reflection wall in the two layers due to its weak three-dimensionality assumption. The leading order approximations of the tangential momentums to the reflection wall in the lower layer and the upper layer at a section that is parallel to the *x'z'*-plane are $\rho_1 c_0 \int_{-\infty}^{+\infty} \theta dx'$ and $-\rho_2 c_0 \int_{-\infty}^{+\infty} \theta dx'$, respectively. Those expressions are again used to estimate the momentums in the control volumes. Hence, the KP theory predicts that $\left|I'_{x'1}\right| / \left|I'_{x'2}\right| \approx \rho_1 / \rho_2 \approx 1$ at any control volume that is parallel to the reflection wall (Figs. 8-46(b) & (e)). From the comparison of the 2D

simulation for an ISW and the 3D simulated result in Fig. 8-45(g), the momentum relation holds in the 2D fully nonlinear simulation no matter of the numerical dissipation, but it may not hold in the 3D problem. The horizontal momentums from the 2D simulation of an ISW of large amplitude are plotted versus time in Fig. 8-47. It is case shown in Fig. 6-20(a). It can be seen that the horizontal momentums in the two layers are still approximately equal for the 2D internal wave of large amplitude. Therefore, if $\left|I'_{x'1}\right|$ and $\left|I'_{x'2}\right|$ are quite different in a control volume, it suggests strong three-dimensionality in that volume.

As discussed in the surface wave case, the KP theory predicts that the excess mass and the tangential momentums to the reflection wall would not be accumulated in the vicinity of the reflection wall, but the energy would be accumulated in the vicinity of the reflection wall to generate the stem wave with larger amplitude (Figs. 8-46(a)-(f)). The parallel lines for $\left|I'_{x'1}\right|$ and $\left|I'_{x'2}\right|$ in Figs. 8-46(b) & (e) imply that the transverse momentum transfers in the two layers are of proportional rates.

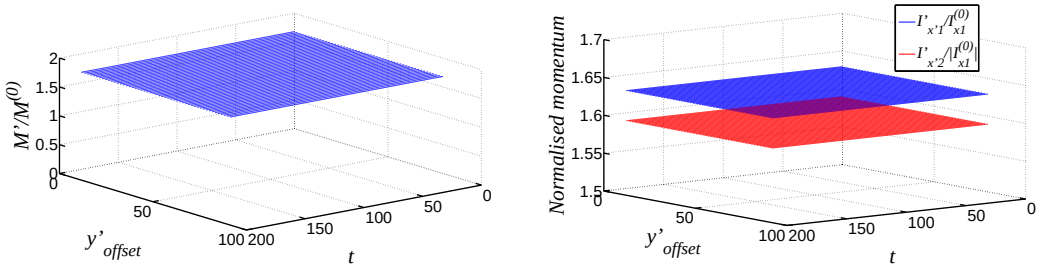

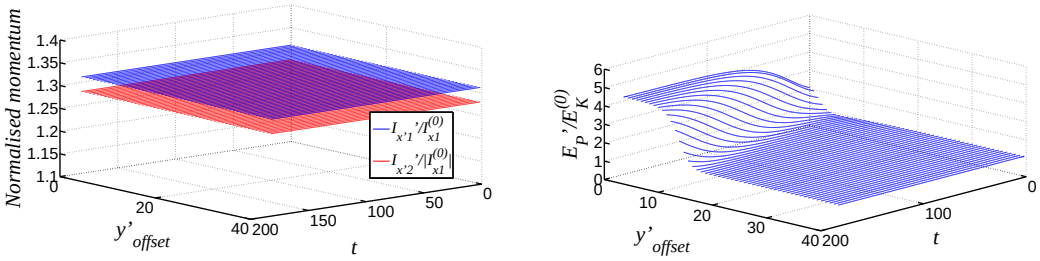

(e) **(f)**

Fig. 8-46 M' **(a),** $I'_{x'1}$**,** $I'_{x'2}$ **(b) and** E'_P **(c) predicted by the (3142)-type solution of the KP equation for the small incident wave case.** M' **(d),** $I'_{x'1}$**,** $I'_{x'2}$ **(e) and** E'_P **(f) predicted by the (3142)-type solution of the KP equation for the moderate incident wave case.**

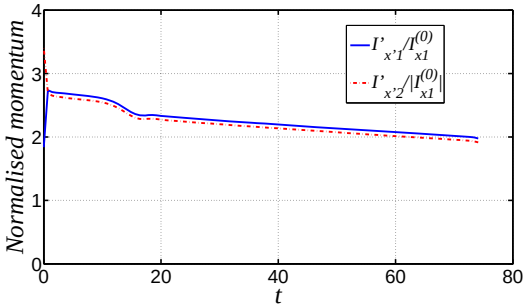

Fig. 8-47 The horizontal momentums of both layers in the 2D simulation of an ISW with large amplitude (numerical case shown in Fig. 6-20(a)). The momentums are normalised by the initial momentum in the lower layer in this case.

The numerical result of the EKP equation with a V-shape initial condition can be also cut into sections and multiplied by the thickness of the control volume. The excess mass, momentum and energy in the slices versus y'_{offset} and time are plotted in Figs. 8-48(a)-(c). From Fig. 8-48(b), it can be seen that the EKP theory predicts the flow in each slice that is parallel to the *x'z'*-plane is still quasi-2D, which is consistent with the KP theory

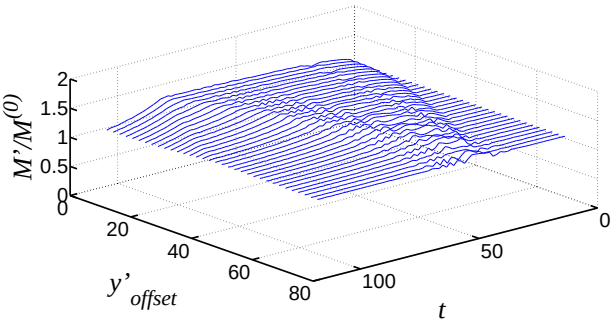

(a)

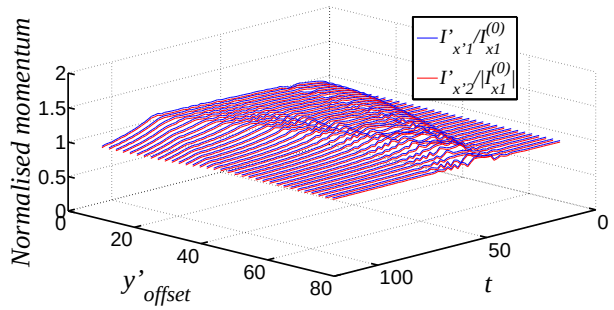

(b)

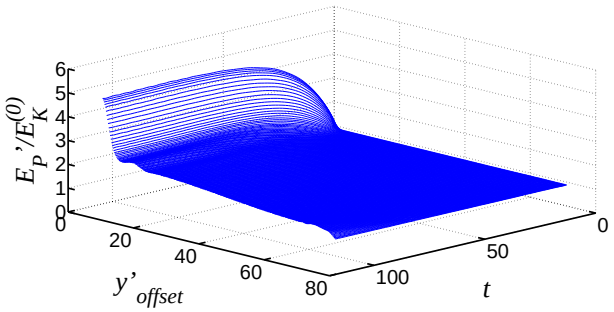

(c)

Fig. 8-48 M' **(a),** $I'_{x'1}$, $I'_{x'2}$ **(b) and** E'_P **(c) predicted by the numerical solution of the EKP equation for the moderate-amplitude ISW case.**

The small incident wave case is firstly analysed. The time histories of the physical quantities in Ω' are plotted in Figs. 8-49 (a)-(d). After the initial impingement period, the excess mass stays constant (Fig. 8-49 (a)), and the potential energy increases (Fig. 8-49 (c)) as predicted by the KP theory (Figs. 8-46(a) & (c)). But, the excess mass in Ω' is overestimated by the KP theory, though the potential energy matches the theory relatively well. As discussed, the injected energy from the incident wave drives the wave profile at the reflection wall to change, and the wave

profile is approximately governed by the nonlinear effect and the dispersion effect in the longitudinal direction. Hence, the numerical error is not the only reason to lead to the deviation between the simulated wave profile and the KP theory in Figs. 8-22(b)-(e). Another reason is that the transverse transfer of the excess mass is not well predicted by the KP theory. The kinetic energies in both layers grow with the potential energy (Figs. 8-49 (c) & (d)). The difference between the tangential momentums to the reflection wall in the two layers gets larger with time (Fig. 8-49(b)). It suggests that as the amplitude of the stem wave gets larger (Fig. 8-22(d)), the 3D effect on the flow field adjacent to the reflection wall becomes stronger.

The physical quantities in the control volumes that are parallel to the *x'z'*-plane are plotted in Figs. 8-50(a)-(d). The transverse variations of the excess mass (Fig. 8-50(a)) and potential energy (Fig. 8-50(d)) agree with the KP theory qualitatively (Figs. 8-46(a) & (c)). However, Figs. 8-50(b) & (c) show complicated variations of the momentums in the two layers. In control volumes that are near the reflection wall, the difference between $\left|I'_{x'1}\right|$ and $\left|I'_{x'2}\right|$ gets larger with time, which indicates stronger 3D effect. The 3D effect near the end of the simulated duration is approximately the strongest at $y'_{offset} = 8$. From Fig. 8-32, that is approximately the position of the junction of the incident wave, the stem wave and the reflected wave. Let us further look into the physical quantities in a control volume that is sufficiently far away from the reflection wall, where the reflected wave and the incident wave are separated, say $y'_{offset} = 40$ (Figs. 8-51(a)-(c)). Both the excess mass (Fig. 8-51(a)) and the momentums (Fig. 8-51(b)) approximately remain constants from $t \approx 60$

after the tip of the reflected wave passes the slice. Fig. 8-51(b) shows $\left|I'_{x'1}\right| \approx \left|I'_{x'2}\right|$ and suggests a quasi-2D flow field.

To sum up, the global 3D effect is supposed to be very weak by the KP theory because of the very small ψ_i in this case. However, the local 3D effect in the vicinity of the reflection wall is enhanced by the nonlinear wave interaction. The local 3D effect is approximately the strongest at the junction of the incident wave, the stem wave and the reflected wave. In the vicinity of the reflection wall, the 3D effect is stronger when the interface displacement becomes larger. The stronger local 3D effect may reduce the elongating rate of the stem wave in the transverse direction (Fig. 8-32).

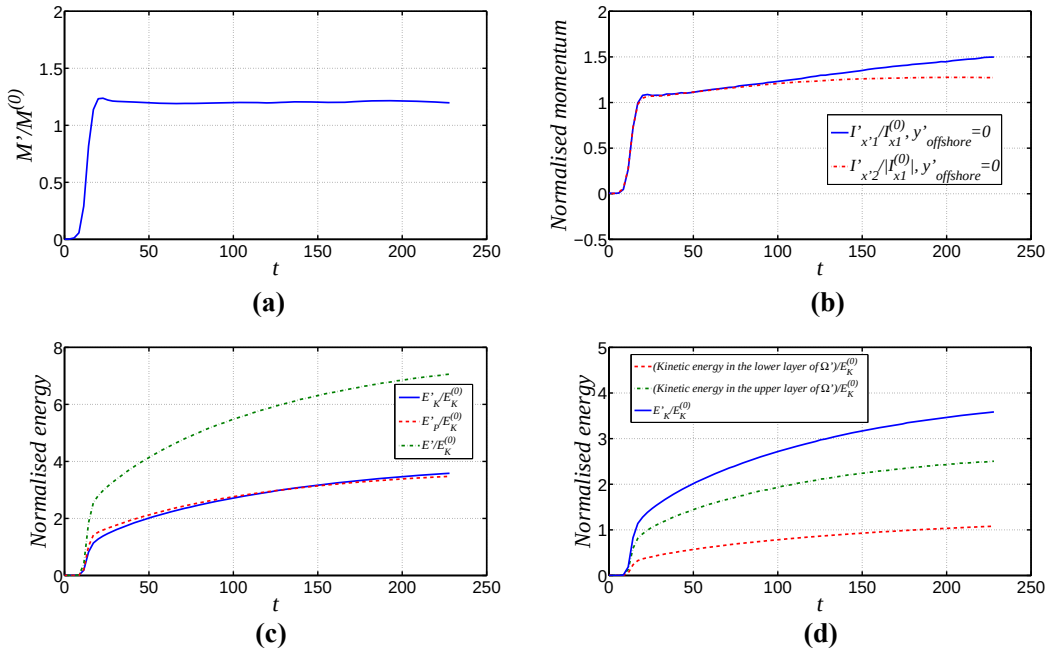

Fig. 8-49 The physical quantities in Ω of the simulated small incident wave case. (a): M' in Ω', which is normalised by $M^{(0)}$, versus time. (b): $I'_{x'1}$ and $I'_{z'1}$ in the lower layer of Ω', $I'_{x'2}$ and $I'_{z'2}$ in the upper layer of Ω', which are normalised by $I^{(0)}_{x1}$ or $\left|I^{(0)}_{x1}\right|$, versus time. (c): E'_K, E'_P and E' in Ω', which are normalised by $E^{(0)}_K$, versus time. (d): Comparison between the kinetic energy in the two layers of Ω'.

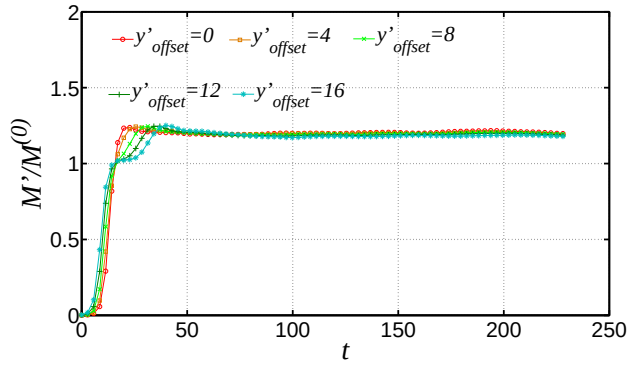

(a)

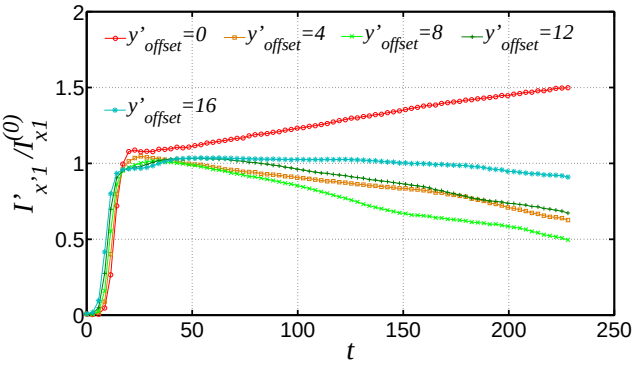

(b)

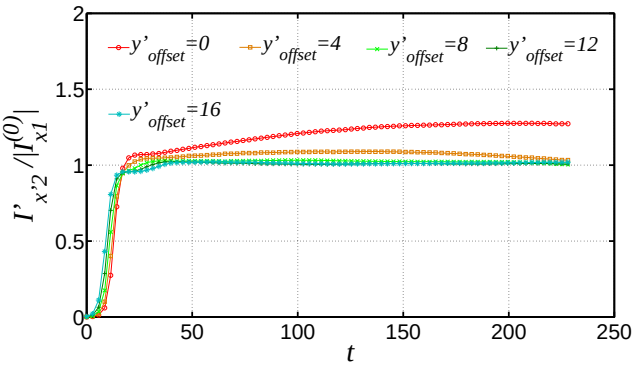

(c)

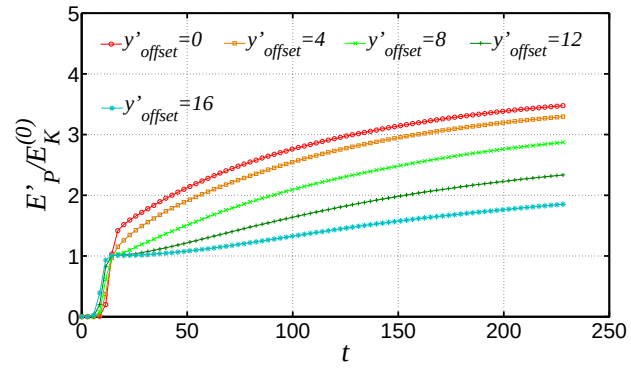

(d)

Fig. 8-50 M' **(a),** $I'_{x'1}$ **(b),** $I'_{x'2}$ **(c) and** E'_P **(d) in the control volumes that are parallel to** Ω **versus nondimensional time for the small-amplitude ISW case.**

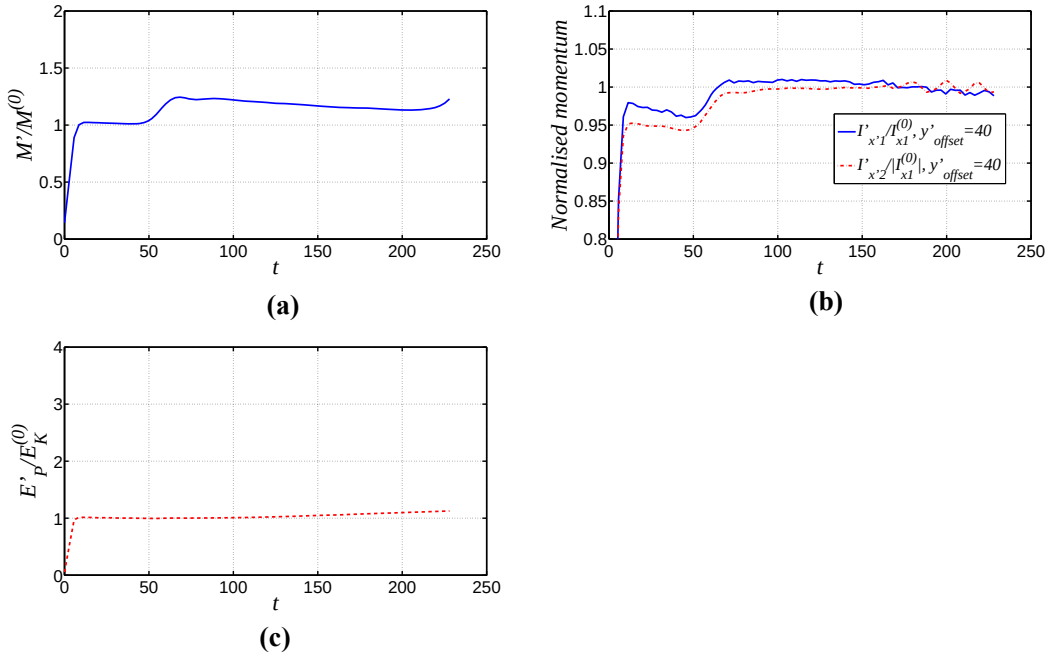

Fig. 8-51 M' **(a),** $I'_{x'1}$ **(b),** $I'_{x'2}$ **(c) and** E'_p **(d) in the control volume that is parallel to** Ω **with** $y'_{offset}=40$ **versus time for the small incident wave case.**

The time histories of the physical quantities in Ω' for the moderate incident wave case are plotted in Figs. 8-52(a)-(d). The physical quantities in the control volumes that are parallel to the *x'z'*-plane are shown in Figs. 8-53(a)-(d). The reason for the sharp drops of the physical quantities in the slice where $y'_{offset}=14$ near the end time is that the control volume is beyond the rightmost of the computational domain as shown in Fig. 7-18. But it does not affect the following analyses.

In terms of the excess mass in the slices (Figs. 8-52(a) & 8-53(a)), the KP theory (Fig. 8-46(d)) agrees well with the simulated result. The excess mass in each slice approaches a constant value that is much smaller than $2M^{(0)}$. It suggests that the reflection cannot be an ideal regular reflection which requires M' in each slice to be approximately a little more than $2M^{(0)}$ due to the obliquity (Fig. 7-22(d)).

The transverse momentum transfers in the two layers are complex. Fig. 8-52(b) shows that $\left|I'_{x'1}\right|$ and $\left|I'_{x'2}\right|$ in Ω' that is adjacent to the reflection wall have a large difference. It suggests very strong 3D effect there. Comparing Figs. 8-53(b) and (c), $\left|I'_{x'1}\right|$ and $\left|I'_{x'2}\right|$ in the two layers of the control volumes that are near the reflection wall all have large deviations. Using the difference between $\left|I'_{x'1}\right|$ and $\left|I'_{x'2}\right|$ to approximate the 3D effect, the 3D effect is the strongest at the location adjacent to the reflection wall where the interface has the largest displacement. In the far field where the incident wave and the reflected wave are separated, the flow field again becomes quasi-2D, for Fig. 8-54 shows $\left|I'_{x'1}\right| \approx \left|I'_{x'2}\right|$ for the whole simulated duration.

Both the kinetic energy and the potential energy in Ω' are approaching constants (Fig. 8-52(c)). The energy within the hump per unit transverse length is much larger than that within the incoming ISW. However, since the hump does not elongate, it is speculated that the energy would not be continuously concentrated in the vicinity of the reflection wall, but spread out fast in the subsequent process.

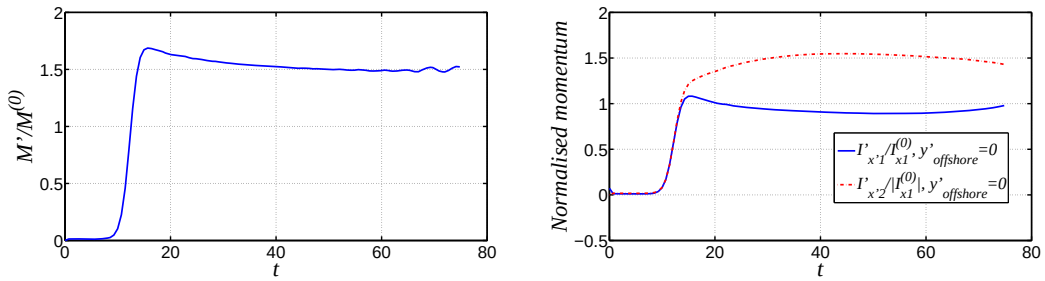

(a) **(b)**

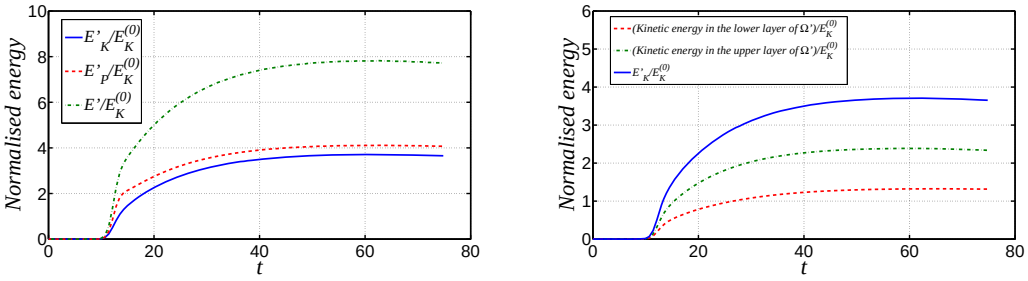

(c) **(d)**

Fig. 8-52 The moderate incident wave case. (a): M' in Ω', which is normalised by $M^{(0)}$, versus time. (b): $I'_{x'1}$ and $I'_{z'1}$ in the lower layer of Ω', $I'_{x'2}$ and $I'_{z'2}$ in the upper layer of Ω', which are normalised by $I_{x1}^{(0)}$ or $\left|I_{x1}^{(0)}\right|$, versus time. (c): E'_K, E'_P and E' in Ω, which are normalised by $E_K^{(0)}$, versus time. (d): Kinetic energies in the lower and upper layers of the control volume Ω'.

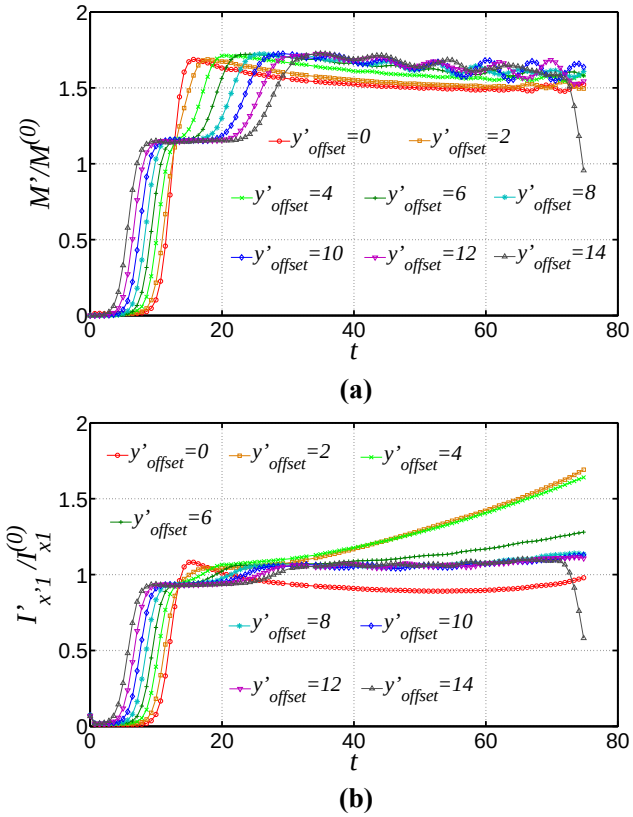

(a)

(b)

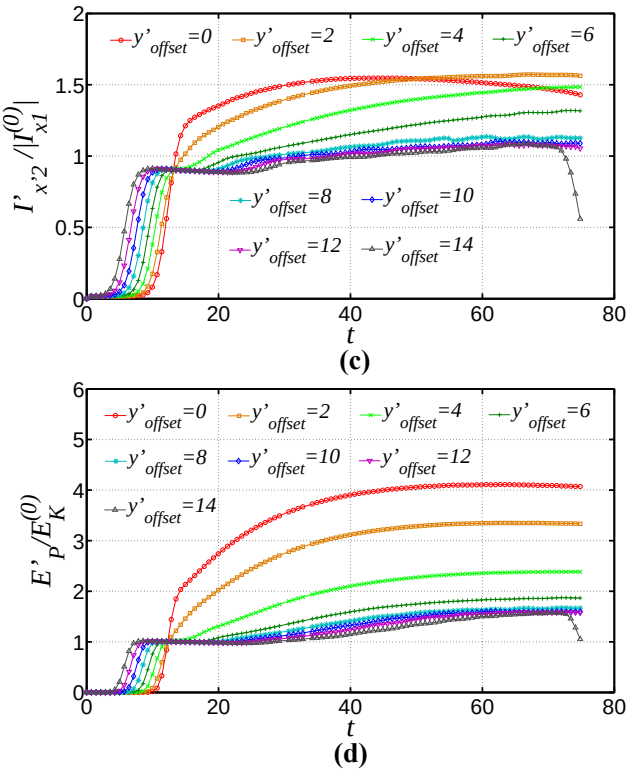

Fig. 8-53 M' **(a),** $I'_{x'1}$ **(b),** $I'_{x'2}$ **(c) and** E'_P **(d) in the control volumes that is parallel to** Ω' **versus time for the moderate incident wave case.**

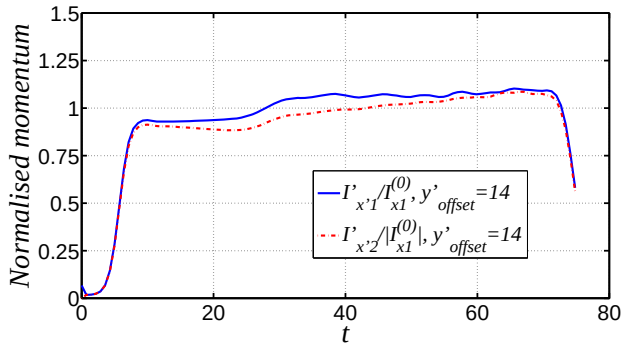

Fig. 8-54 $I'_{x'1}$ **and** $I'_{x'2}$ **in the control volumes that is parallel to** Ω' **with** $y'_{offset} = 14$ **versus time for the moderate incident wave case.**

8.4.8 Summary

The Mach reflection has been observed in the small incident wave case and no typical Mach reflection characteristics have been found in the moderate incident wave case. The phenomenon in the moderate incident wave case is more like a regular reflection. In that case, a steady hump with a nearly constant transverse

length forms in the vicinity of the reflection wall; the reflected wave angle is approximately equal to the incident wave angle; the reflected wave amplitude is smaller than the incident wave amplitude but larger than that predicted by the KP theory.

The energy from the incident wave is not completely transmitted to the far field relative to the reflection wall. Part of the energy is accumulated in the vicinity of the reflection wall within a localised wave form. Since the interface has larger displacement at the reflection wall than that in the far field, special attention has been paid to the wave at the reflection wall. The small incident wave case agrees with the KP theory. It suggests that for 3D interactions of small-amplitude internal waves the scaling relations implied by the KP theory are valid, and the density ratio and depth ratio between the layers only have insignificant effect on those relations. For the moderate incident wave case, although the incoming ISW can be accurately modelled by the third-order KdV theory, the wave motion at the reflection wall is beyond the validity scope of the weakly nonlinear theories. The wave amplitude at the reflection wall only grows to a finite large value that is smaller than the maximum possible amplitude of an ISW. The steady wave has a symmetric profile about the vertical plane passing its trough, which fits the shape of a 2D ISW of the same amplitude, but the phase speed is different from that ISW. Through analysis, the density ratio and depth ratio between the layers should have significant influence on the wave behaviours adjacent to the reflection wall in the moderate incident wave case, and result in that the nonbreaking internal wave can hold enormous energy (4 times of that within the incoming ISW per unit transverse length) with long characteristic wavelength or broad width. That is the reason why the internal wave can become steady at the reflection wall and does not overturn, which is different

from what happens in the surface wave case in the previous chapter. It is noted that, in the nature, the internal wave may break due to instabilities on its interface.

The 3D effect in the nonlinear wave interaction process has been investigated via the transverse transfers of the physical quantities. The relation between the tangential momentums to the reflection wall in the two layers has been used to examine the local three-dimensionality. It is found that the 3D effect is stronger in the vicinity of the reflection wall than that in the far field. Furthermore, the larger interface displacement at the reflection wall can induce the stronger local 3D effect in the vicinity of the reflection wall. In the small incident wave case, the enhanced local 3D effect is an important reason for the slower elongating rate of the stem wave in the transverse direction than expected by the KP theory. In the moderate incident wave case, the enhanced local 3D effect in the vicinity of the reflection wall is remarkable. It may be argued that the enhanced local 3D effect could play an important part in preventing the hump from elongating in the transverse direction. This mechanism has not been covered by the existing theories based on the weak three-dimensionality assumption. An interesting fact has also been found. The study on the transverse transfer of the excess mass suggests that the phenomenon in the moderate incident wave case is unlikely to be an ideal regular reflection in which the reflected wave would be developing to the image of the incident wave about the plane perpendicular to the reflection wall. It suggests other regimes to classify the oblique reflection of an ISW.

The practical concern of the research on internal waves is for the safety of the vehicles and offshore platforms in the deep sea. The large interface displacement of the Mach stem wave/hump would affect the navigation of the underwater vehicles

significantly, for those vehicles are very sensitive to the surrounding density variation. The internal wave can induce shear force and bending moment on the long riser that penetrates the interface. Through the comparisons based on the flow fields in the moderate incident wave case, the hump can induce much larger shear force and bending moment on the riser than the incoming ISW. The shear force has a local maximum magnitude at the intersection of the interface and the riser, for the flows in the two layers have the opposite directions. It is found that the maximum bending moment may happen either near the sea floor or near the floating platform depending on the support conditions. It suggests the potential failure of the riser at those positions, which may result in the oil spill in the deep ocean or in the upper ocean.

Chapter 9 Concluding remarks and future work

9.1 Concluding remarks

The present study focuses on a nonlinear water wave problem, *i.e.*, the oblique reflection of a solitary wave. The nonlinear effect, dispersive effect and 3D effect together may result in the Mach reflection phenomenon in shallow water. The Mach reflection can generate a stem wave in the vicinity of the reflection wall with amplitude larger than that of the incoming solitary wave, and the stem wave elongates in the transverse direction with time. Another "regular reflection" phenomenon is more like an intuitive mirror-like reflection, *i.e.*, the reflected wave would be developing into the mirror image of the incident wave about the plane perpendicular to the reflection wall. However, a steady hump with amplitude larger than that of the incoming solitary wave would be formed adjacent to the reflection wall, and the transverse length of the hump becomes constant after the incipient impingement. The research covers both the surface wave problem and internal wave problem. The applications are for the protection of the coastal areas and offshore structures.

The study started from a single solitary wave, which has uniform transverse cross sections. An ISW solution of the third-order KdV equation has been derived and implemented in the code OpenFOAM to initialise the flow field. The code solves the Euler equations, and tackles the fully nonlinear surface/interface boundary conditions by the VOF method. Through comparisons of the simulated results with various 2D approximate models, the third-order solution can result in the most stable solitary-like internal wave of small and moderate amplitude in the fully nonlinear simulation, for the third-order solution gives more accurate approximations on both

the wave profile and the velocity field. The optimisation of the initial condition can improve the efficiency in the 3D simulation. 2D head-on and overtaking collisions of SSWs and ISWs have also been simulated. The experimental results and analytical results have been used to validate and verify the code. Besides, the simulated results have shown similar behaviours of SSWs and ISWs in the collisions, *i.e.*, the re-emergence of two solitary-like waves after the collision with almost the same amplitudes as the incident waves. The KP theory and the EKP theory are the existing approximate models for the oblique reflection of a solitary wave. There are analytical solutions of the X-shape initial value problems based on the KP theory. The solutions correspond to the Mach reflection and the regular reflection. The V-shape initial value problem based on the EKP theory can be solved by the FEM using PDE2D, which has been verified. The conclusions from the 3D simulations are summarised as follows:

(i) Surface waves

The large-amplitude Mach stem wave induced by oblique reflection of a moderate-amplitude incident SSW has been reproduced by the fully nonlinear simulation. The simulated wave profile agrees well with the experimental measurements. Based on the detailed flow field information provided by the simulation, kinematics and dynamics of the Mach stem wave have been analysed. It is found that the breaking of the stem wave is due to the horizontal particle velocity increases to a value that exceeds the constant stem wave phase speed. The nonbreaking stem wave profile becomes asymmetric gradually to accommodate the energy per unit transverse length that is more than 4 times of that of the incoming solitary wave and 2 times of the maximum possible energy of a solitary wave. That process results in the plunging breaker. It suggests the possible impulsive wave

impact on the structure by the breaking stem wave. The situations when the stem wave encounters the structures with different dimensions have been discussed based on the velocity field and the existing research on SSW-structure interactions. Overall, the stem wave would pose a larger risk to the offshore and near shore structures than the incoming SSW. Furthermore, the strong shear flow has been found in the stem wave, and it would induce 3D ambient flow around the structure. The Morison equation would be inaccurate for calculation of the loads on the structure of small dimension exerted by the stem wave of very large amplitude.

The physical quantities in terms of excess mass, horizontal momentum and energy have been analysed in the transverse direction. It is found that the complex phenomena occurring in the oblique reflection problem are due to different transverse transfer speeds of those physical quantities. In the Mach reflection, the excess mass is not concentrated in the vicinity of the reflection wall. The excess mass of the stem wave per unit transverse length is approximately 1.75 times of that of the incoming solitary wave, which equals the summation of the excess mass within the incident wave and the reflected wave in the far field. The concentration of energy in the vicinity of the reflection wall is the main driving force for the elongation of the stem wave in the transverse direction. The tangential momentum to the reflection wall is also slowly accumulated in the vicinity of the reflection wall. That process is not accurately predicted by the KP theory. Furthermore, those physical quantities also correspond to different aspects in the evaluation of the hazardous damages. For example, the excess mass corresponds to the volume of the flood water, the momentum corresponds to the force on the structure, and the energy corresponds to the velocity of the flood flow. Some coastal configurations, *e.g.*, vertical dyke, slope, and the flooding at the plain area due to overtopping, have been discussed. The stem

wave poses a larger risk to the lives and structures at the coastal area than the incoming wave.

Through the comparison with the KP theory, it can be seen that the first-order approximation, with the orders in terms of the nonlinearity, can still well predict some important features of the nonbreaking wave, *e.g.*, the stem wave amplitude and the transverse length of the stem wave. Higher-order nonlinear terms may improve the approximation on the outskirts of the wave profile at the reflection wall. Although there are no more simulated cases available with different ψ_i to examine the 3D effect, the significance of the 3D effect has been analysed by comparing the transverse transfers of physical quantities with the KP theory that is based on the weak three-dimensionality assumption. Overall, the 3D effect in the simulation case is still weak. However, the higher-order approximation may improve the accuracy, which is reflected in the transverse transfer of the momentum.

(ii) Internal waves

The Mach reflection has been observed in the small incident wave case and no typical Mach reflection characteristics have been found in the moderate incident wave case. The phenomenon in the moderate incident wave case is more like a regular reflection. In that case, a steady hump with a nearly constant transverse length forms in the vicinity of the reflection wall; the reflected wave angle is approximately equal to the incident wave angle; the reflected wave amplitude is smaller than the incident wave amplitude but larger than that predicted by the KP theory.

The energy from the incident wave is not completely transmitted to the far field relative to the reflection wall. Part of the energy is accumulated in the vicinity of the reflection wall within a localised wave form. Since the interface has a larger displacement at the reflection wall than that in the far field, special attention has been paid to the wave at the reflection wall. The small incident wave case agrees with the KP theory. It suggests that for 3D interactions of small-amplitude internal waves the scaling relations implied by the KP theory are valid, and the density ratio and depth ratio between the layers only have insignificant effect on those relations. For the moderate incident wave case, although the incoming ISW can be accurately modelled by the third-order KdV theory, the wave motion at the reflection wall is beyond the validity scope of the weakly nonlinear theories. The wave amplitude at the reflection wall only grows to a finite large value that is smaller than the maximum possible amplitude of an ISW. The steady wave has a symmetric profile about the vertical axis passing its trough, which fits the shape of a 2D ISW of the same amplitude, but the phase speed is different from that ISW. Through analysis, the density ratio and depth ratio between the layers should have significant influence on the wave behaviours adjacent to the reflection wall in the moderate incident wave case, and result in that the nonbreaking internal wave can hold enormous energy (4 times of that within the incoming ISW per unit transverse length) with long characteristic wavelength or broad width. That is the reason why the internal wave can become steady at the reflection wall and does not overturn, which is different from what happens in the surface wave case. It is noted that, in the nature, the internal wave may break due to instabilities on its interface.

The 3D effect in the nonlinear wave interaction process has been investigated via the transverse transfers of the physical quantities. The relation between the tangential

momentums to the reflection wall in the two layers has been used to examine the local three-dimensionality. It is found that the 3D effect is stronger in the vicinity of the reflection wall than that in the far field. Furthermore, the larger interface displacement at the reflection wall can induce the stronger local 3D effect in the vicinity of the reflection wall. In the small incident wave case, the enhanced local 3D effect is an important reason for the slower elongating rate of the stem wave in the transverse direction than expected by the KP theory. In the moderate incident wave case, the enhanced local 3D effect in the vicinity of the reflection wall is remarkable. It may be argued that the enhanced local 3D effect could play an important part in preventing the hump from elongating in the transverse direction. This mechanism has not been covered by the existing theories based on the weak three-dimensionality assumption. An interesting fact has also been found. The study on the transverse transfer of the excess mass suggests that the phenomenon in the moderate incident wave case is unlikely to be an ideal regular reflection in which the reflected wave would be developing to the image of the incident wave about the perpendicular axis to the reflection wall. It suggests other regimes to classify the oblique reflection of an ISW.

The practical concern of the research on internal waves is for the safety of the vehicles and offshore platforms in the deep sea. The large interface displacement of the Mach stem wave/hump would affect the navigation of the underwater vehicles significantly, for those vehicles are very sensitive to the surrounding density variation. The internal wave can induce shear force and bending moment on the long riser that penetrates the interface. Through the comparisons based on the flow fields in the moderate incident wave case, the hump can induce much larger shear force and bending moment on the riser than the incoming ISW. The shear force has a local

maximum magnitude at the intersection of the interface and the riser, for the flows in the two layers have the opposite directions. It is found that the maximum bending moment may happen either near the sea floor or near the floating platform depending on the support conditions. It suggests the potential failure of the riser at those positions, which may result in the oil spill in the deep ocean or in the upper ocean.

9.2 Future work

The next step for surface wave problems is to study the wave breaking induced by the oblique reflection of an SSW. The CFD method can be used to obtain the information of both wave profile and the velocity field. More physical factors should be considered, for example, the turbulence model should be included to take into account the energy dissipation. The wave loads on the structures exerted by both the nonbreaking and breaking stem wave need to be studied.

The present study has revealed some distinct characteristics of the oblique reflection of a moderate-amplitude ISW. Large-scale CFD simulations are in demand to study the oblique reflection problem in a broader parametric space, *i.e.*, various incident wave amplitudes and incident wave angles. Understanding the wave motions is important in order to protect life and property in the sea and on the land. Meanwhile, solving the Euler equations is still time-consuming. The new solver based on the velocity potential theory is going to be developed. The new solver is expected to handle the dynamic mesh to satisfy the fully nonlinear interface boundary conditions. The difficulties would be the implementation of the AMR technique and the efficient parallel computing strategy. The fully nonlinear results can be then used as benchmarks to validate other approximate models, *e.g.*, the 3D two-layer, fully dispersive and strongly nonlinear interfacial wave model by Grue (2015a, b).

The study has suggested the possible amendment on the approximate models. Recently, the KP theory taking into account higher order terms, with the orders in terms of the nonlinearity, has been developed (Kodama and Yeh, 2016). However, it may still be invalid for the internal wave problem when the wave amplitude is not small. The EKP equation suggests the scaling relation between the vertical interface displacement and the characteristic wavelength may be different from the assumption in the KP theory especially for the internal waves of large amplitude. In other words, the Ursell relation should be reconsidered. At the same time, more research is needed to understand the 3D effect in the internal wave problem thoroughly. The enhanced local 3D effect may affect the scale relations profoundly.

Based on the understanding of the mechanisms, it is inferred that a gently upward slope on the seafloor in the propagation direction could reduce the amplitude of the stem wave/hump in the vicinity of the reflection wall and restrain the stem wave/hump from elongating in its transverse direction. Although the artificial slope is not practical at the present stage, there exists natural slope topography, *e.g.*, the continental shelf. The determination of the location of the oil platform and the navigation route in the sea, where the ISWs often interact with each other, should take into account the bathymetry. It should be safer to locate the platform and vehicles on the upper end of the continental shelf. More research is needed to verify this hypothesis.

Experiments on the interactions of internal waves are badly needed. Recently, there has been a report on the small-scale experimental study on the Mach interaction problem (Wang et al., 2016). The two interacting internal waves were generated by two cylindrical barrels. Hence the initial internal waves did not have 2D features as

what have been studied in this thesis. In the future, the similar wave tank as that used by Li et al. (2011) for internal waves should be built to study more complicated problems of internal waves.

APPENDIX A: Proving *S* to be constant

Substituting Eqs. (3.10) and (3.11) to Eq. (3.12), we have

$$S = \int_0^{\eta} \left(p_1 + \rho_1 u_1^2 \right) dz + \int_{\eta}^{H} \left(p_2 + \rho_2 u_2^2 \right) dz, \tag{A.1}$$

which is a function of a single variable x only. It is noted that the upper limit of the integral in the first term, η, which is also the lower limit of the integral in the second term, is a function of a single variable x only too. We assume that both S and η are continuous and differentiable everywhere with $x \in (-\infty, \infty)$. We take the derivative of S with respect to x, *viz.*,

$$\begin{aligned} \frac{dS}{dx} = & \int_0^{\eta} \left(p_{1x} + 2\rho_1 u_1 u_{1x} \right) dz + \eta_x \left[p_1 \left(x, \eta(x) \right) + \rho_1 u_1^2 \left(x, \eta \right) \right] \\ & + \int_{\eta}^{H} \left(p_{2x} + 2\rho_2 u_2 u_{2x} \right) dz - \eta_x \left[p_2 \left(x, \eta(x) \right) + \rho_2 u_2^2 \left(x, \eta \right) \right], \end{aligned} \tag{A.2}$$

where the subscript x denotes differentiation with respect to x. At the interface of two fluids, the pressure is continuous. Thus we have

$$p_1 \left(x, \eta(x) \right) = p_2 \left(x, \eta(x) \right). \tag{A.3}$$

The corresponding terms in Eq. (A.2) are cancelled out, *viz.*,

$$\eta_x p_1 \left(x, \eta(x) \right) - \eta_x p_2 \left(x, \eta(x) \right) = 0. \tag{A.4}$$

The momentum conservation equations in the two layers are

$$\begin{cases} u_1 u_{1x} + w_1 u_{1y} = -\dfrac{p_{1x}}{\rho_1}, \\ u_2 u_{2x} + w_2 u_{2y} = -\dfrac{p_{2x}}{\rho_2}. \end{cases} \tag{A.5}$$

Hence the pressure gradient can be expressed as

$$\begin{cases} p_{1x} = -\rho_1 u_1 u_{1x} - \rho_1 w_1 u_{1z}, \\ p_{2x} = -\rho_2 u_2 u_{2x} - \rho_2 w_2 u_{2z}. \end{cases} \tag{A.6}$$

We rewrite the integrands in Eq. (A.2) to give

$$p_{1x}+2\rho_1 u_1 u_{1x}=-\rho_1 u_1 u_{1x}-\rho_1 w_1 u_{1z}+2\rho_1 u_1 u_{1x}=\rho_1 u_1 u_{1x}-\rho_1 w_1 u_{1z}, \tag{A.7}$$

$$p_{2x}+2\rho_2 u_2 u_{2x}=-\rho_2 u_2 u_{2x}-\rho_2 w_2 u_{2z}+2\rho_2 u_2 u_{2x}=\rho_2 u_2 u_{2x}-\rho_2 w_2 u_{2z}. \tag{A.8}$$

The mass conservation equations in the two layers are

$$\begin{cases} u_{1x}+w_{1z}=0, \\ u_{2x}+w_{2z}=0. \end{cases} \tag{A.9}$$

Substituting them into Eqs. (A.7) and (A.8) yields

$$p_{1x}+2\rho_1 u_1 u_{1x}=-\rho_1 u_1 w_{1z}-\rho_1 w_1 u_{1z}, \tag{A.10}$$

$$p_{2x}+2\rho_2 u_2 u_{2x}=-\rho_2 u_2 w_{2z}-\rho_2 w_2 u_{2z}. \tag{A.11}$$

In order to simplify Eq. (A.2), we integral the terms in Eqs. (A.10) and (A.11) by parts, *viz.*,

$$\begin{aligned} &-\rho_1\int_0^\eta w_1 u_{1z}dz-\rho_1\int_0^\eta u_1 w_{1z}dz \\ &\quad=\rho_1\left(-u_1 w_1\big|_0^\eta+\int_0^\eta w_1 u_{1z}dz\right)-\rho_1\int_0^\eta u_{1z} w_1 dz=-\rho_1 u_1 w_1\big|_0^\eta, \end{aligned} \tag{A.12}$$

$$\begin{aligned} &-\rho_2\int_\eta^H w_2 u_{2z}dz-\rho_2\int_\eta^H u_2 w_{2z}dz \\ &\quad=\rho_2\left(-u_2 w_2\big|_\eta^H+\int_\eta^H w_{2z} u_2 dz\right)-\rho_2\int_\eta^H u_2 w_{2z}dz=-\rho_2 u_2 w_2\big|_\eta^H. \end{aligned} \tag{A.13}$$

The boundary condition on the top and bottom are

$$\begin{cases} w_1=0, \quad z=0; \\ w_2=0, \quad z=H. \end{cases} \tag{A.14}$$

Eqs. (A.12) and (A.13) can be further expanded and simplified taking into account Eq. (A.14), *viz.*,

$$-\rho_1 u_1 w_1\big|_0^\eta=-\rho_1 u_1(x,\eta)w_1(x,\eta), \tag{A.15}$$

$$-\rho_2 u_2 w_2\big|_\eta^H=\rho_2 u_2(x,\eta)w_2(x,\eta). \tag{A.16}$$

Eq. (A.2) can be written as

$$\begin{aligned} \frac{dS}{dx}&=-\rho_1 u_1(x,\eta)w_1(x,\eta)+\eta_x\rho_1 u_1^2(x,\eta)+\rho_2 u_2(x,\eta)w_2(x,\eta)-\eta_x\rho_2 u_2^2(x,\eta) \\ &=\rho_1 u_1(-w_1+u_1\eta_x)-\rho_2 u_2(-w_2+u_2\eta_x). \end{aligned} \tag{A.17}$$

Since the kinematical condition on the interface is

$$\begin{cases} -w_1 + u_1 \eta_x = 0, \\ -w_2 + u_2 \eta_x = 0, \end{cases} \tag{A.18}$$

it is concluded that

$$\frac{dS}{dx} = 0, \tag{A.19}$$

which means S is a constant and is independent of x.

APPENDIX B: The expansion of the stream function

Without loss of generality, only the expansion of the stream function in the lower layer is illustrated hereinafter.

The governing equation is

$$\Delta \Psi_1 = 0. \tag{B.1}$$

The boundary condition on the bottom is

$$\Psi_1\big|_{z=0} = C, \tag{B.2}$$

where C is a constant.

The stream function can be expanded from the bottom as

$$\Psi_1 = \sum_{n=0}^{\infty} z^n f_n(x), \tag{B.3}$$

Substituting it into Eq. (B.1) yields

$$\sum_{n=0}^{\infty} z^n \left(\frac{\partial^2 f_n}{\partial x^2} + (n+2)(n+1) f_{n+2} \right) = 0. \tag{B.4}$$

$$\therefore \quad f_{n+2} = \frac{-1}{(n+2)(n+1)} \frac{\partial^2 f_n}{\partial x^2}. \tag{B.5}$$

According to the boundary condition in Eq. (B.2),

$$f_0 = C. \tag{B.6}$$

From Eq. (B.5)

$$f_{2n} = 0, \quad n = 1, 2, 3, \cdots. \tag{B.7}$$

If we take C as 0, the stream function can be written as

$$\Psi_1 = \sum_{n=0}^{\infty} (-1)^n \bullet \frac{z^{2n+1}}{(2n+1)!} \bullet \frac{\partial^{2n}}{\partial x^{2n}} f_1. \tag{B.8}$$

According to the definition of the stream function, f_1 in Eq. (B.8) is $u_1(x,0)$, which is the horizontal velocity on the bottom, in Eq. (3.15).

APPENDIX C: The coefficients of Eq. (3.50)

$$C_3=\frac{(1-\delta)\left((r-1)^2-\delta\right)}{3(r-1)\left((r-1)+\delta\right)},C_4=\frac{3(1-\delta)\left((r-1)^2-\delta\right)}{2(r-1)\left((r-1)+\delta\right)},$$

$$C_5=-(1-\delta),C_6=\frac{(1-\delta)\left((r-1)^2-\delta\right)}{6(r-1)\left((r-1)+\delta\right)},$$

$$C_7=\frac{(1-\delta)\left((r-1)^2-\delta\right)}{3(r-1)\left((r-1)+\delta\right)},C_8=\frac{(1-\delta)\left((r-1)^2-\delta\right)}{6(r-1)\left((r-1)+\delta\right)},$$

$$C_9=\frac{(1-\delta)\left((r-1)^2-\delta\right)}{3(r-1)\left((r-1)+\delta\right)},C_{10}=\frac{(1-\delta)\left((r-1)^2-\delta\right)}{6(r-1)\left((r-1)+\delta\right)},$$

$$C_{11}=\frac{(1-\delta)\left((r-1)^2-\delta\right)}{6(r-1)\left((r-1)+\delta\right)},C_{12}=\frac{3(1-\delta)\left((r-1)^2-\delta\right)}{2(r-1)\left((r-1)+\delta\right)},$$

$$C_{13}=-\frac{1}{2}(1-\delta),C_{14}=-(1-\delta),C_{15}=-\frac{1}{2}(1-\delta),$$

$$C_{16}=\frac{(1-\delta)\left((r-1)^2-\delta\right)^2\left(1-(1-r)^3\delta\right)}{45(r-1)^3\left((r-1)+\delta\right)\left(1+(r-1)\delta\right)^2},$$

$$C_{17}=\frac{(1-\delta)\left((r-1)^2-\delta\right)^2\left(1-(1-r)^3\delta\right)}{45(r-1)^3\left((r-1)+\delta\right)\left(1+(r-1)\delta\right)^2},$$

$$C_{18}=-\frac{(1-\delta)\left((r-1)^2-\delta\right)^2\left(1-(1-r)^3\delta\right)}{45(r-1)^3\left((r-1)+\delta\right)\left(1+(r-1)\delta\right)^2},$$

$$C_{19}=\frac{(1-\delta)\left((r-1)^2-\delta\right)^2\left(1-(1-r)^2\delta\right)}{45(r-1)^3\left((r-1)+\delta\right)\left(1+(r-1)\delta\right)^2},$$

$$C_{20}=-\frac{(1-\delta)\left((r-1)^2-\delta\right)^2\left(1-(1-r)^2\delta\right)}{90(r-1)^3\left((r-1)+\delta\right)\left(1+(r-1)\delta\right)^2},$$

$$C_{21}=\frac{(1-\delta)\left((r-1)^2-\delta\right)^2\left(1-(1-r)^2\delta\right)}{45(r-1)^3\left((r-1)+\delta\right)\left(1+(r-1)\delta\right)^2},$$

$$C_{22}=\frac{(1-\delta)\left((r-1)^2-\delta\right)^2\left(1-(1-r)^3\delta\right)}{45(r-1)^3\left((r-1)+\delta\right)\left(1+(r-1)\delta\right)^2},$$

$$C_{23}=-\frac{(1-\delta)\left((r-1)^2-\delta\right)^2\left(1-(1-r)^3\delta\right)}{90(r-1)^3\left((r-1)+\delta\right)\left(1+(r-1)\delta\right)^2},$$

$$C_{24}=\frac{2(1-\delta)\left((r-1)^2-\delta\right)^2\left(1-(1-r)^3\delta\right)}{45(r-1)^3\left((r-1)+\delta\right)\left(1+(r-1)\delta\right)^2},$$

$$C_{25}=-\frac{(1-\delta)\left((r-1)^2-\delta\right)^2\left(1-(1-r)^3\delta\right)}{45(r-1)^3\left((r-1)+\delta\right)\left(1+(r-1)\delta\right)^2},$$

$$C_{26}=\frac{2(1-\delta)\left((r-1)^2-\delta\right)^3\left(1-(1-r)^5\delta\right)}{945(r-1)^5\left((r-1)+\delta\right)\left(1+(r-1)\delta\right)^3},$$

$$C_{27}=-\frac{2(1-\delta)\left((r-1)^2-\delta\right)^3\left(1-(1-r)^5\delta\right)}{945(r-1)^5\left((r-1)+\delta\right)\left(1+(r-1)\delta\right)^3},$$

$$C_{28}=\frac{(1-\delta)\left((r-1)^2-\delta\right)^3\left(1-(1-r)^5\delta\right)}{945(r-1)^5\left((r-1)+\delta\right)\left(1+(r-1)\delta\right)^3},$$

$$C_{29}=\frac{(1-\delta)^2\left((1-r)^2-\delta\right)}{6(r-1)\left((r-1)+\delta\right)\left(1+(r-1)\delta\right)},$$

$$C_{30}=-\frac{(1-\delta)^2\left((1-r)^2-\delta\right)}{3(r-1)\left((r-1)+\delta\right)\left(1+(r-1)\delta\right)},$$

$$C_{31}=\frac{(1-\delta)\left((1-r)^2-\delta\right)}{6(r-1)^2\left(1+(r-1)\delta\right)},C_{32}=\frac{(1-\delta)\left((1-r)^4-\delta\right)}{2(r-1)^3\left((r-1)+\delta\right)},$$

$$C_{33}=-\frac{(1-\delta)^2\left((1-r)^2-\delta\right)}{6(r-1)\left((r-1)+\delta\right)\left(1+(r-1)\delta\right)},C_{34}=\frac{2(1-\delta)\left((1-r)^3-\delta\right)}{(r-1)^2\left((r-1)+\delta\right)},$$

$$C_{35}=-\frac{(1-\delta)^2\left((1-r)^2-\delta\right)}{6(r-1)\left((r-1)+\delta\right)\left(1+(r-1)\delta\right)},C_{36}=\frac{(1-\delta)\left((1-r)^3-\delta\right)}{2(r-1)^2\left((r-1)+\delta\right)},$$

$$C_{37}=\frac{3(1-\delta)\left((1-r)^2-\delta\right)}{2(r-1)\left((r-1)+\delta\right)},$$

$$C_{38}=\frac{(1-\delta)\left((1-r)^2-\delta\right)}{2(r-1)\left((r-1)+\delta\right)}. \tag{C.1}$$

APPENDIX D: The third-order solution for the velocity field of an ISW

$$c_0=\sqrt{\frac{gh(1-r)(\rho_1-\rho_2)}{(-1+r)\rho_1+\rho_2}} \tag{D.1}$$

$$\begin{aligned}
\frac{U}{c_0} &= 1+\frac{\varepsilon((-1+r)^2\rho_1-\rho_2)}{2(-1+r)((-1+r)\rho_1+\rho_2)} \\
&\quad +\frac{1}{2}\varepsilon^2(5(-1+r)(-(-1+r)^2\rho_1+\rho_2)^2 \\
&\quad\quad -(20(-1+r)(-(-1+r)^2\rho_1+\rho_2)^2 \\
&\quad\quad\quad -20(-1+r)((-1+r)\rho_1+\rho_2)((-1+r)^3\rho_1+\rho_2) \\
&\quad\quad\quad -\frac{((-1+r)\rho_1+\rho_2)(-(-1+r)^2\rho_1+\rho_2)^2(\rho_1+(-1+r)^3\rho_2)}{(\rho_1+(-1+r)\rho_2)^2})) \\
&\quad\quad /(20(-1+r)^3((-1+r)\rho_1+\rho_2)^2) \\
&\quad +\frac{1}{2}\varepsilon^3(30(-1+r)^8\rho_1^7 \\
&\quad\quad +(-1+r)^4(-210+780r-1930r^2+2068r^3-1893r^4 \\
&\quad\quad\quad +1661r^5-1183r^6+555r^7-144r^8+16r^9)\rho_1^6\rho_2 \\
&\quad\quad +(-1+r)^3(-630+2790r-9140r^2+16104r^3-17465r^4 \\
&\quad\quad\quad +13682r^5-8183r^6+3470r^7-988r^8 \\
&\quad\quad\quad +184r^9-22r^{10}+2r^{11})\rho_1^5\rho_2^2 \\
&\quad\quad +(-1+r)^2(-1050+5400r-19900r^2+46016r^3 \\
&\quad\quad\quad -65266r^4+59950r^5-38689r^6+18965r^7 \\
&\quad\quad\quad -7267r^8+2067r^9-393r^{10}+39r^{11})\rho_1^4\rho_2^3 \\
&\quad\quad +(1050-7200r+29800r^2-86984r^3+175372r^4 \\
&\quad\quad\quad -243202r^5+235543r^6-162699r^7+81881r^8 \\
&\quad\quad\quad -30433r^9+8201r^{10}-1457r^{11}+128r^{12})\rho_1^3\rho_2^4 \\
&\quad\quad +(-630+4140r-15890r^2+44556r^3-90773r^4 \\
&\quad\quad\quad +130581r^5-130652r^6+89850r^7-41659r^8 \\
&\quad\quad\quad +12553r^9-2274r^{10}+196r^{11})\rho_1^2\rho_2^5 \\
&\quad\quad +(210-1320r+4360r^2-10492r^3+20037r^4 \\
&\quad\quad\quad -28989r^5+29813r^6-20807r^7+9344r^8 \\
&\quad\quad\quad -2436r^9+280r^{10})\rho_1\rho_2^6 \\
&\quad\quad -30(-1+r)^6\rho_2^7) \\
&\quad\quad /(280(-1+r)^5((-1+r)\rho_1+\rho_2)^3(\rho_1+(-1+r)\rho_2)^4)
\end{aligned} \tag{D.2}$$

$$\frac{u_1}{c_0} = 1 + \varepsilon(-\operatorname{sech}^2(\alpha x) + \frac{((-1+r)^2\rho_1 - \rho_2)}{2(-1+r)((-1+r)\rho_1 + \rho_2)})$$
$$+ \frac{1}{2}\varepsilon^2(-\frac{\operatorname{sech}^2(\alpha x)((-1+r)^2\rho_1 - \rho_2)}{(-1+r)((-1+r)\rho_1 + \rho_2)}$$
$$- \frac{(-(-1+r)^2\rho_1 + \rho_2)^2}{4(-1+r)^2((-1+r)\rho_1 + \rho_2)^2}$$
$$+ \frac{3y^2(-2+\cosh(2\alpha x))\operatorname{sech}^4(\alpha x)((-1+r)^2\rho_1 - \rho_2)}{2(-1+r)^2(\rho_1 + (-1+r)\rho_2)}$$
$$- ((\rho_1 - \rho_2)(20(-1+r)(-(-1+r)^2\rho_1 + \rho_2)^2$$
$$- 20(-1+r)((-1+r)\rho_1 + \rho_2)((-1+r)^3\rho_1 + \rho_2)$$
$$- \frac{((-1+r)\rho_1 + \rho_2)(-(-1+r)^2\rho_1 + \rho_2)^2(\rho_1 + (-1+r)^3\rho_2)}{(\rho_1 + (-1+r)\rho_2)^2}))$$
$$/ (20(-1+r)^3(-\rho_1 + \rho_2)((-1+r)\rho_1 + \rho_2)^2)$$
$$+ 2(\operatorname{sech}^4(\alpha x) - \frac{(-2+\cosh(2\alpha x))\operatorname{sech}^4(\alpha x)((-1+r)^2\rho_1 - \rho_2)}{4(-1+r)^2(\rho_1 + (-1+r)\rho_2)}$$
$$+ (\operatorname{sech}^2(\alpha x)(3(-1+r)^4\rho_1^3$$
$$+ (-9 + 33r - 57r^2 + 81r^3 - 89r^4 + 59r^5 - 21r^6 + 3r^7)\rho_1^2\rho_2$$
$$+ (9 - 30r + 48r^2 - 24r^3 - 10r^4 + 14r^5 - 4r^6)\rho_1\rho_2^2$$
$$+ 3(-1+r)^3\rho_2^3)\tanh^2(\alpha x))$$
$$/ (4(-1+r)^2((-1+r)^2\rho_1 - \rho_2)(\rho_1 + (-1+r)\rho_2)^2)))$$
$$+ \frac{1}{24}\varepsilon^3$$
$$(-\frac{9y^4(33 - 26\cosh(2\alpha x) + \cosh(4\alpha x))\operatorname{sech}^6(\alpha x)(-(-1+r)^2\rho_1 + \rho_2)^2}{8(-1+r)^4(\rho_1 + (-1+r)\rho_2)^2}$$
$$+ (3(30(-1+r)^8\rho_1^7$$
$$+ (-1+r)^4(-210 + 780r - 1930r^2 + 2068r^3 - 1893r^4$$
$$+ 1661r^5 - 1183r^6 + 555r^7 - 144r^8 + 16r^9)\rho_1^6\rho_2$$
$$+ (-1+r)^3(-630 + 2790r - 9140r^2 + 16104r^3$$
$$- 17465r^4 + 13682r^5 - 8183r^6 + 3470r^7$$
$$- 988r^8 + 184r^9 - 22r^{10} + 2r^{11})\rho_1^5\rho_2^2$$
$$+ (-1+r)^2(-1050 + 5400r - 19900r^2 + 46016r^3$$
$$- 65266r^4 + 59950r^5 - 38689r^6 + 18965r^7$$
$$- 7267r^8 + 2067r^9 - 393r^{10} + 39r^{11})\rho_1^4\rho_2^3$$
$$+ (1050 - 7200r + 29800r^2 - 86984r^3 + 175372r^4$$
$$- 243202r^5 + 235543r^6 - 162699r^7 + 81881r^8$$
$$- 30433r^9 + 8201r^{10} - 1457r^{11} + 128r^{12})\rho_1^3\rho_2^4$$

$$
\begin{aligned}
&+(-630+4140r-15890r^2+44556r^3-90773r^4\\
&\quad+130581r^5-130652r^6+89850r^7-41659r^8\\
&\quad+12553r^9-2274r^{10}+196r^{11})\rho_1^2\rho_2^5\\
&+(210-1320r+4360r^2-10492r^3+20037r^4\\
&\quad-28989r^5+29813r^6-20807r^7+9344r^8\\
&\quad-2436r^9+280r^{10})\rho_1\rho_2^6\\
&-30(-1+r)^6\rho_2^7))\\
&/(70(-1+r)^5((-1+r)\rho_1+\rho_2)^3(\rho_1+(-1+r)\rho_2)^4)\\
&+(9y^2\operatorname{sech}^6(\alpha x)(-\cosh(4\alpha x)(2(-1+r)^5\rho_1^4\\
&+(-1+r)^3(-8+14r-19r^2+19r^3-10r^4+2r^5)\rho_1^3\rho_2\\
&+(-1+r)^2(-12+30r-47r^2+35r^3-11r^4+r^5)\rho_1^2\rho_2^2\\
&+(8-34r+63r^2-56r^3+24r^4-4r^5)\rho_1\rho_2^3\\
&+(-2+8r-9r^2+3r^3)\rho_2^4)\\
&-2\cosh(2\alpha x)(14(-1+r)^5\rho_1^4\\
&-(-1+r)^2(-56+130r-115r^2-54r^3\\
&\quad+149r^4-84r^5+14r^6)\rho_1^3\rho_2\\
&+(-84+306r-493r^2+453r^3-296r^4\\
&\quad+182r^5-87r^6+19r^7)\rho_1^2\rho_2^2\\
&+(56-166r+253r^2-336r^3+324r^4\\
&\quad-164r^5+32r^6)\rho_1\rho_2^3\\
&+(-14+32r-51r^2+49r^3-16r^4)\rho_2^4)\\
&+3(18(-1+r)^5\rho_1^4\\
&-(-1+r)^2(-72+174r-181r^2+22r^3\\
&\quad+91r^4-60r^5+10r^6)\rho_1^3\rho_2\\
&+(-108+414r-731r^2+771r^3-552r^4\\
&\quad+298r^5-113r^6+21r^7)\rho_1^2\rho_2^2\\
&+(72-234r+379r^2-448r^3+372r^4\\
&\quad-172r^5+32r^6)\rho_1\rho_2^3\\
&+(-18+48r-69r^2+55r^3-16r^4)\rho_2^4)))\\
&/(4(-1+r)^4((-1+r)\rho_1+\rho_2)(\rho_1+(-1+r)\rho_2)^3)\\
&+\frac{3}{5(-1+r)^3((-1+r)\rho_1+\rho_2)^2}\\
&\operatorname{sech}^2(\alpha x)(5(-1+r)(-(-1+r)^2\rho_1+\rho_2)^2\\
&-(20(-1+r)(-(-1+r)^2\rho_1+\rho_2)^2\\
&\quad-20(-1+r)((-1+r)\rho_1+\rho_2)((-1+r)^3\rho_1+\rho_2)\\
&\quad-\frac{((-1+r)\rho_1+\rho_2)(-(-1+r)^2\rho_1+\rho_2)^2(\rho_1+(-1+r)^3\rho_2)}{(\rho_1+(-1+r)\rho_2)^2})))
\end{aligned}
$$

$$
\begin{aligned}
&/(5(-1+r)^3((-1+r)\rho_1+\rho_2)^2)\\
&+(12((-1+r)^2\rho_1-\rho_2)(Sech^4(\alpha x)-\\
&-\frac{(-2+\cosh(2\alpha x))\operatorname{sech}^4(\alpha x)((-1+r)^2\rho_1-\rho_2)}{4(-1+r)^2(\rho_1+(-1+r)\rho_2)}\\
&+(\operatorname{sech}^2(\alpha x)(3(-1+r)^4\rho_1^3\\
&+(-9+33r-57r^2+81r^3-89r^4+59r^5-21r^6+3r^7)\rho_1^2\rho_2\\
&+(9-30r+48r^2-24r^3-10r^4+14r^5-4r^6)\rho_1\rho_2^2\\
&+3(-1+r)^3\rho_2^3)\tanh(\alpha x)^2)\\
&/(4(-1+r)^2((-1+r)^2\rho_1-\rho_2)(\rho_1+(-1+r)\rho_2)^2)))\\
&/((-1+r)((-1+r)\rho_1+\rho_2))\\
&+24(-\operatorname{sech}^6(\alpha x)\\
&-\frac{7(33-26\cosh(2\alpha x)+\cosh(4\alpha x))\operatorname{sech}^6(\alpha x)(-(-1+r)^2\rho_1+\rho_2)^2}{320(-1+r)^4(\rho_1+(-1+r)\rho_2)^2}\\
&+\frac{\operatorname{sech}^4(\alpha x)((-1+r)^2\rho_1-\rho_2)\tanh^2(\alpha x)}{(-1+r)^2(\rho_1+(-1+r)\rho_2)}\\
&-(\operatorname{sech}^4(\alpha x)(3(-1+r)^4\rho_1^3\\
&+(-9+33r-57r^2+81r^3-89r^4+59r^5-21r^6+3r^7)\rho_1^2\rho_2\\
&+(9-30r+48r^2-24r^3-10r^4+14r^5-4r^6)\rho_1\rho_2^2\\
&+3(-1+r)^3\rho_2^3)\tanh^2(\alpha x))\\
&/(2(-1+r)^2((-1+r)^2\rho_1-\rho_2)(\rho_1+(-1+r)\rho_2)^2)\\
&-(\operatorname{sech}^4(\alpha x)(5\cosh(2\alpha x)(15(-1+r)^8\rho_1^6\\
&+2(-1+r)^4(-45+165r-297r^2+465r^3-478r^4\\
&+297r^5-102r^6+15r^7)\rho_1^5\rho_2\\
&+(-1+r)^2(225-1200r+3216r^2-6108r^3+9329r^4\\
&-11540r^5+11322r^6-8640r^7+4997r^8-2100r^9\\
&+606r^{10}-108r^{11}+9r^{12})\rho_1^4\rho_2^2\\
&-2(-1+r)^2(150-750r+1962r^2-3348r^3+4632r^4\\
&-5328r^5+4569r^6-2664r^7+995r^8-218r^9+21r^{10})\rho_1^3\rho_2^3\\
&+(225-1500r+4866r^2-9552r^3+12452r^4-11324r^5\\
&+7542r^6-4000r^7+1884r^8-800r^9+272r^{10}\\
&-64r^{11}+8r^{12})\rho_1^2\rho_2^4\\
&+2(-1+r)^3(45-150r+252r^2-120r^3-137r^4+213r^5\\
&-108r^6+20r^7)\rho_1\rho_2^5\\
&+15(-1+r)^6\rho_2^6)
\end{aligned}
$$

$$
\begin{aligned}
&-2(114(-1+r)^8\rho_1^6-(-1+r)^4(684-2508r+3876r^2-2766r^3\\
&\quad-541r^4+3954r^5-4341r^6+2358r^7-648r^8+72r^9)\rho_1^5\rho_2\\
&+(-1+r)^2(1710-9120r+21888r^2-30156r^3+23132r^4\\
&\quad-7496r^5+2295r^6-7968r^7+10922r^8-7266r^9\\
&\quad+2694r^{10}-540r^{11}+45r^{12})\rho_1^4\rho_2^2\\
&-(2280-15960r+51072r^2-98952r^3+127272r^4\\
&\quad-109680r^5+48867r^6+26220r^7-73580r^8+72102r^9\\
&\quad-41802r^{10}+14948r^{11}-3063r^{12}+276r^{13})\rho_1^3\rho_2^3\\
&+(1710-11400r+34428r^2-63324r^3+78338r^4\\
&\quad-63224r^5+27495r^6-778r^7-3939r^8-530r^9\\
&\quad+2057r^{10}-928r^{11}+140r^{12})\rho_1^2\rho_2^4\\
&+(-684+4332r-12084r^2+20034r^3-21593r^4\\
&\quad+16038r^5-9456r^6+5368r^7\\
&\quad-2739r^8+924r^9-140r^{10})\rho_1\rho_2^5\\
&+114(-1+r)^6\rho_2^6))\tanh^2(\alpha x))\\
&\quad/(240(-1+r)^4(-(-1+r)^2\rho_1+\rho_2)^2(\rho_1+(-1+r)\rho_2)^4)\\
&(\operatorname{sech}^2(\alpha x)((21-18\cosh(2\alpha x)+\cosh(4\alpha x))\operatorname{sech}(\alpha x)^4(3(-1+r)^4\rho_1^3\\
&+(-9+33r-57r^2+81r^3-89r^4+59r^5-21r^6+3r^7)\rho_1^2\rho_2\\
&+(9-30r+48r^2-24r^3-10r^4+14r^5-4r^6)\rho_1\rho_2^2\\
&+3(-1+r)^3\rho_2^3)\\
&-4\operatorname{sech}^2(\alpha x)(5(-1+r)^4\rho_1^3\\
&+(-15+55r-103r^2+115r^3-75r^4+29r^5-7r^6+r^7)\rho_1^2\rho_2\\
&+(15-50r+88r^2-100r^3+70r^4-26r^5+4r^6)\rho_1\rho_2^2\\
&+5(-1+r)^3\rho_2^3)\\
&+8(5(-1+r)^4\rho_1^3\\
&+(-15+55r-103r^2+115r^3-75r^4+29r^5-7r^6+r^7)\rho_1^2\rho_2\\
&+(15-50r+88r^2-100r^3+70r^4-26r^5+4r^6)\rho_1\rho_2^2\\
&+5(-1+r)^3\rho_2^3)\tanh^2(\alpha x)))\\
&/(64(-1+r)^4(\rho_1+(-1+r)\rho_2)^3))))
\end{aligned}
$$

(D.3)

$$\frac{v_1}{c_0} = \frac{\varepsilon^{3/2} y \operatorname{sech}^2(\alpha x)}{(5120\sqrt{3}(-1+r)^6 \sqrt{\frac{(-1+r)^2\rho_1 - \rho_2}{(-1+r)^2(\rho_1+(-1+r)\rho_2)}}(\rho_1+(-1+r)\rho_2)^5)}$$

$$(-15360(-1+r)^4((-1+r)^2\rho_1-\rho_2)(\rho_1+(-1+r)\rho_2)^4\tanh(\alpha x)$$

$$+960\varepsilon(-1+r)^2(\rho_1+(-1+r)\rho_2)^2(2y^2\operatorname{sech}^3(\alpha x)$$

$$(-11\sinh(\alpha x)+\sinh(3\alpha x))(-(-1+r)^2\rho_1+\rho_2)^2(\rho_1+(-1+r)\rho_2)$$

$$-(\frac{8(-1+r)(-(-1+r)^2\rho_1+\rho_2)^2(\rho_1+(-1+r)\rho_2)^2}{(-1+r)\rho_1+\rho_2}$$

$$-\operatorname{sech}^2(\alpha x)(39(-1+r)^4\rho_1^3$$

$$(-117+421r-673r^2+469r^3+39r^4$$

$$-241r^5+119r^6-17r^7)\rho_1^2\rho_2$$

$$+(117-374r+592r^2-700r^3+610r^4-302r^5+60r^6)\rho_1\rho_2^2$$

$$+(-39+109r-153r^2+115r^3-32r^4)\rho_2^3$$

$$+\cosh(2\alpha x)(7(-1+r)^4\rho_1^3$$

$$+(-21+85r-169r^2+237r^3-233r^4$$

$$+143r^5-49r^6+7r^7)\rho_1^2\rho_2$$

$$+(21-86r+160r^2-140r^3+50r^4+2r^5-4r^6)\rho_1\rho_2^2$$

$$+(-7+29r-33r^2+11r^3)\rho_2^3)))\tanh(\alpha x))$$

$$\varepsilon^2\operatorname{sech}^4(\alpha x)((-1+r)^2\rho_1-\rho_2)$$

$$(-72y^4\operatorname{sech}(\alpha x)(302\sinh(\alpha x)-57\sinh(3\alpha x)+\sinh(5\alpha x))$$

$$(-(-1+r)^2\rho_1+\rho_2)^2(\rho_1+(-1+r)\rho_2)^2$$

$$-\frac{1}{(-1+r)\rho_1+\rho_2}120y^2(\rho_1+(-1+r)\rho_2)$$

$$((-1+r)^5(-821+152\cosh(2\alpha x)+13\cosh(4\alpha x))\rho_1^4$$

$$+(-1+r)^2(-3284+7930r-8312r^2+1132r^3+4029r^4-2682r^5+447r^6$$

$$-8(-76+166r-96r^2-236r^3+379r^4-198r^5+33r^6)\cosh(2\alpha x)$$

$$+(52-138r+200r^2-204r^3+139r^4-54r^5+9r^6)\cosh(4\alpha x))\rho_1^3\rho_2$$

$$+(-1+r)(-4926+13938r-19443r^2+15936r^3-9533r^4+4240r^5-961r^6$$

$$+8(114-270r+237r^2-48r^3+43r^4-80r^5+31r^6)\cosh(2\alpha x)$$

$$+(78-258r+459r^2-480r^3+277r^4-80r^5+9r^6)\cosh(4\alpha x))\rho_1^2\rho_2^2$$

$$+(-3284+10654r-17234r^2+20344r^3-16851r^4+7770r^5-1444r^6$$

$$+8(76-194r+262r^2-440r^3+525r^4-294r^5+60r^6)\cosh(2\alpha x)$$

$$+(52-206r+370r^2-344r^3+171r^4-42r^5+4r^6)\cosh(4\alpha x))\rho_1\rho_2^3$$

$$
\begin{aligned}
&+(-1+r)(-821+1362r-1737r^2+704r^3\\
&\quad-8(-19+14r-55r^2+32r^3)\cosh(2\alpha x)\\
&\quad+(13-34r+17r^2)\cosh(4\alpha x))\rho_2^4)\tanh(\alpha x)\\
&-((3(-1+r)^{10}(20461+1980\cosh(2\alpha x)-49\cosh(4\alpha x))\rho_1^8\\
&\quad+2(-1+r)^6(-245532+830346r-1155342r^2+436692r^3+797627r^4\\
&\qquad-1281573r^5+877131r^6-347637r^7+82944r^8-9216r^9\\
&\quad+12(-1980+8466r-19258r^2+35432r^3-52581r^4+52499r^5\\
&\qquad-34105r^6+14119r^7-3456r^8+384r^9)\cosh(2\alpha x)\\
&\quad+(588-690r-3114r^2+16140r^3-23927r^4\\
&\qquad+17673r^5-6519r^6+969r^7)\cosh(4\alpha x))\rho_1^7\rho_2\\
&\quad+(-1+r)^4(1718724-8187396r+17703546r^2-19505232r^3\\
&\qquad+6070440r^4+12699600r^5-19887804r^6+13075056r^7\\
&\qquad-3682339r^8-424260r^9+606054r^{10}-154548r^{11}+12879r^{12}\\
&\quad-12(-13860+90804r-301634r^2+679280r^3-1093232r^4\\
&\qquad+1242032r^5-923524r^6+354576r^7+36971r^8-114668r^9\\
&\qquad+55714r^{10}-12108r^{11}+1009r^{12})\cosh(2\alpha x)\\
&\quad+(-4116+1428r+62622r^2-283632r^3+648408r^4\\
&\qquad-949008r^5+995052r^6-787248r^7+471967r^8-206508r^9\\
&\qquad+61698r^{10}-11196r^{11}+933r^{12})\cosh(4\alpha x))\rho_1^6\rho_2^2\\
&\quad+2(-1+r)^3(1718724-8843646r+21723534r^2-31167336r^3\\
&\qquad+26188785r^4-8841120r^5-7113246r^6+12718452r^7\\
&\qquad-10240838r^8+5539250r^9-2042488r^{10}+452142r^{11}-43497r^{12}\\
&\quad+12(13860-108486r+405858r^2-950648r^3+1499981r^4\\
&\qquad-1651480r^5+1293910r^6-754460r^7+366030r^8\\
&\qquad-164526r^9+61968r^{10}-15010r^{11}+1591r^{12})\cosh(2\alpha x)\\
&\quad+(-4116-6090r+112266r^2-433848r^3+1002219r^4\\
&\qquad-1593600r^5+1810854r^6-1477188r^7+853742r^8\\
&\qquad-339674r^9+88504r^{10}-13638r^{11}+957r^{12})\cosh(4\alpha x))\rho_1^5\rho_2^3\\
&\quad+(-1+r)^2(4296810-23749740r+64899450r^2-113350020r^3\\
&\qquad+139043293r^4-123100048r^5+74800872r^6-23291680r^7\\
&\qquad-5693285r^8+9889008r^9-4552688r^{10}+949796r^{11}-70441r^{12}\\
&\quad+12(34650-315420r+1266850r^2-3006980r^3+4694445r^4\\
&\qquad-5151504r^5+4302584r^6-3025536r^7+1863187r^8\\
&\qquad-916736r^9+308776r^{10}-59644r^{11}+4727r^{12})\cosh(2\alpha x)\\
&\quad+(-10290-34020r+414750r^2-1472940r^3+3220223r^4
\end{aligned}
$$

$$
\begin{aligned}
&-4944944r^5+5446968r^6-4274144r^7+2360393r^8\\
&-900336r^9+228176r^{10}-35060r^{11}+2557r^{12})\cosh(4\alpha x))\rho_1^4\rho_2^4\\
&+2(-1+r)(1718724-10156146r+30412284r^2-61232706r^3\\
&+91254585r^4-103412532r^5+89068218r^6-58361436r^7\\
&+29748694r^8-12208668r^9+3963368r^{10}-879470r^{11}+93596r^{12}\\
&-12(-13860+143850r-604280r^2+1441570r^3-2254805r^4\\
&+2523300r^5-2157090r^6+1440460r^7-709814r^8+220604r^9\\
&-26744r^{10}-5026r^{11}+1492r^{12})\cosh(2\alpha x)\\
&+(-4116-21126r+223524r^2-753366r^3+1495875r^4\\
&-2014332r^5+1919838r^6-1307316r^7+633650r^8-215604r^9\\
&+50104r^{10}-7546r^{11}+628r^{12})\cosh(4\alpha x))\rho_1^3\rho_2^5\\
&+(1718724-10812396r+35081046r^2-78054888r^3+129108858r^4\\
&-161864904r^5+155543880r^6-116408856r^7+68303465r^8\\
&-30556412r^9+9639714r^{10}-1857584r^{11}+159920r^{12}\\
&-12(-13860+161532r-698478r^2+1672840r^3-2645986r^4\\
&+3043256r^5-2606080r^6+1558200r^7-529273r^8+9980r^9\\
&+71134r^{10}-26608r^{11}+3280r^{12})\cosh(2\alpha x)\\
&+(-4116-28644r+285138r^2-930168r^3+1659102r^4\\
&-1800408r^5+1181880r^6-400776r^7+1027r^8+52268r^9\\
&-15882r^{10}+368r^{11}+400r^{12})\cosh(4\alpha x))\rho_1^2\rho_2^6\\
&+2(-1+r)(245532-1147314r+3169278r^2-6087846r^3\\
&+8126191r^4-7737176r^5+5354173r^6\\
&-2563942r^7+741596r^8-95200r^9\\
&+12(1980-21642r+67498r^2-115142r^3+138359r^4\\
&-117640r^5+61133r^6-14838r^7-52r^8+480r^9)\cosh(2\alpha x)\\
&+(-588-6342r+38010r^2-78114r^3+70757r^4-15496r^5\\
&-23905r^6+22366r^7-8012r^8+1120r^9)\cosh(4\alpha x))\rho_1\rho_2^7\\
&+3(-1+r)^2(20461-62500r+163750r^2-213460r^3\\
&+167605r^4-77440r^5+15360r^6\\
&-4(-495+5052r-8138r^2+11452r^3\\
&-8383r^4+2080r^5)\cosh(2\alpha x)\\
&+(-49-716r+2434r^2\\
&-2076r^3+519r^4)\cosh(4\alpha x))\rho_2^8)\tanh(\alpha x))\\
&/(((-1+r)\rho_1+\rho_2)^2(-(-1+r)^2\rho_1+\rho_2)^2))
\end{aligned}
\qquad \text{(D.4)}
$$

)

$$\frac{u_2}{c_0}=1+\frac{\varepsilon((-1+r)^2\rho_1-\rho_2+2\operatorname{sech}^2(\alpha x)((-1+r)\rho_1+\rho_2))}{2(-1+r)((-1+r)\rho_1+\rho_2)}$$
$$-\frac{1}{40(-1+r)^3}\varepsilon^2(-\frac{20(-1+r)\operatorname{sech}^2(\alpha x)((-1+r)^2\rho_1-\rho_2)}{(-1+r)\rho_1+\rho_2}$$
$$+\frac{5(-1+r)(-(-1+r)^2\rho_1+\rho_2)^2}{((-1+r)\rho_1+\rho_2)^2}$$
$$+\frac{30(r-y)^2(-2+\cosh(2\alpha x))\operatorname{sech}^4(\alpha x)((-1+r)^2\rho_1-\rho_2)}{\rho_1+(-1+r)\rho_2}$$
$$+\frac{1}{(-\rho_1+\rho_2)((-1+r)\rho_1+\rho_2)^2}(\rho_1-\rho_2)$$
$$(20(-1+r)(-(-1+r)^2\rho_1+\rho_2)^2$$
$$-20(-1+r)((-1+r)\rho_1+\rho_2)((-1+r)^3\rho_1+\rho_2)$$
$$-\frac{((-1+r)\rho_1+\rho_2)(-(-1+r)^2\rho_1+\rho_2)^2(\rho_1+(-1+r)^3\rho_2)}{(\rho_1+(-1+r)\rho_2)^2})$$
$$-10\operatorname{sech}^2(\alpha x)(4(-1+r)\operatorname{sech}^2(\alpha x)$$
$$+\frac{(-1+r)^2(-2+\cosh(2\alpha x))\operatorname{sech}^2(\alpha x)((-1+r)^2\rho_1-\rho_2)}{\rho_1+(-1+r)\rho_2}$$
$$-((3(-1+r)^4\rho_1^3+(-9+33r-57r^2+81r^3$$
$$-89r^4+59r^5-21r^6+3r^7)\rho_1^2\rho_2$$
$$+(9-30r+48r^2-24r^3-10r^4+14r^5-4r^6)\rho_1\rho_2^2$$
$$+3(-1+r)^3\rho_2^3)\tanh^2(\alpha x))$$
$$/(((-1+r)^2\rho_1-\rho_2)(\rho_1+(-1+r)\rho_2)^2)))$$
$$+\frac{1}{6720(-1+r)^5}\varepsilon^3$$
$$(\frac{315(r-y)^4(33-26\cosh(2\alpha x)+\cosh(4\alpha x))\operatorname{sech}^6(\alpha x)(-(-1+r)^2\rho_1+\rho_2)^2}{(\rho_1+(-1+r)\rho_2)^2}$$
$$+\frac{12}{((-1+r)\rho_1+\rho_2)^3(\rho_1+(-1+r)\rho_2)^4}(30(-1+r)^8\rho_1^7$$
$$+(-1+r)^4(-210+780r-1930r^2+2068r^3-1893r^4$$
$$+1661r^5-1183r^6+555r^7-144r^8+16r^9)\rho_1^6\rho_2$$
$$+(-1+r)^3(-630+2790r-9140r^2+16104r^3$$
$$-17465r^4+13682r^5-8183r^6+3470r^7$$
$$-988r^8+184r^9-22r^{10}+2r^{11})\rho_1^5\rho_2^2$$
$$+(-1+r)^2(-1050+5400r-19900r^2+46016r^3$$
$$-65266r^4+59950r^5-38689r^6+18965r^7$$
$$-7267r^8+2067r^9-393r^{10}+39r^{11})\rho_1^4\rho_2^3$$

$$
\begin{aligned}
&+(1050-7200r+29800r^2-86984r^3+175372r^4\\
&\quad-243202r^5+235543r^6-162699r^7+81881r^8\\
&\quad-30433r^9+8201r^{10}-1457r^{11}+128r^{12})\rho_1^3\rho_2^4\\
&+(-630+4140r-15890r^2+44556r^3-90773r^4\\
&\quad+130581r^5-130652r^6+89850r^7-41659r^8\\
&\quad+12553r^9-2274r^{10}+196r^{11})\rho_1^2\rho_2^5\\
&+(210-1320r+4360r^2-10492r^3+20037r^4\\
&\quad-28989r^5+29813r^6-20807r^7+9344r^8\\
&\quad-2436r^9+280r^{10})\rho_1\rho_2^6\\
&-30(-1+r)^6\rho_2^7)\\
&-\frac{630(r-y)^2\operatorname{sech}^6(\alpha x)}{((-1+r)\rho_1+\rho_2)(\rho_1+(-1+r)\rho_2)^3}(\cosh(4\alpha x)((-1+r)^5(-2-2r+r^2)\rho_1^4\\
&\quad-(-1+r)^3(-8+6r-7r^2+9r^3-5r^4+r^5)\rho_1^3\rho_2\\
&\quad+(12-42r+77r^2-93r^3+68r^4-26r^5+4r^6)\rho_1^2\rho_2^2\\
&\quad+(-8+26r-43r^2+34r^3-13r^4+2r^5)\rho_1\rho_2^3\\
&\quad-2(-1+r)^3\rho_2^4)\\
&-2\cosh(2\alpha x)((-1+r)^4(-14+24r-39r^2+13r^3)\rho_1^4\\
&\quad-(-1+r)^2(-56+170r-263r^2+136r^3-14r^4-6r^5+r^6)\rho_1^3\rho_2\\
&\quad+(-84+366r-703r^2+783r^3-596r^4+326r^5-108r^6+16r^7)\rho_1^2\rho_2^2\\
&\quad+(56-206r+305r^2-334r^3+243r^4-94r^5+16r^6)\rho_1\rho_2^3\\
&\quad+14(-1+r)^3\rho_2^4)\\
&+3((-1+r)^4(-18+24r-33r^2+11r^3)\rho_1^4\\
&\quad+(-1+r)^2(72-198r+289r^2-168r^3+42r^4-6r^5+r^6)\rho_1^3\rho_2\\
&\quad+(-108+450r-857r^2+969r^3-732r^4+378r^5-116r^6+16r^7)\rho_1^2\rho_2^2\\
&\quad+(72-258r+391r^2-402r^3+269r^4-98r^5+16r^6)\rho_1\rho_2^3\\
&\quad+18(-1+r)^3\rho_2^4))\\
&+\frac{168}{(1-r)((-1+r)\rho_1+\rho_2)^2}(-1+r)^2\operatorname{sech}^2(\alpha x)(5(-1+r)(-(-1+r)^2\rho_1+\rho_2)^2\\
&\quad-(20(-1+r)(-(-1+r)^2\rho_1+\rho_2)^2\\
&\quad-20(-1+r)((-1+r)\rho_1+\rho_2)((-1+r)^3\rho_1+\rho_2)\\
&\quad-\frac{((-1+r)\rho_1+\rho_2)(-(-1+r)^2\rho_1+\rho_2)^2(\rho_1+(-1+r)^3\rho_2)}{(\rho_1+(-1+r)\rho_2)^2}))\\
&+\frac{840(-1+r)}{(-1+r)\rho_1+\rho_2}\operatorname{sech}^2(\alpha x)((-1+r)^2\rho_1-\rho_2)(4(-1+r)\operatorname{sech}^2(\alpha x)
\end{aligned}
$$

$$
\begin{aligned}
&+\frac{(-1+r)^2(-2+\cosh(2\alpha x))\operatorname{sech}^2(\alpha x)((-1+r)^2\rho_1-\rho_2)}{\rho_1+(-1+r)\rho_2}\\
&-((3(-1+r)^4\rho_1^3\\
&\quad+(-9+33r-57r^2+81r^3-89r^4+59r^5-21r^6+3r^7)\rho_1^2\rho_2\\
&\quad+(9-30r+48r^2-24r^3-10r^4+14r^5-4r^6)\rho_1\rho_2^2\\
&\quad+3(-1+r)^3\rho_2^3)\tanh^2(\alpha x))\\
&/(((-1+r)^2\rho_1-\rho_2)(\rho_1+(-1+r)\rho_2)^2))\\
&+7(-1+r)\operatorname{sech}^2(\alpha x)(960(-1+r)\operatorname{sech}^4(\alpha x)\\
&+(21(-1+r)^3(33-26\cosh(2\alpha x)+\cosh(4\alpha x))\\
&\quad\operatorname{sech}^4(\alpha x)(-(-1+r)^2\rho_1+\rho_2)^2)\\
&\quad/(\rho_1+(-1+r)\rho_2)^2\\
&+\frac{960(-1+r)^2\operatorname{sech}^2(\alpha x)((-1+r)^2\rho_1-\rho_2)\tanh^2(\alpha x)}{\rho_1+(-1+r)\rho_2}\\
&-\frac{480}{((-1+r)^2\rho_1-\rho_2)(\rho_1+(-1+r)\rho_2)^2}\operatorname{sech}^2(\alpha x)(3(-1+r)^4\rho_1^3\\
&\quad+(-9+33r-57r^2+81r^3-89r^4+59r^5-21r^6+3r^7)\rho_1^2\rho_2\\
&\quad+(9-30r+48r^2-24r^3-10r^4+14r^5-4r^6)\rho_1\rho_2^2\\
&\quad+3(-1+r)^3\rho_2^3)\tanh^2(\alpha x)\\
&-(4\operatorname{sech}^2(\alpha x)(5\cosh(2\alpha x)(15(-1+r)^8\rho_1^6\\
&\qquad+2(-1+r)^4(-45+165r-297r^2+465r^3\\
&\qquad\quad-478r^4+297r^5-102r^6+15r^7)\rho_1^5\rho_2\\
&\qquad+(-1+r)^2(225-1200r+3216r^2-6108r^3\\
&\qquad\quad+9329r^4-11540r^5+11322r^6-8640r^7\\
&\qquad\quad+4997r^8-2100r^9+606r^{10}-108r^{11}+9r^{12})\rho_1^4\rho_2^2\\
&\qquad-2(-1+r)^2(150-750r+1962r^2-3348r^3\\
&\qquad\quad+4632r^4-5328r^5+4569r^6-2664r^7+995r^8\\
&\qquad\quad-218r^9+21r^{10})\rho_1^3\rho_2^3\\
&\qquad+(225-1500r+4866r^2-9552r^3+12452r^4\\
&\qquad\quad-11324r^5+7542r^6-4000r^7+1884r^8\\
&\qquad\quad-800r^9+272r^{10}-64r^{11}+8r^{12})\rho_1^2\rho_2^4\\
&\qquad+2(-1+r)^3(45-150r+252r^2-120r^3-137r^4\\
&\qquad\quad+213r^5-108r^6+20r^7)\rho_1\rho_2^5\\
&\qquad+15(-1+r)^6\rho_2^6)\\
&\qquad-2(114(-1+r)^8\rho_1^6
\end{aligned}
$$

$$
\begin{aligned}
&-(-1+r)^4(684-2508r+3876r^2-2766r^3-541r^4\\
&\quad+3954r^5-4341r^6+2358r^7-648r^8+72r^9)\rho_1^5\rho_2\\
&+(-1+r)^2(1710-9120r+21888r^2-30156r^3\\
&\quad+23132r^4-7496r^5+2295r^6-7968r^7+10922r^8\\
&\quad-7266r^9+2694r^{10}-540r^{11}+45r^{12})\rho_1^4\rho_2^2\\
&-(2280-15960r+51072r^2-98952r^3+127272r^4\\
&\quad-109680r^5+48867r^6+26220r^7-73580r^8+72102r^9\\
&\quad-41802r^{10}+14948r^{11}-3063r^{12}+276r^{13})\rho_1^3\rho_2^3\\
&+(1710-11400r+34428r^2-63324r^3+78338r^4\\
&\quad-63224r^5+27495r^6-778r^7-3939r^8-530r^9\\
&\quad+2057r^{10}-928r^{11}+140r^{12})\rho_1^2\rho_2^4\\
&+(-684+4332r-12084r^2+20034r^3-21593r^4+16038r^5\\
&\quad-9456r^6+5368r^7-2739r^8+924r^9-140r^{10})\rho_1\rho_2^5\\
&+114(-1+r)^6\rho_2^6))\tanh^2(\alpha x))\\
&/((1-r)(-(-1+r)^2\rho_1+\rho_2)^2(\rho_1+(-1+r)\rho_2)^4)\\
&+\frac{1}{(\rho_1+(-1+r)\rho_2)^3}15(1-r)((21-18\cosh(2\alpha x)+\cosh(4\alpha x))\\
&\operatorname{sech}^4(\alpha x)(3(-1+r)^4\rho_1^3\\
&\quad+(-9+33r-57r^2+81r^3-89r^4+59r^5-21r^6+3r^7)\rho_1^2\rho_2\\
&\quad+(9-30r+48r^2-24r^3-10r^4+14r^5-4r^6)\rho_1\rho_2^2\\
&\quad+3(-1+r)^3\rho_2^3)\\
&-4\operatorname{sech}^2(\alpha x)(5(-1+r)^4\rho_1^3\\
&\quad+(-15+55r-103r^2+115r^3-75r^4+29r^5-7r^6+r^7)\rho_1^2\rho_2\\
&\quad+(15-50r+88r^2-100r^3+70r^4-26r^5+4r^6)\rho_1\rho_2^2\\
&\quad+5(-1+r)^3\rho_2^3)\\
&+8(5(-1+r)^4\rho_1^3\\
&+(-15+55r-103r^2+115r^3-75r^4+29r^5-7r^6+r^7)\rho_1^2\rho_2\\
&+(15-50r+88r^2-100r^3+70r^4-26r^5+4r^6)\rho_1\rho_2^2\\
&+5(-1+r)^3\rho_2^3)\tanh^2(\alpha x))))
\end{aligned}
$$

(D.5)

$$\frac{v_2}{c_0}=\frac{\sqrt{\frac{(-1+r)^2(\rho_1+(-1+r)\rho_2)}{(-1+r)^2\rho_1-\rho_2}}}{5120\sqrt{3}(-1+r)^5(\rho_1+(-1+r)\rho_2)^5}\varepsilon^{3/2}(-r+y)\operatorname{sech}^2(\alpha x)$$
$$(15360(-1+r)^2((-1+r)^2\rho_1-\rho_2)(\rho_1+(-1+r)\rho_2)^4\tanh(\alpha x)$$
$$-960\varepsilon(\rho_1+(-1+r)\rho_2)^2(2(r-y)^2\operatorname{sech}^3(\alpha x)$$
$$(-11\sinh(\alpha x)+\sinh(3\alpha x))$$
$$(-(-1+r)^2\rho_1+\rho_2)^2(\rho_1+(-1+r)\rho_2)$$
$$+(-\frac{8(-1+r)(-(-1+r)^2\rho_1+\rho_2)^2(\rho_1+(-1+r)\rho_2)^2}{(-1+r)\rho_1+\rho_2}$$
$$+\operatorname{sech}^2(\alpha x)((-1+r)^3(-39+47r-60r^2+20r^3)\rho_1^3$$
$$+(-117+445r-805r^2+745r^3-345r^4$$
$$+95r^5-21r^6+3r^7)\rho_1^2\rho_2$$
$$+(117-398r+604r^2-676r^3+490r^4$$
$$-182r^5+28r^6)\rho_1\rho_2^2$$
$$+39(-1+r)^3\rho_2^3$$
$$+\cosh(2\alpha x)(-(-1+r)^4(-7-8r+4r^2)\rho_1^3$$
$$+(-21+61r-85r^2+105r^3-105r^4$$
$$+63r^5-21r^6+3r^7)\rho_1^2\rho_2$$
$$+(21-62r+100r^2-68r^3$$
$$+10r^4+10r^5-4r^6)\rho_1\rho_2^2$$
$$+7(-1+r)^3\rho_2^3)))\tanh(\alpha x))$$
$$\frac{1}{(-1+r)^2}\varepsilon^2\operatorname{sech}^4(\alpha x)((-1+r)^2\rho_1-\rho_2)$$
$$(72(r-y)^4\operatorname{sech}(\alpha x)(302\sinh(\alpha x)-57\sinh(3\alpha x)+\sinh(5\alpha x))$$
$$(-(-1+r)^2\rho_1+\rho_2)^2(\rho_1+(-1+r)\rho_2)^2$$
$$+\frac{120}{(-1+r)\rho_1+\rho_2}(r-y)^2(\rho_1+(-1+r)\rho_2)((-1+r)^4$$
$$(821-1101r+1476r^2-492r^3$$
$$+8(-19+43r-84r^2+28r^3)\cosh(2\alpha x)$$
$$+(-13+5r+12r^2-4r^3)\cosh(4\alpha x))\rho_1^4$$
$$+(-1+r)^2(-3284+9050r-13224r^2$$
$$+7732r^3-1943r^4+270r^5-45r^6$$
$$-8(-76+262r-432r^2+188r^3+23r^4-30r^5+5r^6)\cosh(2\alpha x)$$
$$+(52-106r+120r^2-116r^3+79r^4-30r^5+5r^6)\cosh(4\alpha x))\rho_1^3\rho_2$$

$$
\begin{aligned}
&+(-1+r)(-4926+15618r-23643r^2\\
&\quad+20976r^3-12893r^4+4656r^5-749r^6\\
&\quad+8(114-414r+597r^2-480r^3+331r^4-144r^5+27r^6)\cosh(2\alpha x)\\
&\quad+(78-210r+339r^2-336r^3+181r^4-48r^5+5r^6)\cosh(4\alpha x))\rho_1^2\rho_2^2\\
&+(-3284+11774r-17922r^2+18496r^3-12407r^4+4530r^5-740r^6\\
&\quad+8(76-290r+406r^2-480r^3+385r^4-158r^5+28r^6)\cosh(2\alpha x)\\
&\quad+(52-174r+290r^2-256r^3+127r^4-34r^5+4r^6)\cosh(4\alpha x))\rho_1\rho_2^3\\
&+(-1+r)^3(-821+152Cosh(2\alpha x)+13Cosh(4\alpha x))\rho_2^4)\tanh(\alpha x)\\
&+\frac{1}{((-1+r)\rho_1+\rho_2)^2(-(-1+r)^2\rho_1+\rho_2)^2}\\
&(3(-1+r)^8(20461-60266r+158165r^2\\
&\quad-225760r^3+191640r^4-82656r^5+13776r^6\\
&\quad-4(-495-2082r+9697r^2-19520r^3\\
&\quad+20240r^4-9408r^5+1568r^6)\cosh(2\alpha x)\\
&\quad+(-1+r)^2(-49+912r-8r^2-448r^3+112r^4)\cosh(4\alpha x))\rho_1^8\\
&+2(-1+r)^6(-245532+1062474r-2829918r^2+4596996r^3\\
&\quad-4841401r^4+3125871r^5-1210293r^6+288939r^7-47628r^8+5292r^9\\
&\quad+12(-1980-3822r+34358r^2-82312r^3+97507r^4-56005r^5\\
&\quad+11879r^6+1943r^7-1224r^8+136r^9)\cosh(2\alpha x)\\
&\quad+(588-11634r+33894r^2-39012r^3+28957r^4-21099r^5\\
&\quad+14793r^6-6999r^7+1836r^8-204r^9)\cosh(4\alpha x))\rho_1^7\rho_2\\
&+(-1+r)^4(1718724-9812292r+29580474r^2-56193072r^3\\
&\quad+71984976r^4-63894240r^5+40720668r^6-19197648r^7\\
&\quad+6547277r^8-1459764r^9+171054r^{10}-6804r^{11}+567r^{12}\\
&\quad+12(13860-4788r-163614r^2+523120r^3-770144r^4\\
&\quad+608688r^5-268428r^6+66928r^7-7787r^8\\
&\quad-3188r^9+2766r^{10}-756r^{11}+63r^{12})\cosh(2\alpha x)\\
&\quad+(-4116+78036r-301602r^2+559728r^3-644880r^4\\
&\quad+509472r^5-257964r^6+48144r^7+36079r^8-32316r^9\\
&\quad+11898r^{10}-2268r^{11}+189r^{12})\cosh(4\alpha x))\rho_1^6\rho_2^2\\
&+2(-1+r)^3(1718724-10468542r+32130462r^2-62421384r^3\\
&\quad+83717301r^4-81422040r^5+59302734r^6-32306028r^7\\
&\quad+12845998r^8-3636214r^9+726764r^{10}-102690r^{11}+8511r^{12}
\end{aligned}
$$

$$
\begin{aligned}
&+12(13860-22470r-63310r^2+261320r^3-401275r^4\\
&\quad+361160r^5-216610r^6+58980r^7+35894r^8-45102r^9\\
&\quad+19896r^{10}-4178r^{11}+343r^{12})\cosh(2\alpha x)\\
&+(-4116+70518r-280518r^2+585576r^3-749049r^4\\
&\quad+577080r^5-202086r^6-63588r^7+111194r^8-58802r^9\\
&\quad+16948r^{10}-2742r^{11}+213r^{12})\cosh(4\alpha x))\rho_1^5\rho_2^3\\
&+(-1+r)^2(4296810-27811980r+87241770r^2-174706980r^3\\
&\quad+247582213r^4-262238896r^5+211668120r^6-130089472r^7\\
&\quad+60678955r^8-21262656r^9+5390392r^{10}-890044r^{11}+71327r^{12}\\
&-12(-34650+100380r-84130r^2-63580r^3+252675r^4\\
&\quad-471024r^5+568744r^6-417216r^7+195053r^8-67008r^9\\
&\quad+20264r^{10}-4836r^{11}+601r^{12})\cosh(2\alpha x)\\
&+(-10290+157500r-638610r^2+1460340r^3-2079337r^4\\
&\quad+1815280r^5-856056r^6+44032r^7+223673r^8-164544r^9\\
&\quad+62696r^{10}-13460r^{11}+1333r^{12})\cosh(4\alpha x))\rho_1^4\rho_2^4\\
&+2(-1+r)(1718724-11781042r+37879212r^2-77786754r^3\\
&\quad+114808581r^4-128295372r^5+110507334r^6-73658604r^7\\
&\quad+37651486r^8-14313804r^9+3808712r^{10}-630686r^{11}+48716r^{12}\\
&-12(-13860+57834r-127272r^2+190402r^3-168269r^4\\
&\quad+4740r^5+205126r^6-321988r^7+291898r^8-172132r^9\\
&\quad+64680r^{10}-14162r^{11}+1412r^{12})\cosh(2\alpha x)\\
&+(-4116+55482r-226380r^2+551658r^3-892713r^4\\
&\quad+992028r^5-766350r^6+400668r^7-126166r^8+12924r^9\\
&\quad+6232r^{10}-2698r^{11}+388r^{12})\cosh(4\alpha x))\rho_1^3\rho_2^5\\
&+(1718724-12437292r+41077974r^2-85342728r^3+127030962r^4\\
&\quad-142889016r^5+123810912r^6-82671288r^7+41805809r^8\\
&\quad-15456476r^9+3936882r^{10}-616304r^{11}+44720r^{12}\\
&-12(-13860+75516r-217550r^2+392040r^3-431282r^4\\
&\quad+257624r^5+21392r^6-226952r^7+252631r^8-155524r^9\\
&\quad+58622r^{10}-13008r^{11}+1360r^{12})\cosh(2\alpha x)\\
&+(-4116+47964r-193326r^2+484392r^3-888090r^4\\
&\quad+1246488r^5-1310496r^6+992280r^7-518405r^8\\
&\quad+174860r^9-32346r^{10}+1328r^{11}+400r^{12})\cosh(4\alpha x))\rho_1^2\rho_2^6
\end{aligned}
$$

$$
\begin{aligned}
&+2(-1+r)(245532-1379442r+3351726r^2\\
&\quad-5025702r^3+5282059r^4-3992840r^5\\
&\quad+2101333r^6-730678r^7+153356r^8-14560r^9\\
&\quad-12(-1980+9354r-22810r^2+28646r^3\\
&\quad-19791r^4+9816r^5-7533r^6+6182r^7\\
&\quad-2748r^8+480r^9)\cosh(2\alpha x)\\
&\quad+(-1+r)^2(-588+3426r-5094r^2+10800r^3\\
&\quad-16273r^4+13590r^5-6012r^6+1120r^7)\cosh(4\alpha x))\rho_1\rho_2^7\\
&+3(-1+r)^6(20461+1980\cosh(2\alpha x)-49\cosh(4\alpha x))\rho_2^8)\tanh(\alpha x))\\
)
\end{aligned}
$$

(D.6)

APPENDIX E: L1-norm

Let us consider a system of linear equations

$$\mathbf{A}\,\mathbf{q} = \mathbf{b}, \tag{E.1}$$

where $\mathbf{q}$ is the vector of unknown variables, $\mathbf{A}$ is the coefficient matrix and $\mathbf{b}$ is a known vector. When an approximate solution for $\mathbf{q}$ is found, the normalisation factor F_{norm} is defined as

$$F_{norm} = \sum \left(\left| \mathbf{A}\,\mathbf{q} - \mathbf{A}\,\bar{\mathbf{q}} \right| + \left| \mathbf{b} - \mathbf{A}\,\bar{\mathbf{q}} \right| \right) + M_{small}, \tag{E.2}$$

where $\sum$ means the summation of all the components, $\bar{\mathbf{q}}$ means averaging the components, and $M_{small} = 1.0 \times 10^{-20}$. The normalised residual can be written as

$$res_N = \frac{\sum \left| \mathbf{b} - \mathbf{A}\,\mathbf{q} \right|}{F_{norm}}. \tag{E.3}$$

res_N reaches the maximum, 1, when the variable is uniform over the field. It is 0 for the exact solution.

Bibliography

Ablowitz, M.J., Baldwin, D.E., 2012. Nonlinear shallow ocean-wave soliton interactions on flat beaches. *Physical Review E* 86 (3), 036305.

Ablowitz, M.J., Segur, H., 1980. Long internal waves in fluids of great depth. *Studies in Applied Mathematics* 62, 249-262.

Abramowitz, M., Stegun, I.A., 1964. Handbook of mathematical functions: with formulas, graphs, and mathematical tables. *Courier Corporation*.

Akylas, T., 1994. Three-dimensional long water-wave phenomena. *Annual Review of Fluid Mechanics* 26 (1), 191-210.

Alford, M.H., et al., 2015. The formation and fate of internal waves in the South China Sea. *Nature* 521 (7550), 65-69.

Amick, C., Turner, R., 1986. A global theory of internal solitary waves in two-fluid systems. *Transactions of the American Mathematical Society* 298 (2), 431-484.

Barakhnin, V.B., Khakimzyanov, G.S., 1999. Numerical simulation of an obliquely incident solitary wave. *Journal of Applied Mechanics and Technical Physics* 40 (6), 1008-1015.

Barros, R., Choi, W., 2013. On regularizing the strongly nonlinear model for two-dimensional internal waves. *Physica D: Nonlinear Phenomena* 264 (0), 27-34.

Batchelor, G.K., 2000. An introduction to fluid dynamics. *Cambridge university press*.

Behrens, T., 2009. OpenFOAM's basic solvers for linear systems of equations: solvers, preconditioners, smoothers.

Benjamin, T.B., 1966. Internal waves of finite amplitude and permanent form. *Journal of fluid mechanics* 25 (2), 241-270.

Benjamin, T.B., 1967. Internal waves of permanent form in fluids of great depth. *Journal of fluid mechanics* 29 (03), 559-592.

Benjamin, T.B., Lighthill, M., 1954. On cnoidal waves and bores. *Proceedings of the Royal Society of London. Series A. Mathematical and Physical Sciences* 224 (1159), 448-460.

Berberović, E., van Hinsberg, N.P., Jakirlić, S., Roisman, I.V., Tropea, C., 2009. Drop impact onto a liquid layer of finite thickness: Dynamics of the cavity evolution. *Physical Review E* 79 (3), 036306.

Boussinesq, J., 1871. Théorie de l'intumescence liquide appelée onde solitaire ou de translation se propageant dans un canal rectangulaire. *Comptes Rendus Acad. Sci (Paris)* 72, 755-759.

Byatt-Smith, J., 1970. An exact integral equation for steady surface waves. *Proceedings of the Royal Society of London. A. Mathematical and Physical Sciences* 315 (1522), 405-418.

Cai, S., Long, X., Gan, Z., 2003. A method to estimate the forces exerted by internal solitons on cylindrical piles. *Ocean Engineering* 30 (5), 673-689.

Cai, S., Long, X., Wang, S., 2008. Forces and torques exerted by internal solitons in shear flows on cylindrical piles. *Applied Ocean Research* 30 (1), 72-77.

Cai, S., Wang, S., Long, X., 2006. A simple estimation of the force exerted by internal solitons on cylindrical piles. *Ocean Engineering* 33 (7), 974-980.

Cai, S., Xie, J., 2010. A propagation model for the internal solitary waves in the northern South China Sea. *Journal of Geophysical Research: Oceans* (1978–2012) 115 (C12).

Cai, S., Xie, J., He, J., 2012. An Overview of Internal Solitary Waves in the South China Sea. *Surveys in Geophysics* 33 (5), 927-943.

Camassa, R., Choi, W., Michallet, H., Rusås, P.-O., Sveen, J., 2006. On the realm of validity of strongly nonlinear asymptotic approximations for internal waves. *Journal of fluid mechanics* 549, 1-23.

Castro, C.E., Käser, M., Toro, E.F., 2009. Space–time adaptive numerical methods for geophysical applications. *Philosophical Transactions of the Royal Society A: Mathematical, Physical and Engineering Sciences* 367 (1907), 4613-4631.

Chakravarty, S., Kodama, Y., 2009. Soliton Solutions of the KP Equation and Application to Shallow Water Waves. *Studies in Applied Mathematics* 123 (1), 83-151.

Chen, J., 1996. The Development of Liuhua 11-1 Oilfield in South China Sea. *China offshore Platform* 1, 012.

Chen, Y., Liu, P.L.F., 1998. A generalized modified Kadomtsev-Petviashvili equation for interfacial wave propagation near the critical depth level. *Wave Motion* 27 (4), 321-339.

Choi, W., Camassa, R., 1999. Fully nonlinear internal waves in a two-fluid system. *Journal of fluid mechanics* 396 (1), 1-36.

Cointe, R., Geyer, P., King, B., Molin , B., Tramoni, M., 1990. Nonlinear and Linear Motions of a Rectangular Barge in a Perfect Fluid, *Proc. of the 18th Symp. on Nav. Hydrodyn., Ann Arbor, Michigan*, 85-99.

Craig, W., Guyenne, P., Hammack, J., Henderson, D., Sulem, C., 2006. Solitary water wave interactions. *Physics of Fluids* (1994-present) 18 (5), 057106.

Djordjevic, V.D., Redekopp, L., 1978. The fission and disintegration of internal solitary waves moving over two-dimensional topography. *Journal of Physical Oceanography* 8 (6), 1016-1024.

Duda, T.F., Lynch, J.F., Irish, J.D., Beardsley, R.C., Ramp, S.R., Chiu, C.-S., Tang, T.Y., Yang, Y.-J., 2004. Internal tide and nonlinear internal wave behavior at the continental slope in the northern South China Sea. *IEEE Journal of Oceanic Engineering* 29 (4), 1105-1130.

Dysthe, K., Krogstad, H.E., Müller, P., 2008. Oceanic rogue waves. *Annual Review of Fluid Mechanics*. 40, 287-310.

Editorial, 08/1996. Soliton wave receives crowd of admirers. *Nature* 376 (6539), 373.

Evans, W.A.B., Ford, M.J., 1996. An integral equation approach to internal (2‐layer) solitary waves. *Physics of Fluids* (1994-present) 8(8), 2032-2047.

Faltinsen, O., 1993. Sea loads on ships and offshore structures. *Cambridge university press*.

Fenton, J., 1972. A ninth-order solution for the solitary wave. *Journal of fluid mechanics* 53 (2), 257-271.

Fitzgerald, R.M., Sewell, G., 2000. Solving problems in computational physics using a general-purpose PDE solver. *Computer Physics Communications* 124 (2–3), 132-138.

Fritsch, F.N., Carlson, R.E., 1980. Monotone Piecewise Cubic Interpolation. *SIAM Journal on Numerical Analysis* 17(2), 238-246.

Funakoshi, M., 1980. Reflection of Obliquely Incident Solitary Waves. *Journal of the Physical Society of Japan* 49(6), 2371-2379.

Funakoshi, M., Oikawa, M., 1986. Long Internal Waves of Large Amplitude in a Two-Layer Fluid. *Journal of the Physical Society of Japan* 55(1), 128-144.

Gear, J.A., Grimshaw, R., 1983. A second‐order theory for solitary waves in shallow fluids. *Physics of Fluids* 26, 14.

Goda, Y., Haranaka, S., Kitahata, M., 1966. Study on impulsive breaking wave forces on piles. *Report Port and Harbour Technical Research Institute* 6 (5), 1-30.

Grilli, S., Svendsen, I., Subramanya, R., 1997. Breaking Criterion and Characteristics for Solitary Waves on Slopes. *Journal of waterway, port, coastal, and ocean engineering* 123(3), 102-112.

Grimshaw, R., 1971. The solitary wave in water of variable depth. Part 2. *Journal of fluid mechanics* 46(3), 611-622.

Grimshaw, R., Pelinovsky, E., Taipova, T., Sergeeva, A., 2010. Rogue internal waves in the ocean: long wave model. *The European Physical Journal-Special Topics* 185(1), 195-208.

Grimshaw, R.H., 2007. Solitary waves in fluids. *WIT Press*.

Grue, J., 2015a. Nonlinear dead water resistance at subcritical speed. *Physics of Fluids* 27 (8), 082103.

Grue, J., 2015b. Nonlinear interfacial wave formation in three dimensions. *Journal of fluid mechanics* 767, 735-762.

Grue, J., André Friis, H., Palm, E., Olav Rusås, P., 1997. A method for computing unsteady fully nonlinear interfacial waves. *Journal of fluid mechanics* 351, 223-252.

Grue, J., Jensen, A., Rusås, P.-O., Sveen, J.K., 1999. Properties of large-amplitude internal waves. *Journal of fluid mechanics* 380, 257-278.

Guo, C., Chen, X., 2014. A review of internal solitary wave dynamics in the northern South China Sea. *Progress in Oceanography* 121 (0), 7-23.

Harten, A., 1983. High resolution schemes for hyperbolic conservation laws. *Journal of Computational Physics* 49(3), 357-393.

Helfrich, K.R., 1992. Internal solitary wave breaking and run-up on a uniform slope. *Journal of fluid mechanics* 243, 133-133.

Helfrich, K.R., Melville, W.K., 2006. Long nonlinear internal waves. *Annual Review of Fluid Mechanics* 38, 395-425.

Hereman, W., 2011. Shallow water waves and solitary waves, *Mathematics of Complexity and Dynamical Systems*. Springer, 1520-1532.

Higuera, P., Lara, J.L., Losada, I.J., 2013a. Realistic wave generation and active wave absorption for Navier–Stokes models: Application to OpenFOAM®. *Coastal Engineering* 71, 102-118.

Higuera, P., Lara, J.L., Losada, I.J., 2013b. Simulating coastal engineering processes with OpenFOAM®. *Coastal Engineering* 71(0), 119-134.

Higuera, P., Lara, J.L., Losada, I.J., 2014. Three-dimensional interaction of waves and porous coastal structures using OpenFOAM®. Part I: Formulation and validation. *Coastal Engineering* 83, 243-258.

Hill, J., Collins, G.S., Avdis, A., Kramer, S.C., Piggott, M.D., 2014. How does multiscale modelling and inclusion of realistic palaeobathymetry affect numerical simulation of the Storegga Slide tsunami? *Ocean Modelling* 83(0), 11-25.

Hirota, R., 2004. The direct method in soliton theory. *Cambridge University Press*.

Hirsch, C., 1988. Numerical Computation of Internal and External Flows, *New York: John Wiley & Sons*, 161.

Hirt, C.W., Nichols, B.D., 1981. Volume of fluid (VOF) method for the dynamics of free boundaries. *Journal of Computational Physics* 39(1), 201-225.

Hrvoje, J., 2009. Dynamic Mesh Handling in OpenFOAM, *47th AIAA Aerospace Sciences Meeting including The New Horizons Forum and Aerospace Exposition*. American Institute of Aeronautics and Astronautics.

Huang, W.-H., You, Y.-X., Wang, X., Hu, T.-Q., 2013. Wave-making experiments and theorectical models for internal solitary waves in a two-layer fluid of finite depth. *Acta Physica Sinica* 62(8), 084705.

Issa, R.I., 1986. Solution of the implicitly discretised fluid flow equations by operator-splitting. *Journal of Computational Physics* 62(1), 40-65.

Jackson, C.R., Apel, J., 2004. An atlas of internal solitary-like waves and their properties, 2nd ed. *Global Ocean Associates, Alexandria, VA*.

Jackson, C.R., da Silva, J.C., Jeans, G., Alpers, W., Caruso, M.J., 2013. Nonlinear Internal Waves in Synthetic Aperture Radar Imagery. *Oceanography* 26(2), 68-79.

Jacobsen, N.G., Fredsoe, J., Jensen, J.H., 2014. Formation and development of a breaker bar under regular waves. Part 1: Model description and hydrodynamics. *Coastal Engineering* 88, 182-193.

Jacobsen, N.G., Fuhrman, D.R., Fredsøe, J., 2012. A wave generation toolbox for the open-source CFD library: OpenFoam®. *International Journal for Numerical Methods in Fluids* 70(9), 1073-1088.

Jasak, H., 1996. Error analysis and estimation for the finite volume method with applications to fluid flows. PhD thesis. *Department of Mechanical Engineering, Imperial College of Science, Technology and Medicine*.

Jasak, H., Jemcov, A., Tukovic, Z., 2007. OpenFOAM: A C++ library for complex physics simulations, *International workshop on coupled methods in numerical dynamics*, 1-20.

Jeans, G., Calverley, M., Jeffery, W., Jackson, C., Vlasenko, V., Osborne, A., 2012. Worldwide internal soliton criteria, *Oceanology International, London, UK*, 14-15.

Jo, T.-C., Choi, W., 2002. Dynamics of strongly nonlinear internal solitary waves in shallow water. *Studies in Applied Mathematics* 109(3), 205-227.

Jo, T.-C., Choi, W., 2008. On Stabilizing the Strongly Nonlinear Internal Wave Model. *Studies in Applied Mathematics* 120 (1), 65-85.

Kadomtsev, B., Petviashvili, V., 1970. On the stability of solitary waves in weakly dispersing media, *Sov. Phys. Dokl*, 539-541.

Kakutani, T., Yamasaki, N., 1978. Solitary waves on a two-layer fluid. *Journal of the Physical Society of Japan* 45(2), 674-679.

Kao, C.-Y., Kodama, Y., 2012. Numerical study of the KP equation for non-periodic waves. *Mathematics and Computers in Simulation* 82(7), 1185-1218.

Keulegan, G.H., 1953. Characteristics of internal solitary waves. *Journal of Research of the National Bureau of Standards* 51, 133-140.

Kharif, C., Pelinovsky, E., 2003. Physical mechanisms of the rogue wave phenomenon. *European Journal of Mechanics - B/Fluids* 22(6), 603-634.

Klettner, C.A., Eames, I., 2012. Momentum and energy of a solitary wave interacting with a submerged semi-circular cylinder. *Journal of fluid mechanics* 708, 576-595.

Klettner, C.A., Eames, I., 2015. On the integral quantities of a low amplitude solitary wave shoaling on a mild slope. *Computers & Fluids* 119, 224-234.

Klymak, J.M., Pinkel, R., Liu, C.-T., Liu, A.K., David, L., 2006. Prototypical solitons in the South China Sea. *Geophysical Research Letters* 33 (11), L11607.

Kodama, Y., 2010. KP solitons in shallow water. *Journal of Physics A: Mathematical and Theoretical* 43 (43), 434004.

Kodama, Y., 2012. KP solitons and Mach reflection in shallow water. *The Autumn Conference of Mathematical Society of Japan*.

Kodama, Y., Oikawa, M., Tsuji, H., 2009. Soliton solutions of the KP equation with V-shape initial waves. *Journal of Physics A: Mathematical and Theoretical* 42(31), 312001.

Kodama, Y., Yeh, H., 2016. The KP theory and Mach reflection. *Journal of fluid mechanics* 800, 766-786.

Koop, C.G., Butler, G., 1981. An investigation of internal solitary waves in a two-fluid system. *Journal of fluid mechanics* 112, 225-251.

Korteweg, D.J., De Vries, G., 1895. On the change of form of long waves advancing in a rectangular canal, and on a new type of long stationary waves. *The London, Edinburgh, and Dublin Philosophical Magazine and Journal of Science* 39(240), 422-443.

Kothe, D., Rider, W., Mosso, S., Brock, J., Hochstein, J., 1996. Volume tracking of interfaces having surface tension in two and three dimensions. *AIAA paper* 96(0859), 1-18.

Kreyszig, E., 2011. Advanced engineering mathematics. *Wiley*.

Laitone, E., 1960. The second approximation to cnoidal and solitary waves. *Journal of fluid mechanics* 9(03), 430-444.

Lamb, K.G., Yan, L., 1996. The evolution of internal wave undular bores: comparisons of a fully nonlinear numerical model with weakly nonlinear theory. *Journal of Physical Oceanography* 26(12), 2712-2734.

Lee, C.Y., Beardsley, R.C., 1974. The generation of long nonlinear internal waves in a weakly stratified shear flow. *Journal of Geophysical Research* 79(3), 453-462.

Lee, S.-K., Yan, D., 2012. Hydrodynamic Loads on Jack-up Legs Due to Oceanic Internal Waves, *The Twenty-second (2012) International Offshore and Polar*

Engineering Conference. International Society of Offshore and Polar Engineering (ISOPE), Rhodes, Greece.

Li, Y., Raichlen, F., 2002. Non-breaking and breaking solitary wave run-up. *Journal of fluid mechanics* 456, 295-318.

Li, W., Yeh, H., Kodama, Y., 2011. On the Mach reflection of a solitary wave: revisited. *Journal of fluid mechanics* 672, 326-357.

Lighthill, M.J., 1949. A Technique for rendering approximate solutions to physical problems uniformly valid. *Philosophical Magazine* 40(311), 1179-1201.

Liu, A.K., Chang, Y.S., Hsu, M.K., Liang, N.K., 1998. Evolution of nonlinear internal waves in the East and South China Seas. *Journal of Geophysical Research: Oceans* (1978–2012) 103(C4), 7995-8008.

Liu, A.K., Holbrook, J.R., Apel, J.R., 1985. Nonlinear Internal Wave Evolution in the Sulu Sea. *Journal of Physical Oceanography* 15(12), 1613-1624.

Liu, A.K., Ramp, S.R., Zhao, Y., Tang, T.Y., 2004. A case study of internal solitary wave propagation during ASIAEX 2001. *IEEE Journal of Oceanic Engineering* 29(4), 1144-1156.

Liu, P.L., 1996. Advances in coastal and ocean engineering, Volume 2. *World Scientific*, 243-246

Long, R.R., 1956. Solitary Waves in the One‐and Two‐Fluid Systems. *Tellus* 8(4), 460-471.

Longuet-Higgins, M.S., 1974. On the Mass, Momentum, Energy and Circulation of a Solitary Wave. *Proceedings of the Royal Society of London A: Mathematical, Physical and Engineering Sciences* 337(1608), 1-13.

Longuet-Higgins, M.S., Cokelet, E.D., 1976. The Deformation of Steep Surface Waves on Water. I. *A Numerical Method of Computation*.

Longuet-Higgins, M.S., Fenton, J., 1974. On the mass, momentum, energy and circulation of a solitary wave. II. *Proceedings of the Royal Society of London. A. Mathematical and Physical Sciences* 340(1623), 471-493.

Lynett, P.J., Liu, P.L.F., 2002. A two-dimensional, depth-integrated model for internal wave propagation over variable bathymetry. *Wave Motion* 36(3), 221-240.

Maderich, V., Talipova, T., Grimshaw, R., Pelinovsky, E., Choi, B., Brovchenko, I., Terletska, K., Kim, D.C., 2009. The transformation of an interfacial solitary wave of elevation at a bottom step. *Nonlinear Processes in Geophysics* 16(1).

Madsen, P.A., Fuhrman, D.R., Schäffer, H.A., 2008. On the solitary wave paradigm for tsunamis. *Journal of Geophysical Research: Oceans* (1978–2012) 113(C12).

Makarenko, N.I., Maltseva, J.L., Kazakov, A.Y., 2009. Conjugate flows and amplitude bounds for internal solitary waves. *Nonlinear Processes in Geophysics* 16(2), 169-178.

Mayer, S., Garapon, A., Sørensen, L.S., 1998. A fractional step method for unsteady free-surface flow with applications to non-linear wave dynamics. *International Journal for Numerical Methods in Fluids* 28(2), 293-315.

Melville, W., 1980. On the Mach reflexion of a solitary wave. *Journal of fluid mechanics* 98(02), 285-297.

Michallet, H., Barthelemy, E., 1998. Experimental study of interfacial solitary waves. *Journal of fluid mechanics* 366, 159-177.

Miles, J.W., 1977a. Obliquely interacting solitary waves. *Journal of fluid mechanics* 79(01), 157-169.

Miles, J.W., 1977b. Resonantly interacting solitary waves. *Journal of fluid mechanics* 79(01), 171-179.

Miles, J.W., 1979. On internal solitary waves. *Tellus* 31(5), 456-462.

Miles, J.W., 1980. Solitary waves. *Annual Review of Fluid Mechanics* 12(1), 11-43.

Miles, J.W., 1981. Korteweg-de Vries Equation: A Historical Essay. *Journal of fluid mechanics* 106, 131-147.

Mirie, R.M., Pennell, S.A., 1989. Internal solitary waves in a two‐fluid system. *Physics of Fluids A: Fluid Dynamics* (1989-1993) 1(6), 986-991.

Mirie, R.M., Su, C., 1984. Internal solitary waves and their head-on collision. Part 1. *Journal of fluid mechanics* 147(1), 213-231.

Mirie, R.M., Su, C., 1986. Internal solitary waves and their head‐on collision. II. *Physics of Fluids* 29(1), 31-37.

Miura, R.M., Gardner, C.S., Kruskal, M.D., 1968. Korteweg‐de Vries Equation and Generalizations. II. Existence of Conservation Laws and Constants of Motion. *Journal of Mathematical physics* 9(8), 1204-1209.

Miyata, M., 1985. An internal solitary wave of large amplitude. *La Mer* 23, 43-48.

Miyata, M., 1988. Long internal waves of large amplitude, *Nonlinear Water Waves*. Springer, 399-406.

Morgan, G., Zang, J., 2011. Application of OpenFOAM to Coastal and Offshore Modelling, *The 26th International Workshop on Water Waves and Floating Bodies*, Athens.

Morgan, G.C.J., Zang, J., Greaves, D., Heath, A., Whitlow, C., Young, J., 2011. Using the rasInterFoam CFD model for wave transformation and coastal modelling. *Coastal Engineering Proceedings* 1(32), 23.

Morison, J., Johnson, J., Schaaf, S., 1950. The force exerted by surface waves on piles. *Journal of Petroleum Technology* 2 (05), 149-154.

Nakayama, K., Kakinuma, T., Tsuji, H., Oikawa, M., 2012. Nonlinear oblique interaction of large amplitude internal solitary waves, *Coastal Engineering Proceedings*, p. waves. 19.

Nguyen, H.Y., Dias, F., 2008. A Boussinesq system for two-way propagation of interfacial waves. *Physica D: Nonlinear Phenomena* 237(18), 2365-2389.

Noh, W.F., Woodward, P., 1976. SLIC (simple line interface calculation), *Proceedings of the Fifth International Conference on Numerical Methods in Fluid Dynamics*. Twente University, Enschede. Springer, pp. 330-340.

Oishi, Y., Piggott, M.D., Maeda, T., Kramer, S.C., Collins, G.S., Tsushima, H., Furumura, T., 2013. Three-dimensional tsunami propagation simulations using an unstructured mesh finite element model. *Journal of Geophysical Research: Solid Earth* 118(6), 2998-3018.

Ono, H., 1975. Algebraic solitary waves in stratified fluids. *Journal of the Physical Society of Japan* 39, 1082.

OpenFOAM documentation, 2014. OpenFOAM user guide. *OpenFOAM Foundation*.

Orlanski, I., 1976. A simple boundary condition for unbounded hyperbolic flows. *Journal of Computational Physics* 21(3), 251-269.

Osborne, A.R., Brown, J.R., Burch, T.L., Scarlet, R.I., 1977. The Influence Of Internal Waves On Deepwater Drilling Operations. *Offshore Technology Conference*.

Osborne, A.R., Burch, T.L., 1980. Internal Solitons in the Andaman Sea. *Science* 208(4443), 451-460.

Ostrovsky, L., Stepanyants, Y.A., 1989. Do internal solitions exist in the ocean? *Reviews of Geophysics* 27(3), 293-310.

Ostrovsky, L.A., Grue, J., 2003. Evolution equations for strongly nonlinear internal waves. *Physics of Fluids* 15, 2934.

Ostrovsky, L.A., Stepanyants, Y.A., 2005. Internal solitons in laboratory experiments: Comparison with theoretical models. *Chaos: An Interdisciplinary Journal of Nonlinear Science* 15(3), 037111.

Pedersen, G., 1988. Three-dimensional wave patterns generated by moving disturbances at transcritical speeds. *Journal of fluid mechanics* 196, 39-63.

Perroud, P.H., 1957. The solitary wave reflection along a straight vertical wall at oblique incidence, *Tech. Rep. University of California, Berkeley*.

Perry, R.B., Schimke, G.R., 1965. Large‐amplitude internal waves observed off the northwest coast of Sumatra. *Journal of Geophysical Research* 70(10), 2319-2324.

Peterson, P., Soomere, T., Engelbrecht, J., Van Groesen, E., 2003. Soliton interaction as a possible model for extreme waves in shallow water. *Nonlinear Processes in Geophysics* 10(6), 503-510.

Popinet, S., 2003. Gerris: a tree-based adaptive solver for the incompressible Euler equations in complex geometries. *Journal of Computational Physics* 190(2), 572-600.

Popinet, S., 2011. Quadtree-adaptive tsunami modelling. *Ocean Dynamics* 61(9), 1261-1285.

Popinet, S., 2012. Adaptive modelling of long-distance wave propagation and fine-scale flooding during the Tohoku tsunami. *Natural Hazards and Earth System Science* 12(4), 1213-1227.

Pullin, D.I., Grimshaw, R.H.J., 1988. Finite‐amplitude solitary waves at the interface between two homogeneous fluids. *Physics of Fluids* (1958-1988) 31(12), 3550-3559.

Ramp, S., Yang, Y., Bahr, F., 2010. Characterizing the nonlinear internal wave climate in the northeastern South China Sea. *Nonlinear Processes in Geophysics* 17, 481-498.

Ramp, S.R., Tang, T.Y., Duda, T.F., Lynch, J.F., Liu, A.K., Chiu, C.-S., Bahr, F.L., Kim, H.-R., Yang, Y.-J., 2004. Internal solitons in the northeastern South China Sea. Part I: Sources and deep water propagation. *IEEE Journal of Oceanic Engineering* 29(4), 1157-1181.

Ray, R.D., Mitchum, G.T., 1996. Surface manifestation of internal tides generated near Hawaii. *Geophysical Research Letters* 23(16), 2101-2104.

Rayleigh, L., 1876. On waves. *Phil. Mag* 1(5), 257-279.

Rusche, H., 2002. Computational fluid dynamics of dispersed two-phase flows at high phase fractions. *PhD thesis, Imperial College London (University of London)*.

Russell, J.S., 1838. Report of the Committee on Waves. *Rept. Brit. Assoc. Advancement Sci* 8(417-496), 14.

Russell, J.S., 1844. Report on waves, *14th meeting of the British Association for the Advancement of Science*, p. 390.

Sarbarish, C., Yuji, K., 2014. Construction of KP solitons from wave patterns. *Journal of Physics A: Mathematical and Theoretical* 47(2), 025201.

Scardovelli, R., Zaleski, S., 1999. Direct numerical simulation of free-surface and interfacial flow. *Annual Review of Fluid Mechanics* 31(1), 567-603.

Schwartz, L.W., Fenton, J., 1982. Strongly nonlinear waves. *Annual Review of Fluid Mechanics* 14(1), 39-60.

Sewell, G., 1993. PDE2D: Easy-to-use software for general two-dimensional partial differential equations. *Advances in Engineering Software* 17(2), 105-112.

Sewell, G., 2005. The numerical solution of ordinary and partial differential equations. *John Wiley & Sons*.

Sewell, G., 2010. Solving PDEs in non-rectangular 3D regions using a collocation finite element method. *Advances in Engineering Software* 41(5), 748-753.

Sewell, G., 2013. Solving the KPI Wave Equation with a Moving Adaptive FEM Grid. *Bulletin of Computational Applied Mathematics* 1, 51-67.

Simmons, H., Chang, M.-H., Chang, Y.-T., Chao, S.-Y., Fringer, O., Jackson, C.R., Ko, D.S., 2011. Modelling and prediction of internal waves in the South China Sea. Oceanography-Oceanography Society 24 (4), 88.

Song, Z.J., Teng, B., Gou, Y., Lu, L., Shi, Z.M., Xiao, Y., Qu, Y., 2011. Comparisons of internal solitary wave and surface wave actions on marine structures and their responses. *Applied Ocean Research* 33 (2), 120-129.

Stewart, R.H., 2008. Introduction to physical oceanography. *Texas A & M University*.

Stokes, G.G., 1880. Considerations relative to the greatest height of oscillatory irrotational waves which can be propagated without change of form. *Mathematical and physical papers* 1, 225-228.

Štrubelj, L., Tiselj, I., 2005. CFD simulation of Kelvin-Helmholtz instability, *International Conference Nuclear Energy for New Europe* 2005, pp. 5-8.

Tanaka, M., 1993. Mach reflection of a large-amplitude solitary wave. *Journal of fluid mechanics* 248, 637-661.

Tsuji, H., Oikawa, M., 2007. Oblique Interaction of Solitons in an Extended Kadomtsev–Petviashvili Equation. *Journal of the Physical Society of Japan* 76(8), 084401.

Turner, R., Vanden‐Broeck, J.M., 1988. Broadening of interfacial solitary waves. *Physics of Fluids* 31, 2486.

Ubbink, O., 1997. Numerical prediction of two fluid systems with sharp interfaces. *PhD thesis, University of London UK*.

Ubbink, O., Issa, R.I., 1999. A Method for Capturing Sharp Fluid Interfaces on Arbitrary Meshes. *Journal of Computational Physics* 153(1), 26-50.

Ursell, F., 1953. The long-wave paradox in the theory of gravity waves, *Mathematical Proceedings of the Cambridge Philosophical Society*. Cambridge Univ Press, pp. 685-694.

von Neumann, J., 1943. Explosive Research Report No. 12, Oblique Reflection of Shocks. *Navy Dept., Bereau of Ordnance, Washington, DC*.

Wang, C., Pawlowicz, R., 2012. Oblique wave-wave interactions of nonlinear near-surface internal waves in the Strait of Georgia. *Journal of Geophysical Research: Oceans* 117(C6), C06031.

Wang, C.Z., Meng, Q.C., Huang, H.C., Khoo, B.C., 2013. Finite element analysis of nonlinear wave resonance by multiple cylinders in vertical motions. *Computers & Fluids* 88(0), 557-568.

Wang, X., Wei, G., Du, H., Gu, M., Wang, C., 2016. Characteristics of Mach effect induced by oblique wave-wave interactions of internal solitary waves in ocean. *Chinese Science Bulletin* 61(4-5), 529-535.

Weller, H.G., Tabor, G., Jasak, H., Fureby, C., 1998. A tensorial approach to computational continuum mechanics using object-oriented techniques. *Computers in Physics* 12(6), 620-631.

Wesseling, P., 2009. Principles of computational fluid dynamics. *Springer Science & Business Media*.

Wiegel, R.L., 1964. Water wave equivalent of Mach-reflection, *Proc. 9th. Conf. Coastal Engng. A.S.C.E*, pp. 82-102.

Wu, G.X., Eatock Taylor, R., 2003. The coupled finite element and boundary element analysis of nonlinear interactions between waves and bodies. *Ocean Engineering* 30(3), 387-400.

Wu, G.X., Hu, Z.Z., 2008. A Taylor series-based finite volume method for the Navier–Stokes equations. *International Journal for Numerical Methods in Fluids* 58(12), 1299-1325.

Xu, G.D., Meng, Q., 2016. Waves induced by a two-dimensional foil advancing in shallow water. *Engineering Analysis with Boundary Elements* 64, 150-157.

Xue, J., Graber, H.C., Romeiser, R., Lund, B., 2014. Understanding Internal Wave-Wave Interaction Patterns Observed in Satellite Images of the Mid-Atlantic Bight. *IEEE Transactions on Geoscience and Remote Sensing*, 52(6), 3211-3219.

Yang, Y.J., Tswen Yung, T., Chang, M.H., Liu, A.K., Ming-Kuang, H., Ramp, S.R., 2004. Solitons northeast of Tung-Sha Island during the ASIAEX pilot studies. *IEEE Journal of Oceanic Engineering*, 29(4), 1182-1199.

Yeh, H., Li, W., Kodama, Y., 2010. Mach reflection and KP solitons in shallow water. *The European Physical Journal Special Topics* 185(1), 97-111.

Zabusky, N.J., Kruskal, M.D., 1965. Interaction of" solitons" in a collisionless plasma and the recurrence of initial states. *Physical Review Letters* 15(6), 240.

Zhang, Z., Fringer, O.B., Ramp, S.R., 2011. Three-dimensional, nonhydrostatic numerical simulation of nonlinear internal wave generation and propagation in the South China Sea. *Journal of Geophysical Research: Oceans* 116(C5), C05022.

Zhou, B.Z., Wu, G.X., Meng, Q.C., 2016. Interactions of fully nonlinear solitary wave with a freely floating vertical cylinder. *Engineering Analysis with Boundary Elements* 69, 119-131.